THE MAJIS VIS-NIR CHANNEL: DETECTORS' CHARACTERIZATION AND RADIATIVE TRANSFER MODELING OF JUPITER'S ATMOSPHERE

Thèse présentée en vue de l'obtention du grade de
Docteure en Sciences

MIRIAM ESTEFANÍA CISNEROS GONZÁLEZ

SUPERVISORS:

Prof. Clément Lauzin
Dr. Séverine Robert

MEMBERS OF THE JURY:

Dr. François Poulet
Prof. Manuel López Puertas
Dr. Özgür Karatekïn
Dr. Matthieu Génévriez (secretary)
Prof. Xavier Urbain (chairman)

UCLouvain
Institute of Condensed Matter and Nanosciences

December 2024– version 2.0

To those who helped me
to believe in myself

ACKNOWLEDGMENTS

I would like to express my sincere gratitude to everyone who supported me through this experience that strengthened my personal and professional growth.

My deepest thanks go to Séverine Robert who, through her words and actions, has been a pillar of my professional life, mainly guiding me toward new research areas, and fostering my personal confidence. You always show a sincere concern for the competencies I needed to develop for my research and beyond. I am also grateful to Justin Erwin, who also took part of my supervision, taking care of my progress down to the smallest details and helping me address new problems.

I am thankful to Ann Carine Vandaele and David Bolsée, respectively heads of the *Planetary Aeronomy* and *Solar Irradiance and Radiometry* departments during most of my Ph.D. journey, for their considerate support, trust and concern for my well-being. I also appreciate the healthy work environment fostered by both teams, where fairness and collaboration were always evident. Special thanks to Nuno Pereira, Lionel van Laeken, Cédric Depiesse, Ian Thomas, Philip Vanhellemont, Yannick Willame, Lori Neary, Loïc Trompet, Arianna Piccialli, João Dias, and Alexis Libert, for their honest advice and partnership.

I am grateful to the MAJIS team, particularly François Poulet, who provided consistent support and valuable guidance throughout my Ph.D. I also appreciate the opportunity of working with Paolo Haffoud, Yves Langevin and Davide Grassi, as well as Jean-Pierre Dubois, Cydalise Dumesnil, Véronique Hervier, Christian Ketchazo, John Carter, Nicolas Ligier, Claudia Ruiz-de-Galarreta-Fanjul, Benoît Lecomte, and Pierre Guiot, whose expertise enriched my professional development.

I acknowledge Lars Jacobs, Pierre Gerard, Sophie Berkenbosh, Birgit Ritter, B.USOC, CNES and ESA, for their support and availability in the characterization facility, particularly to Pierre-Elie Crouzet for his collaboration. I also appreciate the invaluable time of Manuel López-Puertas for assisting me in the validation of the radiative transfer model, in addition to Gianrico Filacchione who kindly provided the observational data used for that same purpose.

I thank my colleagues at UCLouvain, to Clément Lauzin, who provided feedback to enhance my work, besides Sorin Melinte and Benoît Hackens for their advice on the cryogenic system. Additionally, I am grateful to Ali BenMoussa, Özgür Karatekïn, and Sergey Shestov from the Royal Observatory of Belgium (ROB) for introducing me to the space missions world and supporting my path to this Ph.D.

At the beginning of this journey, I did not think that leaving my family, friends and loved ones behind would be so hard. I finally thank my closest friends, some of them already mentioned, who became my second family in Belgium and for which I will be always thankful. I extend my deepest gratitude to Zachary Flimon, Ermioni Dimitropoulou, Daniele Minganti, Shohei Aoki, Lucie Lamort, Sieglinde Callewaert, Antonio Martínez, Bert van Opstal, Oindrila Nath, and María Luisa Alonso, for their genuine friendship. Thanks to Nora Tanarro, Marisol Jimenez, Gerardo Alejos, Eva Puebla, Pepe Vilaplana, and Zoylo Puglia for your unforgettable company. I am also sincerely grateful to the Latin American Catholic Community of Brussels, who filled my life with music and faith, making this journey more easy. Thanks to P. Óscar for your great assistance and the work you provide to the community. Special thanks also to my old friends who supported me in the distance, Rogelio Higuera, Chava Ventura, Aline Galindo, Sergio Rojas, Rafa Hasegawa, César Rojas, Daniel Olmedo, Israel Zapata, Óscar Cinco, Balaam Alarcon, Vianey Yañez, Richard García, Octavio Marín, and Héctor and Lalo Ibarra.

Agradezco enormemente a mi familia, que espera paciente cada año la oportunidad de coincidir nuevamente, y que me ayuda a valorar el tiempo que compartimos sin importar lo que pasemos. Gracias por la fuerza y el amor con que siguen mi vida, sus enseñanzas trascienden en mi corazón y las llevo conmigo como si les llevara a ustedes. Los quiero mucho.

Finalmente agradezco a Dios quien, a través de todos ustedes, me mostró lo importante que es compartir cuando se tiene y lo valioso que resulta compartir cuando no es el caso.

This thesis was funded by BIRA-IASB in 2018-2019 and 2023-2024, and by the *Fonds de la Recherche Scientifique* (FNRS) in 2019-2023, under the Aspirant Grant: 34828772, MAJIS Detectors and Impact on Science.

ABSTRACT

Jupiter is the largest planet in the Solar System and is of interest to the scientific community due to the extreme conditions at which its constituents are exposed. The planet has no surface and is surrounded by an envelope of hydrogen and helium with the presence of methane, ammonia and water among other species. The dynamic atmosphere produces different phenomena that contribute to the mixing of compounds, making it difficult to determine the spatial distribution of molecules and aerosols. Moreover, sunlight is responsible for the photodissociation of molecules, especially methane whose absorption shapes the temperature profile of the atmosphere by warming it up in the intermediate regions. A new mission to the Jovian system was launched in 2023 to constrain the current information about Jupiter and the Galilean moons, with additional observations and measurements. The Jupiter ICy Moons Explorer (JUICE) contains different scientific instruments that contribute to the characterization of the planet. This thesis work focuses on the Moons and Jupiter Imaging Spectrometer (MAJIS), a hyperspectral imager to cover wavelengths between 0.5 and 5.5 μm. The visible and near-infrared (VIS-NIR) channel of MAJIS is of interest due to its capabilities for the study of aerosols and atmospheric composition from 0.5 to 2.35 μm.

To understand the actual performances of the MAJIS VIS-NIR channel, it was necessary to characterize its detectors by providing information about the quantum efficiency, linearity, full-well capacity, uniformity and noise of each pixel. This was possible with the development of a characterization facility, from which the cryogenic system was the main responsibility for this work. The measured performances of the VIS-NIR detectors constituted key parameters for the development of the radiometric model of the MAJIS instrument, after its complete calibration. The radiometric model is able to provide the Signal-to-Noise Ratio (SNR) of a simulated radiance, which can be derived from a radiative transfer model of Jupiter's atmosphere.

ASIMUT-ALVL was the radiative transfer software to model planetary atmospheres available for this work but did not include the necessary capabilities to model Jupiter's atmosphere. Therefore, the

second main objective of this thesis consisted of the implementation of the Jupiter case in ASIMUT-ALVL, which later can be used to assist the scientific activities of the MAJIS team, especially at wavelengths smaller than 2 μm. The starting point included the understanding of the different spectral contributions that shape the spectrum of Jupiter's atmosphere between 0.5 and 2.35 μm. An extensive review of the literature was performed during this work, and finally, a new version of ASIMUT-ALVL with the most recent information to constitute the different spectral contributions was implemented. It includes the molecular absorption of methane, ammonia and water; Rayleigh scattering due to hydrogen and helium; Collision Induced Absorption (CIA) due to the interaction between the main species in Jupiter's atmosphere; and Mie scattering due to aerosols models from different authors. The radiative transfer model was used to produce a forward simulation of Jupiter's atmosphere to assess the preliminary VIS-NIR capabilities of MAJIS and the scientific breakthroughs that will be made possible.

This thesis is composed of four parts. The first part consists of an introduction to Jupiter's science and exploration, to open the interest of studying Jupiter and its atmosphere. This part finishes with a brief description of the JUICE mission and focuses on MAJIS. Later, the second part discusses the need to characterize the detectors of MAJIS and the development of a facility to perform such measurements in the VIS-NIR wavelength range. This part also includes the main results of the different characterization campaigns that took place. The third part is dedicated to remote sensing theory and the development of the radiative transfer model to study Jupiter's atmosphere. Finally, the last part of this thesis joins the main results of parts II and III by providing the assessment of the actual performances of the VIS-NIR channel. The thesis finalizes with the description of further activities that can be made with the products of this work to support the MAJIS science team in the preparation activities for the expected arrival of the JUICE mission around Jupiter, in 2031.

CONTENTS

LIST OF FIGURES

LIST OF TABLES

Part I

INTRODUCTION AND OBJECTIVES

1 JUPITER AND ITS EXPLORATION

Jupiter is the most massive planet in the Solar System. Its gravity is able to retain the lightest atomic elements in the universe. Besides, it played a crucial role in the formation of the other planets in the Solar System, as the giant planets are typically the first ones to form. Jupiter is mostly composed of hydrogen and helium with a similar composition to that of the Sun. As a gas giant planet, it does not have a surface. The circulation within the atmosphere is mainly due to convection driven by its internal heat. The structured gas bands, observed in its atmosphere, are very dynamic and have different colorations and compositions that are still under study. The local abundances and distribution of the atmospheric compounds need to be better constrained, including the properties of the aerosols forming the clouds. Despite Jupiter is probably the most observed gas planet in the Solar System, many open questions remain. This chapter introduces the current known properties and characteristics of the planet and describes the different missions that have studied the Jovian system. Most of the presented information was extracted from *Jupiter: The planet, satellites and magnetosphere* [1], and *Giant planets of our solar system: atmospheres, composition, and structure* [2]. The chapter concludes by discussing some of the main scientific questions related to its atmosphere.

1.1 OVERVIEW

Together with Saturn, Uranus and Neptune, Jupiter is part of the *giant planets* of the Solar System. They comprise 99.56 % of the planetary mass, being by far the largest planetary bodies in the Solar System [2]. Jupiter and Saturn constitute the *gas planets* since they are mainly composed of the lightest and most abundant gases in the universe: hydrogen (H_2) and helium (He). Uranus and Neptune are known as *ice planets* because they are mainly composed of ices of water (H_2O) and methane (CH_4). All giant planets in the Solar System have fast rotation periods (between 10 and 17 hours), in comparison with terrestrial planets (>24 hours). In consequence, giant planets have significantly *oblate* shapes and *differential rotation*, meaning that different rotation

Property	Value	Jupiter/Earth[d]
Mean radius[a]	69 911 ± 6 km	10.97
Mean distance from the Sun[a]	5.203 AU	5.203
Mass[a]	1.89826×10^{27} kg	317.83
Equatorial gravity at 1 bar[b]	24.79 m/s^2	2.53
Rotation period[b]	9.93 hours	0.41
Orbit eccentricity[b]	0.0487	2.92
Temperature at 1 bar[c]	166.1 K	0.58
Bond albedo[b]	0.343	1.17
Obliquity[b]	3.13°	0.134
Molar mass of dry air	2.305 g/mol	0.08
Scale height[b]	27 km	0.315

Table 1.1: Main physical properties of Jupiter. [a] Bagenal, Cambridge University Press, 2006 [1], [b] NASA Jupiter's Fact Sheet [3], [c] Moses et al. 2005 [4], [d] NASA Earth's Fact Sheet [5].

rates are present at different latitudes and depths of the planet [2]. For comparison, Jupiter's equatorial radius is 71492 km against a polar radius of 66854 km [3], while corresponding Earth's radii variations is no higher than 0.3 %. Table 1.1 presents the main physical parameters of Jupiter in comparison to those from Earth. They are further explored hereafter.

Giant planets have no surface. Instead, the pressure merely increases towards their core. In Jupiter, a dense but dilute core expands through a region 0.3 to 0.5 times the planet's radius [6]. Pressures in the center of Jupiter can reach $\sim 40 \times 10^6$ bar [2]. Therefore, the core is immersed in a metallic hydrogen-helium envelope that extends over 90 % of the radius of the planet and is able to sustain a dynamo responsible for the powerful magnetic field of Jupiter, which on the night side can extend to Saturn's orbit [2]. A helium rain layer surrounds the metallic hydrogen-helium envelope. This layer is still under study and corresponds to a region where droplets of liquid helium form but are not able to mix with the liquid metallic hydrogen below [2]. Finally, the molecular layer surrounding the helium layer constitutes Jupiter's atmosphere [6]. The boundary is expected to be smooth although representing some kind of barrier to convective heat transfer. Actually, the circulation of Jupiter's interior is not well understood but the most accepted assumption

expects convective heat transfer to be the main mechanism, becoming weaker in the atmosphere where radiative heat transfer should be dominant at levels, even from pressure values below 10^3 bar [2].

As in other planets with no surface, the radius of Jupiter is arbitrarily defined by the distance from its center of mass to the 1 bar pressure level [7]. On Earth, this pressure level corresponds to the sea level and defines the zero elevation or *altitude*. Therefore, on Jupiter, altitude has positive values above the 1 bar pressure level and negative values below the 1 bar pressure level. The polar and equatorial radii of Jupiter were determined after measurements performed by Pioneer and Voyager spacecrafts [8]. Jupiter's mass was also defined from Pioneer data [8], while the gravity field was measured from Voyager flybys [1]. For terrestrial planets, an arbitrary reference on the surface allows the definition of a longitude system and the determination of their rotation period. The lack of a fixed reference for gas planets originates the assumption that the rotation period is tied to the rotation rate of their magnetic fields, which represents the true rotation of the planet [9]. This can actually be measured and is how the System III of coordinates for Jupiter is defined [10]. Therefore, the wind speeds of the atmosphere can be measured with respect to the rotation period.

Another important aspect in planetary sciences is the *obliquity* of the planet, defined as the angle between the rotational axis and the normal to its orbit [11]. It is expected that giant planets show obliquity angles near zero. Obliquity is generally related to seasonal climate changes. However, Jupiter's low obliquity is not relevant to seasonal changes in its weather. The seasonal effects in Jupiter are actually linked to the eccentricity of its orbit, which originate temperature waves with maximum amplitudes of 3 K below 0.3 bar [9].

The *albedo* can be understood as the reflectivity of a planet. It can only have a value between 0 and 1, which means that the planet absorbs all incident radiation when the albedo is zero, or reflects all incident radiation when the albedo is one [12]. This quantity will depend on the characteristics of the planet and the wavelength of radiation. The radiation that is absorbed by the planet will heat it. The *bond albedo*, also known as *spherical albedo*, refers to the fraction of incident radiation on the planet that is scattered out into space in all directions and for all wavelengths. The difference against *geometric albedo* is that, in this case, the fraction of incident radiation that is scattered out, comes in the same direction as the incident radiation [13].

Finally, the *molar mass of dry air* is related to the average molar mass of the molecules constituting the atmosphere without considering water vapor [14]. In radiative transfer models, this value is typically used to interpolate atmospheric pressures through the use of the hydrostatic law and the *scale height* of the planet. The scale height is defined as the decrease in altitude for which the atmospheric pressure decreases by a factor of e [2].

It is worth mentioning that Jupiter has 95 satellites officially recognized by the International Astronomical Union (IAU), without considering other bodies in Jupiter's orbit, such as the *trojan asteroids* [15]. However, only eight of these satellites can be considered *regular moons*, as they orbit in Jupiter's equatorial plane with almost circular orbits. The largest moons of Jupiter are also known as the *Galilean satellites*, after their discovery by Galileo Galilei in 1610, and include Io, Europa, Ganymede and Callisto [16]. The last three moons harbor water oceans below their icy surfaces, and are referred to as *icy moons*.

Finally, Jupiter has a small ring that was first observed in 1979, although is not as brilliant as the one of Saturn since it is mainly composed of dust [15].

1.2 STRUCTURE AND COMPOSITION

Jupiter's appearance at visible (VIS) wavelengths is dominated by a structure of bands parallel to the equator with different properties such as coloration, speed, rotation sense, and composition (Figure 1.1). This band structure is typically present on fast-rotating planets due to the dominance of the Coriolis force over solar heating [9]. The atmospheric gas parcels preferably move in a direction perpendicular to the rotation axis of the planet, instead of simply rising at the equator where the temperature is high, to move towards the poles until they descend because of lower temperatures, and return to the equator later again. Therefore, latitudinal wind velocities are generally much lower than longitudinal wind velocities [2]. Still, the Coriolis force is stronger close to the equator and thus gas is deflected eastwards as it moves towards the poles at high altitude, and deflected westwards as it returns to the equator at low altitudes [2]. These bands are traditionally classified as *zones* if they have clear coloration, or *belts* if they have dark coloration (Figure 1.2).

The general structure of Jupiter bands is considered stable but not necessarily the color contrasts observed in each of them nor their widths

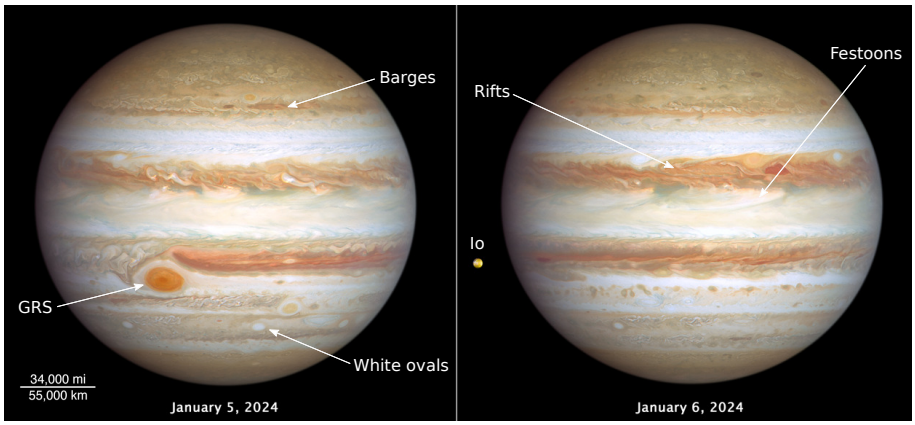

Figure 1.1: Pictures of Jupiter and main visible features, taken from the Hubble Space Telescope (HST), capturing both sides of the planet. GRS stands for Great Red Spot. The picture is available in [17].

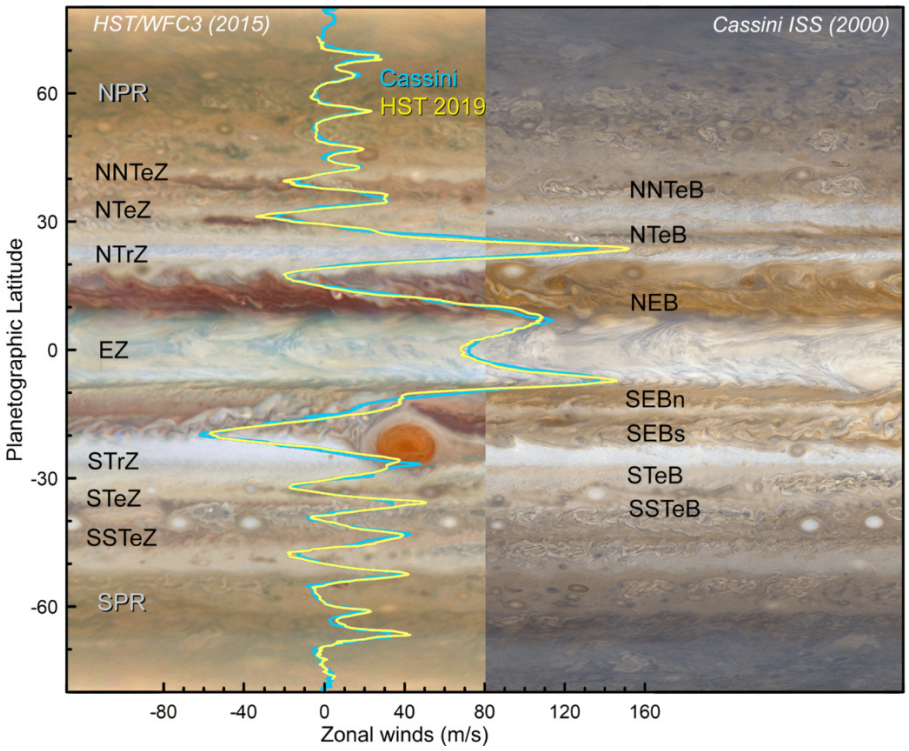

Figure 1.2: Jupiter bands and zonal winds presented by latitude, as extracted from [18]. Acronyms definition for zones (left) and belts (right) can be found in the list of acronyms E.2.

[1, 2]. This can be seen in Figure 1.2 by comparing the band structure of the picture taken by the Hubble Space Telescope (HST) (left) and the picture taken by Cassini some years before (right). Moreover, vortices and oval structures can be observed in some of the bands, being the Great Red Spot (GRS) the most characteristic one. Additionally, as observed in Figure 1.2, the winds in each of the bands have different speeds and actually alternate direction from belts to zones. For instance, the zonal wind at the equator reaches speeds up to 100 m/s in the eastward direction, while the north temperate belt reaches speeds no higher than 50 m/s in the westward direction [1]. Since some molecules appear depleted over belts and relatively enhanced over zones, and belts appear to have low aerosols content and warmer air temperatures around the equator, it is clear that the abundances of these compounds are not driven only by condensation but by dynamics [19].

Other visible features in Jupiter's atmosphere include barges, festoons, rifts, and white ovals (Figure 1.1). *Barges* typically appear in regular chains, while *white ovals* appear to be isolated but they eventually merge with others to form larger vortices [2]. Actually, the white ovals are the most prominent features in Jupiter's atmosphere, together with the GRS, and are subjected to color changes [20]. Moreover, additional cyclones are observed at the polar regions of Jupiter's atmosphere, where a central cyclone is surrounded by a ring of *circumpolar cyclones* in both poles [21].

If Jupiter's atmosphere is now observed from top to bottom (Figure 1.3), different layers can be defined depending on how the temperature varies along altitude:

- **Exosphere:** Typically defined as the *escape region* of a planet. It corresponds to the altitude level at which an atmospheric particle has a mean free path larger than the scale height of the planet. For Jupiter, this happens above 2000 km (not visible in Figure 1.3), where the temperature reaches 700 K [9], and an atmospheric particle can travel up to 27 km before colliding or substantially modifying its trajectory.

- **Thermosphere:** The temperature at this region decreases with decreasing altitude and is normally the result of absorption of Extreme Ultraviolet (EUV) radiation and charged particles from Jupiter's magnetic field, producing *ionization* and causing a drop in molecular abundances except for the lightest species [23]. However, measured temperatures at these altitude levels are much

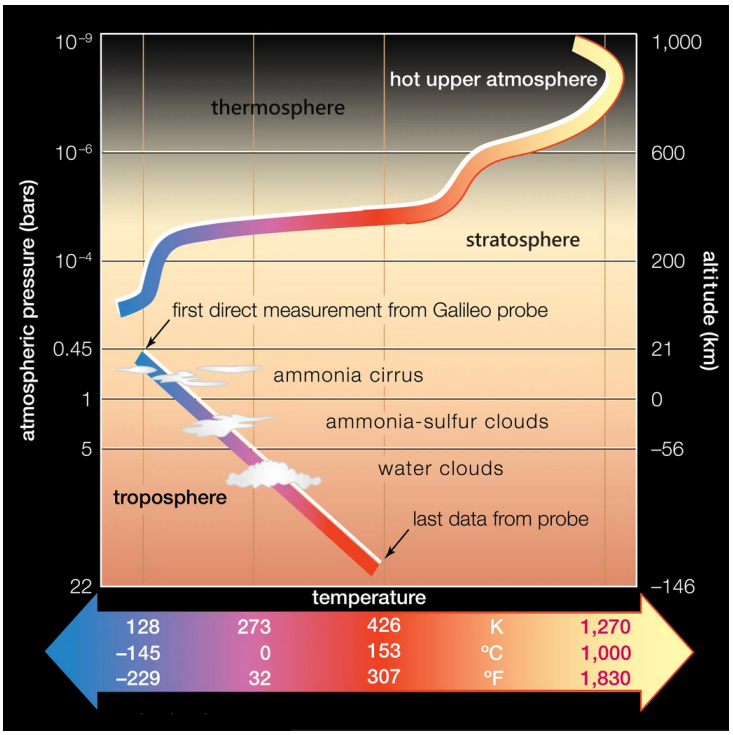

Figure 1.3: Jupiter's atmospheric structure (extracted from [22]).

higher than predicted by theory. The reason for this energy crisis is common to other giant planets and is an object of study [1, 24].

- **Stratosphere:** In this region, the atmosphere is considered to form stable stratified layers. Heat is still transferred by radiation. Temperature decreases with decreasing altitude at a different rate from the thermosphere, depending on the absorption of ultraviolet (UV) radiation and the amount of radiation absorbed by aerosols [1]. Absorption of UV radiation leads to *photodissociation*. Therefore, temperature, composition and dynamics in the stratosphere relate to each other by the incoming sunlight [23]. In consequence, the vertical distribution of aerosols, and especially the photochemical products, is critical to determine the temperature along this layer [2].

- **Troposphere:** It is the lowest part of the atmosphere and is also known as the *weather layer* since it is constituted by layers of condensate clouds. It extends from tens of bars to hundreds of millibars. Temperature increases with decreasing altitude due to

the increasing pressure towards deeper levels in Jupiter's atmosphere. Therefore, the atmosphere is heated by the interior of the planet by convection [2, 9].

Finally, the composition of Jupiter's atmosphere can be described by the relative abundance of one molecular species with respect to the total gas mixture, which is known as the *Volume Mixing Ratio* (VMR) [25]. Table 1.2 lists nominal values for the deep abundances of the most common compounds in Jupiter's atmosphere, i.e., at the 1 bar level. Spectral observations and models help to constrain those values and define the chemical processes that take place [2].

Note that after H_2 and He, the most abundant species in Jupiter's atmosphere are hydrogenated molecules formed from heavier elements such as carbon (C), nitrogen (N), oxygen (O), and sulfur (S) [18]. Although these molecular compounds were also present in the solar nebulae, *exogenic species* are additionally introduced or even generated by cometary impacts in the atmosphere of Jupiter, including carbon monoxide (CO), carbon dioxide (CO_2) and hydrogen cyanide (HCN) [2, 23]. Tracing the spatial distribution of these and other long-lived or *disequilibrium* species, including phosphine (PH_3), germane (GeH_4) and arsine (AsH_3), allows to provide an insight on Jupiter's atmospheric dynamics [2].

Molecules are constantly lifted through the atmosphere without mixing with the surrounding air. Some of them, the *volatiles*, reach the appropriate temperature and pressure conditions to condense around small particles and form clouds [9]. Typically these aerosols will not be able to continue rising above the troposphere and re-evaporate, limiting their molecular abundances in the stratosphere [2]. In this way, it is expected to encounter NH_3 clouds between 0.8 and 0.4 bar, ammonia-sulfur (NH_4SH) clouds around 2 bar, and H_2O clouds between 6 and 2 bar (Figure 1.3) [9]. NH_4SH results from reactions between NH_3 and hydrogen sulfide (H_2S).

CH_4 is the only hydrogenated molecule that does not condense in Jupiter's atmosphere. CH_4 plays a major role in the photochemistry of Jupiter's atmosphere by breaking due to UV radiation in the stratosphere and recombining in other hydrocarbons. As these new hydrocarbons are typically heavier than CH_4, they eventually fall deeper into the atmosphere until they encounter high temperatures that convert them back into CH_4 [4]. CH_4 is again transported upwards through the troposphere and continues the cycle. Similarly, NH_3 can also photo-

Species	Symbol	VMR
Hydrogen	H_2	0.86
Helium	He	0.136
Methane	CH_4	0.0018
Ammonia	NH_3	0.007
Water	H_2O	0.005
Hydrogen Sulfide	H_2S	77 ppm
Neon	Ne	20 ppm
Argon	Ar	16 ppm
Hydrogen deuteride	HD	15 ppm
Ethane	C_2H_6	4 ppm
Phosphine	PH_3	0.5 ppm
Deuterated methane	CH_3D	0.3 ppm
Acetylene	C_2H_2	35 ppb
Propane	C_3H_8	26 ppb
Krypton	Kr	8 ppb
Carbon monoxide	CO	0.8 ppb
Hydrogen cyanide	HCN	0.8 ppb
Xenon	Xe	0.8 ppb
Germane	GeH_4	0.6 ppb
Ethylene	C_2H_4	0.3 ppb
Arsine	AsH_3	0.2 ppb

Table 1.2: Molecular abundances in Jupiter's atmosphere at 1 bar [1, 2].

dissociate following significant EUV absorption at the low troposphere [26].

1.3 AEROSOLS MODELS

Aerosols in Jupiter are constituted of *haze* and clouds. Following the definitions in [1], Jupiter haze refers to groups of particles suspended at pressure levels lower than 500 mbar, while *clouds* refer to groups of particles suspended at deeper pressure levels of Jupiter's atmosphere generally larger in size. The precise composition, size distribution and

structure of Jupiter's aerosols are still uncertain. The understanding of such characteristics together with the determination of their vertical distribution, can reveal information about the atmospheric processes on the planet, including meteorology, circulation mechanisms, and the impact of the jovian aerosols in Jupiter's radiative budget [1].

Different models have been proposed to constrain and define aerosols in Jupiter to reproduce spectral observations from ground-based or space telescopes. A reference starting point is the *Equilibrium Cloud Condensation Model* (ECCM), which provides a general shape of the abundance profile of a condensable species by locating it at the appropriate temperature and pressure conditions to form clouds (Figure 1.3). However, precipitations and Jupiter's dynamics move volatiles vertically and horizontally, and the cloud density profiles as predicted by this model, are rarely observed in Jupiter's atmosphere [9].

The model of West et al. in [1] is the more generalized cloud model for Jupiter's atmosphere. It summarizes a large collection of observations made until 2004, including the Pioneer [8], Voyager [27], HST [28], and Galileo [29] missions. The model has the advantage of having a robust experimental basis while being consistent with the ECCM [19]. Figure 1.4 shows the scheme of this proposed cloud structure. It consists of an upper haze of sub-micron particles at the top of a denser cloud from 0.9 to 0.5 bar, followed by a deeper cloud located around 1.5 bar and probably constituted of NH_4SH. Below 3 bar, the model suggests the presence of a deeper H_2O cloud.

Dahl et al. [30] illustrates at least 10 cloud models from different references that can successfully reproduce the spectra of various atmospheric regions on Jupiter. Some examples discussed in this section include the work of López-Puertas et al. [26], and the *Crème Brulée* (CB) model from Baines et al. [31], which explains the coloration of the clouds by a single universal compound.

The model proposed by López-Puertas et al. [26] matches a measured spectrum of Jupiter's atmosphere from 0.5 to 2.5 μm, detailed in section 6.2. It consists of three different layers of haze near the equator with particle sizes between 0.1 and 0.6 μm at pressure levels from 100 to 0.01 mbar, and a layer of crystalline H_2O ice with particle sizes in the order of 10 nm below 0.1 mbar. This was the first time the presence of H_2O ice in Jupiter's stratosphere was reported. The remaining differences between the simulated and the observed spectrum could not be adjusted in the continuum by changing the particle sizes or concentrations of the aerosols (Figure 6.4). According to López-Puertas

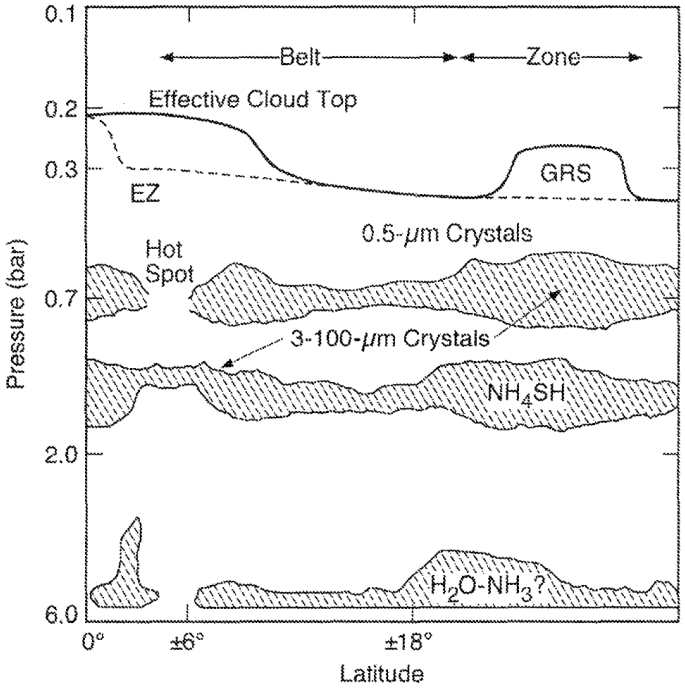

Figure 1.4: Aerosols structure extracted from West et al. in [1]. The thick solid curve at the top corresponds to the haze layer in northern latitudes and the dashed curve to that in the southern latitudes. EZ designates Jupiter's Equatorial Zone and GRS to the Great Red Spot.

et al. [26], such differences could be reduced by considering other haze compositions, or by adding another condensed chemical species in the spectral contributions. Figure 1.5 shows the aerosols distribution proposed by López-Puertas et al. [26]. They considered the refractive index of haze to have a real part equal to that of NH_3 ice and an imaginary part consistent with mixtures of CH_4 and H_2.

The work of Baines et al. [31] is one of the main references in the scientific community to explain the variety of red colorations in clouds and hazes of Jupiter's atmosphere. They explored the use of the reddish compound proposed by Carlson et al. [32], to reproduce the color of the GRS as observed by the Visual Infrared Mapping Spectrometer (VIMS) onboard the Cassini mission. This compound would be the result of acetylene (C_2H_2), which is already the result of reactions between photolytic products of CH_4, reacting with photolytic products of NH_3, such as NH_2 and H radicals. The scientific community refers to the

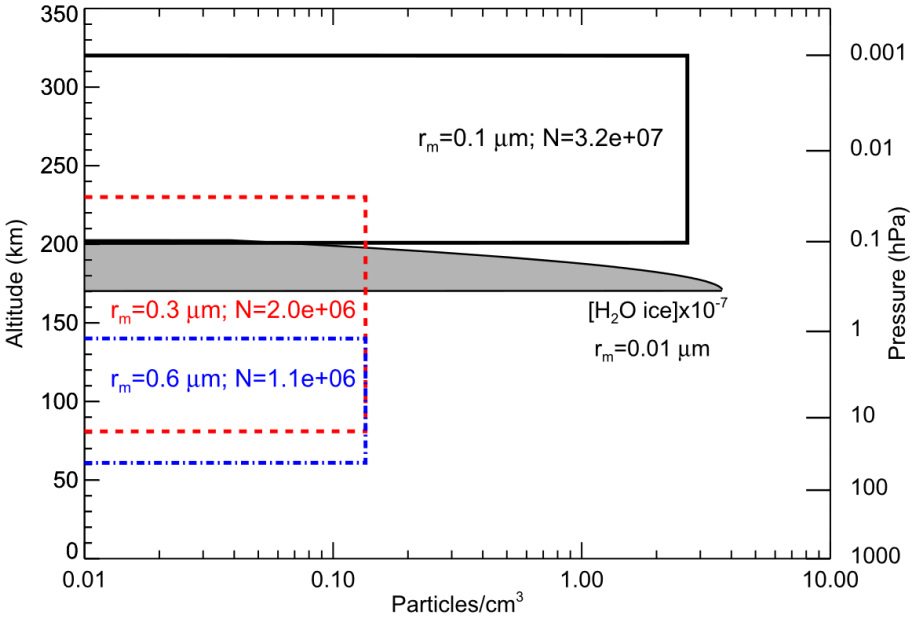

Figure 1.5: Aerosols distribution extracted from the model proposed by López-Puertas et al. [26]. r_m refers to the mean radius of the lognormal particle size distributions, and N to the number density of the layers, in particles/cm^3.

"color" compound as *chromophore*, which condenses around ice particles to form aerosols.

Baines et al. [31] actually proposed three different cloud models by mainly varying the height at which the chromophores might be located (Figure 1.6). Model A considers the chromophores as particles coated by the chemical compounds suggested by Carlson et al. [32] and distributed along the main tropospheric cloud. Model B places the chromophore particles suggested by Carlson et al. [32] at an optically thin layer in the stratosphere. Model C places the chromophore layer on top of the tropospheric cloud and includes an additional cloud layer in the stratosphere. The model that better fits VIMS observations is model C, also referred to as the *Crème Brulée* (CB) model. The proposed particle sizes and locations of this model are consistent with results from Sromovsky et al. [33]. They were the first ones to propose the chromophore reported in Carlson et al. [32] as a universal chromophore for the modeling of the color variations in Jupiter's atmosphere. This proposition was later analyzed by Braude et al. [34] and Dahl et al. [30] and is recently under study [35, 36].

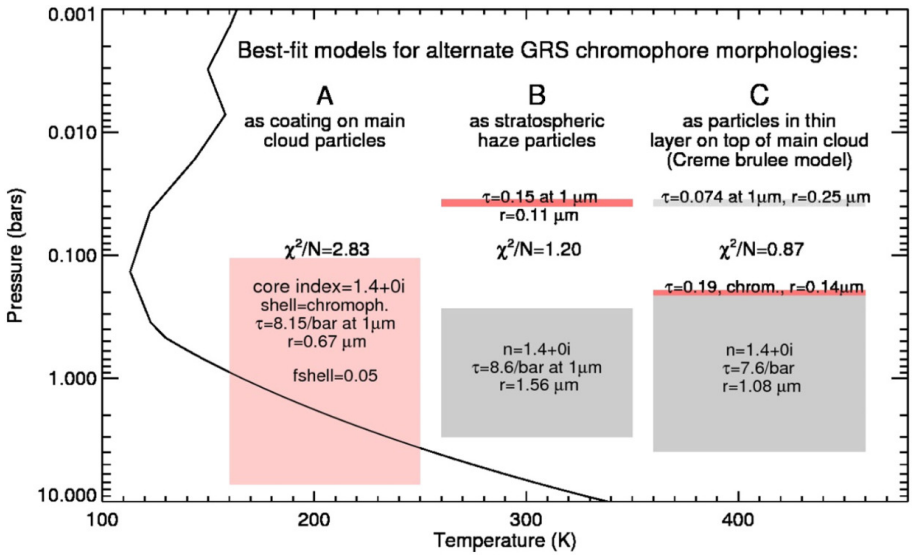

Figure 1.6: Vertical structures of the aerosols models extracted from Baines et al. [31]. Each of the models (A, B, C) suggests a different configuration of clouds (grey layers). The red layers imply the presence of chromophores in that layer. τ refers to the optical depth of the corresponding layer (see section 5.3), r to the mean radius of the particle size distributions, n to the refractive index of the particles contained in the layer, and χ^2/N to the reduced chi-square of the model fit against the reference GRS spectrum. The thick solid curve corresponds to the temperature profile of Jupiter's atmosphere according to Seiff et al. [29].

Certainly, to identify Jupiter's aerosols chemistry, a variety of techniques including imaging, spectroscopy, polarimetry, and *in situ* measurements are necessary [19]. However, laboratory data is also required, especially to properly constrain the origin of chromophores [35, 37]. Moreover, to determine the latitudinal and vertical distribution of aerosols, together with their optical properties, the analysis of at least UV to near-infrared (NIR) spectra is essential [38].

1.4 JOVIAN SYSTEM EXPLORATION

Much of what is known about Jupiter comes from observations of the upper parts of the atmosphere, which are complemented by observations of the vertical cloud structure by remote sensing and *in situ* measurements (section 5) [2]. Certainly, VIS images reveal information about atmospheric dynamics but spectroscopy is necessary to reveal

the composition and distribution of the atmospheric compounds at the different layers of the atmosphere [18]. In order to constrain atmospheric models of Jupiter with observations, data with higher accuracy is needed, and new instruments that comply with those requirements should be developed.

The first space missions that travelled close to Jupiter were the *Pioneer 10* and *Pioner 11* in 1972 and 1973, respectively [1]. They had the purpose of exploring the outer Solar System and were the first ones in traversing the asteroids belt. Among other scientific instruments, they carried a UV photometer (58.4 and 121.6 nm), an imaging photopolarimeter (395-485 nm and 590-690 nm), and an infrared (IR) radiometer (20 and 40 μm). With these instruments, it was possible to investigate H_2 and He emissions from Jupiter's atmosphere, and produce thermal maps of the planet [39–41].

Voyagers 1 and *2* were the next missions to flyby Jupiter and the rest of the giant planets, which were located at the same quadrant during that decade. On this occasion, the spacecrafts were stabilized and could image and point targets of interest. The corresponding closest approaches happened in 1979 with a difference of four months between both spacecrafts [1]. The VIS camera (0.33-0.62 μm) provided two resolution modes (200 and 1500 mm) and, among other instruments, the missions additionally included a UV spectrometer (50-170 nm) with a resolution better than 1 nm, a photopolarimeter (8 wavelengths from 235 to 750 nm), and a VIS-NIR radiometer (0.4-1.2 μm) combined with an IR interferometer spectrometer (1.4-10 μm and 17-170 μm) with two resolution modes (0.57 and 1.84 μm). The main scientific objectives concerning Jupiter included: characterizing the composition and circulation of the atmosphere, determining its vertical thermal structure and compounds distribution, measuring the total amount of sunlight reflected by the atmosphere at the specified wavelength ranges, and measuring the intensity and linear polarization of scattered sunlight along the atmosphere [42].

Other missions performed flybys to Jupiter, including *Ulysses* in 1992 [43], Cassini in 2000 [44], and New Horizons in 2007 [45]. In all cases, as part of gravitational assists to reach their primary objectives in the adequate orbit. Ulysses was dedicated to the study of the Sun and its payload did not include any camera or spectrometers. Cassini was dedicated to Saturn, and actually performed valuable observations of Jupiter's atmosphere during the flyby, as it will be discussed later. New Horizons continued with the heritage of the Voyagers to explore

Instrument	Wavelength range	Spectral Resolution
SSI	0.37-1.1 μm	N/A
NIMS	0.7-5.2 μm	25 nm (>1 μm) 12.5 nm (<1 μm)
UVS	115-430 nm	0.7 nm (<190 nm) 1.3 nm (>190 nm)
PPR	410-945 nm 15-100 μm	N/A N/A

Table 1.3: Spectral performances of part of the instruments of the Galileo mission [47–50].

the edge of the Solar System and provided spectral maps of Jupiter's atmosphere from 1.25 to 2.5 μm, with a spectral resolution of 480 μm during its flyby [46].

The first mission that actually orbited Jupiter was *Galileo*, becoming also the first mission to orbit a giant planet. Galileo had a payload of 10 scientific instruments and an atmospheric probe. This is the only time that *in situ* measurements of the atmosphere of a giant planet have been performed [2]. The probe measured composition, temperature, pressure, wind speed and lighting burst during its descent into the atmosphere, reaching 22 bar [29]. From the instruments onboard Galileo, Table 1.3 summarizes the main performances of those that required stable pointing to perform measurements, including a solid-state imager camera (SSI), a NIR mapping spectrometer (NIMS), a UV spectrometer (UVS) and a photopolarimeter-radiometer (PPR). The mission reached the Jovian system in December 1995 and remained active for almost 14 years, performing a total of 34 orbits of Jupiter with several flybys to its moons [16].

Juno has been orbiting Jupiter since 2016. It is complementary to Galileo, especially because of its eccentric polar orbit around the planet. This minimizes the exposure of the spacecraft to the jovian radiation environment while performing close-in measurements of Jupiter [51]. The payload is composed of eight instruments, from which Jupiter's atmosphere is explored by a conventional VIS imaging camera (JunoCam), an IR imaging spectrometer (JIRAM), a UV imaging spectrometer (UVS), and a microwave radiometer (MWR). Table 1.4 summarizes their main performances. The Juno mission is dedicated to map variations in

Instrument	Wavelength range	Spectral Resolution
JunoCam	0.37-1.1 μm	N/A
JIRAM	2.0-5.0 μm	12.5 nm
UVS	68-210 nm	0.4-1.1 nm
MWR	0.6-22 GHz	N/A

Table 1.4: Spectral performances of the main atmospheric instruments of the Juno mission [51–54].

atmospheric composition, temperature, cloud opacity and dynamics, to depths much greater than 100 bars at all latitudes. It is focused on determining the global water abundance of the planet, and Jupiter's mass distribution and internal structure [51].

During its six-month flyby, Cassini was able to provide valuable data on Jupiter's atmosphere despite it did not pass very close to the planet ($\sim$ 136 Jovian radii) [1]. It actually coincided with the Galileo orbiter and performed simultaneous observations of the Jovian magnetosphere. Among other instruments, Cassini's payload included an imaging camera (ISS) and some spectrometers to cover UV-IR wavelengths. Table 1.5 summarizes the main properties of these instruments. Note that Cassini/VIMS covers VIS-NIR wavelengths that Juno spectrometers did not include and with a significantly better spectral resolution than Galileo/NIMS. In fact, observational data from Cassini/VIMS was considered for the verification of the radiative transfer model of Jupiter, developed for this work (see chapter 6).

Instrument	Wavelength range	Spectral Resolution
ISS	0.2-1.1 μm	N/A
VIMS	0.35-1.05 μm	7.3 nm
	0.85-5.10 μm	16.6 nm
CIRS	7-1000 μm	7.8-317.8 mm
UVIS	55-115 nm	0.21 nm
	115-190 nm	0.24 nm

Table 1.5: Spectral performances of the UV-IR instruments onboard the Cassini mission [55].

It is worth mentioning that some other spacecrafts orbiting Earth have also performed observations of the Jovian system [2]. For instance, the HST has performed spectral observations of Jupiter in a wavelength range of 0.115-1.03 μm, sometimes simultaneously supporting the mentioned space missions. Currently, the James Webb Space Telescope (JWST) is complementing the HST spectral capabilities with a spectral coverage of 0.6-29 μm. It has been in operation since July 2022 and has already performed observations of Jupiter [56–58]. Nevertheless, saturation is observed in most of the spectrographs of the payload during Jupiter observations, limiting the spectral coverage to 5-10 μm [59]. Still, ground-based telescopes are available for the study of Jupiter's atmosphere, providing information from the ionosphere to the troposphere, although limited by Earth's atmospheric absorption [1]. Additionally, the tracking offered by amateur astronomers, especially regarding cometary impacts and disturbances evolution, is always useful.

1.5 OPEN SCIENTIFIC QUESTIONS

Jupiter is an archetype for other gas giant planets both in the Solar System and around other stars throughout our galaxy. Therefore, its complete characterization will unravel the origins of the giant planets and the potentially habitable environments on their satellites [60]. However, although Jupiter has been intensively observed and the understanding of many aspects has progressed, some questions still remain open. Those concerning Jupiter's atmosphere will be discussed in this section. For reference, Figure 1.7 shows the cross-sections at which the optical depth (section 5.3) of different compounds in a typical Jupiter's atmosphere reaches unity, revealing the different pressure levels accessible at different wavelengths. The example was extracted from the work of Sromovsky and Fry [46] and does not consider aerosols.

For instance, a detailed study of the local and global abundances, distribution, and variability of the atmospheric compounds of Jupiter, is important to constrain the conditions and chemical processes that originate them at each of the levels of the atmosphere. Therefore, the following questions can be highlighted:

- **What is the abundance of H_2O?** It is known that Jupiter is enriched in O and C if compared to the protosolar nebulae, where part of the icy planetesimals were composed of H_2O [2]. There-

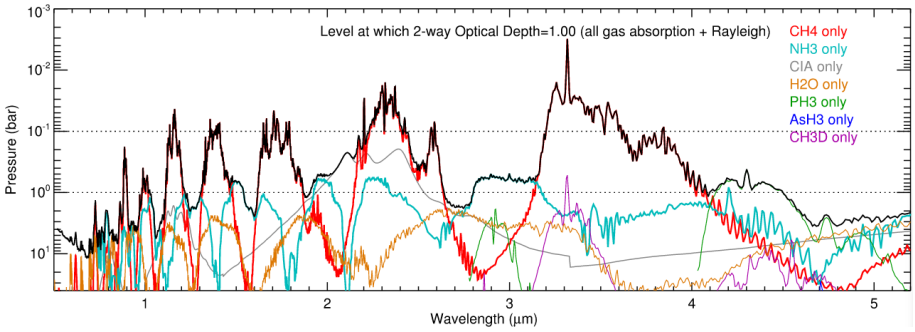

Figure 1.7: Pressure at which the vertical optical depth in a nadir geometry reaches unity, as extracted from [46], for a typical Jupiter atmosphere without considering aerosols. The spectral contribution of all gases combined constitutes the black line.

fore, the measurement of Jupiter's H_2O abundance is central in understanding giant planets' formation and the delivery of volatiles throughout the solar system [51]. However, some difficulties present for this study include the fact that the main NH_3 and other volatile reservoirs remain hidden below the clouds, where the measurement of their abundances is limited due to the strong opacities encountered at these altitudes [18].

- **What is the spatial distribution of CH_4?** As already discussed in section 1.2, CH_4 plays a major role in the photochemistry of Jupiter's atmosphere by driving its thermal structure [61]. Therefore, revealing its spatial distribution and vertical profile constrains temperature variations on the planet, which influence vertical winds and turbulence [18, 62]. Nevertheless, NH_3 significantly absorbs radiation at wavelengths also absorbed by CH_4. Information from the low troposphere is limited in consequence, as spectra are saturated due to the major abundance of CH_4 [26].

- **What is the spatial distribution of NH_3?** Even if some specific information is limited, understanding the global variability of each species provides useful context for the study of different atmospheric processes. For instance, NH_3 is not as abundant over zones as over belts, meaning that its abundance is driven by both condensation and dynamics [19]. Moreover, although NH_3 has long been assumed to be the main source of volatiles for the upper cloud layer on Jupiter, distinctive spectral features associated with NH_3 have been seen only rarely [46].

- **What is the origin and abundance of the exogenic species?** Estimating the elemental abundances in Jupiter's atmosphere constrains the origin and abundances of the exogenic species as well as the composition of the deepest levels of the troposphere [18]. This is based on the isotopic ratios of molecules such as D/H in H_2O, although this is normally performed in submillimeter wavelengths [18]. Moreover, mapping the vertical profiles of H_2O and CO provides an indicator for the origin of the external O [18].

Aerosols properties are also exposed to measurements where CH_4 does not dominate absorption, typically between 0.4 and 3.2 μm [18, 62]. Therefore, NIR wavelengths can reveal signatures of condensed ices of NH_3, NH_4SH and H_2O, especially in strong convective regions of the atmosphere [60]. Actually, even after the descent of the Galileo probe into a relatively cloud-free region with low water content in Jupiter's atmosphere (section 1.4), no compelling evidence for a deep H_2O cloud, as predicted by the ECCM, was found. The observational evidence of this cloud is currently limited to a few small regions [1, 35]. Therefore, open questions related to aerosols in Jupiter's atmosphere may include:

- **What is the variability of aerosols in different regions?** For instance, belts around the equator seem to have a lower content of aerosols and a warmer air temperature than at other locations [19]. Bands with warmer temperatures than average will produce horizontal convergence of gasses, while cooler bands will produce divergence, heat release and up-welling gas from deeper levels [2]. Therefore, cooling caused by the upward motion of atmospheric parcels causes the condensation of cloud particles in parts where the atmosphere contains volatiles. The subsequent release of latent heat causes the temperature to slowly drop in height, compared to an atmosphere with less volatiles [2]. This is why NH_3 ice is typically expected to be found in zones, where temperatures are cooler and NH_3 can condense, while in warmer bands NH_3 ice sublimates [18]. Since convective motions involve precipitation and transport of material depending on temperature, these mechanisms shape the vertical structure of aerosols besides their composition in different regions and are objects of study.

- **How aerosols are formed?** Both clouds and hazes are linked to volatiles, photochemical products, and ices around which the volatiles might condense. If aerosols are observed under a range

of illumination conditions and viewing geometries, it is possible to extract information about their size, shape, and chemical composition. Therefore, studying the properties of aerosols reveals information about their formation environment. For instance, chromophores in the GRS might be supplied from a variety of circulation mechanisms, but the chemistry involved must still be explained [18]. Similarly, polar hazes are exposed to different chemistry than hazes at other latitudes due to auroral heating processes [62]. Moreover, hazes from both poles show properties that are not fully symmetric between them [18].

- **What is the chemistry of the chromophores?** Several colors have been observed in Jupiter's atmosphere over the years, including different tonalities of red, brown, grey and yellow [1]. Although the ice clouds predicted from the ECCM are typically white at VIS wavelengths, results from the Galileo mission concluded that there is some reddish material present in the clouds, especially in features like the GRS [63]. This "color" compound or *chromophore*, should be mainly composed by colorless condensates [36]. Some compounds involving C, N, S and P atoms have already been proposed as chromophore candidates [32, 37, 64]. Nevertheless, the required amount of such compounds and the photochemistry involved in their production must still be justified, and spectral evidence in different wavelength ranges must be provided [1]. The difficulty in identifying a candidate is based on the fact that there are no narrow, distinguishing spectral features in Jupiter spectra that can be related to chromophores, either comprehensive Jupiter spectral data at the required wavelength and resolution [34]. Moreover, the lack of laboratory spectral information related to the proposed candidates, especially for the UV-VIS range, is also an obstacle for modeling the jovian aerosols [1, 31].

Furthermore, the upper atmosphere and exosphere of Jupiter at low to mid-latitudes are systematically far hotter than what can be explained by solar heating, and additional sources of heating are needed [18]. Understanding the heating mechanisms in Jupiter is important not only because they expand atmospheric parcels, but because they can also drive vertical winds and affect turbulence. Therefore, it is necessary to characterize Jupiter's vertical structure and the dynamical coupling between atmospheric layers [18].

Addressing these questions states the importance of characterizing Jupiter's atmosphere, to continue obtaining information about the Jovian system. Therefore, tackling this series of scientific questions requires the prediction of the detection capabilities of new instruments sensitive to VIS-NIR wavelengths, with the support of radiative transfer models of Jupiter's atmosphere, both objectives of this thesis work (section 2.4). The Jupiter ICy Moons Explorer (JUICE) is the next mission to orbit Jupiter in 2031 and is expected to provide a global picture of the processes shaping the Jovian atmosphere from the thermosphere down to the troposphere [65]. In this way, JUICE will continue the characterization of the atmospheric composition and vertical structure of the different compounds, including aerosols, as well as the dynamics and circulation of the planet [18].

2 JUICE AND THE MAJIS INSTRUMENT

The Jupiter ICy moons Explorer (JUICE) is the next mission to the Jovian system, with an expected arrival in July 2031. The Moons And Jupiter Imaging Spectrometer (MAJIS) is the hyperspectral imaging spectrometer onboard JUICE for visible (VIS) and infrared (IR) wavelengths. It is part of the remote sensing package of the mission, covering the wavelength range between 0.5 and 5.54 μm by two independent spectral channels. In comparison against previous instruments such as JIRAM/Juno and NIMS/Galileo, it offers an extended wavelength coverage, especially at VIS wavelengths, with an improved spectral resolution of 2-3 times better than that of JIRAM. Similarly compared against Cassini/VIMS, which covered a spectral range from 0.35 μm, MAJIS provides higher resolving power. Moreover, MAJIS offers extended mapping capabilities and the possibility to study Jupiter in all local time conditions, thanks to its adaptability for different operational phases and scenarios of the mission during observations.

This chapter provides a detailed description of the MAJIS instrument, including the specific scientific objectives of the JUICE mission related to Jupiter's atmosphere, and ends by describing the specific objectives of this work.

2.1 THE JUICE MISSION

JUICE is a Large class (L-class) mission from the European Space Agency (ESA) already launched in April 2023. It will orbit Jupiter for 3.5 years and perform several flybys to its moons. Besides the missions dedicated to exploring the Moon, JUICE will become the first space mission orbiting a natural satellite in the Solar System, since it will end in orbit around Ganymede. JUICE will coincide with the *Europa Clipper* from the National Aeronautics and Space Administration (NASA), which is expected to arrive in 2030 [66], allowing synergistic observations of Jupiter's atmosphere [67].

JUICE is composed of 10 scientific instruments divided into three scientific packages (Figure 2.1): The *remote sensing package* provides VIS imaging capabilities with the JANUS camera, and spectral-imaging

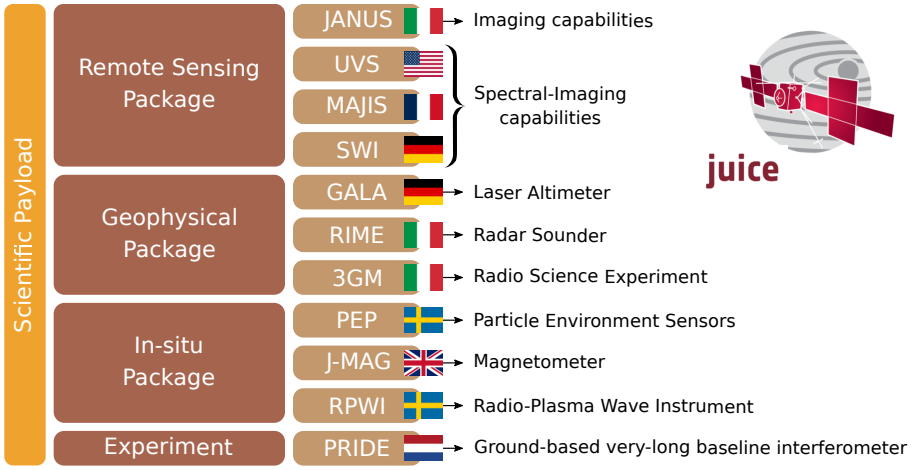

Figure 2.1: The JUICE scientific payload.

capabilities from ultraviolet (UV) to submillimeter wavelengths; the *geophysical package* is especially dedicated for exploring the surface and subsurface of the icy moons, although it complements the remote sensing package for the study of Jupiter's atmosphere; and the *in situ package* allows the study of the plasma environment and the magnetic fields in the Jovian system. Additionally, PRIDE is an experiment to perform very-long baseline interferometry to improve the ephemerides of Jupiter's regular moons [60]. Table 2.1 summarizes the main features of the instruments constituting the JUICE remote sensing package. It is worth mentioning that JUICE is able to provide co-alignment between JANUS, MAJIS, UVS, GALA, and SWI to perform simultaneous observations [18].

JUICE will follow a near-equatorial orbit able to provide global views of the planet and long-term monitoring of aspects of interest, different but complementary to what was performed by Juno, whose observations are typically limited to one single passage. In its closest approach, JUICE will be at 11-13 jovian radii from Jupiter [18]. Moreover, it is possible for JUICE to observe the same latitudes more than once in order to monitor regions of interest with periodicities from hours to months, and with the flexibility to update JUICE pointing up to one week in advance [18]. Thanks to its broad spectral coverage and its robust orbital tour, JUICE will have access to a wide range of latitudes and phase angles, including a high-inclination phase to study the polar atmosphere of Jupiter [18].

Instrument	Wavelength range	Spectral Resolution
JANUS	0.34-1.08 μm	N/A
UVS	50-204 nm	<1 nm
MAJIS	0.49-2.36 μm	3.7-5.0 nm
	2.27-5.56 μm	9.2-10.5 nm
SWI	235-281 μm	($R \sim 10^7$)
	479-565 μm	

Table 2.1: Performances of the instruments onboard the JUICE mission that are part of the remote sensing package [18]. R stands for spectral resolving power.

2.2 THE MAJIS INSTRUMENT

Among the different instruments onboard JUICE, MAJIS is a key instrument for the study of most of the major scientific goals of JUICE (section 2.3) [62]. As a hyperspectral imaging spectrometer (section 5.1), MAJIS is able to acquire cubes of data from which it is possible to extract nearly monochromatic images of an observation or the complete spectrum of each pixel in the image. MAJIS is composed of two spectral channels: the visible and near-infrared (VIS-NIR) channel sensitive from 0.5 to 2.35 μm, and the infrared (IR) channel, sensitive from 2.25 to 5.55 μm [62]. It was developed by a consortium lead by the *Institut d'Astrophysique Spatiale* (IAS) [68] in Orsay, France, with the major contributions from the *Istituto di Astrofisica e Planetologia Spaziali* (IAPS) [69] in Rome, and the *Leonardo Company* [70], in Florence, Italy.

MAJIS is a state-of-the-art instrument designed from the heritage of other imaging spectrometers, including JIRAM/Juno and the Visible and Infrared Thermal Imaging Spectrometer (VIRTIS) of Rosetta [71] and VenusExpress [72] ([73]). However, MAJIS benefits from customized improvements that will hopefully allow the achievement of the scientific objectives of the mission, especially regarding spatial and spectral resolution (section 4.1) [62].

The optical part of the instrument mainly consists of a scanning mirror, a telescope, and a spectrometer with a dichroic filter that allows the division of the light beam into the two spectral channels. Both spectral channels are co-aligned and operate simultaneously. Each of them can be seen as an independent spectrometer with its own detector,

which is harbored by its corresponding Focal Plane Unit (FPU). Figure 2.2 shows a schematic of the MAJIS instrument.

As a remote sensing instrument, MAJIS is expected to measure radiance from Jupiter's atmosphere, which includes thermal emission and reflected sunlight [74]. The light beam passes through the entrance baffle which removes stray light from the observation. The baffle ensures the maximum Field of View (FoV) of the instrument ($3.4 \pm 1.7^{\circ}$) and the maximum motion compensation of the scanning mirror ($\pm 4^{\circ}$). Additionally, the entrance baffle contains an Internal Calibration Unit (ICU) which provides the instrument with a Quartz-Tungsten-Halogen (QTH) lamp and a blackbody source (193-323 K) to perform calibration tests in-flight for the VIS-NIR and the IR channel, respectively [62, 75]. Both light sources are equipped with a spectral filter to be used as a reference for monitoring the spectral response of the instrument along the mission and are powered with a stabilized current to provide a high repeatability of the flux [73].

The light beam, either from the science target or from the ICU, is reflected by the scanning mirror to the MAJIS telescope. The scanning mirror is actually a mechanism that provides MAJIS with pointing, scanning, and motion compensation capabilities [74]. In this way, MAJIS is able to generate cubes of data with two spatial dimensions and one spectral dimension. As a push-broom scanner (section 5.1), MAJIS produces images at each of the spectral sampling points by spatially stacking the projection of the individual slits of the spectrometer during a temporal sequence, only driven by the spacecraft's motion. The mirror is generally fixed at a certain position and motion compensation can be applied to ensure an optimized spatial resolution during the acquisition, especially at short distances from the target [62]. However, MAJIS is subjected to two typical optical aberrations of push-broom hyperspectral scanners: smile and keystone effects [76]. The *smile effect* can be seen as a spectral shift of the sensor over its entire FoV, while the *keystone effect* produces a spectral tilt of the spectrum along the focal plane [77]. Both effects are minimized by the optics of the spectrometer and their final impact was characterized during the instrument calibration (section 4.6) [73].

The MAJIS telescope is constituted by three conic mirrors. The Three Mirrors Anastigmatic (TMA) configuration of the telescope eliminates coma, distortion, and spherical aberration by balancing them at the same field zone [73]. Four additional folding mirrors mechanically restrict the optical path within the allocated volume [62]. The light

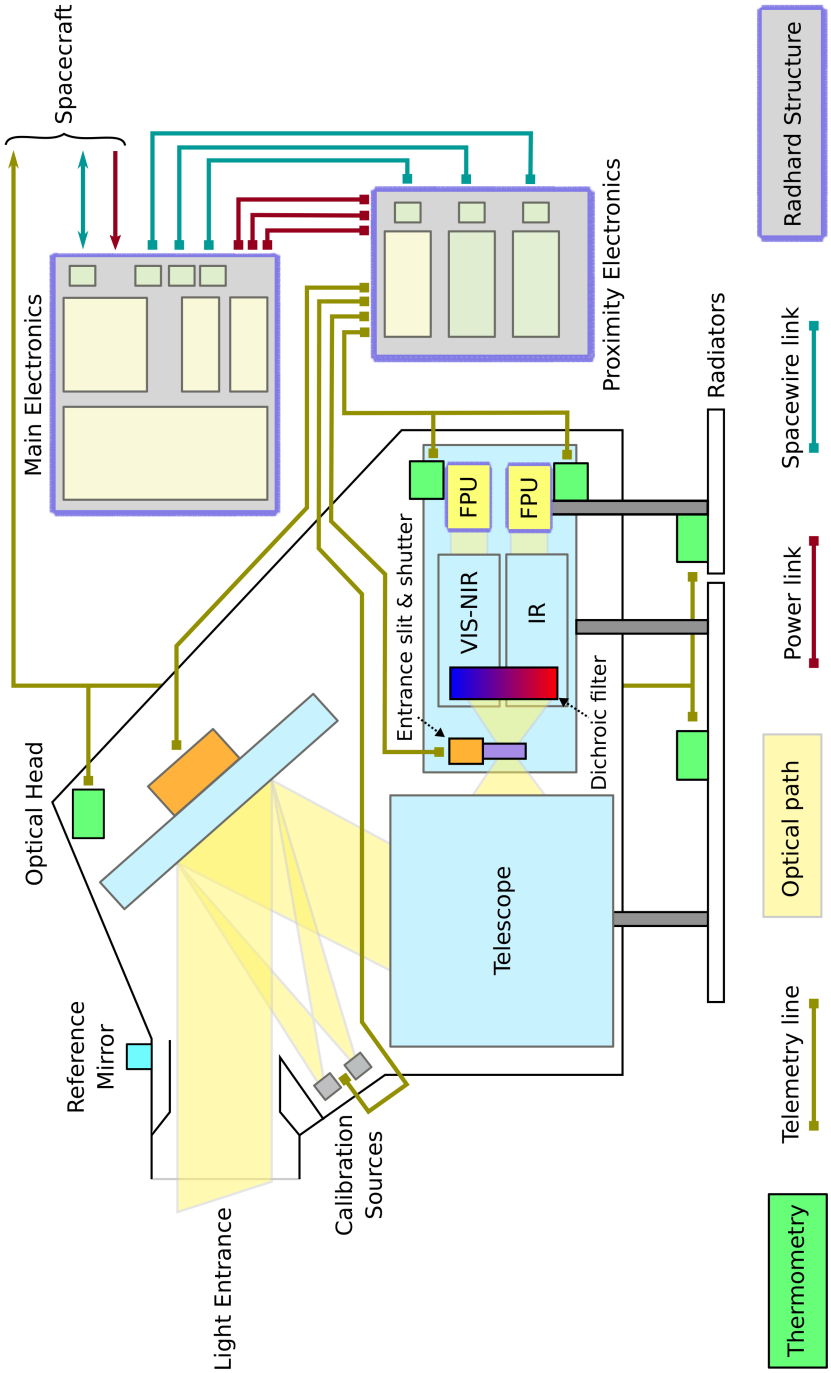

Figure 2.2: Schematic diagram of MAJIS (extracted from [62]). FPU stands for Focal Plane Unit.

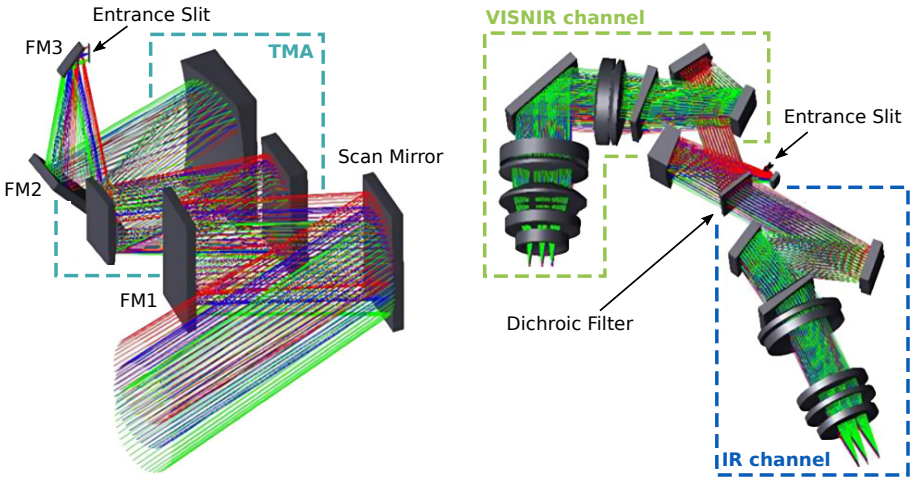

Figure 2.3: Optical design of MAJIS: (left) telescope, (right) spectrometer (extracted from [73]). FM# stands for a Folding Mirror number.

beam is then directed to the entrance slit of the spectrometer. Figure 2.3 shows the optical design of MAJIS.

As any other typical spectrometer (section 5.1), MAJIS is composed of slit, collimator, disperser, camera, and detectors. The slit is placed at the focal plane of the collimator, so the divergent light beam from the slit can be converted into a parallel beam by the collimator. Since MAJIS is constituted by two spectral channels, the parallel beam is directed to a dichroic filter that reflects the VIS-NIR wavelengths and transmits the IR wavelengths to the following optical elements corresponding to each channel. Each beam is then reflected by a correcting plate to the corresponding flat ruled grating, optimized for each spectral channel, to correct any curvature and tilt. The spectrum generated by each of the gratings is then directed to the camera of each channel, where other aberrations are compensated. Finally, each channel beam is focalized on its corresponding detector, which is already part of the FPU of each channel. The spectrometer includes a shutter mechanism for dark measurements, close to the entrance slit, that can be either closed or opened, as necessary for science data correction [62, 73]. Moreover, MAJIS provides flexible acquisition capabilities, including spatial windowing and summing, spectral selection, and spectral and spatial binning [78].

Figure 2.4 shows the mechanical drawing of MAJIS. All the optical elements of the instrument are enclosed in the Optical Head (OH),

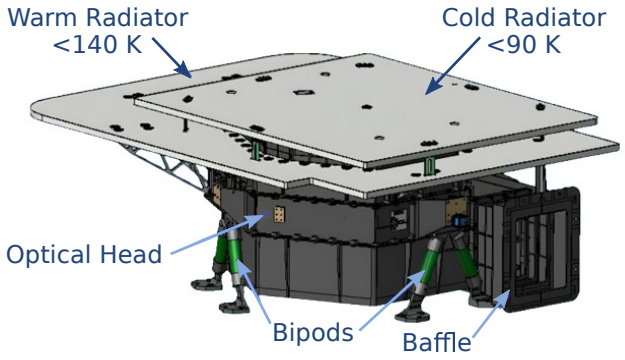

Figure 2.4: Mechanical drawing of MAJIS (extracted from [79]).

which is thermally isolated from the spacecraft interface by bipod supports and Multi-Layer Insulation (MLI). The thermal emission from all the elements constituting the instrument must be restricted, especially at the wavelength range at which MAJIS is sensitive. Therefore, the VIS-NIR channel should be kept at temperatures below 140 K, and the IR channel below 90 K [79]. The cryogenic temperatures are reached by two dedicated radiators external to the OH that dissipate the thermal loads of the instrument. There is no active cooling for the optics. All optical and mechanical subsystems were designed and optimized to work from 100 to 140 K, and their materials were chosen with a similar Coefficient of Thermal Expansion (CTE) to reduce thermal deformations as much as possible [62]. Several survival and anticontamination heaters located near sensitive devices are monitored by temperature sensors that complete the thermal design of MAJIS. They keep the devices within their operating temperature range and avoid condensation on their surfaces [79]. Thermal control is performed independently from the spacecraft.

The harsh radiation environment to which MAJIS will be exposed during the mission also constrained its design. Besides shielding, specific data processing strategies to be performed onboard had to be developed and validated for handling the impact on data quality of the deposition of charges by high-energy particles. The *de-spiking* procedure basically consists of splitting the integration time of the observation into small intervals, which are then sorted before spatial and spectral binning, in order to select a number of acquisitions with the lowest Digital Unit (DU) values and average them. The splitting of the integration time also reduces the possibility of saturation, especially for the VIS-NIR channel [78]. The intention is to operate the detectors

allowing full-frame retrievals over short integration times ($\ll$ 1 s) while maintaining good noise performance (>100) [80].

MAJIS has the necessary capabilities to produce global maps of Jupiter and guarantee continuous coverage of Jupiter's disk, besides the tracking of cloud systems and dynamical features on the planet [62]. Since JUICE orbit enables observations with a variety of phase angles, that were actually not available in Galileo nor Juno missions [74], MAJIS will be able to study Jupiter's atmosphere in all local time conditions. In fact, no previous space mission or ground-based facility has achieved the Jupiter's time coverage and monitoring expected from MAJIS. Since JUICE will dedicate a substantially higher data volume to MAJIS than equivalent instruments in previous missions [74], the extensive monitoring of features with a periodicity in the order of hours or months is possible. In fact, data will be acquired over the same geographical region at time intervals of $\sim$2 hours, except when observing the auroral region, which will be observed once every perijove passage with time gaps of 50 minutes [62].

Other observation strategies will be possible with MAJIS, including limb observations and stellar occultations (section 5.2) [18]. Limb observations support the study of coupling waves and global circulation across the atmospheric layers, which is necessary to characterize the vertical structure of Jupiter's atmosphere [62]. Stellar occultations support the study of methane (CH_4) abundances in the stratosphere, which is connected to temperature variability in the atmosphere (section 1.2), and complement the constraints of aerosol properties and vertical distribution at higher altitudes [62, 74].

2.3 SCIENTIFIC OBJECTIVES OF THE MISSION

The main scientific objectives of JUICE are shared between the characterization of Jupiter and the exploration of its icy moons. MAJIS will address most of the major scientific goals of the JUICE mission [62, 78]. For comparison, the Jovian Infrared Auroral Mapper (JIRAM), currently onboard Juno (section 1.4), is the instrument equivalent to MAJIS but its spectral coverage is more limited than that of MAJIS, both in VIS and IR wavelengths. The wider spectral coverage of MAJIS gives access to pressure levels between 10 and 0.02 bars (see Figure 2.5) [62, 74], with the possibility of studying features that had not been investigated in detail with VIS-NIR spectroscopy, including white ovals [20]. Furthermore, the spatial coverage of JIRAM/Juno was typically

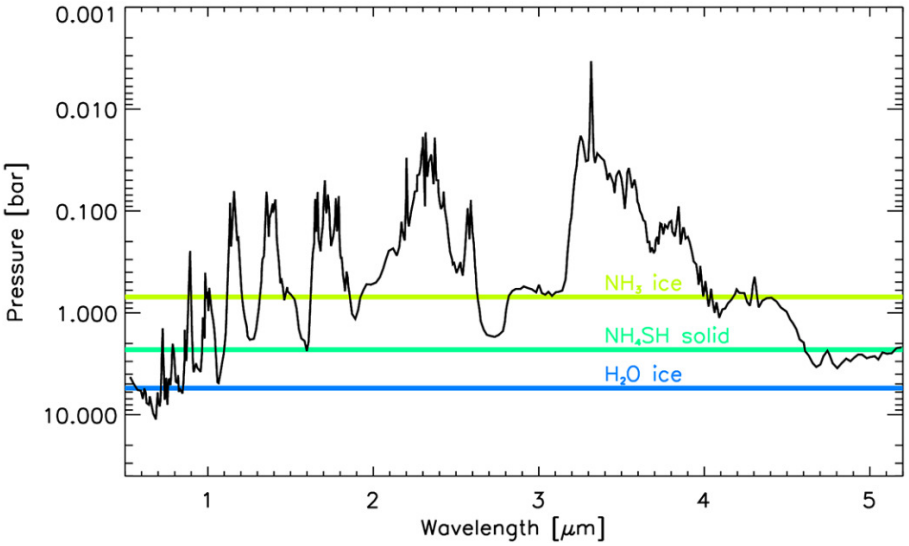

Figure 2.5: Simulated pressure levels accessible by MAJIS in Jupiter's atmosphere without considering aerosols (extracted from [62]). The black curve shows when the optical depth reaches unity after each specific wavelength of radiation crosses the atmosphere twice (nadir). The cloud positions are defined as predicted by the ECCM.

limited to one close passage per region, restricting monitoring and variability studies [18].

JUICE's scientific objectives can be consulted in [60]. A summary of those concerning Jupiter's atmosphere is presented here below with an emphasis on MAJIS contributions. Note that a detailed description of the scientific objectives and key investigations of MAJIS is also available in [62].

Study of Jupiter's atmospheric dynamics and circulation

Studying the dynamical phenomena in the troposphere, which is thought to be driven by sunlight radiation and deeper internal processes, allows the understanding of the global circulation of the planet. All phenomena of atmospheric turbulence are responsible for vertically and horizontally mixing and transporting energy, momentum, and tracer compounds between the different layers of the atmosphere. Their study allows the understanding of the relationship between atmospheric motion and composition, including clouds' composition, and the mechanisms that maintain turbulences in the atmosphere [60].

MAJIS will offer key insights into the vertical and horizontal dynamics of Jupiter's troposphere, which drives the distribution of condensable species and the transport of clouds. In other words, the study of the time-variable distribution of cloud opacities, volatiles, and disequilibrium species will reveal information about the global circulation of Jupiter's atmosphere [62]. This contribution dominates Jupiter's spectrum from 0.4 to 3.2 μm, a spectral range almost totally covered by MAJIS [74]. Moreover, after evaluating the morphology of deep cloud layers, it will be possible to understand their motion and extract their velocities at different altitudes [62]. This is especially interesting for the Great Red Spot (GRS) and other large anticyclones. Additionally, MAJIS will be able to perform short-term evolution studies of special features such as the circumpolar cyclones, and continue with the long-term evolution studies from Juno [62].

Characterization of Jupiter's atmospheric composition and chemistry

The complete characterization of the atmospheric compounds provides insights into the formation and evolution of gas giant planets. To determine the cloud's structure, the radiative energy balance, and the condensation processes necessary for the understanding of the convective mechanism in the atmosphere, it is necessary to describe the spatial distribution and variability of stratospheric compounds, including volatiles and disequilibrium species, and constrain the origin and distribution of exogenic species [60].

MAJIS will characterize the distribution and variability of atmospheric constituents to determine Jupiter's elemental composition, which also constrains dynamical models. Thanks to the larger spatial and temporal coverage of MAJIS in comparison against JIRAM/Juno and previous missions [18], better monitoring of the variability of aerosols properties between the upper troposphere and the lower thermosphere will be possible. Moreover, the spectral sampling of MAJIS will allow the detection of subtle differences in aerosol properties that will provide insights into their chemical composition, size, and origin, with special attention to chromophores [62, 74]. Therefore, the spectral coverage of MAJIS will better constrain the composition and scattering properties of aerosols at different locations [74].

Since the needed spatial and temporal coverage for characterizing atmospheric compounds is similar to that for aerosols, it is possible to study Jupiter's atmospheric composition from the stratosphere to the

thermosphere [18]. The spatial coverage of MAJIS will allow the study of the potential correlation between the abundance of different volatiles at different spatial scales, for instance, NH_3 and H_2O, and constrain their origin [62]. Moreover, the better spectral resolution of MAJIS, in comparison with previous instruments, will allow a better distinction of the spectral signatures of different molecules, especially at regions where these are expected to be partially superimposed [62].

Characterization of Jupiter's atmospheric vertical structure and clouds

By characterizing the vertical structure and evolution of Jupiter's atmosphere as well as the coupling processes from the deep interior to the thermosphere, it is possible to provide a map and a detailed description of the optical properties of aerosols in Jupiter's atmosphere, especially concerning the chromophores. Processes such as photochemical production, sedimentation, condensation, and uplift of NH_3 ices, will constrain the understanding of aerosols production in Jupiter's atmosphere [60].

MAJIS will characterize the upper stratosphere and thermosphere, and map the magnetic phenomena occurring especially at the poles. This will allow the understanding of the coupling conditions between those layers of the atmosphere with the magnetosphere, which can be studied between 3.2 and 4.0 μm. Even if the near-equatorial orbit of JUICE does not reach the spatial resolutions of JIRAM/Juno, which performed polar orbits, MAJIS will provide larger temporal coverage to explore variability with time scales of a few hours [18]. Additionally, thanks to this valuable spatial and temporal coverage, MAJIS will be able to investigate the redistribution of aerosols after asteroidal or cometary impacts [62].

2.4 OBJECTIVES OF THIS WORK

Since the VIS-NIR spectrometry represents a remarkable potential for characterizing the composition and dynamics of planetary atmospheres [81], this work focuses on the VIS-NIR channel of the MAJIS instrument through two main objectives:

1. **The characterization of the MAJIS/JUICE VIS-NIR detectors**, to determine the actual capabilities of the VIS-NIR channel of MAJIS, and

2. **The forward modeling of Jupiter's VIS-NIR spectrum** to assess the performances of MAJIS for the scientific objectives of the mission.

Both objectives required the development of additional instruments and tools. For instance, the first objective requested the development and validation of an experimental setup suitable for characterizing space-based detectors from 0.4 to 2.65 μm. This is discussed in part II of this work, in which chapter 3 describes the development of the facility used to perform the characterization of the VIS-NIR detectors of the MAJIS instrument, and chapter 4 describes the measured performances of the detectors during the measurement campaigns that took place. The results obtained from the characterization campaign of the flight model detectors were essential for the complete on-ground calibration of MAJIS, in which the baseline performances of the instrument were established.

The second objective of this thesis work required the update of ASIMUT-ALVL, a radiative transfer model already used for the study of terrestrial atmospheres. This is discussed in part III of this work, in which chapter 5 provides an overview of the theory behind atmospheric radiative transfer simulations, and chapter 6 describes the implementation and validation of the developed functionalities for the forward model of Jupiter's atmosphere in the VIS-NIR range.

The functional forward radiative transfer model of Jupiter's atmosphere (part III) was based on the current knowledge of Jupiter's atmospheric compounds. Together with the established performances of the detectors (part II), they enabled us to simulate realistic remote sensing observations of the MAJIS instrument. This is summarized in part IV of this thesis work, in which chapter 7 assesses the impact of the actual performances of the MAJIS VIS-NIR channel, especially in relation to the study of the abundances of CH_4, NH_3 and the chromophores. Chapter 8 summarizes the results and outcomes achieved during this work. The characterization of the MAJIS VIS-NIR detectors together with the forward model of Jupiter's VIS-NIR spectrum, supported both technical and scientific activities of the MAJIS/JUICE team.

Part II

THE MAJIS/JUICE VIS-NIR DETECTORS

3 THE VIS-NIR CHARACTERIZATION FACILITY

This chapter is mostly published in the Journal of Astronomical Telescopes, Instruments and Systems (JATIS) in the frame of the issue "Detector Systems and Sensor Technologies" in August 2023, under the title "Facility for the radiometric characterization of space-based visible-near infrared detectors" [82]. It describes the facility developed to characterize the VIS-NIR detectors of the MAJIS/JUICE instrument. This facility was developed from the ground up and validated according to the requirements for manipulating spatial devices defined by the European Space Agency (ESA). As described later in this chapter, the facility can actually be used for the characterization of other astronomical detectors sensitive to the same spectral range and is available at the Belgian Radiometric Characterization Laboratory (B.RCLab) [83], at the Royal Belgian Institute for Space Aeronomy (BIRA-IASB) [84].

A general introduction concerning VIS-NIR detectors is presented in the next section, followed by the actual paper.

3.1 VIS-NIR DETECTORS OVERVIEW

The visible (VIS) and infrared (IR) regions of the electromagnetic spectrum are considered for this work. IR radiation is typically divided into Near-Infrared (NIR), Mid-Infrared (MIR), and Far-Infrared (FIR) radiation. Figure 3.1 shows the blackbody spectrum for different temperatures highlighting the different parts of the electromagnetic spectrum regions. In this way, an object at room temperature (300 K) emits radiation detectable in the NIR domain, while the thermal emission from an object can be detected in VIS wavelengths only if its temperature is higher or around 1000 K.

A detector is a device able to convert radiation into electrical signals by taking advantage of the photoelectric effect [85]. In astronomy, detectors are largely used for imaging, astrometry, photometry, and spectroscopy [86]. Following the use of photographic plates in the 19th century, the first detectors used for astronomy were the PhotoMultiplier Tubes (PMTs) which amplify the signal produced by a single absorbed photon by causing a cascade of electrons that can be measured [87].

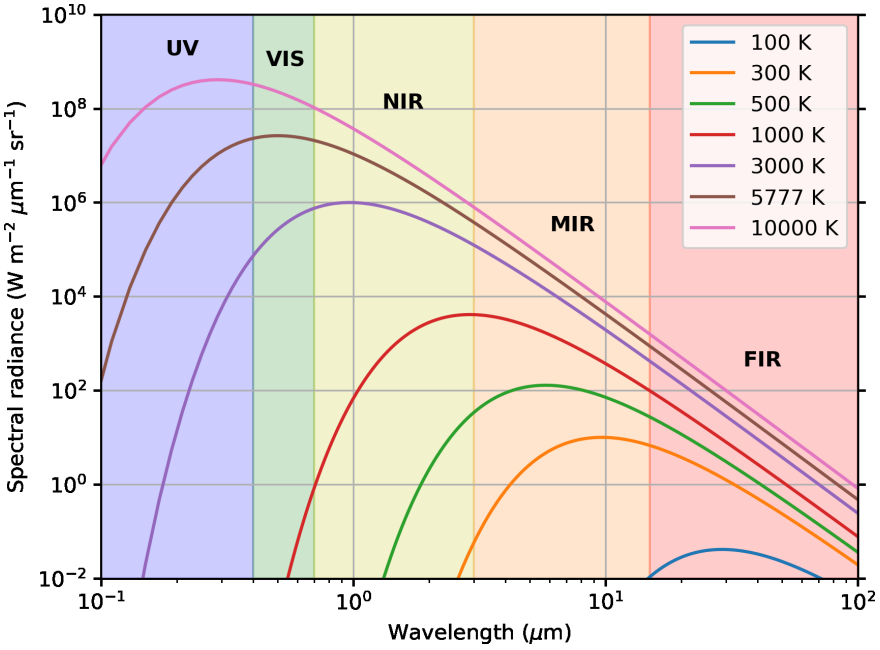

Figure 3.1: Blackbody spectrum for different temperatures and the corresponding regions of the electromagnetic spectrum. The brown line corresponds to the temperature of the Sun, while the orange line is that of an object at room temperature.

Later in the 70s, the Charge Coupled Devices (CCDs) provided the possibility of temporarily storing the produced charge in a regular array format, suitable for bidimensional detectors. In this case, photons with the correct energy are absorbed by a *capacitor*, which accumulates charge proportional to the intensity of radiation [86]. Several capacitors are placed in proximity to constitute the different pixels of a CCD. To read the charge stored in each pixel, the charge flows from one capacitor to another by readout electronics that detect and measure each charge in series [88]. Figure 3.2 shows a schematic of the readout methodology used for CCDs and other detector types, which will be described hereafter.

Complementary Metal Oxide Semiconductor (CMOS) detectors are similar to CCDs with the advantage of having readout electronics that allow each pixel to be addressed directly [87]. This is done through Metal-Oxide-Semiconductor Field-Effect Transistors (MOSFETs) which now constitute the pixels in the array [85]. The main disadvantage of

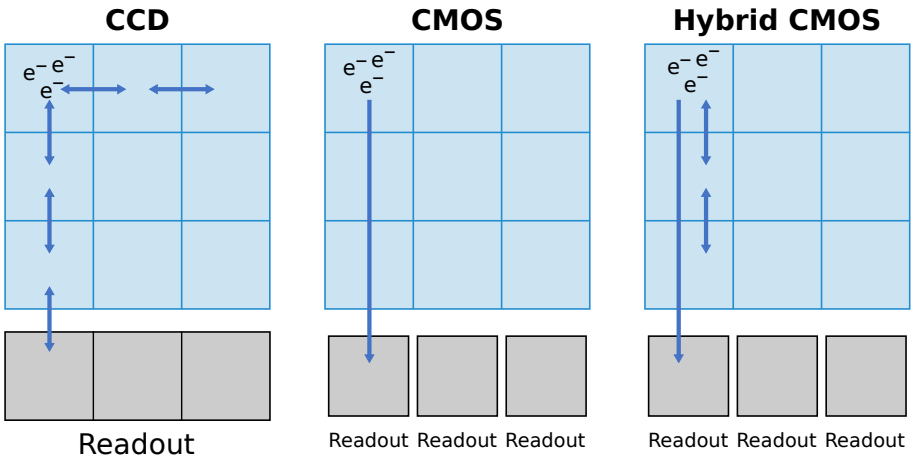

Figure 3.2: Differences between CCD, CMOS and hybrid CMOS detectors (extracted from [89]). CCD (left) transfers the signal between pixels until it is pulled down into a single readout node. CMOS (center) directly reads the signal of each pixel by independent readout nodes. Hybrid CMOS generally transfers the signal between pixels in a column with its own readout node.

CMOS detectors is the additional electronic noise in the signal from the more complex electronics available.

Hybrid CMOS detectors provide electrical connections between some pixels, generally in the same column, but each group of connected pixels has its own readout node. Therefore, compared to a typical CMOS detector, hybrid CMOS detectors produce a higher signal, due to the CCD-like charge accumulation technique, but with less noise [89]. The H1RG[1] arrays used for the Moons and Jupiter Imaging Spectrometer (MAJIS), onboard the Jupiter Icy Moons Explorer (JUICE), are detectors of this type [90].

When a pixel provides more charge than it has in reality, it is called *hot pixel*. In contrast, a pixel that does not provide as much charge as it accumulates is called a *dead pixel*. These pixels are typically discarded for data analysis.

It is worth mentioning that silicon (Si) is commonly used in the manufacture of CCDs, since it offers a photoelectric effect range that is enough to cover from the soft X-ray to NIR regions [86, 91]. However, Mercury Cadmium Telluride (HgCdTe) is preferred for space astronomy mainly due to its low noise levels [90], and especially for the MIR

1 H1RG stands for HAWAII (HgCdTe Astronomical Wide Area Infrared Imager) with 1 block of 1024 pixels in x and y dimensions, Reference pixels and Guide window capability [90]

[92]. Moreover, the cut-off wavelength of HgCdTe detectors can be tuned approximately between 0.7 and 25 μm by controlling the ratio of Mercury (Hg) and Cadmium (Cd) in the corresponding layer [93], while Si covers small wavelengths with a cut-off at 1 μm. MAJIS arrays consist of HgCdTe.

To describe how well a detector performs, the following parameters can be defined. Further details can be found in the given references.

- **Responsivity.** It is a measure of the sensitivity of the detector, seen as the ratio between the electrical signal measured by the detector and the received flux [91, 94].
- **Conversion gain.** It is defined as the number of electrons needed to generate one Digital Unit (DU). Therefore, sometimes it is also referred to as the actual detector's responsivity [85].
- **Quantum Efficiency (QE).** It gives information about the probability that a photon absorbed by the detector will produce a signal in consequence [87]. It is generally a function of wavelength and also determines the spectral response of the detector [85].
- **Spectral response.** Refers to the responsivity of the detector as a function of wavelength (under monochromatic flux) [91]. This parameter is more relevant near the *cut-off* of the detector [85], i.e., at the wavelengths where the detector decreases its responsivity.
- **Linearity.** Describes the relation between the charge collected by each pixel and the DU stored in the output image, which is expected to be linear over a wide dynamic range [87].
- **Full-Well Capacity (FWC).** When a pixel can no longer increase the output signal after the absorption of new photons, *saturation* takes place. FWC corresponds to the maximum number of photo-electrons that can be stored by a pixel [86].
- **Noise.** It is a random fluctuation in the electrical output of a detector mainly due to its electronics and temperature, whether or not the detector is exposed to light [91]. The noise related to the read-out electronics is referred to as *Read-Out Noise* (RON), while the noise related to the temperature of the detector is referred to as *Dark Current* (DC) and can be minimized by reducing the temperature of the detector [86, 87]. An additional noise related to the random nature of a current flow due to photon absorption

is known as *shot noise*, and is influenced by QE in consequence [91].

- **Uniformity.** It describes how well the pixels compare with each other in terms of responsivity, both when the detector is exposed to radiation, or Photo Response Non-Uniformity (PRNU), and when it is not exposed to radiation, or Dark Signal Non-Uniformity (DSNU) [85].

- **Signal-to-Noise Ratio (SNR).** Represents a measure of the uncertainty of the acquired image [87]. Therefore, it is the ratio between the signal measured by the detector and the noise present in the signal. Since the shot noise is considered significantly lower than the signal, the SNR can be considered proportional to the QE [91].

Hereinafter, the following text is directly extracted from the research paper Cisneros-González et al. [82], published in 2023 and whose heading is shown by Figure 3.3. It describes the facility developed for the characterization of the MAJIS VIS-NIR detectors. As part of this work, the major contribution concerned the design and development of the cryogenic system, including the security system. Some additional participation involved the preliminary design of the optical system, the design and arrangement of the different clean areas, and the development of procedures for the integration of the detectors into the facility, and for the operation of the facility during the measurement campaigns.

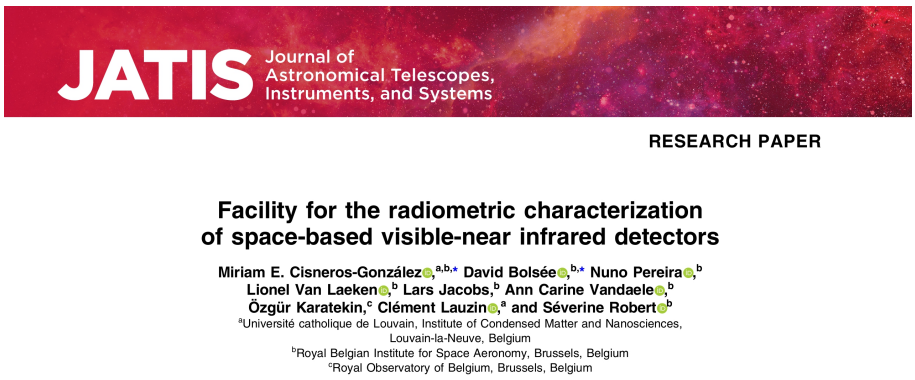

Figure 3.3: Heading of Cisneros-González et al. [82]. Facility for the radiometric characterization of space-based visible-near infrared detectors. *Journal of Astronomical Telescopes, Instruments, and Systems*, 9(03), August 2023. [doi: 10.1117/1.JATIS.9.3.036001].

3.2 TYPICAL CHARACTERIZATION MEASUREMENTS

The need to characterize imaging detectors is essential to confirm their performances for both space and ground-based instruments since often the characterization offered by the manufacturers does not meet the stringent accuracy requirements for scientific instruments. Besides, numerical simulations are vulnerable to conceptual and implementation errors because of the limited understanding of the detector's physics, and the development of data analysis methods to mitigate the detector characteristics can take years [95]. For imaging, the understanding of the behavior and performances of each pixel under different illumination conditions, wavelengths and temperatures, must be accurately evaluated, considering the potential environment to which a detector could be exposed. For instance, depending on their operational spectral range, detectors usually require cryogenic operating conditions to reduce the thermal noise generated during image acquisition, especially infrared (IR) detectors. However, if the thermal control is limited, it might be possible that during observations the nominal temperature of the detector varies, which will directly affect the Signal-to-Noise Ratio (SNR) of the images. In addition, detectors onboard space missions are subjected to harsh radiation environments, and therefore their performances downgrade with time [96, 97]. Hence, to fully understand the instrument and its response over time, to assess the evolution of its performances during observations, the initial measured characteristics of the detector will be the crucial starting reference point for any subsequent analysis [98].

Due to the complexity of characterization, according to Shapiro et al. [95], the resultant measured performances of a detector could bias photometric, astrometric, spectroscopic, and shape measurements at the 1 % level or less. However, if a detector is well characterized by providing the different conditions to which it will be exposed during operation, including the expected image acquisition methods, there will be enough confidence that the detector will perform according to its specifications in all feasible environments, including critical performance parameters [99]. The required optical sources, data acquisition methods, and minimum specifications for both test chambers and optical systems, can be derived from the specific planning of measurements [100] and, for maintaining repeatability, it is desirable to have as simple as an optical system can be [99, 101].

Traditionally, many detector parameters such as responsivity and noise are measured by exposing the detector to a spatially uniform photon flux or dark conditions, respectively [85]. The photon flux uniformity can be achieved by means of a diffuser or an Integrating Sphere (IS), although these devices will highly reduce the irradiance at the detector and special considerations must be taken into account to still provide enough signal to it. The irradiance must be stable, homogeneous, and with a well-known spectral response covering the operating spectral range of the detector to be characterized, and this can only be confirmed by a proper characterization of the sensitive area of the detector, i.e., the working optical plane.

On the other hand, parameters such as Quantum Efficiency (QE) and Spectral Response, which are highly wavelength dependent, require a monochromatic light source to illuminate the detector at the desired wavelength with high spectral purity. Normally for these measurements, the current of a reference calibrated photodiode is measured first to determine the irradiance received at the Working Plane (WP) of the optical setup for a certain illumination. In this way, when exposing the detector to be characterized under the same illumination and exactly at the same position as the reference photodiode, it is possible to determine how many of those photons produced signal in each of the pixels of the detector [100]. Therefore, the accuracy of the measurement will be depending on the stability of the light source and the alignment of the detector. The monochromatic light source can be either obtained from different LED sources or lasers, or through the combination of a continuum light source such as lamps or blackbodies, and a monochromator.

Another parameter relevant to the characterization of a detector is its linearity. Although it is expected that a detector responds linearly with incident light, it is often deviated depending mainly on the transimpedance of the MOSFET amplifiers of the detector array [100]. When measuring linearity, the detector should generate signal from its minimum level to saturation. This can be done by exposing the detector to different incident radiation while acquiring images with the same integration time (linearity versus flux), or by providing constant incident radiation while acquiring images at different integration times (linearity versus integration time). Measuring linearity at a constant photon flux depends also on the stability and homogeneity of the light source to guarantee that each pixel is exposed to the same amount of photons during the complete measurements.

Because background measurements are an important part of the image acquisition procedure, a characterization facility must include a shutter in which the light source can be stopped, so that any emission produced by devices along the optical path can be subtracted from the measurements during data processing. This is also related to the measurement of the persistence effect, which is related to the residual signal in a pixel after a bright exposure. Therefore, the speed of the shutter must be synchronized with the integration time of the detector during data acquisition.

Finally, measuring parameters that do not require the illumination of the detector, such as Dark Current (DC) and Read-Out Noise (RON), requires removing emissions from surrounding bodies at the wavelengths at which the detector is sensitive. For instance, an IR detector is generally enclosed by radiation shields at cryogenic temperatures, so the blackbody emission from bodies at room temperature is blocked, while the radiation from the cold shield does not produce any background signal in the detector. Therefore, these measurements will be accurate if the dark conditions are guaranteed and if the detector is at a stable temperature.

When measuring non-uniformities, as is the case for Dark Signal Non-Uniformity (DSNU) and Photo Response Non-Uniformity (PRNU), the spatial differences between pixels are analyzed. In consequence, there is no need to use reference photodiodes during the measurements. These non-uniformities are due to imperfections during the fabrication process of the detector, which provides different values of capacitance [100].

In the end, the accurate determination of the performance parameters of any imaging detector is a challenge that could be tackled if a single but versatile characterization facility is used [100].

3.3 VIS-NIR CHARACTERIZATION FACILITIES AVAILABLE

Some VIS-NIR facilities are available for the characterization of astronomical detectors. In the case of the European Space Agency (ESA), even if instruments are provided by external consortia, ESA takes responsibility for the procurement of the detectors [102] and can provide infrastructure for their commissioning through ISO-17025 accredited facilities for CCD and CMOS detectors' validation [103]. Similarly, the National Aeronautics and Space Administration (NASA), through the Detectors Characterization Laboratory (DCL), supports flight qualifica-

tion testing of detectors and detector systems, providing a full optical and electrical characterization of detector arrays [104]. However, usually these facilities are state-of-the-art instruments developed to fulfill the needs of each project (often for also state-of-the-art detectors) to comply with the specifications demanded for each required measurement. This was the case for the Euclid mission [105, 106], the James Webb Space Telescope (JWST) [107–109], and the Large Synoptic Survey Telescope (LSST) [110], to mention some examples.

What is typical among these testing facilities is the use of Quartz-Tungsten-Halogen (QTH) and Xenon lamps as their main light source. The stability of the lamp is continuously monitored and reported to be in the order of 1 % [111, 112]. However, the power is not usually higher than 500 W [113, 114] and some considerations must be taken into account to provide enough flux to the detector, especially when the system requires the use of an IS or a diffuser. Other light sources used include 3000 K blackbodies [108, 112] and LED illumination sources [106, 107, 112]. To reach the same level of intensity stability of QTH lamps with LEDs, the temperature of the LED must be stabilized within 300 mK [106]. As LEDs offer illumination at specific wavelengths, it could be possible to disregard the use of a monochromator. This was the case for the Teledyne Imaging Sensors Test Facility [107]. Naturally, if one single facility provides different illumination sources, the optical layout has to be reconfigured.

ISs are the general solution to provide a uniform light beam to the detector, especially when measuring QE. However, depending on its properties, some additional items could be added to achieve the desired homogeneity (usually 1 % [111]). For instance, when the IS is too small and the image of the aperture is still visible at the output port, adding flat diffusers could improve the uniformity of the beam [115] regardless attenuation. Another solution is to place the detector far from the output of the IS under a baffle system that also reduces stray light [98, 114–116]. Neutral Density (ND) filters are also used to vary the light flux of the system [117–119], although other alternatives such as diaphragms, apertures, or pinholes of different sizes have also been adopted [107, 111], sometimes in combination with ND filters [115, 120].

Operating CCD or CMOS detectors at NIR and even VIS wavelengths require their thermalization at cryogenic temperatures. Open-cycle cryostats are used in some characterization facilities [113, 114, 121] to reach these temperatures. Vibrations in such systems would only come from the pumping system, which is normally disabled during

measurements. However, most of the facilities count with closed cycle cryostats, which are chosen depending on their power capabilities. For instance, the facilities used for the characterization of the NIR Spectrograph (NIRSpec) detectors for the JWST [107] needed two-stage cold heads: one stage for thermalizing the detectors with independent thermal controls for their electronics, and one stage for thermalizing the optics of the facility. Typical thermal stability provided by the characterization facilities is in the order of millikelvin with temperature rates below 1 K/min [106, 115, 122].

It is worth mentioning that working with flight detectors requires that the test facilities are installed inside ISO-5 areas to comply with the necessary cleanliness levels when manipulating space detectors, and include a robust security system to protect the detectors during the measurements. Considering the additional challenges of supplying (i) uniform flux stability tunable over a large spectral range and (ii) a cryogenic environment, using a single versatile test bench to perform absolute and relative radiometric measurements of an imaging detector is desirable for optimizing resources, time-saving during the measurements, and repeatability of measurement conditions. Therefore, providing a testbench that is flexible, accurate, and highly automated, while minimizing the need for customized designs, is the main objective of this work. In this paper, a new VIS-NIR characterization facility from the Royal Belgian Institute for Space Aeronomy (BIRA-IASB) is described. This facility has been already used to characterize the VIS-NIR detectors of the Moons And Jupiter Imaging Spectrometer (MAJIS) [80, 123], one of the instruments on board the Jupiter ICy Moons Explorer (JUICE). This facility is offered to the scientific community as another option for future projects and contributions.

3.4 VIS-NIR CHARACTERIZATION FACILITY AT BIRA-IASB

The BIRA-IASB characterization facility follows the requirements specified by the European Space Components Coordination (ESCC) [124], and the European Machine Vision Association (EMVA) [125] current standards for the characterization of imaging detectors. The facility is under a laminar flux certified as an ISO-5 area that includes the optical setup, the thermal vacuum chamber, and a horizontal laminar flux allocating a working area dedicated to the manipulation of equipment (Figure 3.4). The soft-walls are made of anti-static transparent vinyl to allow low outgassing and isolate the ISO-5 area from the grey room,

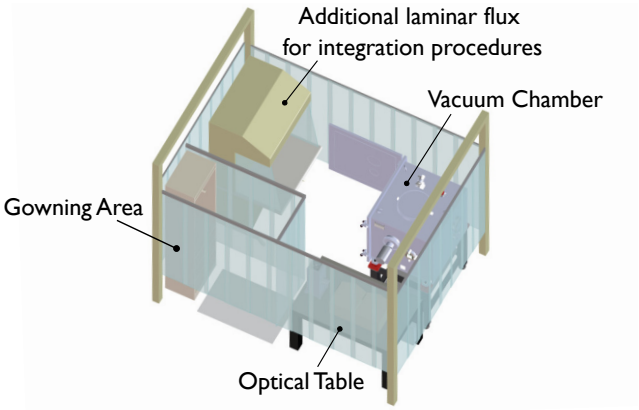

Figure 3.4: Schematic diagram of the ISO-5 area where the characterization facility is located.

which achieves an ISO-7 cleanliness level. Environmental temperature, pressure, and relative humidity are continuously monitored in both areas. The temperature and relative humidity can be actively controlled to remain at 22±3 °C and 40-65 %, respectively. The Ground Support Equipment (GSE) is located in an ISO-8 area, from which the remote control of devices operating in the clean room is possible.

The facility was designed to measure the parameters listed in Figure 3.5. Note that some parameters can be derived from the results of other measurements. Moreover, different illuminating conditions, dynamical illumination levels, temperatures, and exposure times can be provided, besides absolute radiometry to measure parameters such as QE.

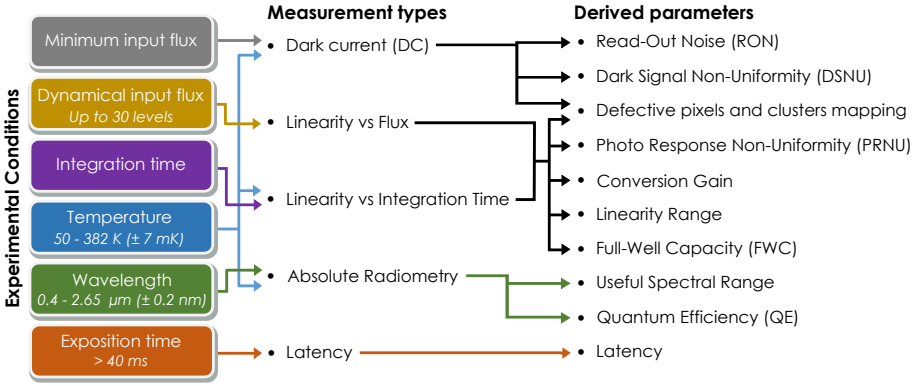

Figure 3.5: List of measurements that can be performed with the VIS-NIR characterization facility, and the parameters that can be derived under different experimental conditions, to characterize an imaging detector.

3.4.1 *Cryogenic system design*

Inside the vacuum chamber, the thermalization of a VIS-NIR detector is made through an Oxygen Free High-Conductivity (OFHC) copper plate on which the detector is installed. The copper plate is thermally connected to the cold finger of the one-stage ARS Closed-Cycle Cryocooler Model CS104FT, which provides a cooling power of 60 W at 77 K, with an ultimate performance of 25 K without thermal load. As implemented in the characterization facility, the cold finger can achieve a minimum temperature of 43 K. Both, the cold finger and the copper plate are provided with a Proportional-Integrative-Derivative (PID) thermal control loop. The copper plate counts with a redundant control loop to ensure thermal protection in case of failure of the primary loop. Two LakeShore 335 and one LakeShore 336 temperature controllers are used to regulate the control loops. The copper plate can be stabilized at a temperature between 50 to 382 K, with a difference of 0.01 % with respect to the target temperature, and a precision within 7 mK after 2 hours of activating the thermal control.

Figure 3.6 shows a diagram of the high-vacuum system of the BIRA-IASB characterization facility. The vacuum chamber is a customized cubical model with a volume of 420 L. The viewport has a diameter of 63 mm and is made of CaF_2. All O-rings are made of Viton. The pumping equipment consists of a dry primary pump with a pumping speed of 4 L/s, in serial connection with a turbo-molecular pump with

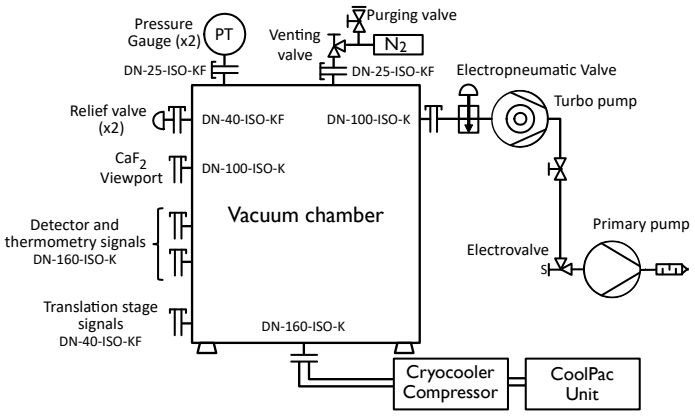

Figure 3.6: Schematic diagram of the vacuum system of the VIS-NIR facility. The detector to be characterized would be mounted in front of the CaF_2 viewport inside the vacuum chamber [126].

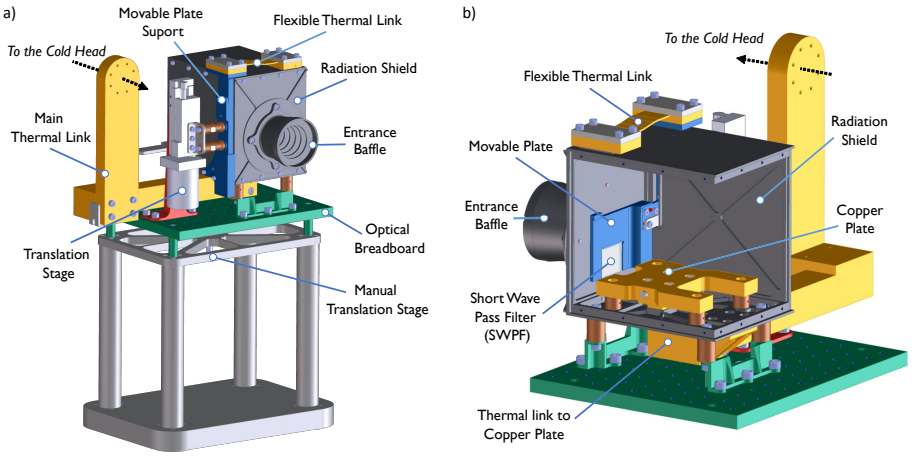

Figure 3.7: Mount developed to support and thermalize VIS-NIR detectors: a) Frontal view, b) internal view of the radiation shield.

260 L/s of pumping speed, that can automatically be activated when a level of 10^{-1} mbar is achieved inside the chamber. A vacuum level of 10^{-5} mbar is achieved in 80 minutes, with an ultimate vacuum level of 10^{-7} mbar [126]. An electro-pneumatic valve can isolate the vacuum chamber from the pumping system if needed. The vacuum chamber was designed to keep a high-vacuum level only with the pumping system permanently active. Thanks to the design of the detector mount, vibrations induced by the pumping system and the cryocooler are countered, even during measurements. The venting process is made with ultra-high purity Nitrogen (N5.0).

Figure 3.7 shows the mount developed to support, thermalize, and optically align the detector in front of the viewport of the vacuum chamber. The four pillars of the base supporting the optical breadboard, are part of a translation system for optical alignment in height. Although it is expected that the temperature of the base is always around room temperature, it is thermally isolated from the vacuum chamber by 4 mm thick polytetrafluoroethylene (PTFE) feet (not visible in the figure). The optical breadboard allows the attachment of different components. However, the detector would be installed inside the radiation shield screwed to the copper plate. The room available at the copper plate is limited by the radiation shield to 138.5 mm $\times$ 106 mm $\times$ 111.5 mm. The Focal Plane Unit (FPU), which normally contains the detector and its electronics, should not exceed these dimensions unless a different design is developed for the radiation shield.

The different parts of the mount were carefully designed. The materials used have low outgassing levels, i.e a Total Mass Lost (TML) lower than 1 % and a Collected Volatile Condensable Materials (CVCM) lower than 0.1 %. The main conductive material used was OFHC copper, while PEI-Ultem^{TM} 1000 was chosen as the main insulating material due to its low thermal conductivity (0.24 $W/m \cdot K$) [127]. Indium foils were used between different mechanical interfaces to improve thermal conductivity when necessary.

It is worth mentioning that fifteen PT100 Resistance Temperature Detectors (RTDs) are installed at the key parts of the mount. In total, the facility offers the possibility of monitoring the temperature of up to 24 locations, from which six can be part of a temperature control loop. NI Data Acquisition (DAQ) modules are used for temperature monitoring besides the LakeShore controllers. The monitoring of critical parts, such as the copper plate and the movable plate, is performed through calibrated temperature sensors and might be redundant. Thermometry is wired by the fourth-lead technique to eliminate the effect of lead resistance on the measurement of the temperature sensors. The systematic error of the temperature measurements varies from 22 to 79 mK, depending on temperature.

In terms of safety the Thermal Ground Support Equipment (TGSE) is continuously monitoring the temperature sensors and the user can configure different alarms to protect sensitive devices from temperatures outside their operating range, including the detector to be characterized. Therefore, if the temperature is too low to compromise the functioning of the detector, the cryocooler is deactivated automatically, and if the temperature is too high (usually during warming up or outgassing processes), the concerned heaters are deactivated. The temperature rate of the copper plate when suddenly disconnecting the cryocooler is not higher than 0.5 K/min. Similarly, the TGSE is continuously monitoring the vacuum level in the chamber through a pressure gauge with 30 % of accuracy between 1×10^{-9} and 1×10^{3} mbar. A redundant pressure gauge is available in case of failure of the main one. The TGSE was developed in LabVIEW with some functionalities in Python. The data acquired during the campaign of measurements is backed up in the servers of BIRA-IASB, including detector frames, radiometry, thermometry, and ambient parameters. Moreover, backup computers can substitute the optical and the thermal GSE systems in case of failure.

The core of the security system is a security rack whose control panel is available from the cleanroom although the main functionalities can be

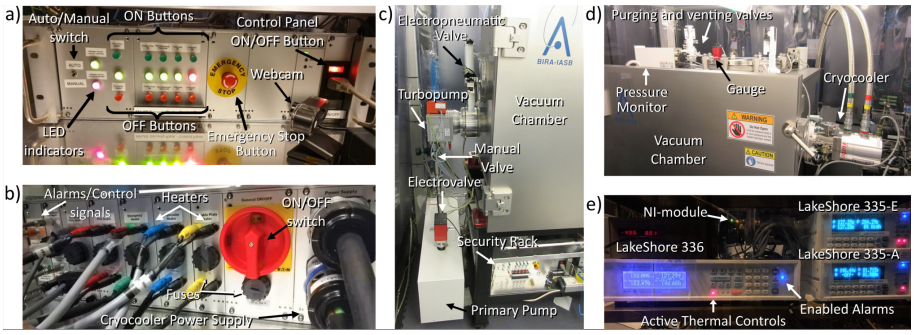

Figure 3.8: Security system components [128]: a) Control panel of the security rack, b) rear panel of the security rack, c) pumping system, d) cryocooler and pressure gauge, e) temperature monitors and controllers.

accessed from the TGSE. The TGSE controls temperature and pressure monitors while displaying and registering data in real time. Together with the pumping system, the TGSE provides the input conditions to the security rack for the activation or deactivation of the different devices of the cryogenic system. If any anomaly is detected, such as failures in the pumping system or leaks, the electro-pneumatic valve is automatically closed to avoid vacuum loss. Additionally, an electrovalve is available to isolate the turbomolecular pump from the primary pump. Overpressure is avoided by means of pressure relief valves installed in the vacuum chamber to mainly protect the viewport during the venting process. In case of a power blackout, the cryogenic system will stop working and the electro-pneumatic valve will close. However, an Uninterruptible Power Supply (UPS) system is available to continue powering the TGSE for the monitoring of pressure and temperature conditions for 4.5 hours after the power blackout. In case of a general power blackout, BIRA-IASB counts with an electricity generator with the capability to supply energy to the institute for $\sim$24 hours during working days, or up to $\sim$48 hours during weekends. Moreover, the control panel of the security rack includes an emergency stop button to immediately suspend the functioning of the pumping and cryogenic systems while the electro-pneumatic valve of the vacuum chamber is closed, without compromising the safety of the sensitive devices installed inside the vacuum chamber. If an irregularity is detected, SMS messages notify the operators in charge. This is especially useful during nights and weekends. Additional details concerning the security system of the VIS-NIR characterization facility can be consulted in Cisneros et

al. [128]. Figure 3.8 shows pictures of the security rack and the vacuum system of the VIS-NIR characterization facility.

3.4.2 *Optical system design*

To perform measurements in dark conditions, the VIS-NIR detector to be characterized must be harbored inside a closed radiation shield designed to limit its own thermal contribution and block the stray light from warm objects around it. Considering a threshold for negligible background radiation of 1 $e^{-}s^{-1}pix^{-1}$ for a VIS-NIR detector with a spectral cut-off at 2.5 μm, the radiation shield must be kept at a temperature below 172 K [129]. From validation tests (section 3.5.1), it was probed that the radiation shield of the BIRA-IASB facility is $\sim$10 K warmer than the cold plate when thermalizing a detector at nominal temperature (132 K), well below the limit of 172 K. The radiation shield of the facility is black anodized to reduce internal reflections, and it is externally covered with Multi-Layer Insulation (MLI) jackets to reflect back radiation from surrounding objects. However, the radiation shield is not completely closed; it was designed to allow the photon flux entrance from the viewport of the vacuum chamber to perform measurements at light conditions when required. For this purpose, the mount was provided with the Standa vacuum-compatible motorized translation stage model 8MT30V-50, which allows the opening and closing of the radiation shield by a movable plate. An optical filter was added to the movable plate to reject the thermal radiation of the viewport for wavelengths larger than 1.47 μm. If required, the movable plate can also be thermalized through a PID temperature control loop, although the minimum temperature achievable will depend on the temperature of the radiation shield. The movable plate is 13 K warmer than the radiation shield (see section 3.5.1), so it will approach the limit of 172 K only when the cold plate has a temperature of 157 K, which would correspond to a temperature already outside the typical range to thermalize a VIS-NIR detector for testing. Therefore, the thermal radiation produced by the radiation shield (and movable plate) on an H1RG^{TM} detector array of 1024x1024 pixels, is estimated as 5.8×10^{-3} $e^{-}s^{-1}pix^{-1}$ for the nominal case (132 K), and 6.5×10^{-2} $e^{-}s^{-1}pix^{-1}$ for the hottest case (144 K). These values are slightly different from what is reported in Bolsée et al. [126] due to the improvements performed to reduce stray light since then (section 3.5.2).

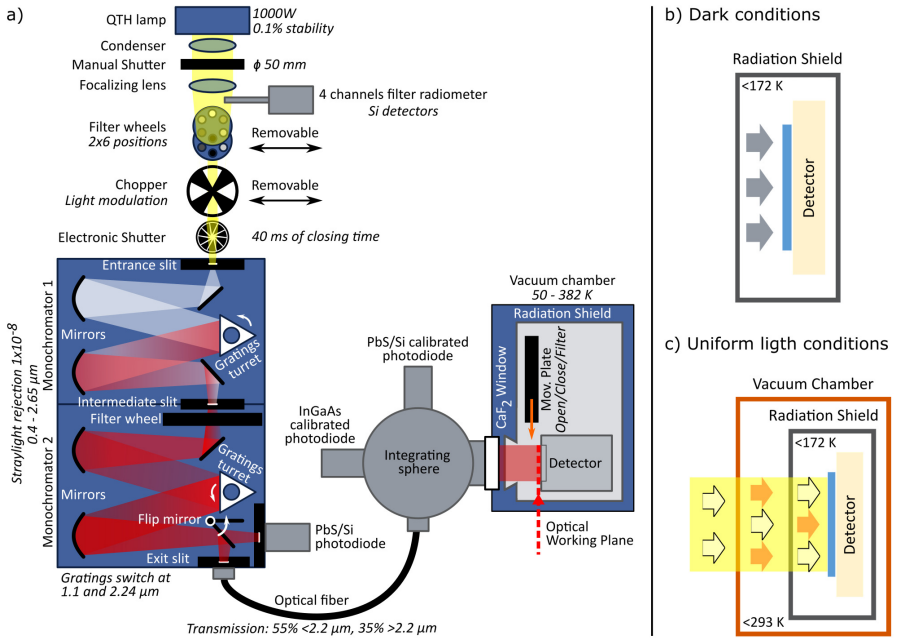

Figure 3.9: Optical diagram of the VIS-NIR characterization facility and equivalence models: (a) wavelength injection and signal monitoring from the QTH lamp to the detector inside the vacuum chamber; (b) radiation model when the movable plate of the radiation shield is closed (dark conditions); (c) radiation model when the movable plate of the radiation shield is opened. When the movable plate of the radiation shield is at the filter position, the thermal radiation from room temperature bodies is removed.

Figure 3.9 shows a schematic diagram of the optical design of the VIS-NIR facility. To let light reach the detector, the movable plate is kept either open or at the filter position. The photon flux is produced by a 1000 W QTH lamp covering the working range from 0.4 to 2.65 μm. The lamp is operated in continuous current mode with 8 A $\pm$80 μA, resulting in radiance stability $\sim$0.1 % [126]. The stability of the lamp is continuously monitored by a VIS-NIR four-channel filter radiometer with $\sim$10 nm of bandwidth (BW). An infrasil condenser and focusing lens collimate the beam from the lamp to focalize it in the entrance slit of a double-monochromator. The DTMc300 Bentham double-monochromator provides a monochromatic and tunable photon flux, with up to 10^{-8} stray light rejection. The diffraction gratings implemented in each monochromator are optimized for the VIS-NIR spectral range between 0.4 and 3.5 μm, with an accuracy on the wavelength scale of $\pm$0.1 nm up to 1.1 μm, and $\pm$0.25 nm for longer wavelengths. The

wavelength selection by the monochromator can be remotely controlled from the GSE room. The only element that must be manually adjusted is the slit width to tune the bandpass for each monochromator.

The output of the double-monochromator is coupled to a four-ports IS of 13.5 cm in diameter through a 1 m long optical fiber. The optical fiber has an average transmission of 48 % and wavelength cut-off around 2.65 μm. As it is configured, the monochromator could be used for wavelengths up to 3.5 μm if the optical fiber is replaced.

The IS is coated with spectralon (PTFE) material, suitable for VIS-NIR wavelengths. The output port of 6.35 cm in diameter is placed at the viewport of the vacuum chamber to transfer the high-homogeneity radiance to the detector. The use of absolute calibrated photodiodes in the additional ports of the IS allows for performing absolute radiometric measurements with the characterization facility, besides monitoring the stability of the signal in real-time during measurements. For this purpose, an experimental transfer function was obtained to determine the ratio of the spectral power available in one reference point of the optical WP and its corresponding point in the reference port of the IS for each wavelength (see section 3.5.2). The inhomogeneity in the illumination intensity provided by the IS at the WP and its spectral dependence were also characterized and allowed the application of a corrective factor to calculate the optical power at any position of the WP. Therefore, the optical alignment of the IS and the detector is critical.

The IS is aligned to the viewport of the vacuum chamber by means of a mechanical interface that also reduces stray light. On the other side of the viewport, the detector is aligned with respect to the baffle of the radiation shield in the optical WP of the facility in such a way that it is possible to determine which pixel of the detector intersects the central axis of the viewport. If the detector is well aligned, then the calibration can be used for absolute radiometry for each pixel.

Performing relative radiometry is simpler. The radiance at the detector must be stable during measurements, which can be demonstrated by monitoring the photodiodes at the IS. The calibration of illumination levels for measurements such as linearity in function of flux can also be performed through the monitoring of the reference photodiodes. The photodiodes used include a Bentham Si detector for wavelengths shorter than 1 μm, and a Bentham PbS detector to replace the Si detector for wavelengths longer than 1 μm. The Si photodiode was calibrated by the National Metrology Institute *Physikalisch-Technische Bundesanstalt* (PTB), and the PbS photodiode was calibrated by Bentham.

Light modulation is necessary when the PbS photodiode is in use to optimize its SNR. Then, a removable chopper is placed at the entrance of the monochromator, and a phase-sensitive detection system is used to read its signal. To allow continuous monitoring of the signal between 0.5 and 2.35 μm, a Hamamatsu InGaAs photodiode is additionally included to stay operational when the chopper is removed to illuminate the detector without phase-sensitive detection. Additional photodiodes can be installed at the dual output of the monochromator for signal monitoring.

The facility can provide up to 30 different levels of attenuation over four orders of magnitude through the combination of several neutral-density filters located in two filter wheels after the light source [126]. To stop any light exposure in the detector, the facility includes the electronic Uniblitz shutter DSS335B at the entrance slit of the monochromator. Since it has a maximum closing time of 40 ms, it can be used for latency measurements.

It is worth mentioning that the optical path between the monochromator and the external side of the viewport of the vacuum chamber is continuously flushed with nitrogen gas to avoid light absorption due to atmospheric water vapor. The Nitrocraft Nitrogen Generator NCS-004C available provides a flow of 0.6 L/min. Special attention was considered to avoid introducing stray light through the pipes.

As it is described, the BIRA-IASB facility to characterize VIS-NIR detectors is versatile enough to allow the measurement of parameters that require dark and uniform light conditions varying dynamical illumination levels and wavelengths, besides the possibility of performing absolute radiometry while stabilizing the detector at different temperatures. All this without modifying the main configuration of the facility and allowing the automation of measurements during the characterization campaigns without compromising the sensitive devices of the facility, thanks to its robust security system. Moreover, the facility is installed in an ISO-5 area that complies with clean environmental conditions continuously monitored, allowing its use for space projects.

3.5 SUBSYSTEMS VALIDATION

Before characterizing a flight model detector, the facility had to be thermally and optically validated to ensure that the capabilities required for a complete characterization of a VIS-NIR detector were met, without compromising the safety of the detector.

3.5.1 *Cryogenic system validation*

The vacuum system was carefully cleaned and degassed as well as every component of the mount was cleaned and baked out above 100°C before the assembly. The filter of the movable plate and the translation stage were installed as provided by the manufacturers, with no need for additional cleaning or baking out.

The design of the mount was initially verified by a thermal analysis performed using the CreoSimulate software before the manufacturing of the parts. However at this stage, the radiation shield and the movable plate were designed to keep a temperature close to 172 K with the cold head thermalized at 77 K. From the optical validation phase, several shielding modifications were performed at the movable plate, besides the use of a stronger thermal connection between the main thermal link and the radiation shield (section 3.5.2). As a result, the movable plate and the radiation shield thermalize around 147 and 130 K, respectively, with the cold head at 80 K.

The thermal tests also revealed the impact that the opening of the movable plate has on the internal temperature of the radiation shield. The temperature of the copper plate is not perturbed thanks to the PID control loop but this will not be the case for the temperature of a detector that is not directly controlled by a PID loop, as was the case for the MAJIS project. For instance, during the characterization of the MAJIS Spare Model (SM) detector (see [123]), the temperature of the movable plate in the open position increased by 9 K and produced a maximum temperature variation on the detector of 1.6 K. Fortunately, even during measurements under light conditions, the movable plate remained below the limit of 172 K and produced a negligible effect on the signal of the detector. However, in order to compensate for the temperature increase of the detector, the copper plate was thermalized 1.6 K below its nominal temperature. Consequently, after a position change of the movable plate, it is necessary to change the thermalization of the copper plate accordingly and wait at least 2 hours for the temperature to stabilize ($\pm$0.5 K from target temperature) [130].

The cooling-down and warming-up processes were defined during the validation phase. Figure 3.10 shows the vacuum and temperature evolution of the cryogenic system with no detector installed in the mount. At least 80 minutes are needed to achieve a vacuum level from room pressure to below 1×10^{-4} mbar in the vacuum chamber and activate the cryocooler for the cooling down of the mount. About

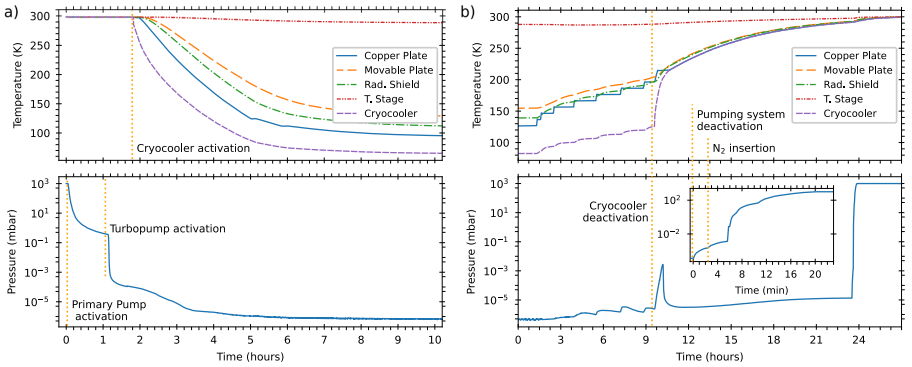

Figure 3.10: Performances of the cryogenic system of the characterization facility: (a) Pumping down of the vacuum chamber (bottom) and cooling down of the mount (top), (b) warming up of the mount (top) and venting of the vacuum chamber (bottom).

4 more hours are needed to stabilize the temperature of the copper plate to its target temperature, with a maximum rate of -0.9 K/min [126]. The temperature rate of the warming-up process is defined by the capabilities of the vacuum system to pump out the outgassing of materials, and by the rate at which the detector can be exposed. For instance, the temperature changes for the MAJIS VIS-NIR detectors could not exceed 5 K/min [128]. To avoid molecular contamination on the detector during the warming-up process, the coldest item must never be the detector itself. So depending on the temperature evolution of the mount and the vacuum level of the chamber, the cryocooler could be deactivated when the detector is above 200 K [126]. Once every item of the mount is at room temperature, the vacuum system can be stopped and the venting process can be performed.

To validate the security system, it was necessary to produce the conditions that would cause the system to fail. No real detector was installed in the facility during these tests but two additional temperature sensors were installed in the copper plate to reproduce the thermometry signals of the detector itself and its electronics. The tests included: power blackout at different stages of the pumping-out and cooling-down processes, interruption of the operation of the primary pump at different vacuum regimes, interruption of the operation of the cryocooler, activation of every low- and high-temperature alarm, leak simulation in the vacuum chamber, and activation of the emergency button at different stages of the pumping-out and cooling down processes. The only situation

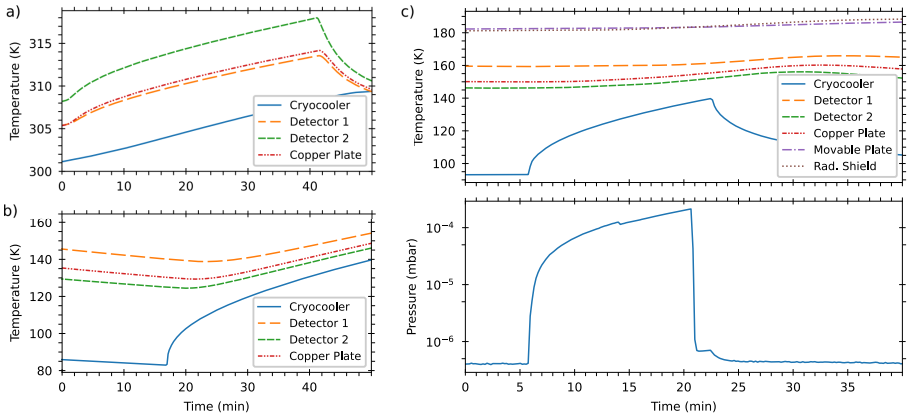

Figure 3.11: Results from the most representative validation tests of the security system: a) High-temperature alarm test, b) Low-temperature alarm test, c) Emergency stop button test. No real detector was installed in the facility but additional temperature sensors on the copper plate were used to reproduce the required thermometry signals to the security system.

that was not tested during the validation of the security system was overpressure inside the vacuum chamber.

Figure 3.11 shows the thermal-vacuum behavior of the chamber during the most representative tests. The temperature alarms are activated by considering the thermal inertia of the temperature change due to the deactivation of either the heaters or the cryocooler. Therefore, the corresponding actuator is always deactivated before the real temperature limit of the sensitive device is achieved. For instance in Figure 3.11a, the copper plate is heated until the temperature measured by Detector 2 reaches 318 K; the heaters in the copper plate are deactivated by the security system and although the temperature continues increasing, Detector 2 does not reach the temperature limit defined at 320 K. Similarly in Figure 3.11b, the copper plate is cooled down until the temperature measured by Detector 2 reaches 125 K; the cryocooler is deactivated by the security system and although the temperature continues decreasing, Detector 2 does not reach the temperature limit defined at 120 K. In both cases, the temperature of the copper plate recovers the defined safe temperature level around five minutes later [128].

The results of the emergency stop button tests (Figure 3.11c) are representative of those obtained from other tests such as power blackout, leak detection, and failure of the pumping system. Each of them causes

the closing of the electro-pneumatic valve and the deactivation of the cryocooler. In this case, the test started from the nominal vacuum level. A quick increase in pressure of about two orders of magnitude is observed after the closing of the electro-pneumatic valve. Shortly after, there is an increase in temperature due to the disconnection of the cryocooler, which in consequence produces outgassing that increases the pressure level of the vacuum chamber as well. If the vacuum level increases to 10^{-2} mbar, the turbopump can no longer be activated. However, no contamination is expected even if the detector returns to room temperature because as soon as the turbopump is activated again, the mount and the detector will release the trapped molecules during their passive warming-up, and once the cryocooler is activated these molecules will be trapped again by the cold head [130]. In case such an event takes place, a reaction time of less than an hour is expected from the personnel in charge of the facility.

3.5.2 *Optical system validation*

The validation of the optical system included the characterization of the stability of the QTH lamp, the photon flux under the different ND filters, the photon flux available per wavelength, the homogeneity of the IS at the optical WP, the transmission of the filter at the movable plate, and the level of stray light inside the radiation shield. The radiometric model of the facility [129] was essential to validate the results, especially to estimate the radiance at the output of each optical component of the facility coming from both the light source and the blackbody emissions of the individual optical surfaces.

The calibration of the power supply of the QTH lamp was verified in-house by using a calibrated multimeter and a calibrated shunt load with 0.1 Ω resistance. The deviation between the current provided by the power supply of the QTH lamp and the measured value by the multimeter, was ∼1.2 %. However, since the QTH lamp is used in a relative scale, the calibration of its power supply is not critical.

The attenuation of the light source when passing through the two filter wheels of the facility was characterized at the IS level. Each filter wheel has six different positions where nine ND filters are placed (optical densities from 0.17 to 2.3). The ND filters were selected in such a way that all cross combinations contribute to a uniform sampling of the illumination level, from the maximum flux to a flux lowered by three to four orders of magnitude [126], reaching up to 30 different

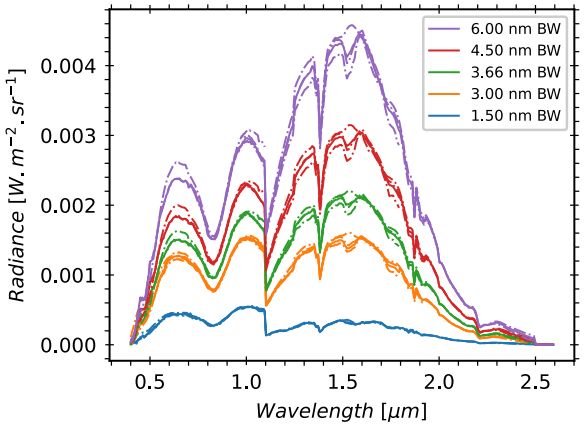

Figure 3.12: Measurement of the spectral radiance produced by the 1000 W QTH lamp of the facility, and available at the main output port of the IS for different BWs (extracted from [129]). The thick lines represent the average radiance whose measurements are represented by the dashed lines. The drop in radiance at 1.1 μm is due to the replacement of the Si photodiode by the PbS photodiode.

levels of attenuation at a certain wavelength. The analysis of the level of illumination is based on the ratio between the maximum flux at the selected wavelength (obtained from the OPEN position available) and the set of all other possible combinations, including the OPEN position. Since there is a variable level of available radiance at the viewport due to the spectrum of the light source and the wavelength-dependent transmission of the optical components, a slight change in a selected wavelength would provide a new set of 30 slightly different levels of illumination. Therefore, it can be considered that the VIS-NIR facility provides high tunability in terms of illumination. However, although the characterization performed provides information about the most appropriate combination of filters to be applied during measurements, the accurate attenuation that a detector is receiving should be characterized in real-time through the photodiodes located at the IS.

The optical power available at every output of the IS, useful for absolute radiometry, was measured with the calibrated photodiodes available (see section 3.4.2). Figure 3.12 shows the spectral radiance available at the main output port of the IS for different BWs, as measured by the Si and PbS photodiodes. The relation between the optical power that the photodiode would receive at the WP and at the actual output port of the IS, is given by a dimensionless transfer function R_0

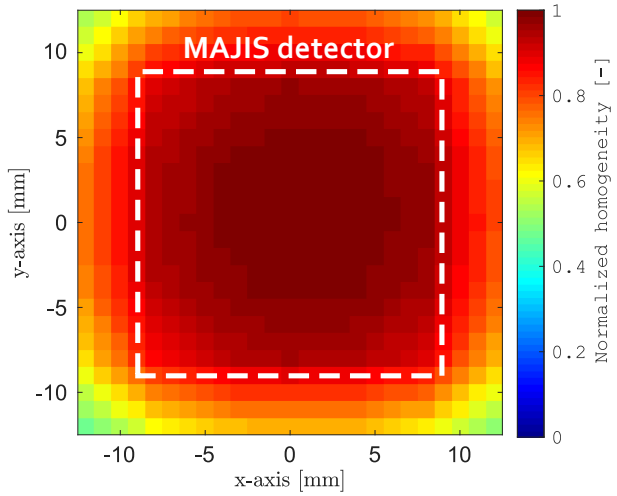

Figure 3.13: Characterization of the homogeneity from the IS at the optical WP interpolated to 1 mm. The center position corresponds to the intersection with the optical axis. The white square represents the sensitive area of the MAJIS VIS-NIR detector.

determined by equation 3.1. The parameters S_{IS} and S_{WP} were experimentally acquired and constitute the net signal of the photodiode in A, as measured at the output of the IS and at the WP, respectively. R_0 also takes into account the ratio between the solid angles corresponding to the different geometries where the photodiode was located.

$$R_0(\lambda) = \frac{S_{WP}(\lambda)}{S_{IS}(\lambda)} \tag{3.1}$$

However, the illumination of the WP is not fully homogeneous. The flux homogeneity at the output of the IS was quantified by a calibrated photodiode coupled with a pinhole at the WP. The photodiode was used to scan the illumination from the IS at different wavelengths, passing through the baffle of the radiation shield inside the vacuum chamber, in steps of 2 mm. An inhomogeneity matrix was obtained by interpolating the measurements to get a finner grid, that can be adapted to the pixel width of the detector to be characterized [129]. Since no significant spectral dependence was observed during the performed measurements (∼2 %), no spectral dependence is considered for radiance analysis during characterization campaigns [126]. The final inhomogeneity matrix of the IS (Figure 3.13) is constituted by the average of the matrix as measured in the WP, generated by the output

illumination of the IS for each wavelength, and normalized to one at the orthogonal intersection centered on the viewport. The homogeneity is especially high for the central part, describing a square of ∼16 mm around the central pixel with a homogeneity close to one. The extremes of the matrix, excluding the corners, present a decrease of only 15 % with respect to the center. The remaining inhomogeneity encountered is considered for the estimation of the spectral power in the radiometric model as a multiplicative factor for all wavelengths. Therefore, the spectral power at a certain point in the WP $P_{WP}(x, y, \lambda)$ is deduced by considering the net average spectral power as measured by the reference photodiode at the IS $P_{IS}(x, y, \lambda)$, the homogeneity propagation function $H(x, y)$ and the transfer function $R_0(\lambda)$:

$$P_{WP}(x, y, \lambda) = P_{IS}(x, y, \lambda) R_0(\lambda) H(x, y) \tag{3.2}$$

The QE of the detector $QE(\lambda)$ is defined by equation 3.3; where E_p is the photon energy illuminating the detector in J, F_{WP} is the light signal as measured by the detector (DC already subtracted) in DU, G is the derived conversion gain in e^-/DU, and IT is the integration time in seconds at which the signal was measured. Note that an overestimation of the electronic conversion gain can be induced by interpixel capacitance [131], which can lead to an overestimation of the QE. For the MAJIS VIS-NIR detectors, a factor of 0.93 is applied to the determined conversion gain to correct this effect [80].

$$QE(x, y, \lambda) = \frac{E_p}{P_{WP}(x, y, \lambda)} \cdot G \frac{F_{WP}(x, y)}{IT} \tag{3.3}$$

Optical alignment is ensured by constraining the critical parts of the mount shown in Figure 3.14. The mount itself mechanically constrains the three degrees of freedom present in rotation, since the assembly was performed by using screws with conical heads and a calibrated torquemeter to guarantee consistency between the real mount and the optomechanical design, including the integration of the detector on the cold plate. The optical axis of the facility is defined as the orthogonal light path centered on the viewport of the vacuum chamber. During the alignment validation, the optical axis was identified by a laser beam, and the mount inside the vacuum chamber was aligned by means of a cross-hair installed on the baffle of the radiation shield. The vertical alignment is performed by the translation system of the mount supporting the optical breadboard. One of the three axes of rotation of the mount is constrained by keeping the frontal part of the optical

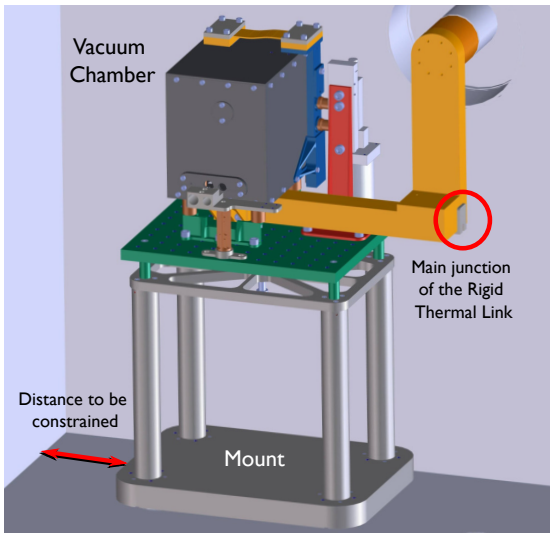

Figure 3.14: Schematic view of the interior of the vacuum chamber. The red arrow on the left shows the linear distance constrained with a calibrated jig during alignment; the red circle on the right, the main junction of the rigid thermal link constrained with an L-shape jig.

breadboard in contact with the vacuum chamber. Therefore, the mount can slide against the wall of the vacuum chamber and be aligned to the viewport by two calibrated jigs manufactured as a result of this validation. This alignment procedure guarantees repeatability with a typical tolerance of 0.2 mm for translations.

The removal of thermal radiation above 1.47 μm is actually performed by two superposed Short Wave Pass Filters (SWPFs) at the movable plate of the radiation shield. The filters are customized by Northumbria Optical Coatings Ltd. The final flux transmission is observed in Figure 3.15. Note that the SWPFs offer an average transmission of 54 % between 0.4 and 0.9 μm but, despite the high rejection above 1.47 μm (Figure 3.15a), only 16 wavelengths between 0.9 and 1.47 μm provide a transmission >30 % (Figure 3.15b). This is the main limitation of the BIRA-IASB VIS-NIR facility (see section 3.6). Therefore, the measured background signal from thermal emitters must be carefully subtracted during measurements. Additionally, measuring QE will require considering windowing techniques or short integration times to avoid saturation of the detector at wavelengths above 1.47 μm. From modeling, the residual stray light from undesirable thermal emit-

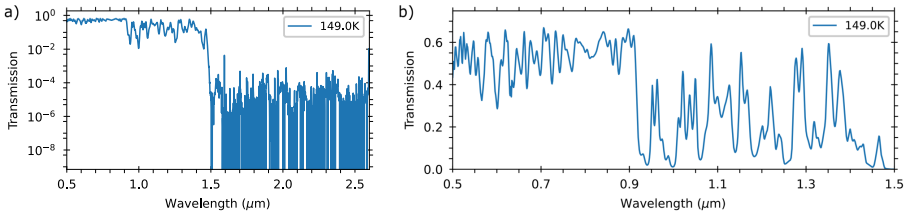

Figure 3.15: Simulated transmission of the SWPF at nominal temperature: (a) for the whole spectral range of the facility, (b) for the spectral region below 1.47 μm.

ters on the optical path was estimated to generate $<10\ e^{-}pix^{-1}s^{-1}$ when using the SWPFs.

Measuring the level of stray light inside the radiation shield requires the mount at cryogenic temperatures and the detector under dark conditions, so the photon flux reaching the detector is only due to thermal emission around it. This validation was a process performed during the characterization campaigns of the MAJIS VIS-NIR detectors [123, 130], and meant the improvements performed between campaigns. The main modifications from the original design were related to the baffling system of the slit of the movable plate, and the main flexible thermal link between the movable plate and the radiation shield. A general improvement was also performed concerning the isolation between the movable plate and the translation stage, which must remain at a temperature above 250 K. As a result, the final level of stray light measured under dark conditions was finally negligible during the MAJIS SM campaign and allowed the stray light characterization inside the radiation shield of the mount [123].

3.6 COMPARISON AGAINST OTHER FACILITIES

The BIRA-IASB VIS-NIR characterization facility was developed to be a simple and versatile option for characterizing space detectors. Other characterization facilities were discussed in section 3.2. Some clear advantages of the BIRA-IASB facility against some of them are discussed in this section.

Light source

The selected light source for the BIRA-IASB facility is a QTH lamp of 1000 W, whose radiance is similar to a blackbody at 3200 K. This lamp provides enough flux not only to saturate the detector but also to persist with enough signal after passing by two ND filters, a double-monochromator, and an IS. Generally, the power of the lamps used in other facilities [111, 113, 114, 116] is not higher than 500 W. Moreover, the radiance stability of the BIRA-IASB lamp is 0.1 %, which is better than the stability achieved by Crouzet et al. [111] (<1 %) and Koshak et al. [112] (0.5 %). Although the spectral range of the QTH lamp covers ultraviolet (UV) to NIR wavelengths, the facility is used between 0.4 and 2.65 μm due to the gratings of the double-monochromator. Therefore, an upgrade to extend the wavelength range of the VIS-NIR facility is possible by replacing the gratings.

Double-monochromator

The facility provides tunability of the VIS-NIR spectral wavelength range with bandpasses from 1 to 10 nm thanks to the use of a double-monochromator. None of the facilities described in section 3.3 specifies the use of a double-monochromator to extract the required wavelength. Typically, when using a single-monochromator, additional filters shall be implemented to improve the purity of the signal, as is the case for Crouzet et al. [111], Coles et al. [116] and Hill et al. [120]. The advantage of using a double-monochromator is to provide a tunable monochromatic flux with a high level of stray light rejection at the output selection; the undesirable high orders of diffraction are removed thanks to the internal filter wheel equipped with high-pass filters. Typically, the wavelength scale accuracy increases from $\pm$0.2 to $\pm$0.1 nm, when compared against a single monochromator, and the wavelength reproducibility also increases from $\pm$0.05 to $\pm$0.025 nm [132]. After calibration, the wavelength scale accuracy of the facility was optimized by using tabulated lines provided by spectral lamps between 0.4 and 3.5 μm.

Some test facilities directly illuminate the detector with LEDs for specific wavelengths, offering accuracy in the order of 5% to 10%, as observed in Rauscher et al. [107]. However, although these facilities can perform measurements such as linearity, they would be limited if a wide spectral range is required for measurements, such as QE. This is the reason why Secroun et al. [106] offer two configurations:

one for specific measurements under LED sources, and one with a continuum wavelength range for QE measurements including the use of a monochromator and a QTH lamp source.

Dynamical illumination levels

Similarly to the BIRA-IASB facility, Cosentino et al. [119] use different ND filters to provide adjustable radiance, while facilities such as Crouzet et al. [111] prefer the use of apertures to vary the intensity of the flux. Another example is the case of Biesiadzinski et al. [115] or Hill et al. [120], where the flux is decreased by varying both the size of a pinhole and the combination of ND filters. The BIRA-IASB facility combines ND filters in two filter wheels to reach up to 30 different levels of attenuation over four orders of magnitude, the same value as provided by Hill et al. [120]. In the BIRA-IASB facility, the ND filters were selected to contribute to a uniform sampling of the illumination level: a slight wavelength change offers a new set of 30 slightly different levels due to the spectral distribution of the QTH lamp combined with the transmissions of the spectrometer and the optical fiber, providing in consequence a great tunability in terms of illumination.

The use of two linear polarizers, from aligned to cross-orientation, could provide different but continuous levels of illumination. This is another solution to be explored in a later upgrade. The IS would remove polarization features but special attention should be paid to the cooling system dedicated to the optics at the light entrance level, since the 1000 W lamp can provide an optical power larger than the threshold limit, and could damage the polarizers.

Absolute radiometry

Thanks to the homogeneity characterization of the light flux at every point of the WP (1 mm steps, see section 3.5.2), the IS can directly illuminate the detector to perform absolute radiometry, with continuous monitoring of the light flux during data acquisition. Facilities such as Serra et al. [98], Christov et al. [113], Weatherill et al. [114], and Coles et al. [116], include a $\sim$1 m long baffle between the output port of the IS and the WP, to reduce stray light and increase uniformity despite sacrificing intensity. In the BIRA-IASB facility, the detector is aligned as close as possible to the output port of the IS outside the vacuum chamber (86 mm from the viewport). Stray light is decreased by the cold baffle of the radiation shield, and beam stability is monitored in

real-time by calibrated InGaAs and PbS/Si photodiodes installed in the additional output ports of the IS. Other facilities such as Crouzet et al. [111], implement a pick-up mirror to either focus the light on the detector under test or on the reference photodiode when necessary, so no monitoring in real-time is possible. Another example is Biesiadzinski et al. [115], where a 70/30 beam splitter is used instead to provide feedback to the reference photodiode while illuminating the detector to be characterized. Therefore, continuous monitoring is possible at the cost of decreasing flux, which is not desirable when using a 50 W lamp. In any case at the BIRA-IASB facility, the accurate alignment of the detector with respect to the IS is critical.

Cryogenic capabilities

The BIRA-IASB facility uses a close-cycle cryostat with one single cold head to thermalize the detector and the radiation shield at cryogenic temperatures. Some facilities such as Crouzet et al. [121] and Biesiadzinski et al. [115] still prefer the use of open cycle cryostats mainly due to the absence of vibrations from the pumping and cryogenic systems that can affect the stability of the detector under test. The clear disadvantage is the periodic refill of the cryostats unless it is performed automatically, as in Weatherill et al. [114]. This is not an issue for the BIRA-IASB facility, since the detector mount was mechanically designed to compensate for any vibration from the cryogenic system. Another disadvantage of the open-cycle cryostats is the minimum temperature achievable by these systems. Typically based on the use of liquid nitrogen (LN2), they do not reach temperatures lower than 120 K, while the BIRA-IASB facility is able to thermalize detectors from 50 to 382 K with a maximum temperature rate of -0.9 K/min, a rate comparable to facilities such as Crouzet et al. [121] and Weatherill et al. [114]. The copper plate is able to stabilize within 0.01 % of the target temperature, with a precision better than 7 mK.

When part of the optical system is also thermalized at cryogenic temperatures, two-stage cold head systems are preferred, as is the case for the Teledyne Imaging Sensors Test Facility [107], the Independent Detector Testing Laboratory (IDTL) [117], and the University of Hawaii Test Facility [122]. The disadvantage of only thermalizing the detector and its surrounding radiation shield at cryogenic temperatures is visible in NIR measurements. Then, the thermal contribution of the viewport of the vacuum chamber and any object behind it within the field of

view of the detector must be removed. The facilities which typically thermalize optical components inside the cryostats, cover wavelengths above 2.0 μm. Since the BIRA-IASB facility covers a spectral range up to 2.65 μm, the approach is similar to that of Crouzet et al. [111], with the use of a cold SWPF to remove the emission of warm objects outside the vacuum chamber at wavelengths longer than 1.47 μm.

Remote control

Thanks to the design of the BIRA-IASB facility, typical detector characterization measurements requiring dark conditions, different temperatures, and dynamical illumination levels and wavelengths, can be performed in one single cooling cycle without the need of changing the configuration of the setup, which ensures the repeatability of measurements. Especially for dark conditions, some facilities such as Serra et al. [98] perform measurements with a lid on the detector and, after a second cooling cycle, perform measurements under light conditions with the lid removed. The LabVIEW-based GSE allows the remote control of both the optical system and the cryogenic system without the need of accessing the clean area where the facility is installed, except for the manual adjustment of the width of the variable slits of the monochromator. Therefore, most of the processes can be automatized, including the pumping and cooling-down, and measurements that do not need the adjustment of the variable slits. This is also the case for facilities such as Secroun et al. [106], Crouzet et al. [111], and Christov et al. [113].

The BIRA-IASB facility was designed to characterize one detector at a time. If the current configuration of the mount is not modified, the size of a detector unit must be less than 138.5 mm $\times$ 106 mm $\times$ 111.5 mm to fit inside the radiation shield of the facility. Other facilities allow the characterization of multiple detectors in a single cooling cycle, including mosaics, although depending on the optical configuration it might be required to perform different cooling cycles to perform measurements at other optical configurations. Some examples are the Ultra-Low Background (ULB) [122], and the Teledyne Imaging Sensors [107] test facilities.

It is worth mentioning that the possibility of remote control and performing automatized measurements is also possible due to the robust security system developed for the BIRA-IASB facility. In this way, the facility can keep the detector under cryogenic conditions for

several weeks, while ensuring protection against thermalization outside the operating range, vacuum loss, and electric failures.

Other measurements

Although the BIRA-IASB facility was developed to perform relative and absolute irradiance measurements at the detector plane, some specialized measurements are not possible to perform in the current configuration, including Modulation-Transfer-Function (MTF), pixel spot scanning, Charge Transfer Efficiency (CTE) and pulse illumination. The pixel spot scanning feature has been used in other facilities, such as Crouzet et al. [111], as a second method to measure QE in combination with a collimated light beam. However, in the BIRA-IASB facility, the QE is measured directly from the exposure to the well-characterized flux of the IS and it was not necessary to develop a scanning system for this purpose. In any case, a non-vacuum-compatible scanning system is available at the laboratory if required. This was used for characterizing the homogeneity of the IS at the optical WP and could be adequate to become a proper pixel spot scanning in the future. Implementing the possibility to perform MTF and CTE measurements would require the inclusion of a movable knife-edge close to the detector and a ^{55}Fe light source to provide high-energy photons.

Additionally, the modularity of both the optical and cryogenic systems allows their use independently. This can be appreciated for the characterization of VIS-NIR detectors with no cryogenic requirements demanded, or if thermal testing of electronic devices is necessary.

Radiation testing is out of the scope of the BIRA-IASB facility and would require the use of radioactive sources such as Ruthenium 106 or Chlorine 36, and a different type of viewport. Moreover, only other than flight or spare detectors would be exposed to these tests. Actually for the MAJIS VIS-NIR detectors, the effect of high-energy electrons impacting their sensitive area was investigated by the *Centre Spatial de Liège* (CSL) [133].

The radiometric capabilities of the BIRA-IASB VIS-NIR characterization facility provide an optical WP with a tunable monochromatic flux between 0.4 to 2.65 μm over a four-decade range of intensity and with a high level of stray light rejection (10^{-8}) and 2 % uniformity. It counts with optical configurations for dark conditions, uniform light beam, and convergent light beam with the same focal ratio as in MAJIS;

with relative and absolute radiometric scales. Thermalization is offered within a precision of 7 mK between 50 K and 382 K, with an ultimate vacuum level in the detector chamber below 10^{-6} mbar. Moreover, the facility is installed in a certified ISO-5 environment and counts with a security system to avoid reaching temperatures outside the operational range of the detector and its electronics, and contamination due to vacuum loss [82].

The facility was already used to characterize the SM and Flight Model (FM) VIS-NIR detectors of MAJIS/JUICE [80, 123], and it is now offered to the scientific community as another option for future characterizations. As previously described in the text, the versatility provided by the VIS-NIR facility allows its use for the characterization of other astronomical detectors. Actually, the VIS-NIR facility was partially used during the cryogenic tests of the GRAvimeter for Small Solar system bodies (GRASS) [134] mission in September 2023.

The next chapter focuses on the MAJIS VIS-NIR detectors and the measurement campaigns that were needed for their complete characterization, which took place under the collaboration of the *Institut d'Astrophysique Spatiale* (IAS) [68], the lead institute of the MAJIS instrument.

4 CHARACTERIZATION OF THE MAJIS VIS-NIR DETECTORS

After the security validation and certification of the visible and near-infrared (VIS-NIR) characterization facility described in chapter 3, the *Centre Nationale d'Études Spatiales* (CNES) approved its use for the characterization of the MAJIS VIS-NIR detectors. The characterization campaigns were preceded by preparation campaigns with the use of the Structural Model (STM) and the Engineering Model (EM) of the Focal Plane Units (FPUs). The design of the characterization facility was influenced by the performances observed along the different measurement campaigns, and several improvements were implemented until reaching the final design of the facility. This chapter describes the work undertaken with the different VIS-NIR FPU models, including the characterization campaigns of the Flight Model (FM) and the Spare Model (SM). The main results concerning the characterization of the MAJIS FM and SM VIS-NIR detectors were published in Haffoud et al. [80] and Pereira et al. [123], respectively. The complete spectral calibration of MAJIS is described in Haffoud et al. [135], while the radiometric calibration is discussed in Langevin et al. [75].

The different campaigns took place through the close collaboration of the *Institut d'Astrophysique Spatiale* (IAS), and the supervision of the Belgian User Support and Operations Center (B.USOC) as the Product and Quality Assurance (PA/QA) of BIRA-IASB. The plan of measurements concerning the FM and SM detectors characterization was approved by the European Space Agency (ESA) and CNES.

4.1 MAJIS VIS-NIR FOCAL PLANE UNIT (FPU)

MAJIS underwent an extensive ground calibration that established its baseline performances. Every component of MAJIS was independently tested before its integration in the different subsystems, and later in the instrument, by reproducing the conditions at which they would be exposed once in operation. Critical components such as the FPUs, were actually tested at different temperatures [62]. The Royal Belgian Institute for Space Aeronomy (BIRA-IASB) [84] was in charge of the

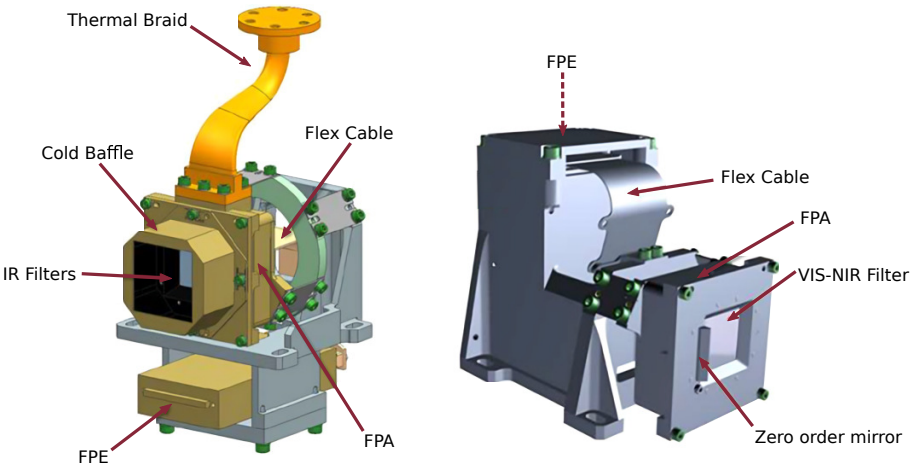

Figure 4.1: MAJIS FPUs: (left) IR channel, (right) VIS-NIR channel (extracted from [62]).

radiometric characterization of the FM and SM of the MAJIS VIS-NIR FPUs, which constitutes a key part of this research work (section 2.4).

As described in chapter 2, each spectral channel of MAJIS has its own FPU to harbor the detector, or Focal Plane Array (FPA), and its electronics, or Focal Plane Electronics (FPE). Figure 4.1 shows a diagram of both MAJIS FPUs. The flex cable is the electronic interface between the FPA and the FPE. In front of both FPA, the FPUs are equipped with Linear Variable Filters (LVFs). The VIS-NIR FPU counts with a high-pass filter, and the IR channel with a band-pass filter [73]. The VIS-NIR LVF sorts wavelengths at specific pixel columns and rejects high diffraction orders from the spectrometer [62]. Moreover, two ®*Cernox* temperature sensors are installed for monitoring the VIS-NIR FPU: one at the FPA and one at the FPE. Additionally, the VIS-NIR FPE counts with a survival line composed of three PT1000 temperature sensors and two heaters with twisted and shielded wiring. All temperature sensors guarantee a relative precision of 0.5 K [136].

Note that the VIS-NIR FPU differs from the IR FPU due to the temperature requirements they must comply with. The FPEs cannot be thermalized at temperatures below 120 K, so they must be thermally isolated from their corresponding FPA which operates at lower temperatures to reduce thermal noise [62]. The IR FPA is thermally coupled to the cold radiator of MAJIS, while the VIS-NIR FPA is thermalized by the mechanical housing of the FPU attached to the OH, which is thermally linked to the warm radiator (Figure 2.2) [79]. Therefore, the

Parameter	Requirement	Comment
LVF precision alignment	$\leq$90 μm	-
FPA precision alignment	$\leq$0.1 mm	-
Functional temperature	116-300 K	FPA
	120-300 K	FPE*
Non-operative	110-323 K	FPA
temperature**	120-323 K	FPE
Storage temperature	290-320 K	-
Maximum temperature rate	5 K/min	-
Cleanliness levels	54 ppm	-
	5×10^{-7} g/cm^2	-
	ISO5 or better	Storage
Vacuum level during tests	$< 10^{-5}$ mbar	-
Outgassing	$\leq$1 %	TML
	$\leq$0.05 %	CVCM
FPU safe distance	>0.64 mm	From other surfaces
Lifetime	$\geq$13.5 years	-

Table 4.1: MAJIS VIS-NIR FPU main requirements [136]. TML and CVCM stand for Total Mass Lost and Collected Volatile Condensable Materials, respectively. **Data acquisition above 160 K will introduce a significant amount of noise that should be avoided. **Including bakeout operations and limited to 24 hours.*

VIS-NIR FPE is inside the rear part of its FPU housing, which also guarantees the cleanliness of the internal components and the alignment of the FPA [136]. Several requirements had to be verified to comply with the scientific objectives of the MAJIS instrument. Table 4.1 shows some design constraints that had to be taken into account during the VIS-NIR characterization campaigns.

The FPAs are Mercury Cadmium Telluride (HgCdTe) detectors optimized to be sensitive to VIS-NIR or IR wavelengths depending on the spectral channel they are part of. They were manufactured by Teledyne Technologies [137], in California, USA, and consist of H1RG type arrays of 1024$\times$1024 pixels. Each *physical pixel* has a dimension of 18$\times$18 μm. Four pixels rows around each side of the array are not light-sensitive to be dedicated as reference pixels for calibration purposes. The acquired signal by each of the 1024 lines of pixels in the array, is converted into

Parameter	Requirement	Comment
Spectral range	0.5-2.35 μm	At nominal temperature
Spectral resolution	$\leq$5.5 nm	For nominal spectel
Spectral sampling	3.65 $\pm$0.25 nm	For nominal spectel
Nominal temperature	$\leq$140 K	-
Averaged QE per pixel	$\geq$70 %	At nominal temperature
FWC per pixel	$\geq$50000 e^-	At nominal temperature
DC per pixel	<25 e^-/s	At nominal temperature
RON per pixel	<50 e^-	-
Non-uniformity	Better than 5 %	At nominal temperature w.r.t. the full frame
Non-linearity	$\leq$5 %	w.r.t. the full frame
Read-out frequency	100 kHz	Slow acquisition mode
	1 MHz	Fast acquisition mode
Operability per pixel	$\geq$97 %	At nominal temperature

Table 4.2: MAJIS VIS-NIR FPA main requirements [80, 135, 136]. QE stands for Quantum Efficiency, FWC for Full-Well Capacity, DC for Dark Current, and RON for Read-Out Noise.

digital data through 16 independent video channels, by sampling the data at two read-out frequencies: 100 kHz and 1 MHz [138].

Teledyne Technologies provided performance estimates of the FPAs, but not an extensive characterization at the pixel level [139], which was done as part of this work. Table 4.2 shows the expected performances defined for the MAJIS VIS-NIR FPA. In practice, Teledyne Technologies manufactured different FPAs aiming at the MAJIS requirements. Depending on their general performances, FM, SM, and EM FPAs were selected for each channel, with the development of their corresponding FPUs.

The parameters used to assess the performances of the FPAs during the characterization campaigns included Dark Current (DC), linearity, Read-Out Noise (RON), Quantum Efficiency (QE) and operability [80], which are also related to the Full-Well Capacity (FWC) of the pixels, their Dark Signal Non-Uniformity (DSNU), Photo-Response Non-Uniformity (PRNU), persistence, bias and conversion gain [62]. Moreover, although misalignment and optical distortions are reduced

by using robust mechanical mounts and optimizing the optical design, it was required to determine the central wavelength position at the FPA, and the spectral response of each pixel after the final integration [135]. Both measurements are related to the alignment of the LVF on the FPU. The VIS-NIR FM FPU was first characterized without LVF and after in its final configuration with LVF, while the SM was directly characterized with LVF.

An additional FPU, the STM, was developed without functional FPA or FPE. It was mainly developed for thermal testing purposes and handling procedures for installation and alignment [136]. The EM FPU was used for the preparation and validation of optical tests and data acquisition procedures.

4.2 STRUCTURAL MODEL PREPARATION CAMPAIGN

The thermal tests with the Structural Model (STM) of the MAJIS VIS-NIR FPU, usefully supported the development of the Thermal Ground Support Equipment (TGSE) of the BIRA-IASB characterization facility and the first preliminary tests of the cryogenic system. These tests allowed the estimation of the time characteristics of the facility to stabilize an FPU at the target temperature. The campaign took place in October-November 2019 [140].

The MAJIS VIS-NIR STM FPU included one heater to simulate the heat dissipation of the FPA and one more for the FPE. Additional PT100 temperature sensors were installed on the dummy FPA and FPE for the complete thermal monitoring of the FPU. Since the STM FPU did not include the FPE harness nor the flex cable (Figure 4.1), it was not possible to realistically simulate the heat dissipation of an operational FPU, nor the thermal link between the FPA and the FPE. Nevertheless, a heat power of 2 W was assumed for the FPE [140]. During the tests, the dummy FPA was thermalized at 140 K, with its heater supplied at the nominal expected power for the FPA while simulating different heating dissipation scenarios on the FPE heater to preliminary evaluate the influence of the FPE on the FPA temperature [140].

Moreover in this campaign, and as part of this work, several procedures were developed and optimized for the proper manipulation and installation of a MAJIS VIS-NIR FPU in the characterization facility. Such procedures included the unpacking of MAJIS equipment from the external areas of the laboratory to the ISO-5 environment, the integration and optical alignment of the VIS-NIR FPU in the radiation shield

of the facility, the optical alignment of the mount with respect to the working plane (WP) of the characterization facility, and the uninstallation of the FPU. Additionally, since a functional MAJIS FPU must not remain at room conditions for more than 24 hours, a special procedure was performed to keep the FPU under static vacuum conditions in case the integration procedures were not finalized during one working day.

Besides the continuous monitoring of the environmental conditions by the Ground Support Equipment (GSE) of the characterization facility (see section 3.4), cleanliness level verification tests of the laboratory were performed before starting campaign operations. Moreover, Molecular Organic Contamination (MOC) and Particle Fall-Out (PFO) witness plates were used to measure the cleanliness conditions to which an FPU was exposed during alignment and its corresponding campaign of measurements.

The integration of a MAJIS VIS-NIR FPU in the characterization facility involved the participation of one operator from IAS and one operator from BIRA-IASB. The IAS operator was responsible for handling the FPU, while the BIRA-IASB operator was in charge of the mount and the characterization facility. Additional tools were manufactured for the mechanical alignment of the FPU. Optical alignment was not preferred to avoid direct illumination of the FPA with a laser, although this was finally done when identifying the pixel intersecting the WP center of the facility during the characterization campaigns, by attenuating the beam with a neutral density filter.

Figure 4.2 shows a picture of a functional MAJIS VIS-NIR FPU during its alignment in the radiation shield of the characterization facility. This is made by using a cubic jig and a special frame to keep the radiation shield assembled as in its final configuration. The four holes on the copper plate ensure that the FPA is at the center of the baffle. While the FPU is partially screwed on the copper plate, the jig is introduced between the rear part of the FPU and the frontal surface of the rear panel of the radiation shield. Next, the FPU is completely moved backward until it enters in contact with the jig, so the FPU can be fully screwed to the copper plate. Then the jig and the metallic blade are removed to finally close the radiation shield and continue with the alignment of the mount inside the vacuum chamber. It was preferred to work with the rear parts of the FPU during the mechanical alignment to minimize the risk on the FPA side during this procedure. To avoid scratching the surface of the FPU, a metallic blade was used as a mechanical interface during the alignment, whose thickness was certainly considered in the

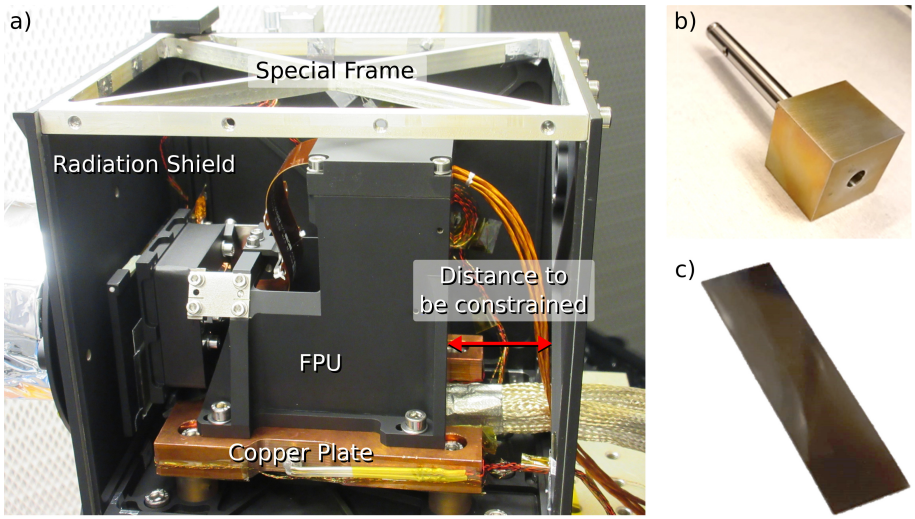

Figure 4.2: MAJIS VIS-NIR FPU alignment inside the radiation shield (extracted from [130]): a) FPU to be aligned inside the radiation shield with a special frame on the top side from which the rear part of the FPU can be easily accessed with the jig, b) cubic jig, c) metallic blade to protect the FPU surface from possible scratches.

adjustment of the distance between the FPA and the front panel of the radiation shield.

Finally, the optical alignment of the mount with respect to the WP of the characterization facility required the participation of two trained operators from BIRA-IASB, and the methodology was previously discussed in section 3.5.2 (Figure 3.14).

It is worth mentioning that the optical alignment procedures were validated in precision and repeatability by a laser aligned to the optical axis of the facility with no operating MAJIS VIS-NIR FPU before the different campaigns. It was considered to perform the optical alignment by removing the viewport from the vacuum chamber to use a laser in front of the baffle of the radiation shield, whose center should have been previously identified by a cross-hair. However, this procedure was discarded due to the potential contamination either from the viewport flange or during the manipulation of the cross-hair, besides the time-consuming task of performing a leak test of the vacuum system before pumping down the vacuum chamber.

4.3 ENGINEERING MODEL PREPARATION CAMPAIGN

The Engineering Model (EM) of the MAJIS VIS-NIR FPU was used for the preparation and optimization of the optical tests and the data acquisition procedures of the characterization campaigns. Working with the EM FPU also allowed the validation of the procedures developed during the STM preparation campaign (section 4.2), and the development of the warming-up procedure of the FPU after cryogenic measurements. Moreover, the nominal thermal-vacuum behavior of the VIS-NIR characterization facility was demonstrated, confirming the influence of the FPE temperature on the thermal stability of the FPA, especially during acquisitions at fast read-out frequency. The measurements campaign took place in November-December 2019 [141].

By requirement, no thermal control was allowed to be fed by any of the thermometry devices available in a MAJIS FPU, especially the heaters of the survival line, to avoid reducing their lifetime and reproduce the passive cooling conditions at which the FPU will be exposed in-flight (section 2.2). The MAJIS VIS-NIR EM FPU did not include a survival line but counted with two additional PT100 temperature sensors on the FPA, and one on the FPE. The measurements performed by the ®*Cernox* sensors were used for the detailed analysis of the thermal behavior of the corresponding FPU components, while the PT100 sensors were used as the reference temperature for stability analysis [141].

During the EM campaign, the FPA was thermalized at 125 K and 140 K [141]. Thermal stabilization was arbitrarily defined as the moment from which the temperature at the device of interest varied less than ± 0.5 K during more than one hour [130]. Therefore, to properly thermalize the FPA at the corresponding target temperature or *setpoint*, the characterization of the temperature difference between the FPA and the copper plate at each campaign was relevant. In this way, the temperature of the copper plate could be adjusted before performing optical measurements, to compensate for this temperature difference. For instance during the EM campaign, the difference corresponded to an average value of 3.8 K and the copper plate had to be thermalized at 136.2 K so the FPA temperature could remain at 140 K.

The temperature influence on the thermal stability of the FPA due to the incoming flux from the different positions of the movable plate inside the radiation shield was also characterized (section 3.5.1). Moreover, although the movable plate was actually provided with a

heater to perform thermal control if necessary, it was disabled after probing that when active, the heater produced undesirable radiation on the FPA. The heaters in the copper plate could also induce similar radiation on the FPA when performing temperature adjustments. For instance, when trying to compensate for a temperature increase in the FPA due to the influence of the FPE or the movable plate. Therefore, no changes in the thermal control of the copper plate were allowed during measurements.

Regarding the optical system of the characterization facility, the campaign allowed the study of the FPA response under dark and uniform light conditions, as shown by Figure 3.9. Absolute radiometry measurements were performed at the following wavelength values: 0.8, 1.0, 1.5, 2.0, and 2.35 μm. Unfortunately, detected stray light levels under light conditions were too high to perform measurements, so they were restricted to the 125 K setpoint only. Thermal radiation from the movable plate was also identified. Therefore, some modifications were performed before the FM characterization campaign to mitigate these issues, including stronger thermal copper connections in the radiation shield and its movable plate (section 3.4.1) and the addition of Multi-Layer Insulation (MLI) jackets. The need to synchronize the electronic shutter to the acquisition system of the FPU, to guarantee a closing exactly between two subsequent images or *frames*, was also revealed at this stage. Some additional issues occurred during the campaign, which allowed the improvement of the VIS-NIR facility, especially regarding the monitoring of the stability of the lamp, the design of the customized Short-Wave Pass Filter (SWPF), and the use of neutral density filters to provide different levels of illumination [141].

After some measurements during the EM campaign, it was decided to adjust the acquisition software of the FPU to automatically reset the registers of the FPA after a series of data acquisition, avoiding a temperature increase of $\sim$0.2 K in the FPA [141]. The data processing of the full campaign was performed by IAS. However, during the campaign, quick data visualization checks were performed quasi-in real-time thanks to a tool developed by IAS that displayed the acquired frame and the signal levels in each pixel by row and column. This tool was also available for the next campaigns.

4.4 FLIGHT MODEL CHARACTERIZATION CAMPAIGN

Several improvements to the VIS-NIR characterization facility resulted from the EM preparation campaign and were implemented before characterizing the Flight Model (FM) of the MAJIS VIS-NIR FPU, besides a general optimization of the characterization measurements. The FM characterization campaign consisted of two stages: the characterization of the FPU without the LVF installed in front of the FPA, and the characterization of the FPU with the LVF, as it is the final configuration of the FPU in the spacecraft. The first characterization campaign took place in June-July 2020, and the second one in August-September 2020. The LVF was installed at IAS between campaigns. Figure 4.3 shows some pictures of the FM FPU integration during both campaigns and the final view of the mount inside the vacuum chamber. A detailed description of the FM campaign is available in Cisneros et al. [130].

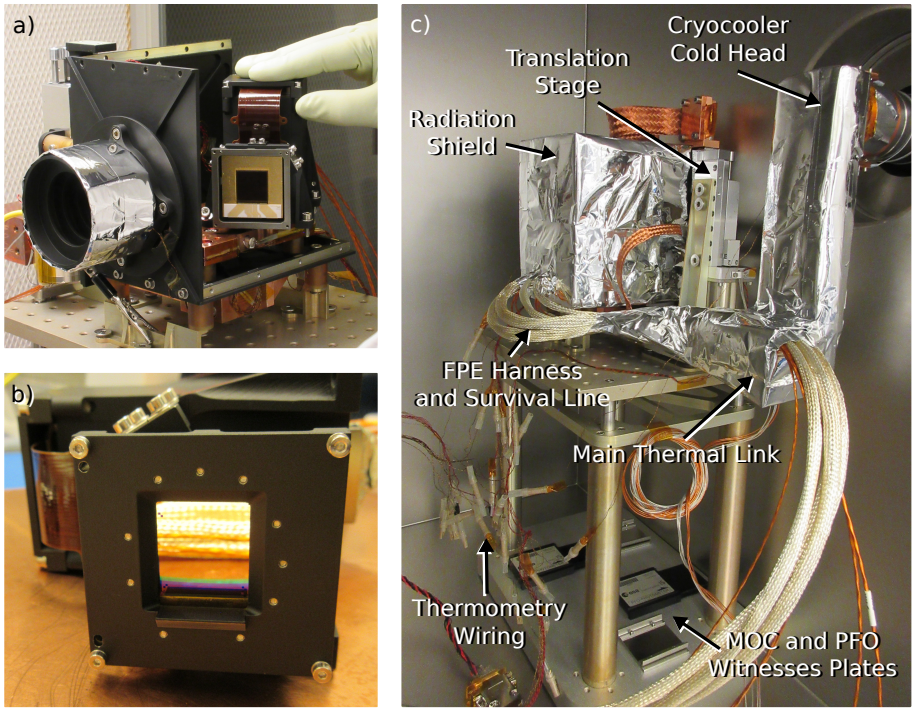

Figure 4.3: FM MAJIS VIS-NIR FPU in the VIS-NIR characterization facility: a) FPU without LVF inside the radiation shield, b) FPU with LVF after unpacking, c) FPU mount inside the vacuum chamber (extracted from [130]).

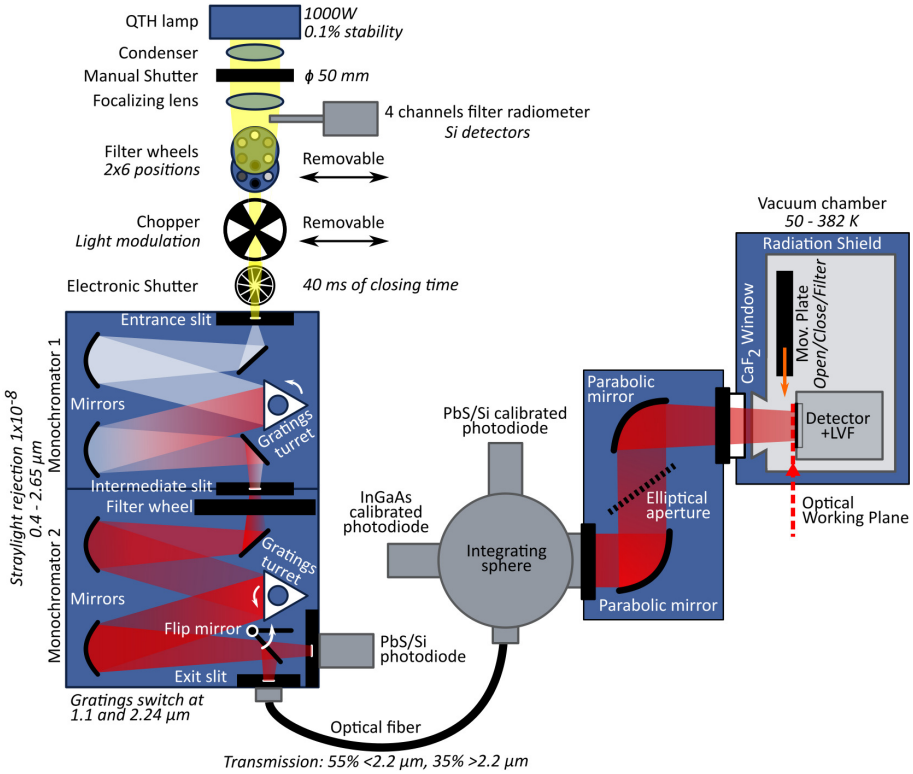

Figure 4.4: Optical diagram of the VIS-NIR facility with the focusing array for characterizing the MAJIS VIS-NIR FPU with LVF.

During this campaign, the FPA was thermalized at 125, 132, 140, and 144 K. Depending on the measurement, the monochromatic flux was adjusted between 0.4 and 2.65 μm under different intensities. Absolute radiometry measurements were performed with the FPA thermalized at 132 K and the following wavelength values: 0.425, 0.45, 0.5, 0.8, 1.02, 1.22, 1.5, 1.75, 2.0, 2.25, 2.35, 2.45, 2.5, and 2.55 μm [142]. An additional optical configuration was used to provide a focalized light beam in the WP of the characterization facility, by reproducing the focal length that the FPA receives at MAJIS (Figure 4.4). This configuration introduces a focusing array between the integrating sphere and the viewport of the vacuum chamber to provide a convergent beam of 11° [130]. The focussing array was designed by Lambda-X [143], and consists of two concave off-axis mirrors and an elliptical aperture.

Before each phase of the characterization campaign, a pre-campaign of 2-3 days of measurements was performed to characterize the temperature differences between the FPA and the copper plate under the

different positions of the movable plate, quantify the stray light present in the detector, verify the optical alignment of the characterization facility, define the fluxes and integration times to be used during the characterization measurements, adjust the frame parameters for acquisition, and verify the synchronization of the electronic shutter and the data acquisition software [80]. Moreover, quasi-real-time data processing was performed to verify that the criteria of success were met after each measurement [130].

Some remaining stray light was found in the radiation shield during the first phase of the campaign, making it unfeasible to perform dark measurements. For the second phase of the characterization campaign, the design was again improved, and dark measurements were possible [130]. The DC of the FM FPA was estimated from a region of the FPA that was not affected by stray light.

Data processing was performed by IAS. The final performances of the FM VIS-NIR FPA are detailed in Haffoud et al. [80]. Conversion gain, noise, and linearity were determined from the same measurements, and the operability per pixel was mainly determined from a combination of results based on the RON, the FWC, and the actual amount of signal per pixel compared to the rest, for both illuminated and dark frames [80]. The methodology excluded dead, hot, and *warm pixels*, for which the signal dispersion between successive images is significantly higher than the expected value from the noise model [75]. Each measurement consisted of 32 frames, varying the full-frame Integration Time (IT) from 80 to 4000 ms for the fast acquisition mode, and from 800 to 4800 ms for the slow acquisition mode. Windowing techniques were used to avoid saturation and when shorter IT values were required.

Frames were acquired under the *Correlated Double Sampling* (CDS) technique, as will be the case for the nominal operation in-flight. Figure 4.5 shows a schematic to visualize some definitions regarding data correction. The CDS technique consists of subtracting two successive frames to remove correlated perturbations: F_R after the registers reset and F_{IT} after the specified IT [75]:

$$F_{CDS}(x,y) = F_{IT}(x,y) - F_R(x,y) \tag{4.1}$$

Data processing starts with row and dark corrections of the CDS acquisitions F_{CDS}, as will be performed in-flight [80]:

$$F_{WP}(x,y) = F_{CDS}(x,y) - x_0(y) - F_{DC}(x,y) \tag{4.2}$$

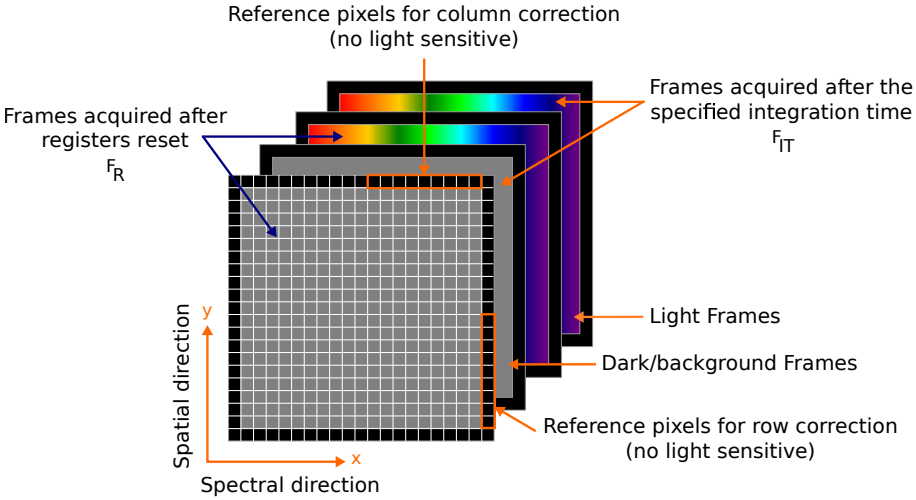

Figure 4.5: Definitions for data correction. The CDS technique consists of subtracting the signal of corresponding pixels of two consecutive frames F_R and F_{IT} acquired under the same settings. The reference pixels constitute 4 rows surrounding the sensitive area of the detector. Depending on the correction type, the median average signal of the reference pixels located at the corresponding row/column is removed from each of the pixels in the respective row/column after the CDS correction.

where F_{WP} corresponds to the frame measured by the detector after data correction, x_0 is the median average signal value of the reference pixels in each row (the zero-level signal of the acquisition), and F_{DC} corresponds to dark frames or even background frames with the same IT and settings as F_{WP}, typically acquired before or after each measurement. However, due to time constraints, dark frames were not always acquired following this principle during the campaign of measurements. For instance, the waiting time for the FPA temperature to stabilize after the closing of the radiation shield (>2 hours), and the waiting time for the lamp to stabilize after turning it on (>15 minutes). Therefore, when these frames were not available for data correction, a *column correction* subtraction, similar to row correction but considering the reference pixels of each column y_0, was possible:

$$F_{WP}(x,y) = F_{CDS}(x,y) - x_0(y) - y_0(x) \tag{4.3}$$

According to Haffoud et al. [80], this procedure slightly underestimates the FPA performances since the frames are not strictly dark.

Parameter	Physical Pixel	Nominal Spectel	Comment
Conversion gain	2.16 e^-/DU	2.16 e^-/DU	At 100 kHz
	33.56 e^-/DU	33.56 e^-/DU	At 1 MHz
RON	19.5 e^-	39 e^-	At 100 kHz
	34 e^-	68 e^-	At 1 MHz
QE	> 72 %	>72 %	-
FWC	95000 e^-	368000 e^-	At 100 kHz
	>100000 e^-	400000 e^-	At 1 MHz
DC	<15 e^-/s	<30 e^-/s	-
Non-linearity	2 %	2 %	-
Operability	>99.5 %	>99 %	-
Latency	0.07 %	0.14 %	At 1 MHz

Table 4.3: MAJIS VIS-NIR FM FPA measured performances at 132 K between 0.4 and 2.65 μm [80, 142].

The FM characterization campaign revealed the performances of the MAJIS VIS-NIR FM detector. The final results obtained for single physical pixels and nominal spectels are presented in Table 4.3. As no significant effect was observed on the linearity nor the operability of the FPA at different temperatures [75, 135], only results at the nominal temperature value (132 K) are provided. All parameters comply with the requirements presented in Table 4.2, although some measurements could not be performed in nominal conditions. For instance, the conversion gain and the noise model of the FPA, which combines RON with shot noise [123], were characterized by comparing the median standard deviation of the pixels to the mean signal of the observation for a selection of pixels in a homogeneous area of the detector. Haffoud et al. [80] probed that the FPA consistently follows the derived noise model of Langevin et al. [75] to estimate the conversion gain of the FPA. QE was analyzed with SWPFs in front of the FPA at 100 kHz read-out frequency for wavelengths below 1.4 μm, and without SWPFs at 1 MHz above 1.4 μm. Latency measurements were performed with SWPFs at 1 MHz read-out frequency [142] and contributed to the validation of the de-spiking procedure of MAJIS (section 2.2) [75].

The thermal behavior of the FPU while operating at different acquisition modes was also characterized during the campaign. This test was

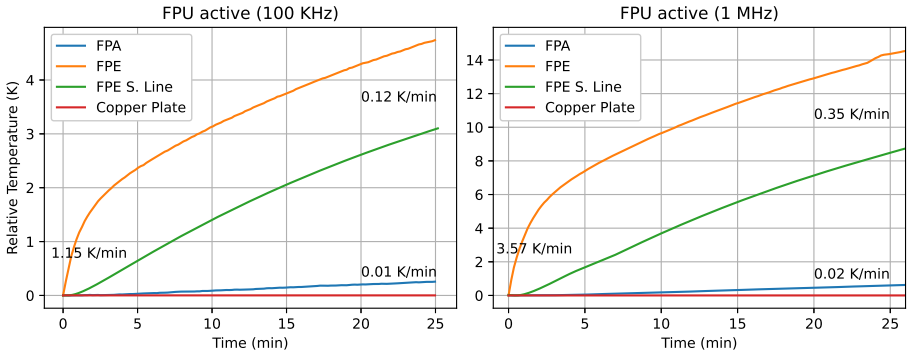

Figure 4.6: Thermal influence of the FM FPE (orange) over the FPA (blue) during different read-out frequencies: (left) slow acquisition mode, (right) fast acquisition mode. For better visualization, the temperature scale is relative to the temperature of the FPA, which was thermalized at 132 K (extracted from [130]).

performed with the FPA thermalized at 132 K. As observed in Figure 4.6, the FPA (blue) started to increase its temperature about 3 minutes after the start of the acquisition, and it achieved a temperature outside the defined setpoint for stability ($\pm$ 0.5 K) after 50 minutes in slow acquisition mode and 20 min in fast acquisition mode [130]. The offset observed between the temperature at the FPE (orange) and its survival line (green) is due to the location of their temperature sensors: the FPE ®*Cernox* sensor is located at the electronics itself, while the PT1000 sensors of the survival line are on the FPE surface. Note that, during the test, the Copper Plate (red) kept its temperature with no variation, meaning that the temperature increase experienced by the FPA was only due to the FPE.

Other tests performed during the FM campaign included the alignment verification and characterization of the LVF, the functioning verification of the survival line, and the simulation of a Ganymede Circular Orbit (GCO-5000) segment observation [130]. This last test consisted of simulating a typical acquisition with the MAJIS VIS-NIR channel in fast acquisition mode during the orbital phase of JUICE, to observe the thermal performances of the FPU and technically confirm the possibility of proceeding with these sequences. The image was acquired in dark conditions with the FPA thermalized at 132 K and lasted about 90 minutes. The FPU behavior is similar to the observed in Figure 4.6, although after the first 30 minutes of measurements, the temperature of the FPE seemed to stabilize [130]. The maximum temperature meas-

ured at the FPE during this test was 171 K. When the FPE was no longer in operation, its temperature decreased roughly by 1 K/min during the first 2 minutes, and later at a rate of 0.3 K/min. These results validated the observational strategy planned for MAJIS along the mission [130].

4.5 SPARE MODEL CHARACTERIZATION CAMPAIGN

The Spare Model (SM) of the MAJIS VIS-NIR FPU was characterized only in its final configuration, i.e., including the LVF [123]. The SIDECAR[1] Acquisition Module (SAM) board was the same as for the FM campaign [144]. This board enables the full control and data acquisition of the FPU and must remain at controlled room conditions. For this campaign, some last improvements were implemented in the facility to mitigate the stray light issues observed during the previous campaign [123]. Moreover, a second radiometric validation of the facility was performed to improve the characterization of the homogeneity at the WP [144]. In fact, the final performances of the VIS-NIR facility, already detailed in chapter 3, correspond to this version of the characterization facility.

The SM characterization campaign took place in May 2021. The integration and alignment procedures were identical to the previous campaigns. Moreover, similarly to the FM campaign (section 4.4), a pre-campaign of measurements was performed to adjust relevant parameters for the characterization measurements. During this campaign, the FPA was thermalized at six different temperatures between 122 and 145 K [123]. The VIS-NIR characterization facility was mainly configured as shown by Figure 4.4, although some measurements, such as QE and linearity, were performed with the integrating sphere directly illuminating the WP (Figure 3.9).

The data processing of the campaign was performed by BIRA-IASB, by following the procedures and recommendations already described for the FM campaign. The performances measured differ from the FM FPU by less than 1 % [123]. The alignment of the LVF and the functioning of the survival line were also verified during the SM campaign. Since the de-spiking procedure was already validated during the FM campaign (section 4.4), no latency measurements were performed during this campaign [123]. Similarly, the thermal influence of the FPE at different acquisition modes over the temperature of the FPA was not

1 System Image, Digitizing, Enhancing, Controlling, And Retrieving

characterized, as these measurements were already performed during the FM campaign, and similar performances were expected (Figure 4.6).

In practice, the MAJIS FM FPUs were not integrated into the instrument until the SM FPUs were characterized, so they could immediately be used for replacement of the FM FPUs if necessary, during the integration procedure in MAJIS.

4.6 FINAL PERFORMANCES

The science return of MAJIS critically depends on the reliability of its calibration [75]. After the integration and final alignment of the FM FPUs into the MAJIS instrument, the final performances of both spectral channels were characterized by the MAJIS team. This is discussed in Langevin et al. [75] and Haffoud et al. [135]. The Optical Head (OH) structure of MAJIS was thermalized at 110, 130, and 150 K, the corresponding lower, nominal, and upper-temperature operative cases [77]. Characterizing the final central wavelength position and spectral response per pixel in each detector provides information about the final optical distortions of the spectrograph and how they are influenced by the temperature of the OH. No significant difference was found in the absolute calibration of the VIS-NIR channel between the lower and upper thermal configurations, so no correcting calibration had to be derived [135]. However, the analysis suggested that the spectral response of a nominal spectel in the VIS-NIR channel can increase up to 10 % from nominal to upper-temperature cases, and must be considered in-flight acquisitions [135].

As discussed in section 2.2, the expected optical aberrations in MAJIS include the smile and keystone effects. After the complete characterization of MAJIS spectral channels, it was concluded that no correction of the smile effect is required to account for the variation of the temperature at the OH between the nominal and the hot temperature case [135]. Similarly, the keystone effect is within the requirements for the VIS-NIR channel, below one nominal spectel across the full spectral range and Field of View (FoV) [77]. However, a small rotation of $\sim$2 pixels along the spectral dimension was observed [77].

Unfortunately, stray light issues were identified in the MAJIS VIS-NIR channel with an impact on its radiometric calibration between 0.6 and 1.0 μm [75]. However, the stray light signal was observed to be generally larger in the center of the FPA than towards the ends of the FoV. During the instrument calibration, it was possible to model the

Parameter	VIS-NIR channel	IR channel
Spectral range	0.49-2.35 μm	2.27-5.56 μm
Spectral resolution	2.9-4.6 nm	5.5-7 nm
Spectral sampling	3.5-3.8 nm	5.9-6.9 nm
Spatial resolution at 1 bar*	$\sim$150 km	$\sim$150 km
Field of view along the slit	<150 μrad	<150 μrad
Detector temperature	127 K	88 K
Signal-to-Noise Ratio (SNR)	>100**	>100

Table 4.4: Main final MAJIS/JUICE performances [135].**From Ganymede's orbit.* ***Impacted by stray light mainly between 0.6 and 0.7 μm* [62].

stray light contribution from the pixels out of the FoV, in combination with the lamp of the MAJIS Internal Calibration Unit (ICU), which produces a very low signal at the concerning spectral range [75].

Naturally, after the JUICE launch in April 2023, the consistency of MAJIS performances was monitored and compared against the ground characterization results, during the Near-Earth Commissioning Phase (NECP). The OH had a temperature of 133.5 K during this phase, and the measurements were acquired with the ICU [77, 135]. During these measurements, although an absolute calibration shift was observed in both spectral channels, for the VIS-NIR channel this shift has a constant value of -3.8 nm along the wavelength range [135]. Furthermore, the spectral response did not change significantly after the launch (below 10 % of relative variations) [135]. Since the VIS-NIR FoV also encountered a shift of $\sim$4 pixels, it is recommended to select a read-out window from rows 100 to 899 to overcome this issue [77].

The stray light was also assessed in-flight during the JUICE Lunar-Earth Gravity Assist (LEGA) on August 2024 by the MAJIS team. The stray light contribution was directly measured from reflected sunlight when observing the Moon, as it was expected that the lunar disk covered 30 to 40 spectels of the VIS-NIR FPA [75]. Results aligned with the on-ground calibration.

Table 4.4 shows the final performances of MAJIS for both channels. It is worth mentioning that operability maps will be updated along the mission by monitoring observations of physical pixels [75]. Results from the MAJIS radiometric calibration are implemented in the data pipeline, which will be available during nominal observations, and also

includes the de-spiking procedure [75].

The complete characterization of the MAJIS detectors constituted the validation of their performances against the requirements, which is only possible before their integration into the instrument. Then, the measured performances constitute the reference starting point of the on-ground calibration to later allow the rapid and accurate analysis of the in-flight performances of the instrument. The next step was to assess the impact of these performances on the scientific objectives of MAJIS (part IV). Since this work is focused on the study of the VIS-NIR spectrum of Jupiter's atmosphere, a functional radiative transfer model of the VIS-NIR spectrum of Jupiter was developed, which is described in the next part (chapters 5 and 6).

Part III

RADIATIVE TRANSFER MODEL OF JUPITER'S ATMOSPHERE

5 SATELLITE REMOTE SENSING

When the sunlight passes through the atmosphere of any planet, depending on the wavelength of radiation, it is gradually absorbed or scattered in different directions by a variety of compounds present in the atmosphere. These compounds are constituted by molecules and aerosols. The concentration of these compounds and their spatial distribution vary according to the altitude since the temperature and pressure conditions vary as well. In some cases, atoms and molecules will even interact with each other and with radiation to produce new compounds, changing the chemistry of the atmosphere. In consequence, each level of the atmosphere will affect differently the incoming radiation and only part of it will be able to reach subsequent levels in the atmosphere. Depending on the type of compounds present in the medium, part of this radiation will be absorbed, scattered or even reflected back to space. Moreover, since these compounds being at a certain temperature, emit some radiation, this will experience the same scattering and absorption mechanisms. All these processes can be studied by *radiative transfer* theory. Measuring atmospheric processes from a certain distance, only based on radiation properties, is known as *remote sensing*. Both topics will be covered in this chapter. Most of the presented information was extracted from *A first course in atmospheric radiation* [12], *An introduction to atmospheric radiation* [145] and *Atmospheric Radiation: A primer with illustrative solutions* [25].

5.1 REMOTE SENSING AND SPECTRAL IMAGING

Descending probes, balloons, landers, and rovers are classified as *in situ* instrumentation as they enter in direct contact with the atmosphere [145]. With the exception of *in situ* atmospheric probes, the most useful way to study the atmospheres of other planets is to observe their electromagnetic spectra through remote observations, either from ground-based telescopes or from spacecrafts [146]. Nevertheless, observing other planets only from Earth restricts the wavelength range that can be explored since Earth's atmosphere absorbs part of the radiation to be measured [12]. Performing observations from space telescopes is

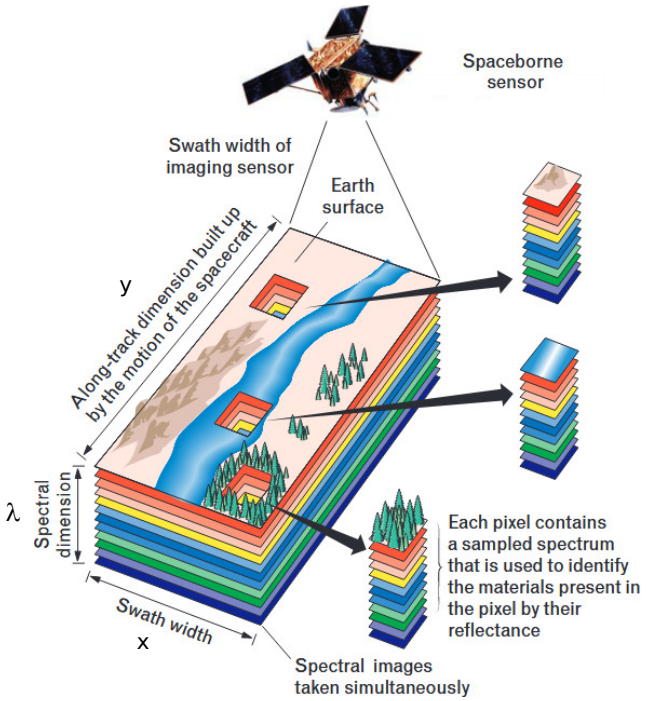

Figure 5.1: Principle of imaging spectroscopy (adapted from [147]).

not constrained by *telluric absorption* but by the current technological capabilities. The larger the optical aperture of a telescope, the more photons can be collected, which increases the angular resolution of the observation [9]. However, it is complex and costly to send large instrumentation to space, and difficult to guarantee complete coverage and continuous monitoring of a specific object, since the observing time is usually shared between different scientific interests. Certainly, manageable instruments onboard space missions, to perform satellite remote sensing around a specific planet, provide advantages complementary to the use of ground-based instrumentation for the characterization of atmospheres, including spatial and temporal coverage among other aspects.

Combining spectroscopy with methods to acquire data over large areas, is known as *imaging spectroscopy* [147]. One example is illustrated in Figure 5.1, where an imaging sensor onboard a remote sensing satellite simultaneously samples multiple spectral bands over a large area. After appropriate processing, each pixel in the resulting image contains a sampled spectral region of the light reflected and emitted by the surface. Additionally, a visual representation of the scene at

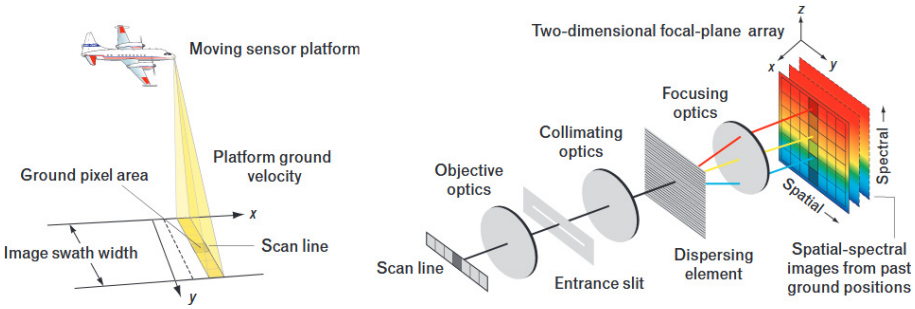

Figure 5.2: Principle of a push-broom spectral imaging system (adapted from [147]): The instrument inside the aircraft scans the ground area as one-dimensional row of cross-track pixels or *scan line*; this reflected light is dispersed by a spectrometer and registered by the focal plane array of the instrument. As the aircraft moves, the next scan line is acquired.

different wavelengths can be constructed from this spectral information [147]. The result is a three-dimensional cube of data. If the captured images are acquired by a discrete number of specific wavelengths, this technique is called *multispectral imaging*. In contrast, if the images are acquired across a vast number of continuous and narrow spectral bands, the technique is known as *hyperspectral imaging*.

In satellite remote sensing, acquiring two spatial-dimension images over many narrow spectral bands through an array of pixels, necessarily involves some form of time-sequenced imaging [147]. One way is acquiring spatial images at each of the spectral bands of interest. Another way is acquiring the spectrum of one part of the spatial image at a time. This technique is also known as *push-broom* (Figure 5.2), and involves the use of a spectrometer. Depending on the design of the instrument, the chosen spectral bands of the spectrometer could vary in resolution, be overlapping, contiguous, or disparate [147]. Although there is an integration time associated with the image formation process, the time between the collection of images of the same scene is known as *temporal sampling*.

5.2 VIEWING GEOMETRIES

A spacecraft orbiting a planet can perform remote observations under different geometries and solar illumination angles, following the chosen orbit. The orbit will be *equatorial* if the spacecraft lies around the equatorial plane of the planet, or *polar* if it passes through both poles.

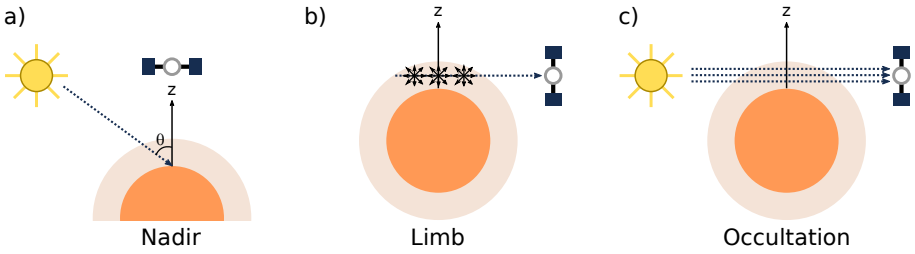

Figure 5.3: Viewing geometries in satellite remote sensing.

Moreover, if the aim is to provide uniform visibility and resolution, the orbit will be *circular*. When it is of interest to pass from high-resolution imaging to full-disk observations, the orbit will be *eccentric* so the spacecraft can approach the planet and sample part of the atmosphere, to later move away and provide full views of the planet at lower spatial resolution [9]. The nearest and farthest points of a body orbiting the Sun are called *perihelion* and *aphelion*, respectively. Similarly, an object in orbit around Jupiter will be at the *perijove* during its nearest approach, and at the *apojove* at its farthest distance. Flyby observations are also possible when a spacecraft is passing by another object of interest, either on its journey to the primary objective or during the main science orbit.

The different viewing techniques for satellite remote sensing used to study the atmosphere of a planet are shown in Figure 5.3:

- **Nadir:** The remote sensing instrument is directly observing the planet's atmosphere. Therefore, it is sensitive to the sunlight reflected and scattered by the planet. The main advantage of this technique is the possibility of continuous data acquisition and latitudinal coverage.

- **Limb:** The instrument onboard the satellite is tangentially observing the planet's atmosphere, providing a longer optical path than in nadir viewing. This technique is typically used for vertical sampling of the atmosphere, useful for characterizing its composition and structure [145]. However, the spatial resolution and coverage are limited.

- **Occultation:** The remote sensing instrument observes a natural source of radiation, such as the Sun (*solar occultation*) or stars (*stellar occultation*), while tangentially observing the planet's atmosphere [9]. Because of this reason, the level of signal acquired

by this technique will be higher than simple limb observation, in which the atmosphere itself is the radiation source.

5.3 ATMOSPHERIC RADIATIVE TRANSFER CONTRIBUTIONS

Radiative transfer corresponds to the study of the propagation of radiation through a medium. If this energy is propagated in a system much larger than the wavelength of radiation, it can be considered that the energy is propagated as rays [148]. If there are no particles that can interact with radiation, a single ray will continue propagating in a straight line. However, radiation is emitted from a source at a certain solid angle. If this source is punctual, radiation will propagate isotropically around it and the intensity of radiation will decrease inversely proportional to the square of the distance from the source (Figure 5.4). The total energy from the source or *radiance* will continue to be the same but, as it spreads in the medium, only part of the total energy will be accessible at a certain distance (*irradiance*).

If a ray passes through a non-empty medium, such as the atmosphere of a planet, energy can either be added or subtracted by *emission* or *extinction* processes, including *absorption* and *scattering* [148]. If only absorption is considered, the intensity of radiation decreases as:

$$I_\lambda(z) = I_\lambda(0)e^{-\tau(z)} \tag{5.1}$$

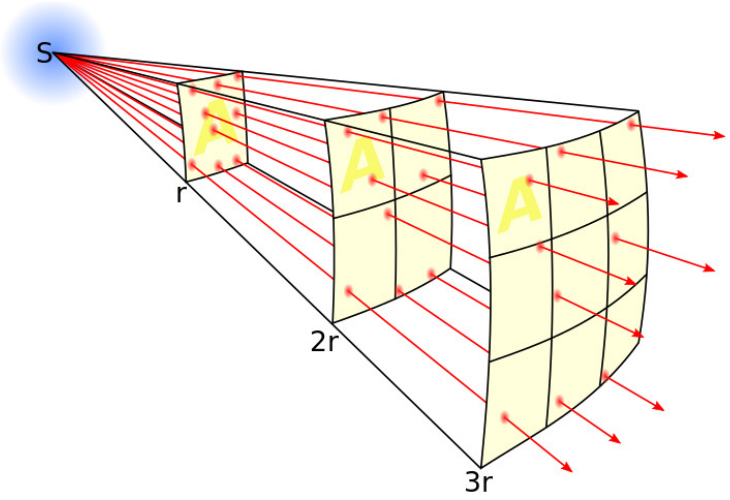

Figure 5.4: Inverse square law: S represents the light source, and r the distance at which its intensity is measured (extracted from [149]).

where $I_\lambda(0)$ corresponds to the intensity of the incident radiation, $I_\lambda(z)$ to the emergent radiation, $\tau(z)$ to the *optical depth* of the medium, dependent on the wavelength λ of radiation, and z to the length limit of the medium [25]. This is known as the *Beer-Bouguer-Lambert's law*. The *transmittance* of the medium $T_\lambda(z)$, which is the ratio between $I_\lambda(z)$ and $I_\lambda(0)$, is then defined as:

$$T_\lambda(z) = e^{-\tau(z)} \tag{5.2}$$

If $\tau(z) \ll 1$, the medium is considered to be *optically thin*, and if $\tau(z) \gg 1$ the medium is considered to be *optically thick*, respectively meaning that radiation is able or not to traverse the medium without being too much absorbed [148]. $\tau(z)$ is also known as *opacity* or *optical thickness* and is defined as the integrated extinction along the optical path at a specific λ:

$$\tau(\lambda, z) = \int_0^z \beta_e(\lambda, z)\, dz \tag{5.3}$$

where $\beta_e(\lambda, z)$ is the *extinction coefficient* of the medium and corresponds to the sum of its *absorption coefficient* $\beta_a(\lambda, z)$ and its *scattering coefficient* $\beta_s(\lambda, z)$:

$$\beta_e(\lambda, z) = \beta_a(\lambda, z) + \beta_s(\lambda, z) \tag{5.4}$$

Since the properties of the medium can be described in terms of the number density n of a same type of particles present in the medium, $\beta_e(z)$ is given by:

$$\beta_e(\lambda, z) = n\sigma_e(\lambda, z) \tag{5.5}$$

where $\sigma_e(\lambda, z)$ corresponds to the *extinction cross-section*, which is the fraction of the area of the incident radiation being blocked by those particles, and depends on their size and shape, besides the wavelength of radiation [25]. Analogously, $\beta_a(\lambda, z)$ and $\beta_s(\lambda, z)$ can also be defined in terms of $n(z)$ and their corresponding cross-sections $\sigma_a(\lambda, z)$ and $\sigma_s(\lambda, z)$ [12, 145].

If $\beta_e(\lambda, z)$ can be considered constant along the medium Δz, then equation 5.3 can be rewritten as:

$$\tau(\lambda) = n\sigma_e(\lambda)\Delta z \tag{5.6}$$

Since the particles constituting a medium have a certain internal energy, *emission* takes place. When emission is considered, the radiative

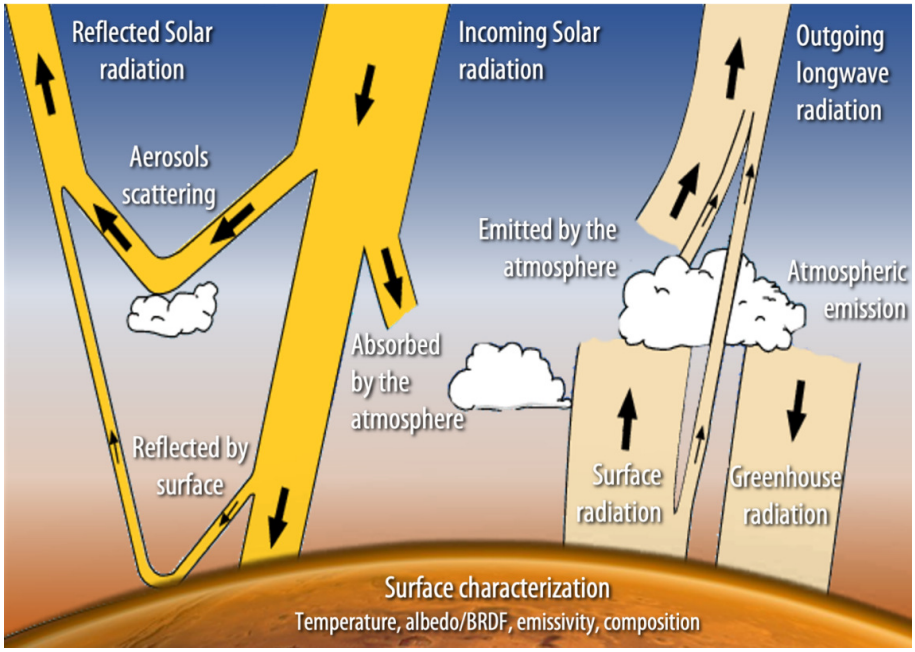

Figure 5.5: Different processes affecting radiation in a planetary atmosphere (extracted from [150]).

transfer equation consists of the sum of two terms: the initial intensity diminished by absorption, and the integrated *source function* $J_\lambda(z)$ diminished by absorption:

$$I_\lambda(z) = I_\lambda(0)e^{-\tau(\lambda,z)} + \int_0^z J_\lambda(z)\beta_e(\lambda,z)e^{-\tau(\lambda,z)}\,dz \tag{5.7}$$

where J_λ can include thermal emission and scattering [148].

In reality, radiation is affected by several processes when passing through a typical atmosphere (Figure 5.5). To simplify the radiative transfer analysis, the atmosphere can be conveniently divided into horizontal parallel layers with different thicknesses. In this way, the absorption coefficient $\beta_a(\lambda,z)$ of an atmospheric layer at a certain temperature T and pressure P can be related to different contributions: the absorption of different molecules, continua absorption associated to aerosols, Collision Induced Absorption (CIA), and Rayleigh scattering. If for convenience, λ is now expressed in terms of wavenumber ($\tilde{\nu}$=1/λ), $\beta_a(\lambda,z)$ can be evaluated as:

$$\begin{aligned}\beta_a(\tilde{\nu}, z) = &\sum_i n_i \sum_j S_{ij}(T)\phi(\tilde{\nu}, \tilde{\nu}_{ij}, T, P, p_i) \\ &+ \sum_c n_c \sigma_c(\tilde{\nu}, P, T, p_c) + \beta_{Rayleigh}(\tilde{\nu}, z)\end{aligned} \tag{5.8}$$

where the first term of the right hand represents the absorption due to single molecular absorption lines, the second term represents broadband absorption due to aerosols or molecules that do not present resolved absorption structures, and the last term corresponds to Rayleigh scattering [151]. Rayleigh scattering is not precisely an absorption term but can be considered a similar decrease of radiation through the atmosphere [152]. n and p, respectively, correspond to the number density and partial pressure of i molecular species and c broad absorption features. The sum on j represents the sum of all transitions $\tilde{\nu}_{ij}$ participating in the absorption per molecular species, given by the intensity of the corresponding line S_{ij} with a normalized line profile ϕ (section 5.3.1) [151].

Dividing the atmosphere into several horizontal parallel layers is a useful approach to consider that the emergent radiation of one layer constitutes the incident radiation of the next one, and so on. However, this approximation is only valid if $\beta_e(\lambda, z)$ is constant along the layer thickness [12], or when the emergent radiation is emitted at angles reasonably close to the normal in the layer [2]. In this way, the optical depth of each layer can be summed to obtain the total optical depth of the atmosphere.

The main mechanisms contributing to the atmospheric extinction, including molecular absorption, Rayleigh scattering, Mie scattering, and CIA, are described in the following sections.

5.3.1 *Molecular absorption*

Each molecule gives rise to a unique spectral fingerprint. Radiative transitions in a molecule can be associated to a variation of quantum numbers related to different degrees of freedom. In the frame of this work, related to the visible and near-infrared (VIS-NIR) wavelength region, the large majority of transitions considered are associated to rovibrational transitions.

The intensity of the different transition lines depends on the population of the molecules and their initial quantum state. The population

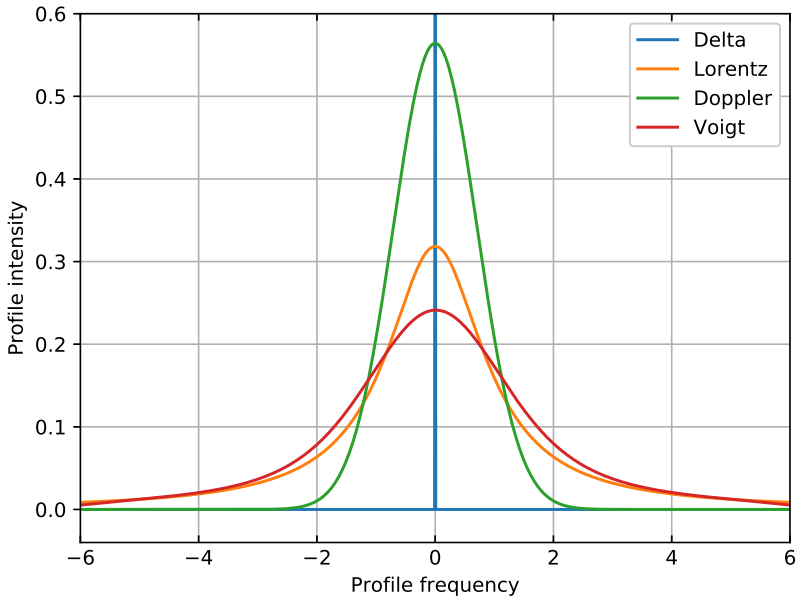

Figure 5.6: Typical spectral line profiles with γ_L=α_D=1, excepting the delta function (reproduced from [155]).

of the energy states is generally given by a Boltzmann distribution, which is related to temperature: at low temperatures, most atoms are in the ground state and, at higher temperatures, they occupy higher energy levels [25, 153]. Local Thermodynamic Equilibrium (LTE) is typically considered when the interaction between molecules is more efficient than with radiation, so the temperature in the sample can be considered uniform [9, 12]. However, under low pressures, collisions between molecules are not so frequent and the gas sample must be considered under non-LTE conditions [154].

A single spectral line should be discrete and infinite in sharpness [25], as represented by the delta function in Figure 5.6. Nevertheless, monochromatic absorption is not physically possible, and spectral lines have always a finite width and a characteristic shape since the energy necessary for a transition can slightly change due to the following mechanisms [153]:

- **Natural broadening.** Molecules in an excited state can spontaneously emit radiation [153]. The longer a molecule remains in a certain energy state, the more precise the energy of the transition is defined. Therefore, the ground state of a system will have an

extremely large lifetime and will be more sharply defined, while more energetic states will have shorter lifetimes. As the energy of a state decays exponentially in time, this effect produces a spectral line with Lorentzian line shape (Figure 5.6).

- **Pressure broadening.** Collisions between molecules are more likely to occur at high pressures. Since collisions reduce the lifetime of an energy state and increase the line width in consequence, this broadening mechanism is also related to a Lorentzian line profile. At pressures higher than 10^{-2} bar, pressure broadening should be considered [153].

- **Doppler broadening.** Molecules will absorb radiation at a specific central wavelength. However, molecules moving towards the radiation source will absorb at a slightly lower wavelength from the line center and molecules moving away will absorb at a slightly higher wavelength from the line center [153]. In consequence, these broadening mechanisms will give rise to a Doppler line profile (Figure 5.6). This line profile follows the Gaussian function as this effect is related to the thermal velocities of the individual molecules [156].

When Doppler and pressure broadening play a role, a Voigt profile can be used to describe the line profile, which is the convolution of the Lorentzian and the Gaussian functions [25]. Figure 5.6 compares the mentioned line profiles obtained for the same Half-Width at Half-Maximum (HWHM) and with the same area beneath each curve, except for the delta function. γ_L and α_D correspond to the HWHM for Lorentz and Doppler broadening, respectively. Note that the line wings of the Voigt profile are slightly more extended than those of the Lorentz profile, which makes it flatter than the other profiles.

It is worth mentioning that the Voigt profile is used to approximate a certain line shape. However, sometimes it is possible that this profile is not accurate enough. Such differences could be related to changes in the distribution of velocities, for instance, and additionally perturb a line shape [157]. Although other approximations can be more adequate for matching measurements, these corrections are not needed for this work.

Extensive tabulations with information about spectral line positions, intensities, and broadening parameters for several molecules at different pressure and temperature conditions can be found in the literature.

The HIgh-resolution TRANsmission molecular absorption database (HITRAN) is one of the most complete and widely used line list databases among different scientific communities to simulate the IR transmission and emission of electromagnetic radiation in gaseous media [12]. The most recent release of the database is HITRAN2020 [158].

Line lists efficiently store spectroscopic information that can be used to calculate molecular absorption cross-sections at a desired spectral resolution, line profiles, and with the pressure and temperature conditions at which the molecules are exposed [156]. In fact, some databases also or only provide the molecular cross-sections determined for specific applications, as is the case of ExoMol (for exoplanets and hot atmospheres [159]), and the MPI-Mainz UV/VIS Spectral Atlas [160]. Other spectroscopic databases available to the community, without being exhaustive, include HITEMP (for high-temperature modeling [161]), GEISA (atmospheric spectroscopic information for IR wavelengths [162]), CDMS (for submillimeter to microwave wavelengths [163]), and TheoReTS (theoretical line lists [164]).

Naturally, databases are continuously corrected and updated following new laboratory measurements, theoretical calculations, and empirical models [165]. Nevertheless, due to the different purposes of their line lists, databases do not necessarily include all the necessary molecules at all temperature ranges or pressure conditions. Besides, measurements and predictions become more complicated when approaching more energetic wavelengths [166, 167]. Indeed, spectral data is very limited as the visible (VIS) range is approached. For instance, the spectroscopic knowledge gathered in HITRAN for CH_4 extends from wavelengths longer than 0.8 μm [158].

5.3.2 *Rayleigh Scattering*

Scattering is a physical process by which a particle reradiates incident radiation energy in all directions. This happens because the incident radiation produces a homogeneous electric field that partially polarizes the particle, generating a dipole, which in consequence generates its own electric field that constitutes the scattered radiation [12]. The scattered radiation has a slightly different wavelength than that of the incident radiation. Nevertheless, it is generally considered identical in atmospheric processes because particles are so separated from each other, that the analysis can be made by considering independent particles (*single scattering*) [145].

Rayleigh scattering refers to the scattering of light by particles much smaller than the wavelength of the incident radiation [168]. In this regime, the particles tend to behave as isotropic scatters [2, 25]. For the VIS-NIR range, Rayleigh scattering of molecules will dominate the spectrum at wavelengths between 0.2 and 0.7 μm [4]. Rayleigh scattering limits the penetration of sunlight in planetary atmospheres, determining the altitude range over which photodissociation takes place for each molecule [1].

To determine the absorption coefficient due to Rayleigh scattering $\beta_{Rayleigh}$, it is necessary to know the total Rayleigh scattering cross-section per molecule at each atmospheric layer $\sigma_{Rayleigh}$, which represents the amount of radiation removed from the original direction that is redistributed isotropically by the area of the scatter [145]. The classical equation used to calculate $\sigma_{Rayleigh}$ can be defined as follows:

$$\sigma_{Rayleigh} = \frac{24\pi^3}{\lambda^4 N^2} \left[\frac{n_\lambda^2 - 1}{n_\lambda^2 + 2} \right]^2 F_K \tag{5.9}$$

where λ is the wavelength of radiation in meters, N is the molecular number density in m^{-3}, n_λ is the refractive index of the atmosphere, and F_K is the unit-less King correction factor [169, 170]. In fact, equation 5.9 is an approximation of the original Rayleigh's equation for $n_\lambda \approx 1$, including F_K to account for the depolarization of the molecule [25, 171].

Although molecules tend to scatter radiation isotropically in this domain, the radiation scattered by a molecule depends on its geometry and the polarization characteristics of the incident radiation [145]. In this way, F_K is related to the depolarization ratio of randomly oriented molecules illuminated by natural light, which is by definition unpolarized:

$$F_K = \frac{6 + 3\rho_n}{6 - 7\rho_n} \tag{5.10}$$

where ρ_n is defined as the ratio of intensities parallel and perpendicular to the plane of scattering [170]. For a particle with isotropic polarizability, the induced electric field will be in the same direction as the incident radiation for any particle orientation [168]. Therefore, for a spherical molecule, F_K will be close to one, so it is valid to assume unity if there is no measured value available. However, non-spherical molecules will have non-zero ρ_n values, while molecules with linear configuration will have large ρ_n values [170]. So, for molecules with similar shapes, it is valid to assume similar F_K values.

5.3.3 *Mie Scattering*

Mie theory studies light scattering produced by spherical particles, although it provides a first approximation to describe scattering by more realistic (non-spherical) shapes [19, 172]. It considers that the incident and the scattered radiation have the same wavelength [173]. However, in contrast with Rayleigh scattering, radiation is not expected to be isotropically scattered. For this regime, the scattering medium is optically characterized by its *complex refractive index* and by the size of the scattering particle [9, 25].

The complex refractive index of a medium m_λ depends on temperature and pressure, and is different for every wavelength:

$$m_\lambda = n_\lambda + ik_\lambda \tag{5.11}$$

where the real part of the refractive index n_λ describes how fast the light travels through the medium, and the imaginary part of the refractive index k_λ accounts for attenuation. An increasing n_λ value corresponds to a decreasing speed of light in the medium, which absorbs radiation only when $k_\lambda > 0$ [12]. n_λ and k_λ are coupled to one another by the Kramers-Koning relations, which can be consulted in detail in [172].

The size of the particle and the wavelength λ of the incident radiation are related through the *size parameter*:

$$x \equiv \frac{2\pi r}{\lambda} \tag{5.12}$$

where r is the radius of the particle. Thanks to this relationship, it is possible to determine if specific particles must be considered in scattering studies [12]. Figure 5.7 shows a diagram where the different scattering regimes are identified. Rayleigh scattering can be seen as an approximation of Mie scattering theory for small-size parameters [173]. Similarly, when the particles are much larger than the wavelength of incident radiation, the scattering problem can be directly addressed by *geometric optics* [145].

It could be incorrectly assumed that a particle should not extinguish more radiation than its geometrical cross-section allows it. However, this is possible for certain particles and at certain wavelengths [12]. The ratios between the extinction, absorption, or scattering cross-sections (σ_e, σ_a and σ_s, respectively) and the *geometric cross-section* of the particle XS, are known as *efficiency factors*:

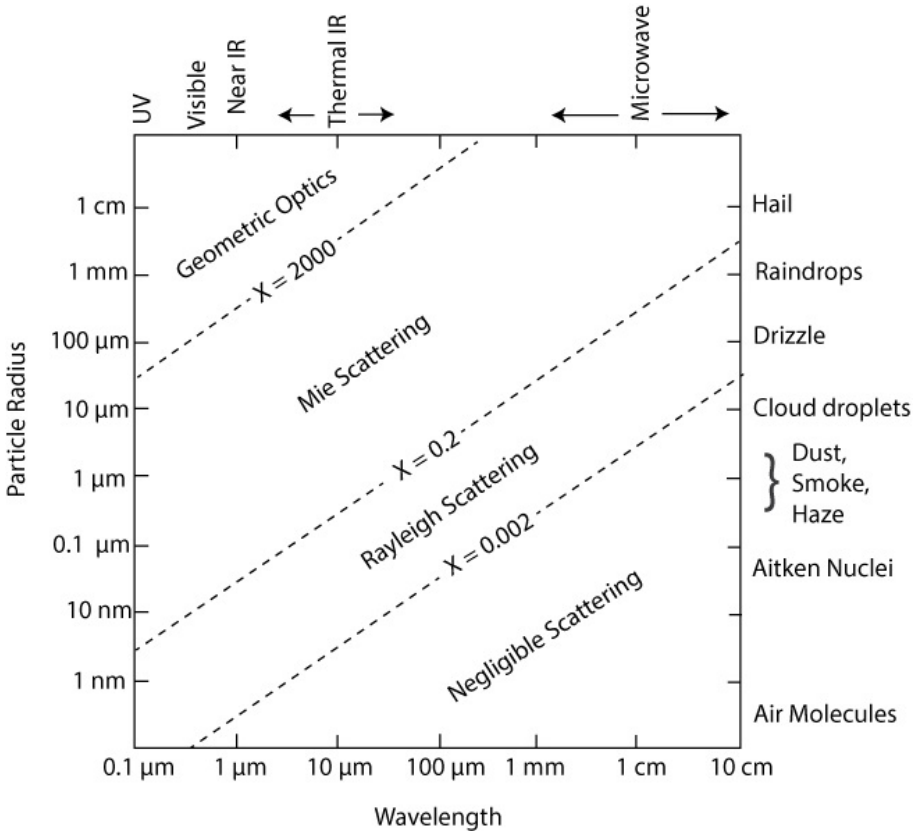

Figure 5.7: Size parameter diagram to define the scattering regime for a scatter according to its radius and the wavelength of the incident radiation (extracted from [12]).

$$Q_e = \frac{\sigma_e}{XS}, \qquad Q_a = \frac{\sigma_a}{XS}, \qquad Q_s = \frac{\sigma_s}{XS} \tag{5.13}$$

Mie theory can be used to determine the efficiency factors based on m_λ and x, in order to obtain σ_e and σ_s relative to given scatters in the medium [157]. The efficiency factors relate to the following parameters:

- **Single Scattering Albedo (SSA):** Corresponds to the ratio between the amount of radiation being scattered and that being extinguished by the particles in a medium:

$$SSA = \frac{Q_s}{Q_e} = \frac{Q_s}{Q_s + Q_a} \tag{5.14}$$

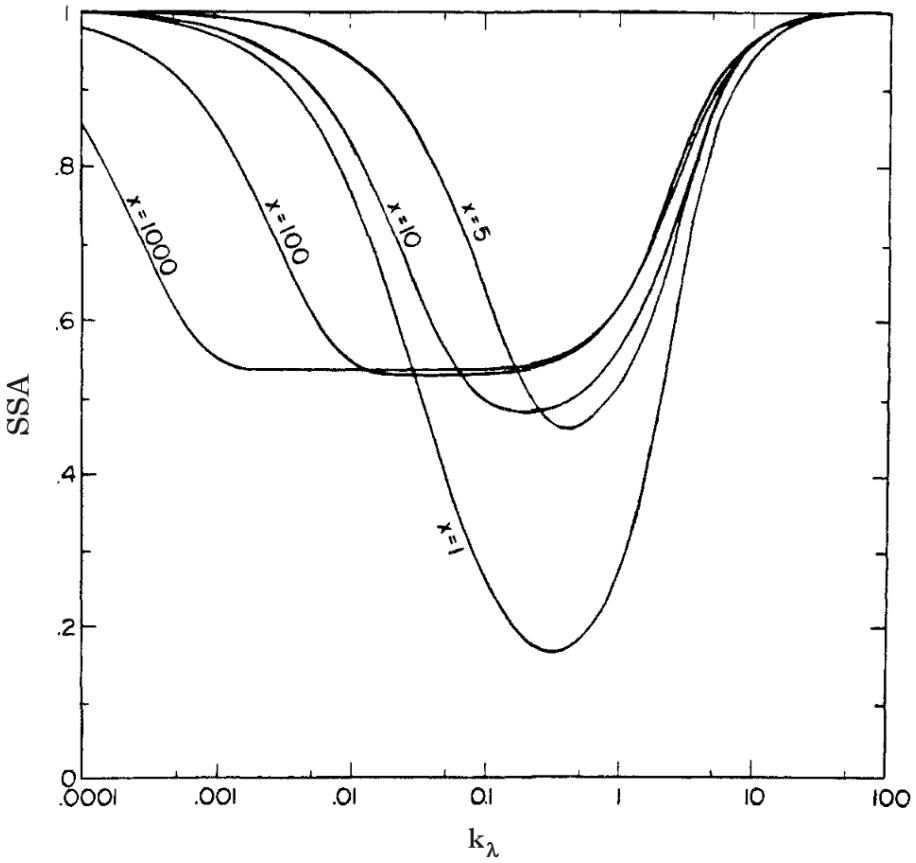

Figure 5.8: SSA in function of k_λ for different x values with $n_\lambda = 1.33$ (extracted from [157]). For large k_λ values (>10), SSA ≈ 1 independently of x since most of the radiation is simply scattered. On the other hand, when k_λ approaches zero, meaning that there is almost no absorption, SSA takes values above 0.5 for large x values. Therefore, $\sim$50 % of the radiation is scattered light and starts decreasing when x reaches smaller values since the Rayleigh scattering regime approaches and radiation is mostly absorbed.

SSA ranges from zero in a *purely absorbing medium* to one in a *purely scattering medium* [12]. Figure 5.8 shows SSA as a function of k_λ for different x values.

- **Asymmetry parameter** g**:** Describes the preferable direction of the scattered light, ranging from -1 to $+1$ [12]. In other words, it is a measure of the forward-to-backward asymmetry of the scattering pattern [157]. For scattering concentrated in the forward direction $g > 0$, for scattering concentrated in the backward direction $g < 0$,

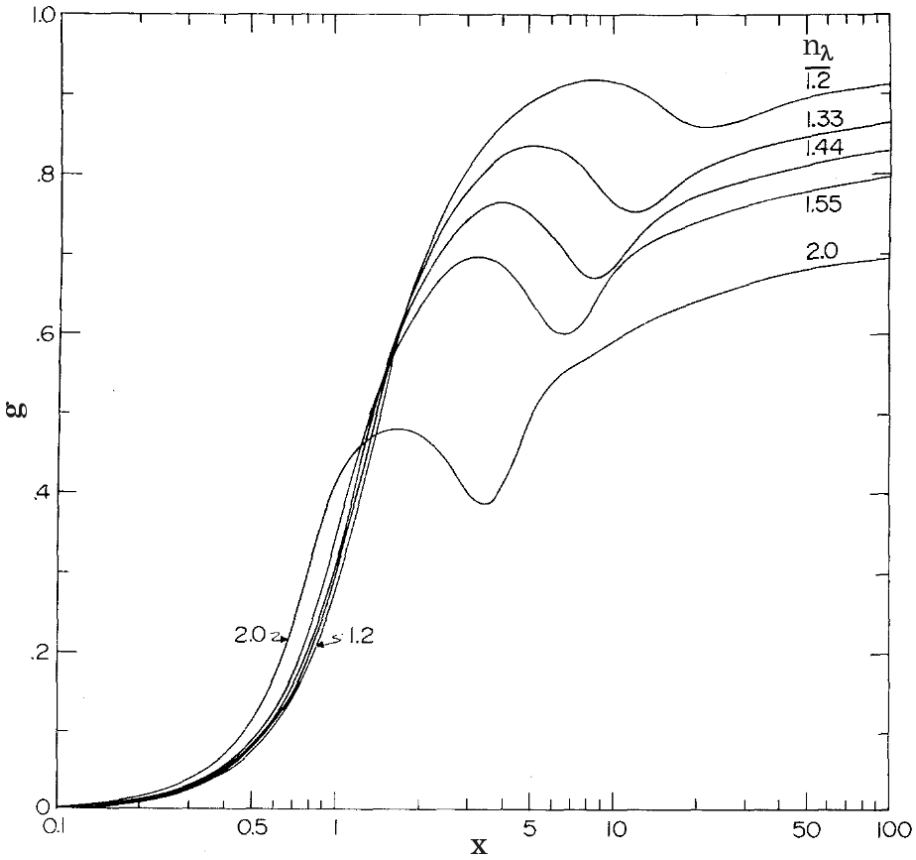

Figure 5.9: g in function of x for different n_λ values (extracted from [168]). For small x values, $g = 0$ independently of n_λ, as expected in the Rayleigh scattering regime. Moreover, while x increases, g increases but at a faster rate for larger n_λ values, since scattering is more likely to occur. Finally, for large x values (>10), g seems to stabilize around a single forward scattering value, which approaches unity for $n_\lambda \sim 1$.

and for isotropic scattering $g = 0$, as is the case for Rayleigh scattering [145]. Figure 5.9 shows g in function of x for different refractive indexes.

g is related to the scattering *phase function*, which represents the relative angular distribution of the scattered radiation [145, 173], by considering the angle between the original direction of the incident radiation Ω and the scattered direction Ω' [12]. In the Rayleigh scattering regime, the scattering phase function has the value of 1 because the probability of scattering is the same in all directions [25].

Now that the scattering phase function $P_\lambda(\Omega, \Omega')$ is defined, it is possible to specify the source function $J_\lambda(z)$, previously introduced by equation 5.7:

$$J_\lambda(z) = B_\lambda(T) - B_\lambda(T)SSA + \frac{SSA}{4\pi} \int_{4\pi} I_\lambda(z, \Omega') P_\lambda(\Omega, \Omega') d\Omega' \quad (5.15)$$

where the first term accounts for emission by involving the blackbody radiation $B_\lambda(T)$, and the second and third terms account for scattering. For practical computations, the phase function can be approximated by the *Henyey-Greenstein function*, which is parametrized by g and involves Legendre polynomials. Nevertheless, a double Henyey-Greenstein phase function is often recommended to better reproduce backscattering behavior. Further details about the definition of the phase function can be consulted in [157].

The aerosol particle size is modeled with *Particle Size Distributions* (PSDs). A PSD mathematically expresses the number density of particles within an interval of radii values and is typically normalized with the total number density of the particles [168, 174]. As with any other distribution, PSDs are defined by their mean and variance. However, these parameters should still be related to the scattering properties of the particles. Therefore, Hansen & Travis [168] defined the *effective radius* of a particle r_{eff} as the ratio between the integrated volume of the spherical particle and its surface area, and the *effective variance* v_{eff} as the expectation of the squared deviation of the particle from r_{eff}. Since then r_{eff} is independent of the functional form of the PSD, r_{eff} and v_{eff} result in useful variables to compare different PSDs (Figure 5.10). Depending on the PSD, r_{eff} and v_{eff} can be analytically related to the mean radius r_m and the geometric standard deviation s of the PSD, respectively [173]. Lognormal and gamma PSDs are typically used to model aerosols in the community, as they often match measurements [175]. Further details about the lognormal and gamma PSDs, including r_{eff} and v_{eff} relations are given in Appendix A.

The combined scattering properties of the particles can be defined in function of all possible radii of the PSD as following:

$$\beta_e = \int_{r_{min}}^{r_{max}} \pi r^2 \, Q_e(r) \, PSD(r) \, dr \quad (5.16)$$

$$\beta_s = \int_{r_{min}}^{r_{max}} \pi r^2 \, Q_s(r) \, PSD(r) \, dr \quad (5.17)$$

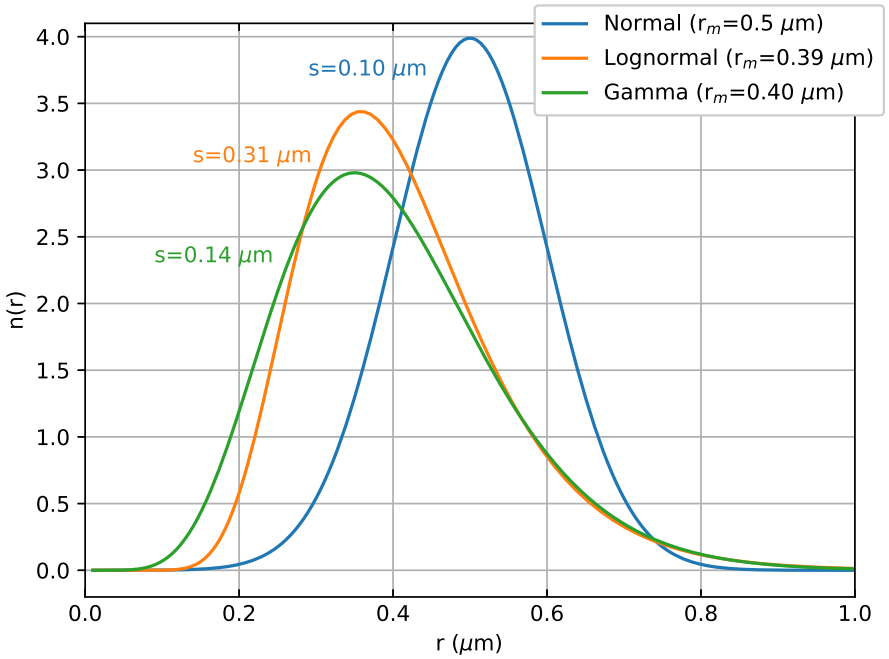

Figure 5.10: Comparison of different PSDs for $r_{eff} = 0.5$ μm and $v_{eff} = 0.1$. Note that r_m and s respectively differ from r_{eff} and v_{eff} depending on the distribution, except for the normal distribution. The analytical equivalences between those quantities can be consulted in Appendix A.

$$g = \frac{1}{\beta_s} \int_{r_{min}}^{r_{max}} \pi r^2 \, g(r) \, Q_s(r) \, PSD(r) \, dr \tag{5.18}$$

where r_{min} and r_{max} are the minimum and maximum radii of the PSD, respectively, and $g(r)$ corresponds to the asymmetry parameter for a particular r value [12]. Therefore, the defined scattering properties integrate over all possible radii included in the PSD.

5.3.4 *Collision Induced Absorption (CIA)*

A transitory dipole moment can be induced into a molecule when colliding with another molecule [157]. These kinds of transitions have a very short lifetime (in the order of picoseconds) and are difficult to detect in consequence [176]. However, collisions are more likely to occur in dense atmospheres and CIA can produce spectral broad absorption features.

In CIA case, the absorption coefficient has to consider the contribution of all possible molecular collisions. Therefore, for a sample with only two molecular species, A and B, the CIA absorption cross-section contribution is given by:

$$\sigma_a^{(2)} n^2 = \sigma_a^{(A-A)} n_A^2 + \sigma_a^{(A-B)} n_A n_B + \sigma_a^{(B-B)} n_B^2 \tag{5.19}$$

Note that if n is given in molecules/cm^3, the absorption cross-section $\sigma_a^{(2)}$ will have units of cm^5/molecule^2 because the probability of absorption is referenced to the number of pairs of molecules in the medium [158, 177]. Similarly to the molecular case, CIA cross-sections are typically derived from measurements, models, and calculations for several temperature and pressure values. The CIA absorption cross-sections are then compiled in spectral databases, such as HITRAN [158] and that from A. Borysow [178].

5.4 DESCRIPTION OF ASIMUT-ALVL

The calculation of the radiative transfer equation for a modeled atmosphere is generally done by software. ASIMUT (Atmospheric Spectra Inversion Modular Utility Tool) is a modular program for radiative transfer calculations in planetary atmospheres, developed by the Royal Belgian Institute for Space Aeronomy (BIRA-IASB) [84] that has been extensively used to characterize the atmospheres of Earth [179], Mars [180] and Venus [181], as measured with different instruments [152]. ASIMUT itself considers only absorption effects in the modeled atmospheres. ASIMUT-ALVL is the combination of ASIMUT with LIDORT (Linearized Discrete Ordinate Radiative Transfer), to also account for scattering effects due to aerosols.

ASIMUT-ALVL is able to simulate remote sensing measurements, depending on the specified characteristics of the instrument (typically a spectrometer) performing observations under the viewing geometries described in section 5.2, to obtain atmospheric radiance. The synthetic spectrum, obtained by radiative transfer calculations for a spectral region of interest, is then convolved with the Instrumental Line Shape (ILS) function to obtain the simulated spectrum of a measurement. The ILS function is the line profile produced by the spectrometer when it is illuminated by a nearly monochromatic reference wavelength.

ASIMUT-ALVL considers atmospheres in which parameters such as pressure, temperature, and molecular density depend only on altitude

Parameter	ASIMUT [152]	NEMESIS [185]	KOPRA [183]
Type	LBL	Correlated-k & LBL	LBL
Spectral range	UV-IR	UV-microwave	VIS-IR
Scattering	Yes	Yes	Single
Layering	Plane Parallel & Spherical	Plane Parallel	Spherical
Non-LTE	No	No	Yes
Institute	BIRA-IASB	Univ. of Oxford	IAA

Table 5.1: Comparison between the capabilities of different radiative transfer models. LTE stands for Local Thermodynamic Equilibrium, and IAA refers to the *Instituto de Astrofísica de Andalucía*.

[151]. This is known as *one-dimensional* atmospheres. As previously mentioned in section 5.3, dividing the atmosphere of a planet into horizontal parallel layers simplifies the radiative transfer calculation because each layer can be individually analyzed before summing them up to obtain the total optical depth of the atmosphere. For each layer defined by the user in ASIMUT-ALVL, the radiation path is calculated with a ray-tracing program by considering the refractive index of the atmosphere, typically based on equation 5.9. ASIMUT-ALVL then determines the effective temperature, pressure, and number densities for each layer, by considering homogeneous sublayers through the Curtis-Godson approximation [25, 182] to reduce computing time. Up to 70 layers can be defined in ASIMUT-ALVL [151]. The radiative transfer calculation is performed for each layer depending on the radiation path and considering the emissivity from the planetary surface, the thermal emissions from the surface and the atmospheric layers, and reflections from those thermal emissions and the Sun.

Besides ASIMUT-ALVL, other radiative transfer models exist, most of them developed for Earth's atmospheric studies. However, NEMESIS (Non-linear Optimal Estimator for MultivariatE Spectral analySIS) [146] and KOPRA (Karlsruhe Optimized and Precise Radiative transfer Algorithm) [183] are known to be used for analyzing Jupiter's atmosphere [184]. Table 5.1 compares the capabilities of each of them against ASIMUT-ALVL.

As a line-by-line (LBL) program, ASIMUT-ALVL computes the monochromatic optical depth at certain atmospheric layer by evaluating the sum of the contributions of all relevant absorption lines, weighted by their molecular abundances, to the absorption coefficient of each compound, under the corresponding pressure and temperature conditions [12]. This is repeated for all layers and eventually for other wavelengths [9]. The line parameters file read by ASIMUT-ALVL can have different formats, preferably that from HITRAN or GEISA databases [151].

The LBL method is the most accurate way of calculating a synthetic spectrum [146]. Unfortunately, it is also a time-consuming procedure only suitable for narrow wavelength ranges [12, 186]. To reduce computing time, one solution is to precompute absorption cross-sections for a grid of pressure and temperature values around those from the atmospheric temperature profile for each compound in the atmosphere [187]. These are known as *Look Up Tables* (LUTs) and constitute an additional format accepted by ASIMUT-ALVL to significantly reduce computing time.

Another solution, offered by other radiative transfer models such as NEMESIS, is to divide the spectral range of interest into intervals. Instead of including a significant number of absorption lines, it is assumed that they are randomly distributed across the interval, and the average transmittance for each of the intervals is provided for a defined grid of pressure and temperature conditions [186]. Naturally, the spectral resolution provided by this solution will be lower than the actual absorption spectrum of the individual lines, but it will be preferred in applications where the spectral resolution to be simulated is even lower (spectral resolving powers below $\sim$1000 [188]) or the wavelength range to analyze is significantly long to be computationally suitable [159, 182]. This methodology includes *band transmission models* and *correlated k-tables*. The difference between them is that band models are not suitable for analyzing scattering while correlated-k methods are [146]. In any case, the crucial point in achieving accuracy is the calculation of the absorption cross-sections on an appropriate spectral grid [183].

When considering correlated k-tables, the optical depth $\tau(\tilde{\nu})$ is obtained from k absorption coefficients as:

$$\tau(\tilde{\nu}) = \sum_i \Delta G_i \cdot e^{-k_i(\tilde{\nu})nz} \tag{5.20}$$

where ΔG_i represents the cumulative distribution function for the i absorption coefficient k of the molecule in the atmospheric layer, given by different ordinates within the $\tilde{\nu}$ interval, n corresponds to the number density of the molecule, and z to the thickness of the layer [25]. In this way, the corresponding σ_a is obtained from the transmittance of the layer (equation 5.2) as:

$$\sigma_a(\tilde{\nu}, z) = -\frac{1}{nz} \ln \left(\sum_i \Delta G_i \cdot e^{-k_i(\tilde{\nu})nz} \right) \tag{5.21}$$

which has to be computed for all interval wavelengths in the spectral range at each pressure and temperature value of the correlated-k table.

ASIMUT-ALVL provides radiance and transmittance as main outputs. Transmittance will be relevant in occultations and limb observations, where the absorption of the atmosphere is measured. Radiance can be used to determine the *reflectance* relative to a diffuse surface I/F, which is relevant for nadir observations. This measure of reflectance corresponds to the ratio between the radiation reflected by a diffuse surface in a given direction $L_{reflected}$, and the incoming radiation averaged overall directions L_{total}:

$$I/F = \frac{L_{reflected}}{L_{total}} = \frac{L_{simulated}}{L_{sun} + L_{planet}} \tag{5.22}$$

In this case of study, $L_{reflected}$ corresponds to the simulated radiance $L_{simulated}$, and L_{total} to the radiance from the Sun reflected by the planet L_{sun} and the radiance from the planet L_{planet}, all provided by ASIMUT-ALVL [151].

Concerning Mie Scattering, ASIMUT-ALVL offers different formalisms to determine the optical depth of aerosols [151]. If the radiative transfer simulation only accounts for absorption and emission, as is the case for occultations and limb observations, specifying aerosols σ_e through the `ModAngstrom` formalism is enough to obtain the optical depth of each atmospheric layer by following equation 5.6. Nevertheless, for nadir observations, σ_e, SSA, and g must be given in a single file for each of the aerosols considered in the atmosphere, as expected by the `LidortG` formalism available in ASIMUT-ALVL [151]. As it is done by several authors [19, 30, 34, 189–191], this formalism approaches the non-spherical particle case by smoothing the scattering phase function with the Henyey-Greenstein approximation [189, 192]. Typically, 100 Legendre polynomials are used to expand the phase function, as performed by other models [193].

It is worth mentioning that ASIMUT-ALVL was developed in *C* language, and thanks to its modularity, it is relatively easy for the user to create new functions or add new options to the existing ones. The user can access every parameter required for every study, and implement different ways to model a radiative contribution for its study. One of the main tasks that were performed for this work, consisted in upgrading ASIMUT-ALVL to include the modeling of Jupiter's atmosphere. This was not available before and was not straightforward to model through the capabilities already available for the implemented planets, including Earth, Mars, and Venus. This was the first time a gas planet was modeled in ASIMUT-ALVL, and required the implementation of new functionalities in the program, among other aspects. Details of the implementation and the validation of this new version of ASIMUT-ALVL are further discussed in chapter 6.

6 RADIATIVE TRANSFER MODEL

As discussed in chapter 1, Jupiter is a gas giant planet with no surface in its interior. It can actually be considered as a massive ball of light gasses with a consequent pressure increasing toward its core. On the envelope of this ball, the light gasses interact with other compounds present in the atmosphere. Since Jupiter has a rotation period of almost ten hours, the complexity of studying Jupiter's atmosphere is mainly due to the highly dynamic and turbulent environment to which all compounds are exposed. The interaction of light with the dynamic atmosphere of Jupiter can be understood with radiative transfer models by allowing the analysis of scientific observations. In preparation for the scientific data that will be provided by MAJIS/JUICE in the next decade, it is necessary to develop a functional radiative transfer tool for the characterization of Jupiter's atmosphere. Within this context, ASIMUT-ALVL has been updated and now it is offered to the scientific community for its use in the radiative transfer model of Jupiter's atmosphere for visible and near-infrared (VIS-NIR) wavelengths.

This chapter will focus on the development of the radiative transfer model to study the atmosphere of Jupiter and its differences concerning those of terrestrial planets, including a detailed description of the typical contributions that can be observed in Jupiter's VIS-NIR spectrum and had to be implemented in the model.

6.1 CONSIDERATIONS FOR GAS PLANETS

For radiative transfer analysis, as discussed in chapter 5, it is necessary to define the light source, the body or medium it affects, and the device to observe the interaction between both. For this work, the solar spectral irradiance was taken from Thuiller et al. [194]. Jupiter was defined by its physical parameters, including radius, mass, gravity, albedo, and distance from the Sun, already described by Table 1.1.

Additionally, a temperature profile of Jupiter's atmosphere allows the understanding of the evolution of its temperature along the different altitudes or pressure levels. Thanks to the measurements performed by the probe of the Galileo mission (Seiff et al. [29]), the temperature

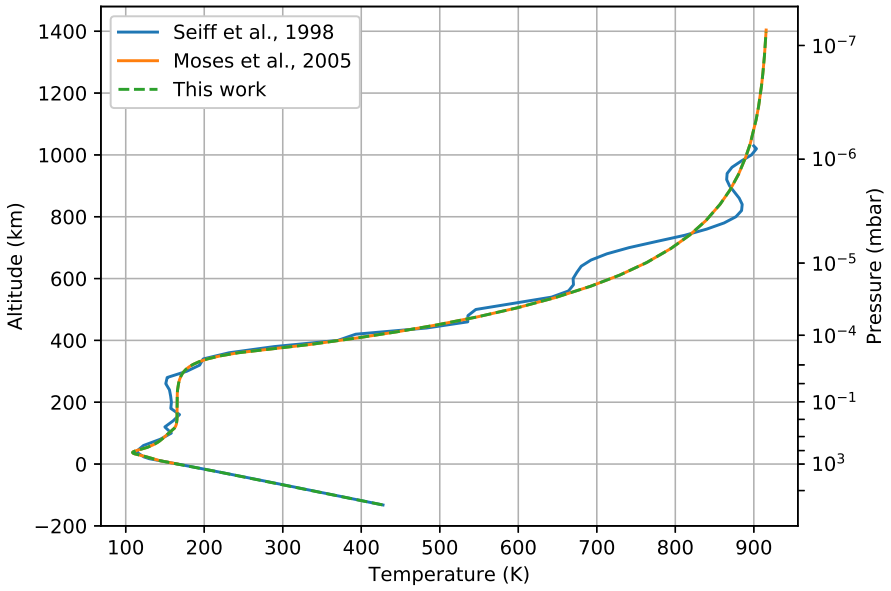

Figure 6.1: Temperature profiles of Jupiter's atmosphere.

and pressure values at different depths are known. However, since the probe entered a relatively cloud-free region with low water content, such measurements cannot be generalized to explain the profile of every location on the planet. Instead, this temperature profile should be considered a starting point to be adapted depending on the region under study. In this sense, this work takes the model of Moses et al. [4], which is a temperature profile derived from the one of Seiff et al. [29] at pressures lower than 10^{-3} mbar, and is based on observations from the Infrared Space Observatory (ISO) for pressures deeper than 1 mbar from Lellouch et al. [195]. The data available from this model[1] did not include information below 0 km, so it was supplemented with data from Seiff et al. [29] for pressure levels down to 20 bar. Figure 6.1 shows a comparison between the mentioned temperature profiles and the one used for this work.

The composition of Jupiter's atmosphere is defined by the Volume Mixing Ratio (VMR) profile of every molecular species. The reference atmospheric profile for this work was taken from González et al. [196][1], following the work of López-Puertas et al. [26]. This reference

1 Obtained from personal communication with M. López-Puertas, Permanent Research Professor at the *Instituto de Astrofísica de Andalucía* (IAA)

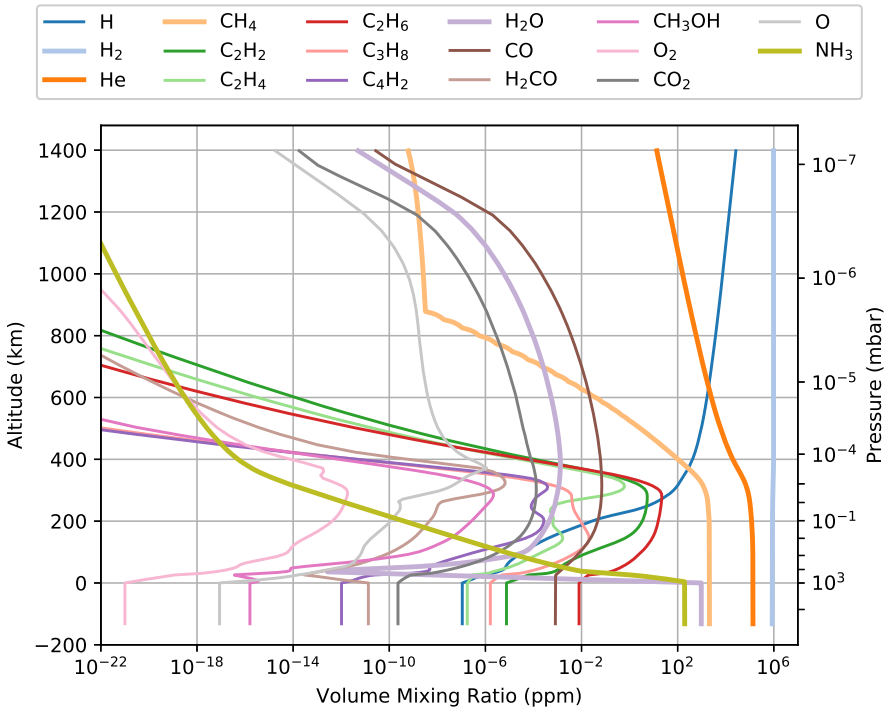

Figure 6.2: Jupiter's atmospheric composition from González et al. [196]. Values are extrapolated below 0 km. The data related to the main molecules shows a thicker line width.

atmosphere is also incomplete below 0 km altitude, but it was extrapolated with constant values for higher pressure levels in the troposphere (Figure 6.2). Again, the reference profile represents an estimation of Jupiter's composition, originally based on the measurements performed by the probe of the Galileo mission [197], and should not be generalized as the absolute composition for each location. Besides, as it will be demonstrated in section 6.3.3, in the wavelength range considered for the radiative transfer model, the absorption of the atmosphere around 0 km is dominated by an optically thick tropospheric cloud, so an extrapolation is acceptable at these altitudes.

6.2 JUPITER'S VIS-NIR SPECTRUM

If Jupiter were seen as a blackbody, it would radiate the same energy as a sphere at 124 K [2]. This is called *bolometric temperature*, and can also be understood as the average temperature of the atmosphere. When

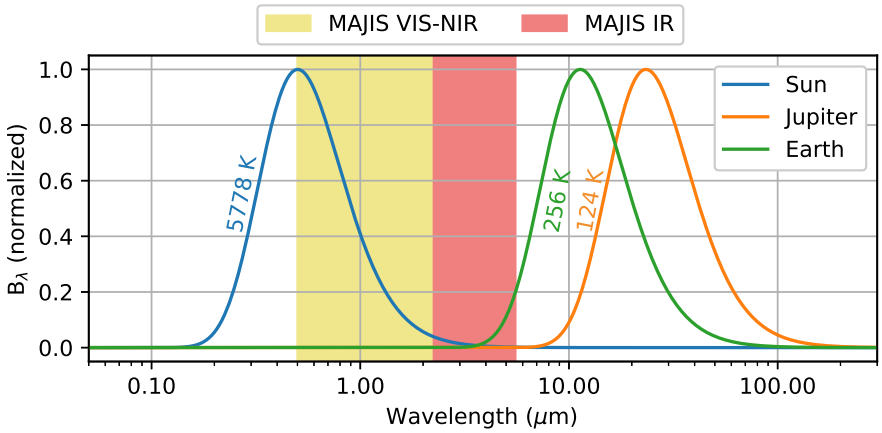

Figure 6.3: Blackbody curves of Jupiter, Earth and the Sun against MAJIS wavelength range of each channel.

the bolometric temperature is lower than the mean temperature of the planet at 1 bar, as it is the case for Jupiter, it reveals that most of the radiation to space is coming from the atmosphere [25]. Figure 6.3 compares the blackbody curve of Jupiter against that of the Sun and Earth to observe the wavelength range at which the thermal radiation impacts the wavelength range of MAJIS (0.5-5.5 μm). It is then clear that the sensitive range of MAJIS does not involve the thermal radiation from Jupiter, which starts being significant around wavelengths longer than 7 μm. Instead, Jupiter's spectrum is dominated by reflected sunlight, especially for the VIS-NIR channel. The MAJIS infrared (IR) channel is sensitive to the vibrational bands of the different molecules present in the atmosphere. Moreover, in the ultraviolet (UV) spectral range, the spectrum of Jupiter is dominated by Rayleigh scattering from hydrogen (H_2) and helium (He) [2].

In addition, Jupiter contains clouds and hazes in its atmosphere. Along with Rayleigh scattering, these are the main contributions shaping the VIS-NIR continuum of the spectrum. In this sense, VIS-NIR spectroscopy in Jupiter provides relevant information to determine the vertical clouds structure of the planet, and the microphysical parameters of its aerosols.

Figure 6.4 shows the main spectral contributions in Jupiter's VIS-NIR spectrum, as observed in limb geometry at an altitude between 80 and 300 km, by López-Puertas et al. [26]. This altitude range corresponds to Jupiter's stratosphere at the equator. The measured transmission

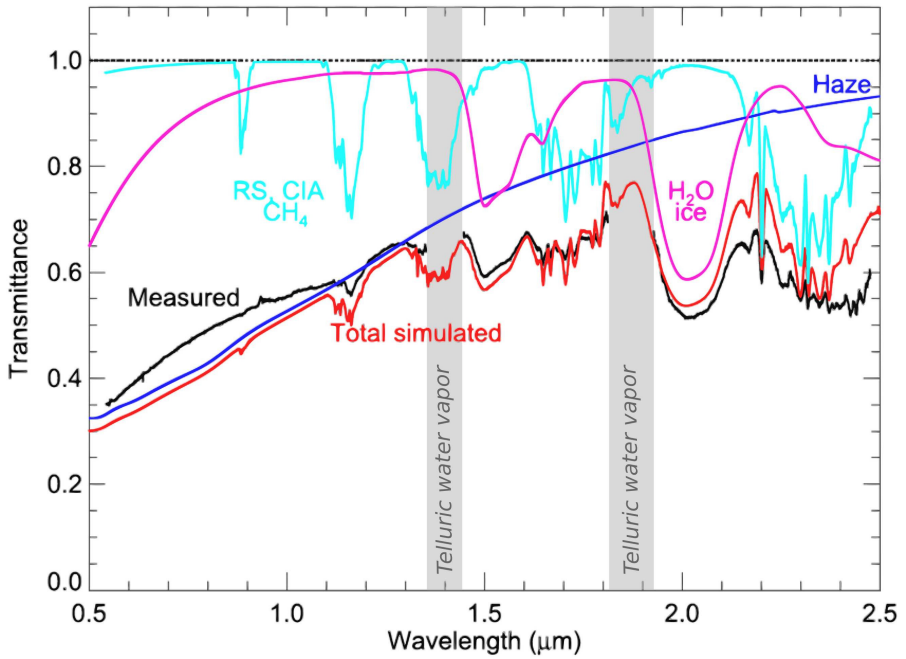

Figure 6.4: Jupiter's VIS-NIR spectrum with its main spectral contributions (extracted from [26]). The measured spectrum (black) was acquired from a ground-based limb observation, and the simulated spectrum (red) was generated with KOPRA. Rayleigh Scattering (RS), Collision Induced Absorption (CIA), and CH_4 absorption bands are shown in cyan. Aerosols included haze (blue) and H_2O ice (pink).

spectrum (in black) was acquired with the Very Large Telescope (VLT) at the Paranal Observatory in Chile. KOPRA (section 5.4), was the radiative transfer tool used by López-Puertas et al. [26] to generate the simulated spectrum of the observation (in red) and to model each of the spectral contributions in the figure.

It is noticeable that the shape of the continuum is dominated by the haze (in blue) at wavelengths smaller than 1.3 μm. Methane (CH_4) absorption bands (in cyan) are clearly responsible for most of the signatures in the spectrum, except for the bands around 1.5 and 2.0 μm, which are due to a water (H_2O) ice cloud (in pink). Rayleigh scattering is mainly visible at wavelengths smaller than 0.7 μm (in cyan), and Collision Induced Absorption (CIA) associated to H_2 collisions with He and other H_2 molecules corresponds to the smooth features centered near the 2.0 μm region (in cyan). The gaps around 1.4 μm and 1.8 μm

in the observed spectrum are due to H_2O vapor absorption by Earth's atmosphere.

Note that due to the altitude range of the limb observation at the wavelength range of interest (~80-300 km), mechanisms such as CIA and Rayleigh scattering are not as significant as they would be at lower altitude levels. This is also the case for additional molecular absorption bands that are expected to be present at this spectral range, such as ammonia (NH_3) and H_2O [26]. The next section describes in detail how each of the mentioned spectral contributions was finally implemented in ASIMUT-ALVL to model the VIS-NIR spectrum of Jupiter's atmosphere.

6.3 IMPLEMENTATION OF JUPITER CASE IN ASIMUT-ALVL

As discussed in section 5.4, ASIMUT-ALVL is a radiative transfer tool currently used for the study of Earth [179], Mars [180], and Venus [181]. In order to be able to generate Jupiter VIS-NIR spectra, new functions and inputs had to be implemented in ASIMUT libraries. The first step was to include the properties previously listed in Table 1.1, as well as a predefined atmospheric model with both the temperature and abundance profiles as discussed in section 6.1. File formats and units were also considered to be consistent with those expected by ASIMUT-ALVL. The main changes performed in ASIMUT-ALVL are described in the following subsections. At the end of this section, Table 6.4 summarizes the data currently available for ASIMUT-ALVL after the development of this work. The validation process of these changes is detailed in section 6.4.

6.3.1 *Molecular absorption in Jupiter's atmosphere*

As a line-by-line (LBL) program, ASIMUT-ALVL calculates the molecular absorption cross-sections for each molecule from a specified line list database by considering the appropriate pressure and temperature conditions per atmospheric layer at each wavelength of interest. The pressure and temperature conditions of the line list should be close to those found in Jupiter's atmosphere [198]. Additionally, ASIMUT-ALVL accepts Look Up Tables (LUTs) to interpolate the required cross-section value depending on the pressure and temperature conditions defined by the atmospheric model for each atmospheric layer. For Jupiter,

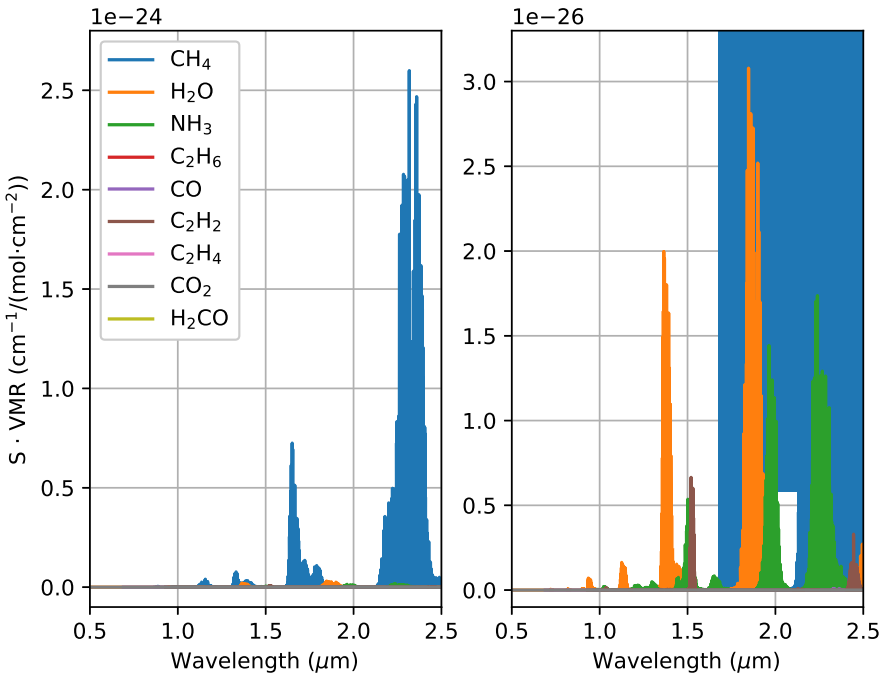

Figure 6.5: Molecular bands of Jupiter species in the VIS-NIR range: (left) main contribution, (right) minor contributions. The intensity of the spectral lines of each molecule S is multiplied by the average VMR of the atmospheric profile above 0 km.

temperatures and pressures about the 0 km level (∼160 K, 1 bar) are adequate. Moreover in Jupiter's atmosphere, the absorption line profiles of the molecules are broadened through collisions against H_2 and He, so the corresponding broadening parameters should be taken into account if available. For instance, among the molecules of interest in Jupiter's VIS-NIR range, the HITRAN database only contains H_2 and He broadening parameters for NH_3. Similarly, other functions than Lorentzian or Gaussian may be more accurate in approximating the line profiles for molecules in Jupiter's environment, so the selection between one or another type should be analyzed in detail when possible.

Figure 6.5 allows the visualization of the molecular species that contribute to the absorption spectrum of Jupiter's atmosphere at VIS-NIR wavelengths (0.5-2.5 μm). Data for the spectral lines were taken from the HITRAN database in April 2022. It is clear that the main structured molecular contribution in this wavelength range will be due to CH_4, although there are some other molecular absorption contributions due

to the main minor trace gases, such as H_2O and NH_3, that appear to be relevant.

For the radiative transfer model of Jupiter's VIS-NIR spectrum in this work, only the absorption bands of CH_4, NH_3 and H_2O were assessed. Since the HITRAN database does not extend for wavelengths approximately shorter than 1 μm, except for H_2O, additional references from the literature were considered to complete the spectral information of the other molecules. This aspect is addressed for each molecule here below.

Methane (CH_4)

According to the recent work of Yurchencko et al. [199], one of the most accurate and complete line lists for CH_4 is the one from Rey et al. [165]. It consists of a theoretical line list, part of the TheoReTS database [164], for wavelengths above 0.75 μm and temperatures from 50 to 350 K. This line list was actually combined with data from HITRAN 2016 [200] to provide accurate line lists for high-temperature applications (up to 1173 K) by Hargreaves et al. [201]. The improved line list version is currently available at HITEMP [161], although it is only validated for wavelengths above 1.1 μm [201]. Other databases such as HITRAN 2020 [158] and ExoMol [159], are also limited for wavelengths shorter than 0.8 μm.

Nevertheless, the jovian community has extensively used the empirical CH_4 band model proposed by Karkoschka et al. [198] until nowadays because it matches absorptions observed in planetary atmospheres between 0.4 and 5.5 μm [165]. Some works include those from Baines et al. [31], Sromovsky et al. [33], Braude et al. [34], Zhang et al. [38] and Anguiano-Arteaga et al. [202]. In fact, the accuracy of the work of Hargreaves et al. [201] is insufficient at short wavelengths when compared to the band model of Karkoschka et al. [198]. The band model was developed by combining transmission measurements from laboratory and astronomical observations, including data from the atmospheres of Jupiter and Titan. Pressure and abundance dependence of molecular absorption is given by the Voigt-Goody band model, which considers Voigt line profiles. The model proves Beer's law as a fair approximation at most wavelengths (>1 μm) if CH_4 absorbs at pressures higher than ~1 bar [198]. Moreover, the model of Karkoschka et al. [198] might include other gases than CH_4 [165].

P. G. Irwin[2] approached the Karkoschka et al. [198] model as a correlated-k table of absorption coefficients that can be obtained from [203] with a resolution of 10 cm $^{-1}$. The dataset includes 12 k-coefficients in units of amg$^{-1}\cdot$km^{-1}, with their corresponding uncertainty, for 10 pressure values between 10^4 and 10^{-5} mbar, 11 temperature values between 50 and 300 K, 3460 wavenumbers uniformly distributed between 2000 and 19295 cm^{-1} (0.5-5.0 μm), and 10 g-ordinates to weight each of the coefficients for each pressure value. Following Jupiter's temperature profile (Figure 6.1), these pressure values correspond to altitudes between -241 and 452 km in Jupiter's atmosphere. To implement the Karkoschka et al. [198] model in ASIMUT-ALVL, it was necessary to independently compute the corresponding CH_4 cross-sections (equation 5.21) and implement them as LUTs. The code to perform these computations is now available at BIRA-IASB for further use if necessary.

Another aspect that had to be considered was the unit's consistency. ASIMUT-ALVL works with σ_a as the absorption cross-section of a molecule for radiation at a given frequency, with units in cm^2/molecule; while the absorption coefficients provided by P. G. Irwin will result in the absorption cross-section $\tilde{k}$ of a volume containing Loschmidt's number n_0 of molecules. Therefore, to convert $\tilde{k}$ from amg$^{-1}\cdot$km^{-1} to σ_a in cm^2/molecule, it is necessary to divide by n_0 [204], which is actually the value of 1 amg, and consider the factor 10^{-5} km/cm for z:

$$T(\tilde{\nu},z) = e^{-\tilde{k}(\tilde{\nu},z)nz/n_0} = e^{-\sigma_a(\tilde{\nu},z)nz} \tag{6.1}$$

Figure 6.6 shows a comparison of the absorption cross-section of CH_4, at 200 K and 1013 mbar from HITRAN[3] [158], ExoMol[4] [159], and Karkoschka et al. [198]. Some minor differences are visible between HITRAN and ExoMol, while the band model of Karkoschka et al. [198] behaves as a softened version of the other datasets. Indeed, the spectral sampling of Karkoschka et al. [198] data is very low; the k absorption coefficient is an average for spectral ranges of 5 cm^{-1} width, while HITRAN was set to provide spectral information every 0.001 cm^{-1}. In any way, for this study, the limiting factor will be the spectral resolution of the instrument to be simulated in the radiative transfer model, typically worse than 40 cm^{-1} for VIS-NIR wavelengths. Nevertheless, as far as the spectral resolution of the instrument is twice

2 Professor of Planetary Physics at the University of Oxford
3 Line list downloaded in April 2022
4 Data downloaded in February 2024

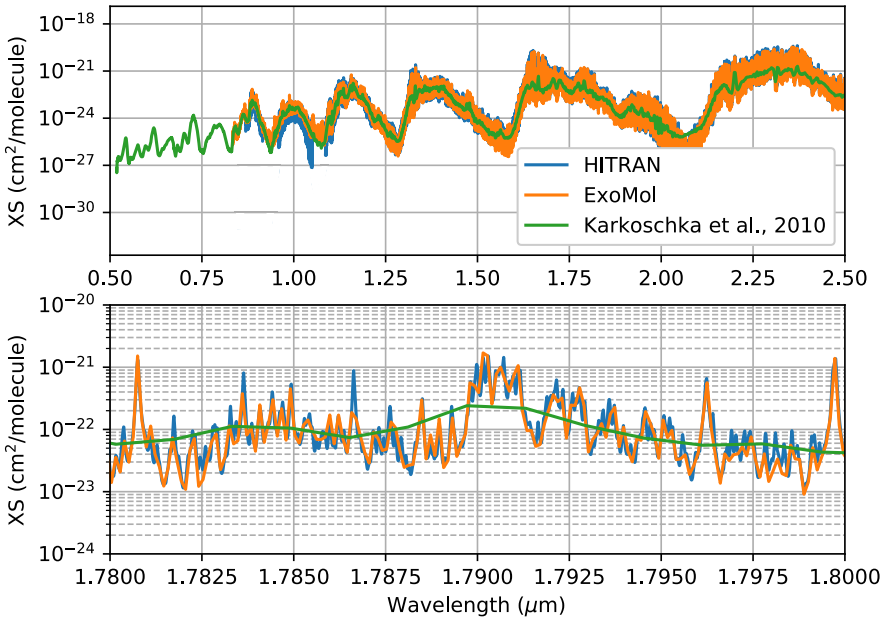

Figure 6.6: Cross-section of CH_4 from different references, including HITRAN [158] (for 86 % H_2 and 14 % He atmosphere), ExoMol [159] (for 85 % H_2 and 15 % He atmosphere) and Karkoschka et al. [198]: (top) complete VIS-NIR range, (bottom) closer look at an arbitrary wavelength range. Pressure and temperature conditions correspond to 1013 mbar and 200 K, respectively. Voigt line profiles were assumed in the three cases (γ_L=0.069 cm^{-1} and α_D=0.015 cm^{-1}). Around 1 μm HITRAN presents some artifacts that were removed.

as low as the resolution of the dataset to be used, the radiative transfer calculations will be adequate.

HITRAN cross-sections were computed with *Pytran*, a Python package developed by J. T. Erwin[5] to read and use the HITRAN database [205]. Voigt profiles were considered as line shapes, and the considered broadening parameters correspond to 86 % H_2 and 14 % He. Data were stored as a LUT for a grid of pressure and temperature values representative of those in Jupiter's atmosphere. Both, the LUT and the line list are available for their use in ASIMUT-ALVL.

ExoMol cross-sections were directly downloaded from ExoMol as a LUT [206]. It includes 22 pressure values logarithmically distributed between 10^5 and 10^{-2} mbar (below ~260 km in Jupiter's atmosphere),

5 Research Scientist at the Royal Belgian Institute for Space Aeronomy (BIRA-IASB)

27 temperature values between 100 and 3400 K, and 76744 wavenumbers uniformly distributed between 200 and 33333 cm^{-1} (0.3-50.0 μm), although the spectral information is empty at wavelengths smaller than 0.83 μm. The original data comes from the recent work of Yurchenko et al. [199]. Both dataset versions were implemented as LUTs in ASIMUT-ALVL to model Jupiter's atmosphere.

The choice of working with one or another dataset depends on the wavelength range of interest. Karkoschka et al. [198] is the only available option for wavelengths smaller than 0.8 μm and is recommended for wavelengths up to 1.6 μm, where HITRAN, ExoMol and HITEMP are more reliable. Fortunately, the combined use of two or more molecular datasets for different wavelength ranges is possible in ASIMUT-ALVL.

Ammonia (NH_3)

To model the absorption spectra of NH_3 for Jupiter's atmosphere at VIS-NIR wavelengths, the scientific community generally uses the works from Coles et al. [207] and Bowles et al. [208], as is the case for Baines et al. [31], Sromovsky et al. [33], and Pérez-Hoyos et al. [189]. HITRAN [158] and GEISA [162] are sometimes used when the wavelength range of interest is above 1 μm [190, 209, 210]. HITRAN only provides spectral information for NH_3 above 0.96 μm, and has some gaps at 1.12-1.15 μm, 1.35-1.43 μm, 1.78-1.84 μm, and 2.09-2.12 μm (see Figure 6.7). However, after the detailed reviews of Irwin et al. [192, 211], their resultant correlated-k table of absorption coefficients became the main reference for NH_3 [30, 34, 35].

Irwin et al. [192, 211] reviewed and compared the most used references for modeling the radiative properties of NH_3 for VIS-NIR spectra of giant planets. They first compared the laboratory data from Bowles et al. [208], Giver et al. [212], and Lutz et al. [213], and later compared them against calculated data from Coles et al. [207]. The main differences between the first-mentioned datasets include the spectral resolution and the temperature conditions of the measurements. Only Bowles et al. [208] performed measurements between 217 and 296 K and pressures ranging from 75 to 1020 mbar, covering wavelengths longer than 0.741 μm. Moreover, the three works were measured under self-broadening conditions, leading to some uncertainties about how to correct such observations when considering different broadening conditions. Again, only Bowles et al. [208] provided a self-to-foreign

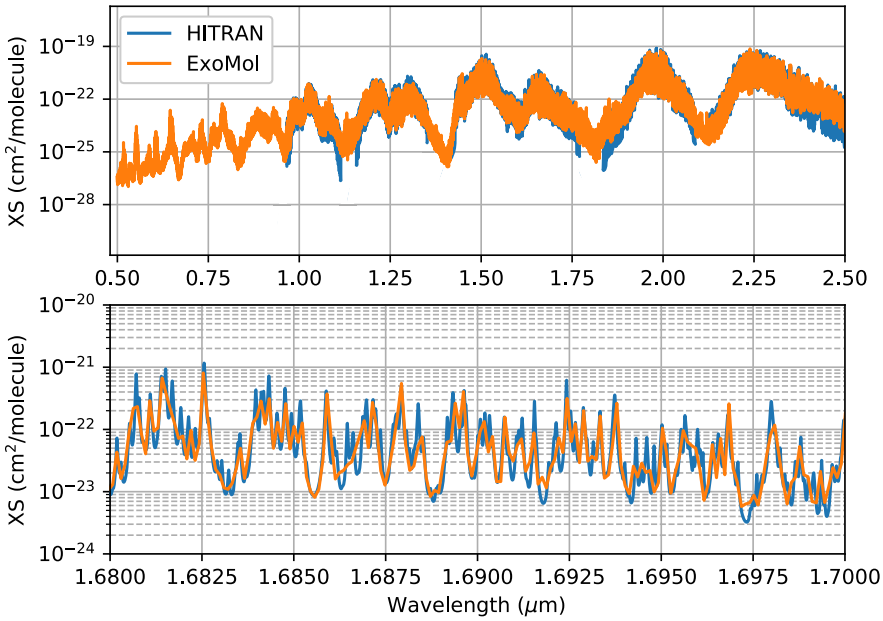

Figure 6.7: Cross-section of NH_3 from different references, including HITRAN [158] (for 86 % H_2 and 14 % He atmosphere) and ExoMol [159] (for 85 % H_2 and 15 % He atmosphere): (top) complete VIS-NIR range, (bottom) closer look at an arbitrary wavelength range. Pressure and temperature conditions correspond to 1013 mbar and 200 K, respectively. Voigt line profiles were assumed in both cases (γ_L=0.0.089 cm^{-1} and α_D=0.015 cm^{-1}).

broadening ratio to adapt their measurements to other broadening conditions and reduce this uncertainty.

The most recent work of Coles et al. [214] is currently part of the ExoMol database [159]. Although it is still remarkably consistent with the data from Bowles et al. [208], it demonstrated to be more reliable at wavelengths close to 0.758 μm, where the measurements of Bowles et al. [207] became more noisy. P. G. Irwin generated a correlated-k table based on data from Coles et al. [214], after performing some modifications for its use on gas planets. For instance, they considered the corresponding broadening parameters for an atmosphere constituted 86.5 % by H_2 and 13.5 % by He. These correlated-k tables are currently available at [203]. Similarly to those for CH_4, the k-tables were computed for 20 pressure values between 10^4 and 10^{-4} mbar and 20 temperature values between 50 and 400 K, including 10 g-ordinates

to weight each of the coefficients for each pressure value with a spectral coverage for wavelengths larger than 0.7 μm.

Figure 6.7 shows a comparison of the absorption cross-sections of NH_3 that were implemented in ASIMUT-ALVL as LUTs. Similarly to the CH_4 case, HITRAN cross-section[6] was computed with Pytran [205], while ExoMol cross-section[7] was downloaded directly as a LUT. The mean average difference between HITRAN and ExoMol is ∼22 %, without considering the spectral regions where HITRAN does not offer any data. Note that the spectral resolution provided by ExoMol is lower than that determined with HITRAN data. Nevertheless, the spectral resolution of the instruments to be simulated in the radiative transfer model will be significantly higher than that of ExoMol or HITRAN, and therefore will not be sensitive to such differences. Both LUTs are available for ASIMUT-ALVL if required. However, since ExoMol offers more spectral coverage, this dataset is preferred for this work.

Water (H_2O)

So far, H_2O is the most well-spectroscopically characterized molecule [215]. HITRAN improved the general quality of its line list parameters in the 2020 version. Thanks to the work of Conway et al. [215], the line list of H_2O received a significant update by extending its initial spectral range to UV wavelengths providing more accurate and reliable data at short wavelengths, now starting at 0.238 μm [158]. Similarly to CH_4 and NH_3, a LUT for a grid of pressure and temperature values representative of those in Jupiter's atmosphere, considering Voigt line profiles and adequate broadening parameters due to H_2 and He, was computed to make it available for ASIMUT-ALVL in this work.

To keep consistency with respect to the other molecules, the LUT with cross-sections from ExoMol[8] [216] is also available. ExoMol provides data based on Polyansky et al. [217], restricted to wavelengths longer than 0.4 μm.

Figure 6.8 shows a comparison of the cross-sections from both datasets for similar pressure and temperature conditions. Note the different order of magnitude between the H_2O cross-section and those for CH_4 and NH_3. H_2O absorbs less radiation at this wavelength range than the other molecules. As was the case in the previous cases, HITRAN

6 Line list downloaded in April 2022
7 Data downloaded in November 2023
8 Data downloaded in November 2023

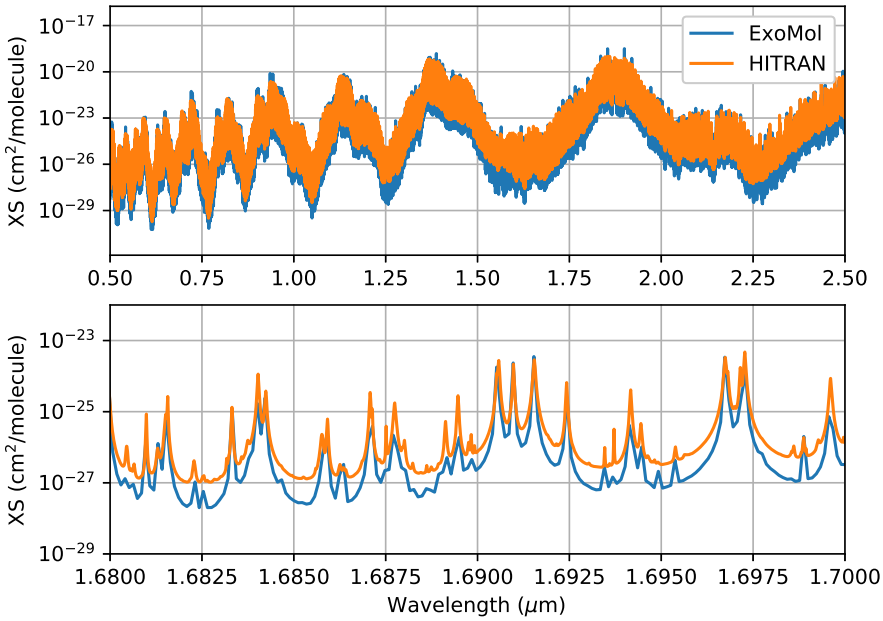

Figure 6.8: Cross-section of H_2O from different references, including HITRAN [158] (for 86 % H_2 and 14 % He atmosphere) and ExoMol [159] (for 85 % H_2 and 15 % He atmosphere): (top) complete VIS-NIR range, (bottom) closer look at an arbitrary wavelength range. Voigt line profiles were assumed in both cases. Pressure and temperature conditions correspond to 1013 mbar and 200 K for ExoMol (γ_L=0.057 cm^{-1} and α_D=0.014 cm^{-1}), and 1022.12 mbar and 206.2 K for HITRAN (γ_L=0.068 cm^{-1} and α_D=0.015 cm^{-1}). These differences in pressure and temperature, together with the different spectral resolutions used (0.8 cm^{-1} for ExoMol and 0.001 cm^{-1} for HITRAN), explain the observed difference between both datasets.

cross-section[9] was computed with Pytran [205], by considering Voigt line profiles and broadening parameters for an atmosphere of 86 % H_2 and 14 % He. Data is complete in both databases for the VIS-NIR range of interest and compares well in terms of line positions. The mean difference between both datasets in the zoomed region is about 75 %, where ExoMol presents a much lower spectral sampling than that defined for HITRAN (0.35 cm^{-1} against 0.001 cm^{-1}). This difference is also due to the slightly different pressure and temperature values at which both cross-sections were determined. Since HITRAN includes improved data in contrast to ExoMol, HITRAN is more recommended

9 Line list downloaded in April 2022

for this work. Again, the radiative transfer model will not be sensitive to these differences mainly due to the spectral resolution of the instruments to be simulated (worse than 40 cm^{-1}).

It is worth mentioning that although H_2O is one of the most abundant molecules in Jupiter's atmosphere, most radiative transfer models limit the molecular contributions to CH_4 and NH_3 [30, 31, 34–36, 189, 192, 218], and some works even only consider CH_4 [26, 38]. For instance, López-Puertas et al. [26] considered H_2O following the work of Montañés-Rodríguez et al. [219], but finally neglected it together with CO and CO_2 after probing that these molecules did not contribute significantly to Jupiter's absorption spectrum in the VIS-NIR range at the altitude range under consideration.

Indeed, following Figure 6.5, the strongest absorption bands due to CH_4 are expected to be two orders of magnitude stronger than those of other molecules. Actually, it is possible to observe that absorption due to H_2O should be stronger than NH_3, but it continuously overlaps with CH_4 bands. Therefore, it is valid to expect that H_2O will finally not impact Jupiter's VIS-NIR spectrum significantly, except for some specific spectral regions. However, the decision to neglect H_2O should also depend on the latitude and the viewing geometry to simulate.

Table 6.1 summarizes the specifications of the datasets discussed in this section for each molecule.

Parameter / Source	P. G. Irwin		HITRAN	ExoMol
	Karkoschka et al., 2010	Coles et al., 2019		
Molecules	CH_4	NH_3	CH_4, NH_3, H_2O	CH_4, NH_3, H_2O
Dataset source type	Correlated *k*-table	Correlated *k*-table	Line list	Cross-section
Wavelength range	0.5-5.5 μm	0.5 - 5.5 μm	0.5-5.5 μm	0.3-50 μm
Spectral resolution	10 cm^{-1}	10 cm^{-1}	0.001 cm^{-1}	CH_4: 16.8 cm^{-1} NH_3: 12.0 cm^{-1} H_2O: 0.8 cm^{-1}
Spectral sampling	5 cm^{-1}	5 cm^{-1}	0.001 cm^{-1}	0.013-2.222 cm^{-1}
Line profile	Voigt	Voigt	Voigt	Voigt
Pressure range	10^4-10^{-5} mbar	10^4-10^{-4} mbar	10^3-10^{-5} mbar	10^5-10^{-2} mbar
Number of pressure values	10	20	*	22
Temperature range	50-300 K	50-400 K	50-800 K	100-3400 K
Number of temperature values	11	20	*	27
Broadening parameters	*Not provided*	86.5 % H_2 13.5 % He	86 % H_2 14 % He	85 % H_2 15 % He

Table 6.1: Considered parameters to determine molecular absorption cross-sections and implement their corresponding LUTs in ASIMUT-ALVL during this work. **Based on Jupiter's atmospheric temperature profile.*

6.3.2 *Rayleigh Scattering in Jupiter's atmosphere*

According to Wong et al. [35], Rayleigh scattering and gas opacity limit the penetration depth of sunlight in Jupiter's atmosphere down to ∼20-50 bars, even in the absence of aerosols. In fact, most of the solar UV radiation falling on Jupiter is deposited in the stratosphere, where CH_4 is photodissociated and the most intense photochemical activity takes place (section 1.2). Since the penetration of sunlight is limited at short wavelengths, Rayleigh scattering could take part in the explanation of why deep clouds in Jupiter can appear red [35].

Rayleigh scattering for Jupiter's atmosphere is typically considered from cross-sections found in the literature, such as those from Ford & Browne [220] or Dalgarno & Williams [221] for H_2, and Chan & Dalgarno [222] or Kurucz [223] for He. However, these Rayleigh scattering cross-sections can also be derived from the refractive index of the gases present in the atmosphere, as discussed in section 5.3.2. The total Rayleigh scattering cross-section of Jupiter's atmosphere would correspond to the sum of the cross-sections of all its significant species weighted by their VMRs [170, 192], following equation 5.9.

ASIMUT-ALVL includes different functions to calculate Rayleigh scattering in other planets. To continue with this format, and as part of this work, it was decided to implement an additional function for computing Rayleigh scattering for Jupiter's atmosphere. The advantage is to provide more versatility and control of the related variables. Moreover, the obtained results are similar to those given when directly defining the cross-section (see section 6.4.1).

This work included the sole contributions of H_2 and He in the Rayleigh scattering calculation, since considering other molecules, such as CH_4, NH_3 or H_2O, increased the atmospheric refractive index only by 1 %. The refractive index of every molecule is obtained from the dispersion formulas of their measured refractivities. The refractivity of H_2 (equation 6.2) was taken from Peck & Huang [224]. It fits well with the measurements performed by different authors for wavelengths between 0.4 and 1.7 μm, including that of Ford & Browne [220]. For He (equation 6.3), refractivity was taken from Mansfield & Peck [225].

$$(n_\lambda - 1)_{H_2} = \frac{0.0148956}{180.7 - \lambda^{-2}} + \frac{0.0049037}{92 - \lambda^{-2}} \tag{6.2}$$

$$(n_\lambda - 1)_{He} = \frac{0.00645686373}{318.1312 - \lambda^{-2}} + \frac{0.0129041989}{895.3867 - \lambda^{-2}} \tag{6.3}$$

Since refractivity equations are typically given for pressure and temperature conditions of 1 atm (P_0) and 0°C (T_0), respectively, they need to be scaled to the pressure P and temperature T values of the atmospheric layer under analysis [169, 225]. Therefore, the refractive index n_λ for each molecule corresponds to:

$$n_\lambda = (n_\lambda - 1)\left[\frac{P}{T}\right]\left[\frac{T_0}{P_0}\right] + 1 \tag{6.4}$$

It is worth mentioning that ASIMUT-ALVL uses internal functions to compute the refractive index of a planetary atmosphere, even if Rayleigh scattering is not considered. For Jupiter case, an additional function was implemented by following the procedure described for Earth's atmosphere by Sneep & Ubachs [170], but adapted to Jupiter's atmosphere:

$$n_\lambda = \sum_i c_i n_{\lambda i} \tag{6.5}$$

where c is the VMR of the corresponding molecule i at each atmospheric layer. In this case, H_2 and He.

Similarly, the depolarization ratio (see section 5.3.2) of Jupiter ρ_n must be included in the common ASIMUT-ALVL library. Some authors such as Sromovsky & Fry [218] directly use the value for H_2. For this work, ρ_n is obtained from equation 5.10 by first deriving Jupiter's King correction factor F_K, which was computed by following the procedure of Tomasi et al. [169], also adapted to Jupiter's atmosphere:

$$F_K = \frac{\sum_i c_i F_i}{\sum_i c_i} = \frac{c_{H2}F_{H2} + c_{He}F_{He}}{c_{H2} + c_{He}} \tag{6.6}$$

The depolarization ratios considered for H_2 and He were extracted from Parthasarathy [226], and correspond to 0.0221 and 0.0250, respectively. The resultant F_K value for Jupiter's atmosphere is 0.0225. Differences are no larger than 1 % when more molecular species are considered.

6.3.3 *Mie Scattering in Jupiter's atmosphere*

As part of this work, a Python routine independent of ASIMUT-ALVL was developed to determine the wavelength-dependent scattering parameters of aerosols, including extinction cross-section σ_e, single scattering albedo (SSA), and asymmetry parameter g for each proposed

aerosol in Jupiter (see section 5.3.3). The developed routine is called ASIMie and was based on that of G. Villanueva[10], currently used for the Planetary Spectrum Generator (PSG) [227]. It includes the well-known Mie scattering code from Bohren & Huffman [172], and a function to define either lognormal or gamma distributions as Particle Size Distributions (PSDs). Additionally, an optimization to define the best bounds for the PSDs was implemented. A detailed explanation of the definition of lognormal and gamma PSDs is presented in Appendix A. The main advantage of ASIMie is the flexibility for generating the scattering parameters of aerosols of any size and composition that can be proposed.

For this work, aerosols based on both the work of López-Puertas et al. [26] and the *Crème Brulée* (CB) model of Baines et al. [31] were implemented, although aerosols from the model B of Baines et al. [31] are also available if required. These models were already introduced in section 1.3. Figure 6.9 and Figure 6.10 show a comparison between the scattering properties obtained for the main aerosols in the mentioned models, which are now available in ASIMUT-ALVL, for different wavelength ranges.

López-Puertas et al. [26] consider lognormal PSDs with effective variance v_{eff} of 0.1 for all aerosols at equatorial latitudes. The crystalline H_2O ice cloud was defined for an effective radius r_{eff} of 12.5 nm, while the proposed hazes were defined with r_{eff} of 0.13, 0.34 and 0.75 μm. The complex refractive index for the H_2O ice cloud is based on that from Mastrapa et al. [228], although data was not complete for wavelengths smaller than 1 μm. Then, the real part of the refractive index was linearly extrapolated to shorter wavelengths and the imaginary part was completed with data from amorphous H_2O ice from Warren & Brandt [229]. Similarly, the complex refractive index used for hazes[11] has a real part equal to that of NH_3 ice, as measured by Martonchik et al. [230], and an imaginary part equal to the values derived by Zhang et al. [38], which are consistent with measurements from Khare at al. [231] concerning mixtures of CH_4 and H_2. It is worth mentioning that the scattering properties of H_2O ice based only on the refractive index from Warren & Brandt [229], and those for hazes based only on the refractive index of Khare at al. [231], with analogous PSDs to the actual aerosols proposed by López-Puertas et al. [26], were additionally

10 Obtained from personal communication. G. Villanueva is Associate Director of the Solar System Exploration Division at NASA Goddard Space Flight Center

11 Obtained from personal communication with M. López-Puertas

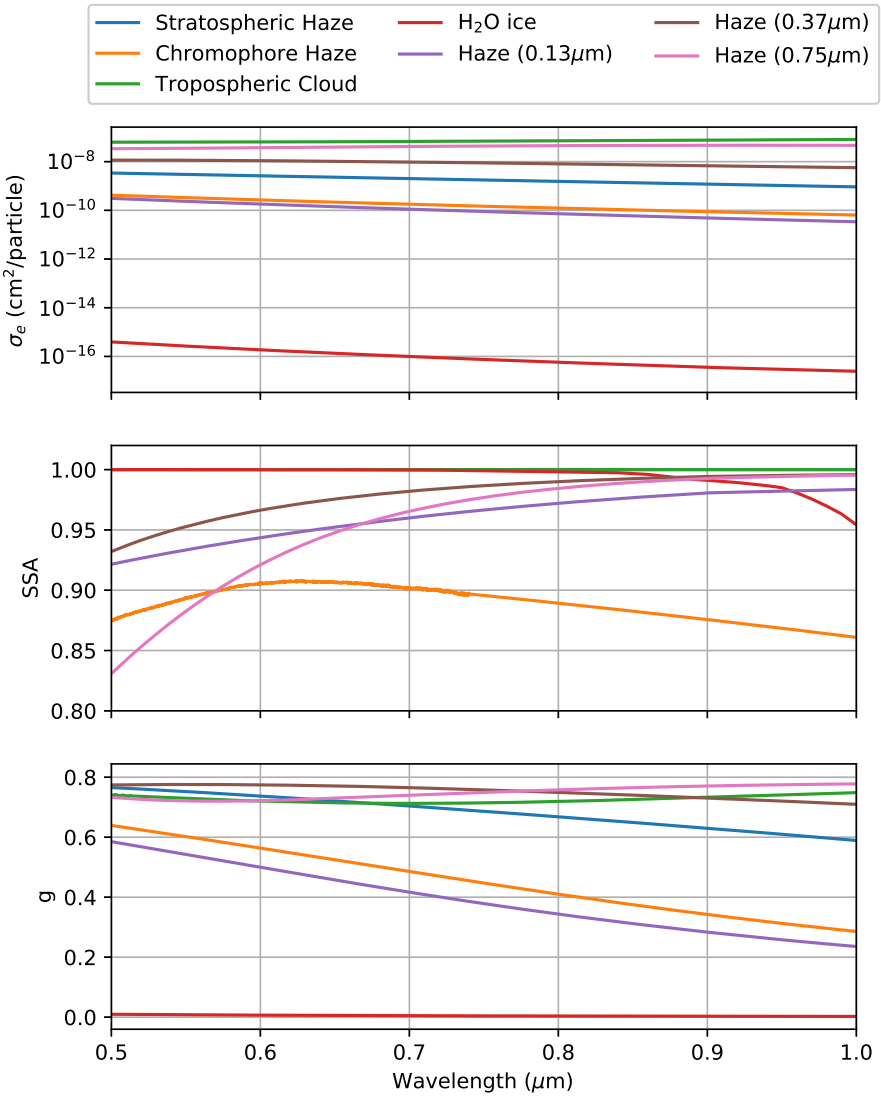

Figure 6.9: Aerosols parameters for Jupiter models at wavelengths smaller than 1 μm. Stratospheric Haze (SH), Chromophore Haze (CH), and Tropospheric Cloud (TC) correspond to aerosols' layers defined by Baines et al. [31] for the CB model. The rest of the aerosols correspond to layers defined by López-Puertas et al. [26]. Please refer to the text for specific information on the optical properties of each aerosol.

calculated and are available for ASIMUT-ALVL if required. Note that all scattering parameters were determined, even if only σ_e was necessary

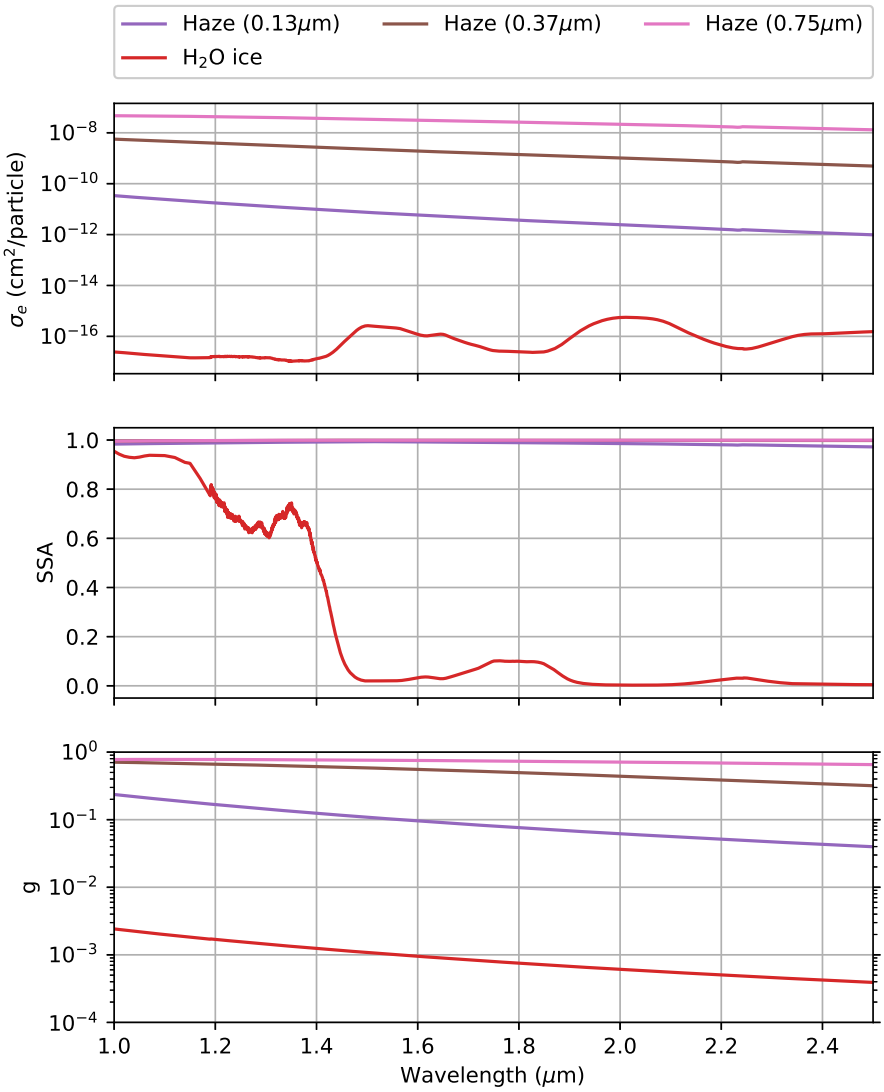

Figure 6.10: Aerosols parameters for Jupiter models above 1 μm, as defined by López-Puertas et al. [26]. Please refer to the text for specific information on the optical properties of each aerosol.

to reproduce the limb geometry observation of López-Puertas et al. [26] (see section 6.4.1).

The CB model of Baines et al. [31] considers gamma PSDs with v_{eff} of 0.1 and r_{eff} of 0.14 μm for the Chromophore Haze (CH), 0.25 μm for the Stratospheric Haze (SH) and 1.08 μm for the Tropospheric Cloud (TC). The three layers have similar composition. The non-chromophoric

aerosols have a complex refractive index with a constant value of 1.4 for the real part, which is a value generally assumed for NH_3 dominated atmospheres [33]; and zero for the imaginary part, to not account for light attenuation since no absorption is expected. The complex refractive index of the red-tinted chromophore is composed of the same constant value for the real part as before, but with the imaginary part from the chemical compounds suggested by Carlson et al. [32]. This chromophore is the result of acetylene (C_2H_2) and photolytic products of NH_3, coating NH_3 ice. Since the data from Carlson et al. [32] only covers wavelengths from 0.4 to 0.74 μm, it was linearly extrapolated to cover also wavelengths from 0.35 to 1.05 μm, as performed by Baines et al. [31], by taking as reference the behavior between 0.40 and 0.45 μm for the short wavelengths and between 0.68 and 0.73 μm for the long wavelengths.

Refer to Figure 6.9 to note the similarity in σ_e and g between the CH and the 0.13 μm haze; the TC and the 0.75 μm haze; and roughly the SH and the 0.37 μm haze. This is because they have similar size parameters x. Since there is no information to apply the CB model at wavelengths above 1 μm, the behavior described by the aerosols proposed by López-Puertas et al. [26] at these wavelengths can be assumed. In any way, the absorption observed in Jupiter's spectra will be less dominated by hazes with increasing wavelengths, since σ_e is generally decreasing at longer wavelengths [2], as observed in Figure 6.10. On the other hand, scattering by aerosols becomes more isotropic when g approaches zero. This is mainly visible for H_2O ice, whose particles are already in the Rayleigh scattering regime ($x \sim 0.04$) [12] and, as observed in SSA, becomes strongly absorbing at 1.5 and 2.0 μm.

SSA accounts for light attenuation and is influenced by the imaginary part of the refractive index of the particle, in addition to x and g (Figure 5.8) [168]. Since the imaginary part of the refractive index is considered zero for the TC and the SH of the CB model, radiation will be fully transmitted at all wavelengths and SSA will describe purely scattering (Figure 6.9). For the hazes proposed by López-Puertas et al. [26], the imaginary part of their corresponding refractive index is in the order of 10^{-2}, therefore SSA is also close to purely scattering. It is worth mentioning that the real part of the refractive index is mostly constant at VIS-NIR wavelengths for all aerosols, except for the hazes proposed by López-Puertas et al. [26]. However, the exact choice of this value has no significant impact on the general behavior of the aerosols parameters

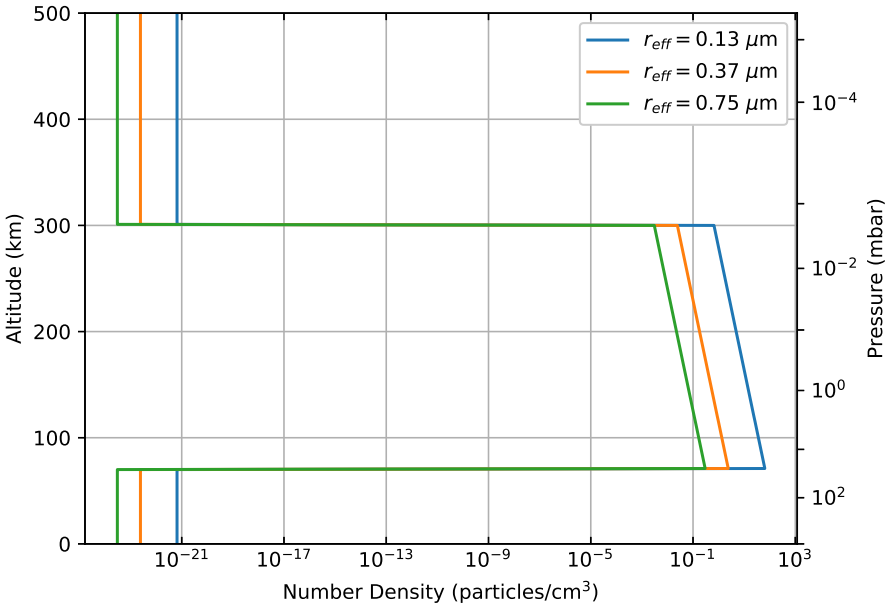

Figure 6.11: Number density for hazes proposed by López-Puertas et al. [26] at equatorial latitudes, according to their particle size.

[168] since it accounts for the refraction of light in the spherical particle, but not for attenuation, as it is the case for the imaginary part [12].

The nominal abundance profile for hazes in the aerosols model proposed by López-Puertas et al. [26] corresponds to one defined for a lognormal PSD with $r_{eff} = 0.31\ \mu$m and $v_{eff} = 0.1$, obtained from personal communication with M. López-Puertas. To apply it to different PSDs and obtain the proper abundance profile for a particular haze N_{haze}, the nominal abundance profile N_{ref} has to be scaled according to the volume ratio between the particle size of the haze V_{haze}, and that of the reference particle V_{ref}:

$$N_{haze} = \frac{V_{ref}}{V_{haze}} N_{ref} \tag{6.7}$$

Figure 6.11 shows the resultant abundance profiles corresponding to the different particle sizes involved in the aerosols proposed by López-Puertas et al. [26]. Larger particles require less abundance to keep the same volume.

In their work, Baines et al. [31] provided the pressure limits of the different aerosols involved in the CB model besides their corresponding optical depth τ at 1 μm, instead of the abundance profile for each

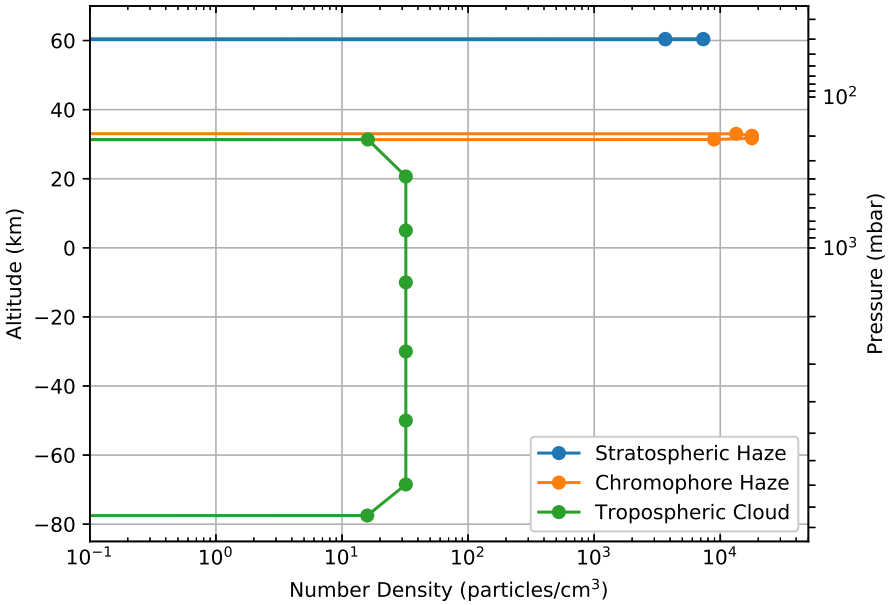

Figure 6.12: Number density N for aerosols in the CB model as implemented in ASIMUT-ALVL considering 21 atmospheric layers. The dots correspond to N in the intermediate altitude of the atmospheric layers defined in the forward model.

defined aerosol. Since τ is related to the transmittance of the medium, the aerosols number density n, and the aerosols σ_e, as expressed by equations 5.2 and 5.6, it is possible to obtain the column number density N for a given aerosol layer τ. Then N is fit to match the precise τ value by taking σ_e at 1 μm as reference, for each aerosol layer.

Table 6.3 shows the obtained parameters that define the different aerosol layers of the CB model implemented in ASIMUT-ALVL. In order to guarantee that N is kept at the defined atmospheric layers, and therefore τ does not change, the modeled atmosphere was divided into 21 vertical layers defined by altitude, that include at least 4 points in the layers concerning the aerosols. Figure 6.12 shows the resultant N profiles by considering the intermediate altitude of the defined atmospheric layers. Since ASIMUT-ALVL is limited to analyzing up to 70 layers when considering scattering [151], it is still possible to increase the number of points of the proposed division if necessary for further analysis, although it is not recommended to modify those defining the aerosols for the CB model, at least for the hazes.

Aerosol type	Refractive index	PSD	r_{eff}	r_m	v_{eff}	Reference	Valid?
H_2O ice	Mastrapa et al., 2008	lognormal	0.013 μm	0.01 μm	0.1	[26]	λ>1 μm
	Warren & Brandt, 2008	lognormal	0.013 μm	0.01 μm	0.1	N/A	Yes
Haze	Martonchik et al., 1984 + Zhang et al., 2013	lognormal	0.13 μm	0.1 μm	0.1	[26]	Yes
		lognormal	0.37 μm	0.3 μm	0.1	[26]	
		lognormal	0.75 μm	0.6 μm	0.1	[26]	
	Khare et al., 1987	lognormal	0.13 μm	0.1 μm	0.1	N/A	Yes
		lognormal	0.37 μm	0.3 μm	0.1	N/A	
		lognormal	0.75 μm	0.6 μm	0.1	N/A	
Chromophore	1.4 + Carlson et al., 2016	gamma	0.141 μm	0.11 μm	0.1	CH model C [31]	λ<1.05 μm
		gamma	1.56 μm	1.25 μm	0.1	TC model B [31]	
Non-absorbing	$1.4 + i0$	gamma	0.114 μm	0.09 μm	0.1	SH model B [31]	Yes
		gamma	0.25 μm	0.20 μm	0.1	SH model C [31]	
		gamma	1.08 μm	0.86 μm	0.1	TC model C [31]	

Table 6.2: Summary of aerosols' properties implemented in ASIMUT-ALVL as part of this work. CH stands for Cromophore Haze, TC for Tropospheric Cloud, and SH for Stratospheric Haze.

Parameter	Stratospheric Haze (SH)	Cromophore Haze (CH)	Tropospheric Cloud (TC)
τ (unitless)	0.074	0.194	28.5
σ_e (cm^2/particle)	9.18×10^{-10}	6.40×10^{-11}	8.16×10^{-8}
N (part/cm^3)	21988.98	57965.80	224.36
Pressure (bar)	40.1 - 39.9	212 - 191	3940 - 212
Temperature (K)	133.6 - 133. 7	113.5 - 111.3	331.8 - 113.5
x (unitless)	1.57	0.89	6.79

Table 6.3: Parameters defining the different aerosols in the CB model as implemented in ASIMUT-ALVL. τ, σ_e and x are values at 1 μm.

The main properties of the aerosols implemented in ASIMUT-ALVL as part of this work are summarized in Table 6.2 (previous page).

6.3.4 *Collision Induced Absorption (CIA) in Jupiter*

Although CIA is not really an overlap of lines that shape the continuum of a spectrum (see section 5.3.4), it is defined as part of the continuum in ASIMUT-ALVL [151]. CIA is already implemented in ASIMUT-ALVL for pairs of molecules such as O_2-O_2, N_2-O_2 and O_2-O_2, following well-known formalisms for the modeling of Earth's atmosphere [151]. Unfortunately, CIA associated to H_2-H_2 and H_2-He molecular pairs, necessary for modeling Jupiter's atmosphere, are not yet implemented. As part of this work, new global variables and functions were added into ASIMUT-ALVL for this purpose by taking as input the corresponding CIA cross-sections from the literature.

Following equation 5.19, the absorption cross-section due to the collision of two molecules $\sigma_a^{(2)}$, in this case H_2 and He, is given by:

$$\sigma_a^{(2)} n^2 = \sigma_a^{(H_2-H_2)} n_{H_2}^2 + \sigma_a^{(H_2-He)} n_{H_2} n_{He} + \sigma_a^{(He-He)} n_{He}^2 \qquad (6.8)$$

where σ_a and n respectively correspond to the absorption cross-section and number density relative to each molecular pair. Only the first two terms contribute significantly to shaping the VIS-NIR spectrum of Jupiter's atmosphere [30, 34, 219, 232]. In consequence, only those terms were implemented in ASIMUT-ALVL as independent functions. However, these functions are not yet operational since ASIMUT-ALVL does not count with the possibility of multiplying σ_a by two n columns

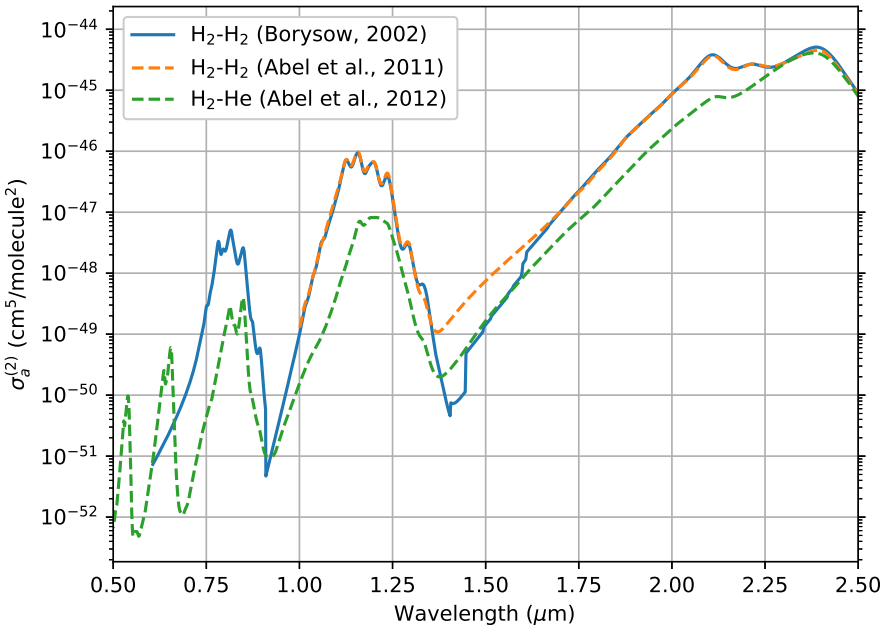

Figure 6.13: Cross-sections for CIA contribution in Jupiter's atmosphere at 200 K. Data from Abel et al. is shown in dotted line style.

from the atmospheric file, among other technical aspects. Therefore, the current forward model of Jupiter's atmosphere needs CIA contribution to be specified as an absorption cross-section.

So far, data from Borysow [233] have been extensively used to model H_2-H_2 CIA in Jupiter's atmosphere. Some works include those from López-Puertas et al. [26], Carlson et al. [32], Sromovsky et al. [33], Fry & Sromovsky [36] and Kedziora & Bailey [234]. This is the reason why, as part of this work, Borysow [233] data[12] was implemented in ASIMUT-ALVL as the default CIA cross-section for H_2-H_2 for a temperature of 150 K. However, recent experimental studies from Vitali et al. [235] at temperature and pressure conditions of Jupiter's troposphere, show that the work of Abel et al. [236] is in better agreement with measurements than data from Borysow [233]. Figure 6.13 compares the data from Abel et al. [236], also available in HITRAN [158][13], and the data from Borysow [233], for 200 K. As discussed in section 6.2, the main broadband CIA spectral features are present from 2 to 2.5 μm [1, 234].

12 Downloaded in November 2023
13 Downloaded in November 2023

The relative mean difference between both references is ∼7 % between 1.1 and 1.3 μm and ∼4 % between 1.7 and 2.5 μm. Moreover, note that data from Abel et al. [236] does not cover wavelengths smaller than 1 μm. Therefore, the data coverage of both references is complete for the spectral region where CIA contribution is expected to be significant, although it does not cover the complete VIS-NIR range under analysis. In any way, the relative difference between both references should not have a significant impact on the simulated spectrum, at the spectral resolution of the instrument.

According to Vitali et al. [235], when CIA associated to H_2-He pairs is considered, data from Abel et al. [237] is generally used as extracted from HITRAN [177]. This cross-section is also included in Figure 6.13 for comparison[14] . The main spectral feature is near 2.4 μm and coincides with that of CIA associated to H_2-H_2.

All CIA cross-sections discussed in this section are now available for ASIMUT-ALVL. For their use, they must be declared as typical cross-sections in the input file of the forward model. If necessary, a new CIA cross-section must be multiplied by the Loschmidt number n_0 before using it, since CIA cross-sections are usually normalized in density [177].

Table 6.4 summarizes the data implemented in ASIMUT-ALVL during this work, except data related to aerosols which was already summarized in Table 6.2.

14 Data downloaded in November 2023

Contribution	Reference	Previously available?	Implemented as	Recommended?
CH_4	Gordon et al. 2022	Without broadening	LUT + line list	λ>1.1 μm
	Karkoschka et al. 2010	No	LUT	λ<1.6 μm
	Yurchenko et al., 2017	No	LUT	λ>1.0 μm
	Yurchenko et al., 2024	No	LUT	λ>1.0 μm
NH_3	Gordon et al. 2022	Without broadening	LUT + line list	λ>2.12 μm
	Coles et al., 2019	No	LUT	λ>0.5 μm
H_2O	Gordon et al. 2022	Without broadening	LUT + line list	λ>0.238 μm
	Polyansky et al., 2018	No	LUT	λ>0.4 μm
Rayleigh scattering	Ford & Browne, 1973 (H_2)	No	Cross-section	Not alone
	Chan & Dalgarno, 1965 (He)	No	Cross-section	Not alone
	From refractive index**	No	Function	Yes
H_2-H_2 CIA	Borysow, 2002	No	Cross-section	Yes
	Abel et al., 2011	No	Cross-section	λ>1 μm
H_2-He CIA	Abel et al., 2012	No	Cross-section	Yes

Table 6.4: Summary of the spectral contributions implemented in ASIMUT-ALVL for the modeling of Jupiter's atmosphere in the VIS-NIR range (aerosols detailed in Table 6.2). **Refractivities from Peck & Huang, 1977 for H_2, and Mansfield & Peck, 1969 for He.

6.4 VALIDATION OF THE RADIATIVE TRANSFER MODEL

During the development of this work (section 2.4), ASIMUT-ALVL was modified to simulate the radiative transfer processes in Jupiter's atmosphere and reproduce VIS-NIR spectra, focusing on the spectral range of the corresponding channel of the MAJIS/JUICE instrument (0.5-2.35 μm). As discussed in section 6.3, new datasets and functions were implemented, and the new ASIMUT-ALVL version was released after the careful validation of the forward model. This validation process was made by reproducing results from another radiative transfer model, KOPRA, and later by comparing a resultant simulated spectrum against observational data of Jupiter's atmosphere acquired by Cassini/VIMS. Both validation stages are detailed in the following sections.

6.4.1 *Validation against KOPRA*

KOPRA is the radiative transfer model used by López-Puertas et al. [26] for their studies about aerosols in Jupiter's stratosphere (section 1.3). KOPRA was previously used to characterize the atmospheres of Earth [238], Titan [239] and Mars [240]. The validation of the new version of ASIMUT-ALVL was performed independently for every implemented spectral contribution by considering the same initial conditions to ensure consistency [241], including the atmospheric profiles already discussed in section 6.1. Naturally, the agreement between two or more radiative transfer codes does not necessarily imply that all of them are correct [241]. Nevertheless, the acceptance of KOPRA by the scientific community, as an option to perform forward models of Jupiter's atmosphere, is a satisfactory indicator of the functionality of the code and its accuracy, which were already compared against other radiative transfer codes by Schreier et al. [241]. Moreover, ASIMUT-ALVL has been extensively validated in the past, especially for its use in the modeling of terrestrial atmospheres, including Earth [179], Mars [180] and Venus [181].

This exercise aims to validate the different modifications performed in ASIMUT-ALVL during the implementation of the Jupiter properties and spectral contributions against a radiative transfer model already validated for its use in modeling Jupiter's atmosphere at the wavelength range of interest. In order to have consistent input data in both radiative transfer models, the followed methodology for the validation process consisted of simulating the same observational scenarios and proving

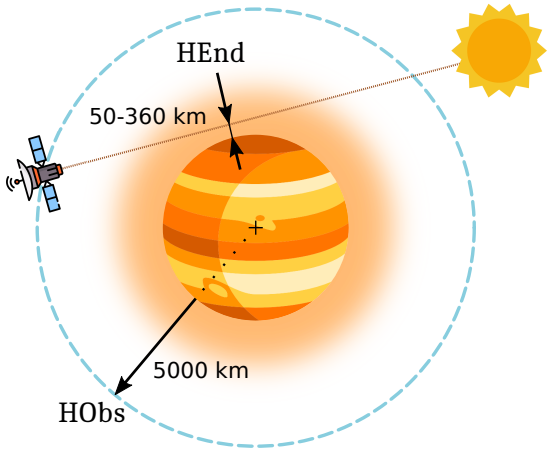

Figure 6.14: Observation geometry used during ASIMUT-ALVL validation against KOPRA. HEnd refers to the tangent height of the observation and HObs to the position of the observer.

that the resultant transmittances are in line with each other. Other inter-comparisons made between radiative transfer codes have encountered differences in the line strength up to 10 % [241], and are considered small when comparing codes using different internal parameters, such as internal layering, integration step width, monochromatic frequency grids, or line rejection criteria [242].

The observation geometry was defined as a solar occultation with the observer at 5000 km from the surface of the planet (Figure 6.14). In this way, the VIS-NIR spectrum is only shaped by the absorption of sunlight radiation by Jupiter's atmosphere. Generally, to define the viewing geometry in radiative transfer models, the user needs to specify the position of the observer (HObs) and the looking direction. These parameters are important to determine the ray path of radiation through the atmosphere [151]. For solar occultations, the looking direction corresponds to the tangent height (HEnd), which in this case was defined at different altitudes, typically between 50 and 360 km above the 1 bar level ($\sim 10^{-2}$ to 10^{-7} bar). The spectral resolution of the instrument was considered to be 0.3 cm^{-1}, with a spectral sampling of 0.01 cm^{-1} and a Gaussian instrumental line shape (ILS), which were the default values for KOPRA. Additionally, since KOPRA considers the equatorial radius of Jupiter for its simulations, instead of the mean radius, the corresponding value (71492 km) was added to the library of ASIMUT-ALVL during the validation tests.

Part of this work took place at the *Instituto de Astrofísica de Andalucía* (IAA) under the supervision of M. López-Puertas, during a scientific stay of two weeks.

Molecular absorption in ASIMUT-ALVL

At the time of the validation, KOPRA worked with the line lists of HITRAN2012 [243]. Therefore, ASIMUT-ALVL was run with the same version of HITRAN to keep consistency. The data for the spectral lines was downloaded in December 2014. Broadening parameters correspond to those from a typical Earth's atmosphere (70 % nitrogen and 20 % oxygen) in both radiative transfer models, considering Voigt line profiles for the absorption cross-sections. The simulation was done for a tangent height of 100 km only. No LUTs were used during the validation. Since the spectral range under test is quite large for the defined resolution, the simulations were divided into three spectral regions: 1.00-1.25 μm, 1.25-1.70 μm, and 1.70-2.50 μm. It took approximately 30 hours to complete a simulation per spectral region. Therefore, it was only performed for CH_4, assuming similar results for other molecules, such as NH_3 and H_2O.

Figure 6.15 shows a comparison between the obtained atmospheric transmittance from ASIMUT-ALVL against that from KOPRA for one of the spectral regions. In general, the transmittance computed by ASIMUT-ALVL is slightly lower than that obtained by KOPRA, and the difference between them is higher when transmittance is lower, i.e., where more molecular absorption took place. The relative mean difference between the resultant transmittance from ASIMUT-ALVL and the transmittance determined by KOPRA is $\sim$4 %, and could be due to differences in the methodology for LBL calculations, including path integration and optimization schemes. For instance, KOPRA uses representative averages of atmospheric state values for each layer, which are calculated as mass-weighted averages along the actual ray path segment through a layer [241]. ASIMUT-ALVL integrates the temperature, pressure, and densities of the atmospheric constituents following the Curtis-Godson approximation (see [12, 182]), which is similar but not exactly the same as the ray tracing methodology followed by KOPRA [151, 241]. Moreover, the methodology followed by KOPRA did not aim to get the best accuracy, and discrepancies can also be related to the rejection of weak lines.

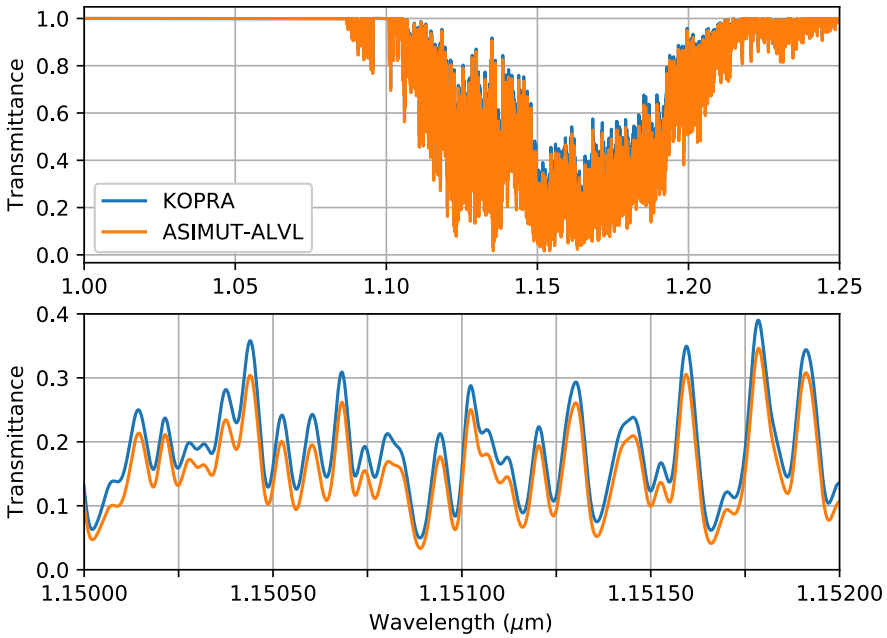

Figure 6.15: Simulated transmittance of Jupiter's atmosphere considering solely CH_4 as computed with KOPRA and ASIMUT-ALVL for the spectral region of 1.00-1.25 μm, taking as reference the HITRAN line list of 2012.

Rayleigh Scattering in ASIMUT-ALVL

For this validation test, two different tangent heights were analyzed: 50 and 100 km. KOPRA determines Rayleigh scattering in Jupiter's atmosphere based on the scattering cross-section proposed by the mathematical model of Ford & Browne [220]. It only considers the initial rotational level of Rayleigh scattering for H_2, since the temperature at such altitudes is below 200 K, and the molecules are assumed to be in the ground state. ASIMUT-ALVL can also be configured to consider Rayleigh scattering as a cross-section. However, a new function was implemented to determine the Rayleigh scattering of Jupiter's atmosphere, as described in section 6.3.2.

Figure 6.16 compares the transmittance obtained by ASIMUT against that obtained by KOPRA for a Jupiter's atmosphere considering solely Rayleigh scattering contributions for the whole VIS-NIR spectral range. It is clear that the optical depth is higher at short wavelengths, and should be therefore considered especially at wavelengths smaller than 1.5 μm, as already discussed in previous sections. Moreover, the optical

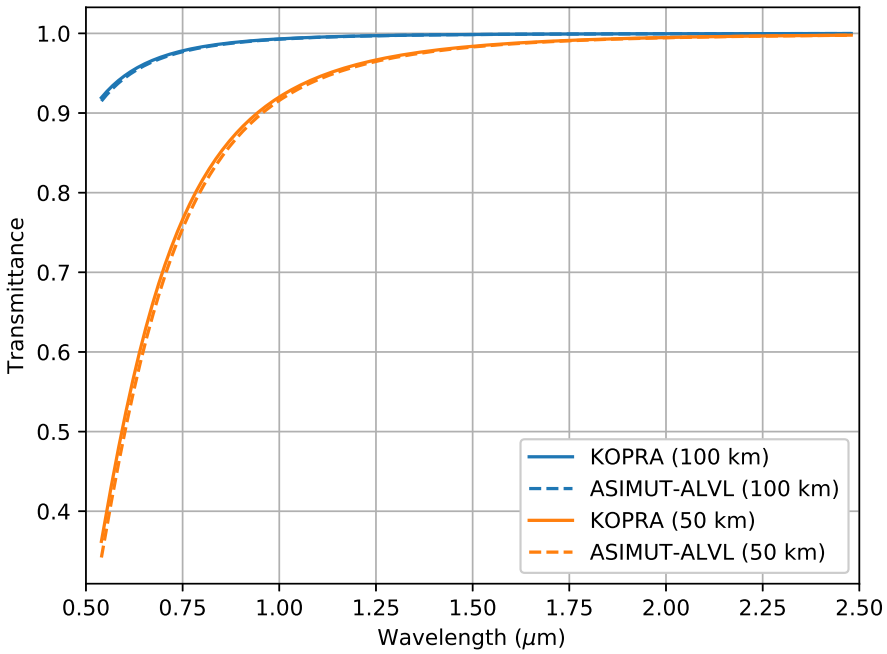

Figure 6.16: Simulated transmittance of Jupiter's atmosphere considering solely Rayleigh scattering as computed with KOPRA and ASIMUT-ALVL for two different tangent heights. KOPRA considers the scattering cross-section of H_2, while ASIMUT-ALVL computes it from the refractive index of Jupiter's atmosphere.

depth is also higher at lower altitudes, where a higher concentration of molecules is present in comparison to higher altitudes. Similarly to the previous validation case, the transmittance computed by ASIMUT-ALVL is slightly lower than that from KOPRA, and the difference is larger at lower transmittance.

The relative mean difference between the transmittance determined by both radiative transfer models can be considered negligible since it is <1 % for 50 km and <0.1 % for 100 km. If ASIMUT-ALVL directly considers the Rayleigh scattering cross-section of H_2, by following the same methodology as KOPRA, the relative mean difference between both radiative transfer models is below 0.05 %.

Aerosols absorption in ASIMUT-ALVL

Two tangent heights were considered for this validation: 100 and 170 km. The transmittance comparison was made by considering a

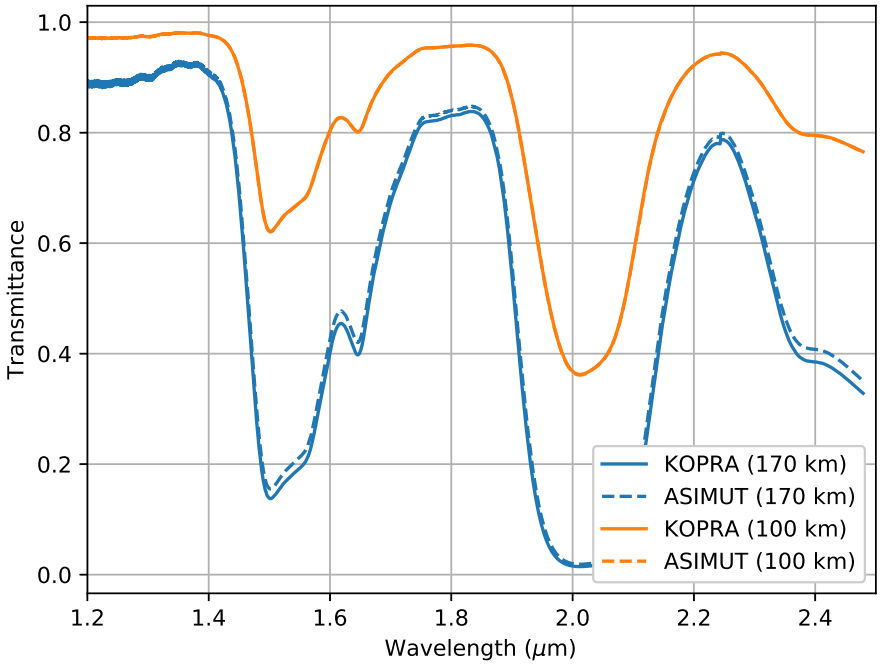

Figure 6.17: Simulated transmittance of Jupiter's atmosphere considering solely the H_2O ice cloud proposed by López-Puertas et al. [26], as computed by KOPRA and ASIMUT-ALVL, for two different tangent heights.

Jupiter's atmosphere constituted solely of the crystalline H_2O ice cloud proposed by López-Puertas et al. [26], which is located between 170 and 200 km (section 6.2). It was expected to obtain similar performances when comparing other types of aerosols, such as hazes and chromophores.

As already discussed in section 5.4, ASIMUT-ALVL includes different formalisms to determine the optical depths associated to aerosols. In solar occultations scattering is negligible (section 5.2). Therefore, considering the extinction cross-section σ_e of the aerosols besides their number density n, as it is done by KOPRA, is enough to obtain atmospheric transmittance. This can be performed in ASIMUT-ALVL through the `ModAngstrom` formalism. The `LidortG` formalism of ASIMUT-ALVL, which also considers SSA and g, will only make sense under nadir geometries. In consequence, both ASIMUT-ALVL formalisms give exactly the same results either in limb or solar occultation in this validation.

Figure 6.17 compares the simulated transmittance obtained by ASIMUT-ALVL and KOPRA for the hypothetical atmosphere described for

this validation test. Note that, in contrast with previous tests where the optical depth was stronger at lower altitudes, now the optical depth is stronger at 170 km instead of at 100 km. This is because the H_2O ice cloud is absorbing radiation at the whole spectral range of interest at that altitude, as shown in Figure 6.9 and 6.10. The relative mean difference between both models when ASIMUT-ALVL directly considers the cross-section of the cloud is 0.07 % for 100 km and 6.2 % for 170 km. This value is similar to that observed when analyzing molecular absorption bands, so it could be related to differences in the ray path integration methodology between both radiative transfer models, although it was not observed when analyzing Rayleigh scattering.

The relative mean difference between the transmittance computed by ASIMUT-ALVL from the absorption cross-section of the cloud and that from one of the formalisms, can be neglected, as it is much lower than 0.001 % for 100 km and <0.2 % for 170 km, where absorption is stronger, probing consistency between both methodologies in ASIMUT-ALVL.

Figure 6.18 shows the result of an additional validation made by comparing the extinction cross-sections from one of the hazes computed by López-Puertas et al. [26] (r_m=0.6 μm), against its equivalent cross-section computed by ASIMie (section 6.3.3). This tool was internally validated with other colleagues at BIRA-IASB before its use for generating the wavelength-dependent scattering parameters of aerosols. The Particle Size Distribution (PSD) corresponds to lognormal with $v_{eff} = 0.1$. The relative difference between both cross-sections is 1.5 % mainly due to the ripple oscillations observed at short wavelengths. Note that the cross-section determined from this work seems simply a smoothed version of the one determined for KOPRA, both assuming the same spherical particles. This behavior is typical of non-absorbing spheres [173].

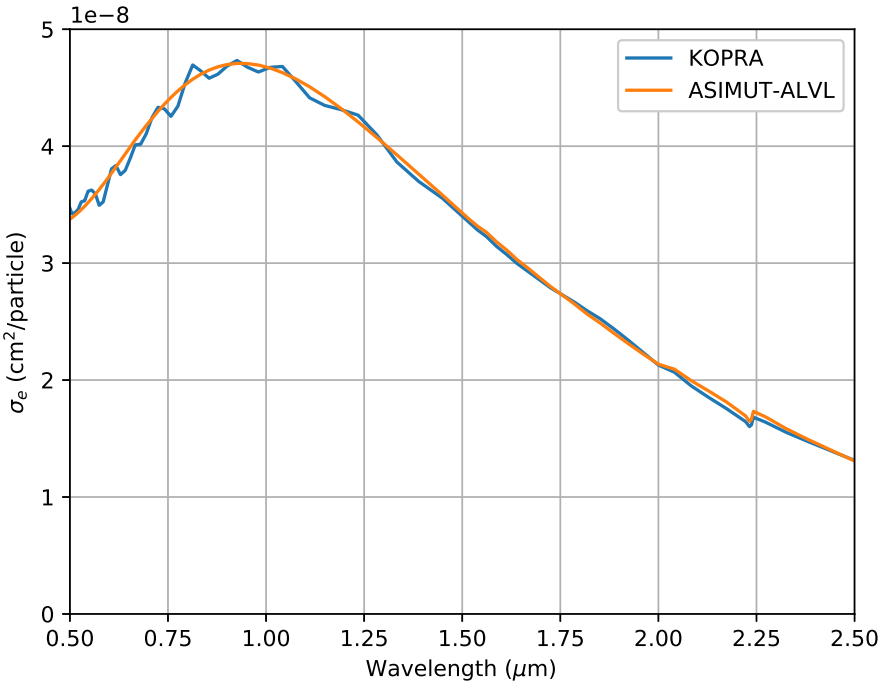

Figure 6.18: Extinction cross-section of r_m=0.6 μm haze proposed by López-Puertas et al. [26], as computed for its use in KOPRA and ASIMUT-ALVL. It considers a lognormal PSD with $v_{eff} = 0.1$. The real part of the refractive index corresponds to NH_3 ice, as measured by Martonchik et al. [230], with an imaginary part equal to the values derived by Zhang et al. [38].

Collision Induced Absorption (CIA) in ASIMUT-ALVL

As discussed in section 6.3.4, despite the efforts to implement a new function in ASIMUT-ALVL to compute CIA associated to H_2-H_2 and H_2-He pairs, the CIA contribution was finally implemented in ASIMUT-ALVL as a single cross-section. Since the functionality of ASIMUT-ALVL regarding spectral contributions defined by their cross-sections was already validated during Rayleigh scattering and aerosols absorption contributions, CIA was not validated in this phase.

Table D summarizes the mean relative differences obtained for the different spectral contributions during the validation of ASIMUT-ALVL against KOPRA. The largest differences correspond to the absorption due to molecular bands and aerosols at the tangent height at which the cloud was located. The mean relative difference observed from

Contribution	HEnd	Relative Mean Difference	Comment
Molecular bands	100 km	4.08 %	Only considering CH_4
Rayleigh scattering	50 km	0.93 %	<0.05 % with same cross-section
	100 km	0.08 %	
Aerosols absorption	100 km	0.07 %	Only considering H_2O ice
	170 km	6.2 %	

Table 6.5: Results from the validation of ASIMUT-ALVL against KOPRA for each spectral contribution type expected in Jupiter's VIS-NIR spectrum.

aerosols absorption at altitudes where no cloud was defined (100 km), is comparable to that of Rayleigh scattering.

This stage validates the functionality of ASIMUT-ALVL, especially concerning the newly implemented capabilities and its auxiliary tools to perform radiative transfer calculations and modeling of Jupiter's atmosphere. Several sensitivity tests were performed during this process in order to choose the best input parameters to define a typical scenario for the observation of Jupiter's atmosphere.

Another aspect necessary to address was the albedo for nadir observation geometries, which represents the main observation geometry for MAJIS. These tests were not compared against similar scenarios with KOPRA but took place during the validation of the CB model of Baines et al. [31] (section 6.4.3).

6.4.2 *Albedo in ASIMUT-ALVL*

For ASIMUT-ALVL, the altitude reference of 0 km typically defines the beginning of the surface of a planet, whose influence is defined by the albedo. Nevertheless, for Jupiter, it is necessary to prove that the light is passing through the atmosphere beyond the 0 km level when performing nadir simulations. Moreover, as defined by Figure 6.3, the thermal radiation from the planet does not play any role at VIS-NIR wavelengths. In other words, the albedo can be directly neglected by ASIMUT-ALVL as no radiation of any type is being reflected by the defined surface, which does not physically exist in Jupiter. Therefore, although Jupiter has an albedo of 0.343 (Table 1.1), it is necessary to make it zero in ASIMUT-ALVL. Similarly, to ensure that there is no

thermal emission by what ASIMUT-ALVL considers a surface, and the thermal emission of the atmospheric layers is determined directly from Jupiter's temperature profile (Figure 6.1), the surface temperature of Jupiter was changed from 166.1 K to 0 K. In this way, the radiation measured by the remote sensing instrument will be equal solely to the solar radiation reflected by Jupiter's atmosphere.

Additionally, ASIMUT-ALVL offers an option to neglect the reflection of the thermal emission from the atmospheric layers by the surface. This option is enabled for Jupiter simulations. For solar occultations and limb geometries, these choices have no impact on the simulated transmittance as long as the tangent height (HEnd) is above the 0 km level of Jupiter. ASIMUT-ALVL will perform the radiative transfer modeling by considering every atmospheric layer until HEnd, even if it is below the surface limit. Certainly, HEnd must have a value included in the limits of the atmospheric file, otherwise, ASIMUT-ALVL will stop the calculations at the minimum specified altitude by the temperature profile. Moreover, if HEnd is below the 0 km level, the same considerations as for nadir geometries must be taken into account.

Several sensitivity tests were performed to evaluate the validity of these assumptions. These simulations were performed under a nadir geometry for a wavelength range between 0.9 and 1.1 μm, with a Jupiter's atmosphere solely consisting of the tropospheric cloud from the CB model of Baines et al. [31]. Other spectral contributions such as molecular absorption and Rayleigh scattering were not considered to prove that radiation can reach the deepest levels of the tropospheric cloud. Table 6.6 indicates the relative mean difference in radiance for some of these cases. The differences are not significant. However, following these assumptions results in a forward model closer to the radiative transfer physics of a gas planet like Jupiter, which has no physical surface and whose bolometric temperature does not provide thermal radiation at the wavelength range of interest.

Finally, the next step required the validation of the model against Jupiter's VIS-NIR observational data acquired in nadir geometry, since this is the main viewing geometry for MAJIS.

Surface Parameter	Jupiter	ASIMUT-ALVL	Relative Mean Difference
Albedo	0.343	0	2.1 %
Temperature at 1 bar	166.1 K	0 K	6.5 %*
Thermal Source	Yes	No	1.7 %
Thermal Reflections	Yes	No	0 %

Table 6.6: Relative mean difference in radiance when performing simulations in ASIMUT-ALVL by considering the physical values of Jupiter against the values that remove the surface contribution in the code. Each parameter was evaluated at a time. Simulations were performed for nadir geometries, considering a wavelength range between 0.9 and 1.1 μm. **Only if albedo has its nominal value, otherwise the difference is 0 %.*

6.4.3 *Verification against observational data*

To verify that the updates implemented in ASIMUT-ALVL can jointly reproduce realistic scenarios of Jupiter's atmosphere, it is necessary to compare, at least qualitatively, the synthetic spectrum obtained from the forward model against observational data. Full-disk data acquired by the Visual and Infrared Mapping Spectrometer (VIMS) on board the Cassini mission (section 1.4) was used for this exercise. VIMS is a multispectral imager that consists of two channels: the VIS channel covering the spectral range from 0.35 to 1.05 μm, and the IR channel covering the range from 0.85 to 5.10 μm [244]. The performances of each channel are described in Table 6.7.

The calibrated observational data used for this work was provided by G. Filacchione[15] from personal communication. The provided observation has the reference `V1354395024` and was performed during the Jupiter flyby on December 2, 2000, with an integration time of 1280 ms/pix for the VIS channel and 20 ms/pix for the IR channel. The observation geometry is illustrated in Figure 6.19.

As a multispectral imager, it is possible to extract either nearly monochromatic images of the planet or spectra of every pixel in the image. Figure 6.20 and 6.21 show an image from an arbitrarily chosen wavelength (*band*) of each channel and the corresponding spectrum extracted from the Great Red Spot (GRS) available in Cisneros et al. [in preparation]. Note that the spatial scale of both channels is different,

15 Academic researcher at the *Istituto di Astrofisica e Planetologia Spaziali* (INAF-IAPS)

Parameter	VIMS-VIS	VIMS-IR
Spectral range	0.35 - 1.05 μm	0.85 - 5.10 μm
Spectral sampling	1.46 nm	16.6 nm
Spectral resolution	7.3 nm 198.64 cm^{-1}	16.6 nm 38.23 cm^{-1}
Resolving power	95.89	179.52
Number of pixels	480	256
Number of spectels	96	256
Spatial scale	166×166 μrad	250×500 μrad

Table 6.7: Cassini/VIMS spectral performances [244].

so the Jupiter disk appears in a different size on each detector. In consequence, the GRS spectrum is extracted from the average signal measured by a group of pixels in the VIS channel, and from a single pixel in the IR channel.

The GRS is an interesting location to validate Jupiter's forward model since it has a strong concentration of chromophores and was already analyzed under different observation geometries by Baines et al. [31]. The continua will be strongly defined by atmospheric scattering, including aerosols, while the absorption bands will be mainly related to molecular bands and CIA.

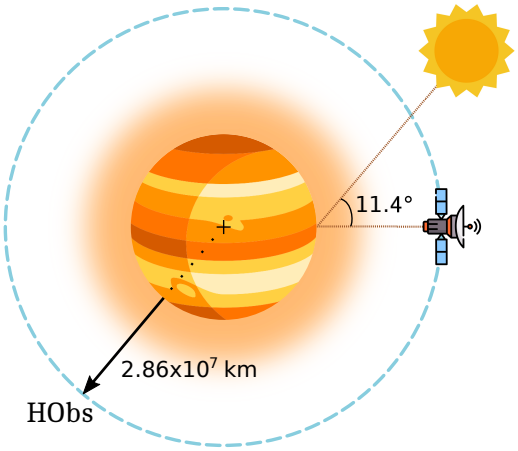

Figure 6.19: Observation geometry of Cassini/VIMS data.

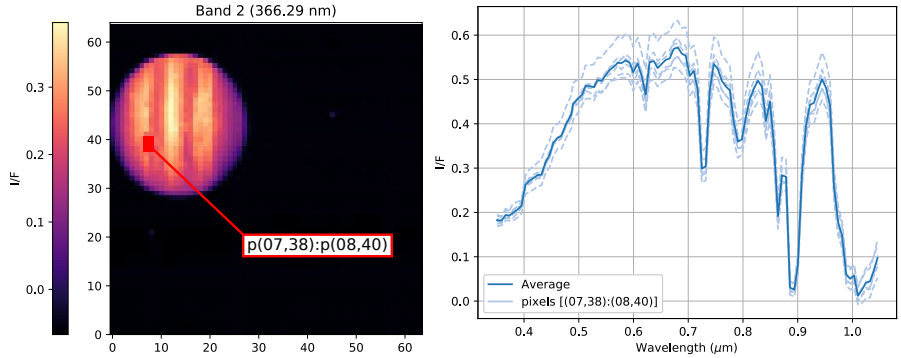

Figure 6.20: Cassini/VIMS observation from the VIS channel: (left) monochromatic image acquired from the spectral band centered at 366.29 nm, (right) spectra extracted from the GRS.

Figure 6.22 and Figure 6.23 compare VIMS observational data against synthetic spectra obtained from forward simulations run in the new version of ASIMUT-ALVL, result from this work, for the VIS and the IR channel, respectively. I/F (section 5.4) is normalized for a better visualization as:

$$(I/F)_{norm} = \frac{I/F - (I/F)_{min}}{(I/F)_{max} - (I/F)_{min}} \tag{6.9}$$

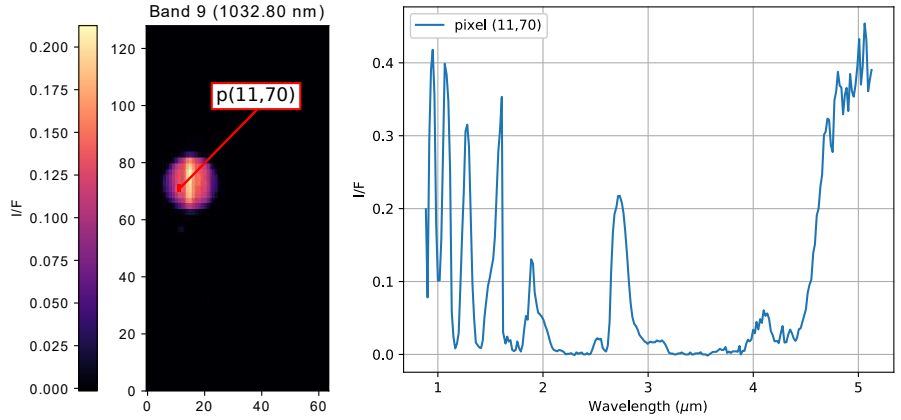

Figure 6.21: Cassini/VIMS observation from the IR channel: (left) monochromatic image acquired from the spectral band centered at 1032.80 nm, (right) spectrum extracted from the GRS.

where $(I/F)_{min}$ and $(I/F)_{max}$ correspond to the minimum and the maximum value of I/F in the spectral range under analysis, restricted to the validated wavelength range of the forward model (0.5-2.35 μm). *I/F* was interpolated according to the wavelength scale of VIMS data. The simulations considered the molecular absorption bands due to CH_4, NH_3 and H_2O, Rayleigh scattering, the CB model of aerosols to shape the continuum, and CIA associated to H_2-H_2. Different combinations of molecules were simulated each time to highlight their contribution to the spectrum. Following the discussion in section 6.3.1, the CH_4 band model of Karkoschka et al. [198] was used for the spectral range of the VIS channel, while the CH_4 LUT from ExoMol was used for the spectral range of the IR channel. Similarly, NH_3 and H_2O were modeled from generated LUTs from ExoMol and HITRAN, respectively. Consult Table 6.1 for more details about the considered broadening parameters, line profiles, and other related characteristics. Similarly, and following section 6.3.4, H_2-H_2 CIA data was taken from Borysow [233] for the VIS channel, and from Abel et al. [236] for the IR channel.

It is not intended for this work to reach a perfect match between the spectra from the model and the observational data, although ASIMUT-ALVL could be used for this purpose if desired. As observed in Figure 6.22 and Figure 6.23, CH_4 is clearly the molecule responsible for the main absorption features in Jupiter's VIS-NIR spectrum. Referring to the VIMS/VIS channel (Figure 6.22), when considering CH_4 + NH_3, the spectral signatures around 0.66, 0.77 and especially 0.92-0.96 μm, are closer to the shape of the VIMS spectrum. When considering CH_4 + H_2O, it is clear that H_2O is only important close to 0.6 μm, since around 0.66, 0.82 and 0.92-0.96 μm, the spectral signatures that were close to the observed spectrum in other dual combinations of molecules, are lost. In fact, the relative mean difference between the case considering all molecules against the one neglecting H_2O differs $\sim$9 % from the observational data.

Similarly, referring to the VIMS/IR channel (Figure 6.23), the simulated spectrum considering CH_4 + H_2O has a lower signal around 0.95 and 1.08 μm, than the observational data. However, at 1.08 μm, the signal is slightly higher than that from the spectrum considering CH_4 + NH_3. It is the same case around 1.25 and 1.5-1.6 μm, where the CH_4 + H_2O spectrum has a slightly higher signal than the spectrum considering only CH_4. As a result, the spectrum considering CH_4 + NH_3 seems closer to the observational data than that considering CH_4 + NH_3 + H_2O, except for the region closer to 1.08 μm. Then for the IR

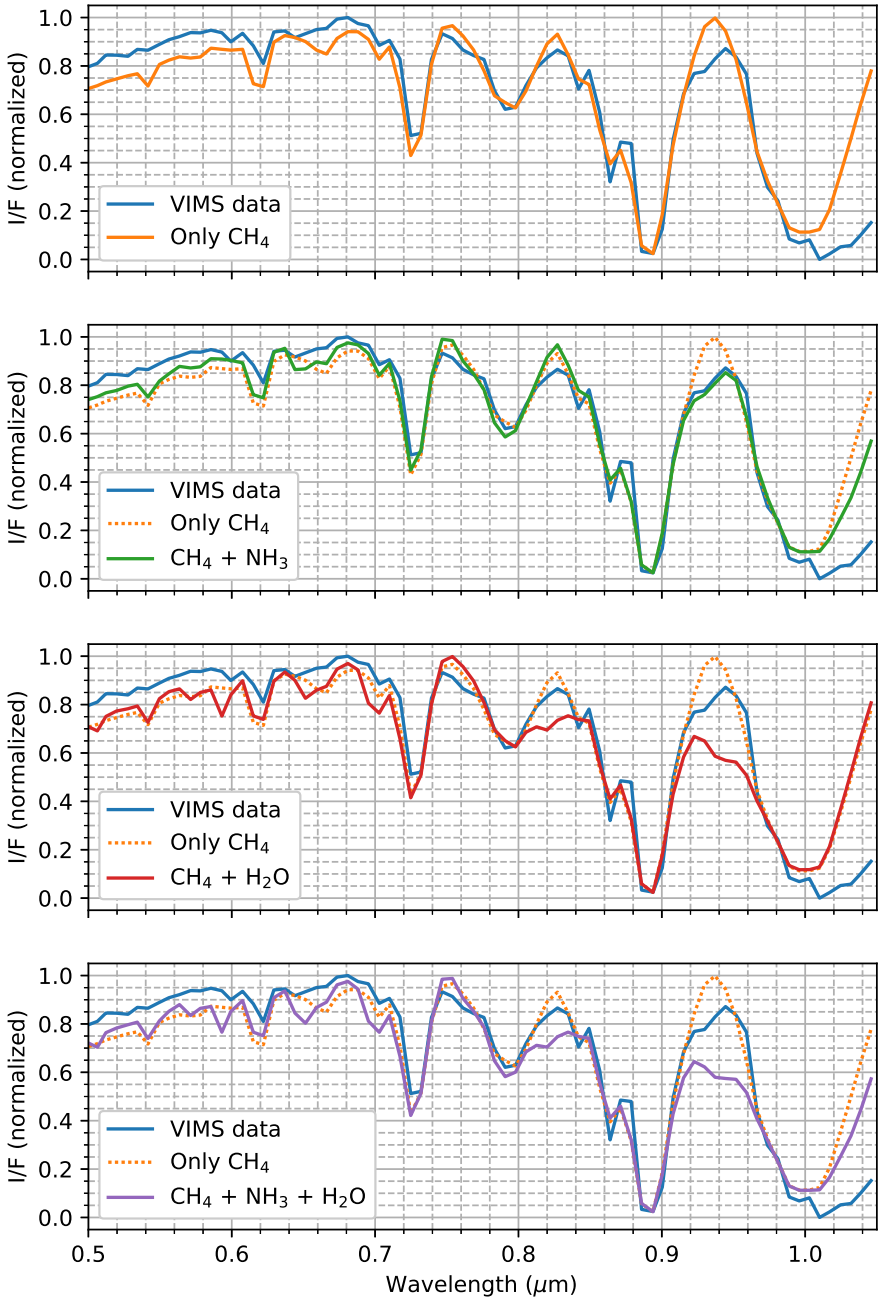

Figure 6.22: Comparison between observational data from the VIS channel of Cassini/VIMS and ASIMUT-ALVL simulations for a Jupiter's atmosphere with Rayleigh scattering, aerosols according to the CB model, and CIA associated to H_2-H_2. Each panel shows a synthetic spectrum with a different combination of molecules to highlight its contribution to the final spectrum, and one reference simulated spectrum to visualize the differences better.

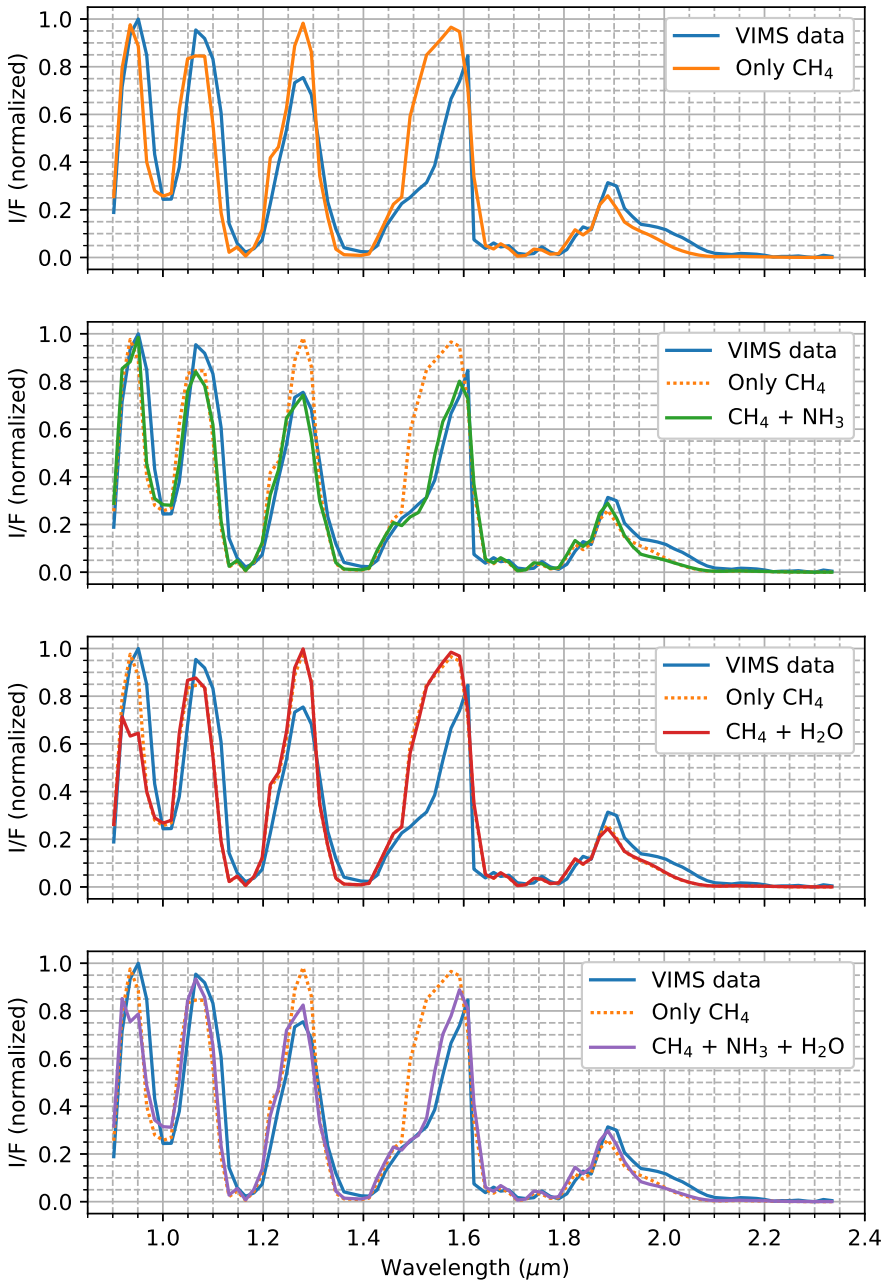

Figure 6.23: Comparison between observational data from the IR channel of Cassini/VIMS and ASIMUT-ALVL simulations for a Jupiter's atmosphere with Rayleigh scattering, aerosols according to the CB model, and CIA associated to H_2-H_2. Each panel shows a synthetic spectrum with a different combination of molecules to highlight its contribution to the final spectrum, and one reference simulated spectrum to visualize the differences better.

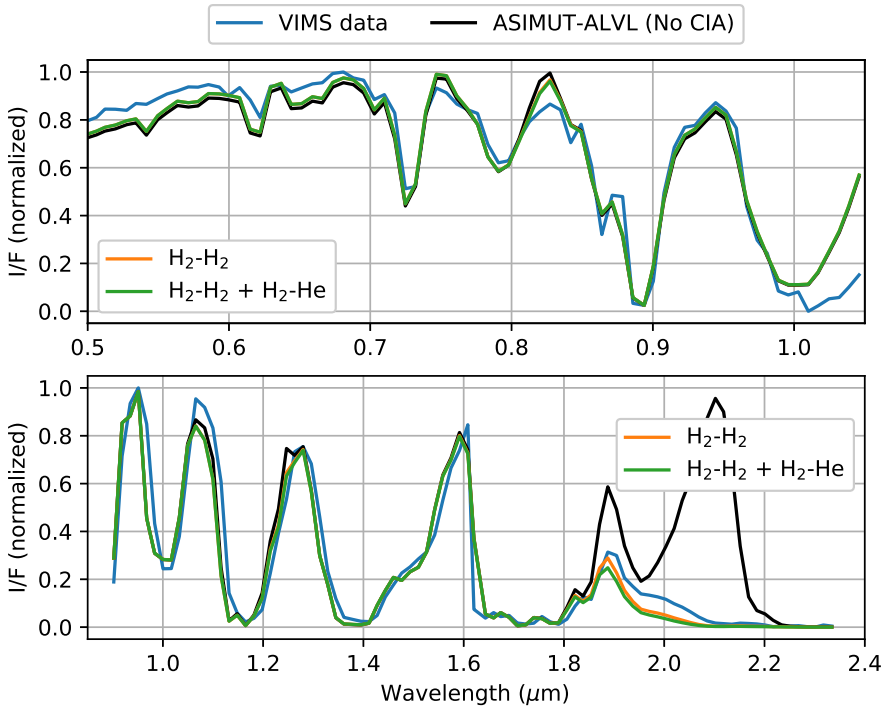

Figure 6.24: Comparison between observational data from Cassini/VIMS and ASIMUT-ALVL simulations for a Jupiter's atmosphere with Rayleigh scattering, aerosols according to the CB model, CH_4 and NH_3. The VIMS VIS channel is at the top and the VIMS IR channel is at the bottom. For each channel, there are additional spectra considering CIA associated to different groups of molecular pairs.

channel, the main difference against the observational data is mainly noticeable at wavelengths shorter than ~ 1 μm. In this instance, the relative mean difference between the case considering all molecules against the one neglecting H_2O is below 3%.

From these results, it was decided to no longer consider H_2O for the next validation analyses. This does not necessarily mean that H_2O is not significant in Jupiter's atmosphere and can be completely discarded from the forward model. Specifically at the GRS, it was found that H_2O does not contribute as much as CH_4 and NH_3, and its abundance could be neglected in this spectral window in consequence.

Figure 6.24 shows the synthetic spectrum obtained for a Jupiter's atmosphere considering again CIA associated to H_2-H_2, Rayleigh scattering due to H_2 and He, aerosols according to the CB model, and

absorption bands due to CH_4 and NH_3, together with the VIMS observational spectrum for both channels. As in the previous figures, *I/F* is normalized according to equation 6.9 for a better qualitative comparison and was interpolated in accordance with the wavelength scale of VIMS data. An additional spectrum considering CIA associated to H_2-He is added in Figure 6.24, although its impact is not significant for none of the spectral channels. The relative difference between the simulation with CIA and without CIA is not higher than 0.8 % for the VIS channel, while the relative difference between the simulation considering CIA only associated to H_2-H_2 and the one considering CIA associated both to H_2-H_2 and H_2-He is much lower than 0.1 %. Therefore, it is confirmed that at short wavelengths it is valid to neglect the CIA contribution. Nevertheless, for the IR channel, CIA must be considered in order to account for the band around 2.1 μm. For the IR channel, there is a relative mean difference of 8 % between the simulation considering CIA only associated to H_2-H_2 and the one considering CIA associated to H_2-H_2 and H_2-He.

The validation of the new functionalities for the forward model of Jupiter's atmosphere in ASIMUT-ALVL is now complete because all required contributions in the spectral range between 0.5 and 2.35 μm were efficiently implemented and validated. It is worth mentioning that the LUTs implemented for molecular absorption reduced the computing time of a complete single simulation to less than 20 minutes. An example of an ASIMUT-ALVL input file for a nadir simulation is available in Appendix B for further reference. Finally, it will be possible to assess the capabilities of the MAJIS VIS-NIR channel to comply with the scientific objectives of the mission, by performing simulations of a realistic scenario for the MAJIS instrument. This is discussed in part IV.

Part IV

FINAL RESULTS AND CONCLUSIONS

7 ASSESSMENT OF MAJIS VIS-NIR PERFORMANCES

Now that the actual performances of the MAJIS VIS-NIR channel are known for each pixel (part II), and there is a new radiative transfer tool available to model Jupiter's atmosphere in the VIS-NIR range (part III), it is possible to simulate realistic observations of MAJIS and assess its sensitivity to comply with the scientific objectives of the JUICE mission. The results of this work are relevant to the MAJIS science team. These efforts are focused on the impact analysis of the use of *spectral masks* to reduce the data volume acquired during observations, with a minimal loss of science return. Additionally, the impact of the detection limit of the MAJIS VIS-NIR channel on the abundance variation of different atmospheric compounds was assessed. The considered observation scenario for this analysis was chosen through the JUICE Events and Segments Visualisation and Coverage tool, while the Signal-to-Noise Ratio (SNR) of the simulated observation was generated from the MAJIS Radiometric Simulator tool (version 1.3). This work supports the preparation activities for the expected arrival of the JUICE mission in 2031. A comparison of the expected response of MAJIS against previous similar instruments under the same observation geometry, considering the wavelength range between 0.5 and 2.35 μm, is also presented.

7.1 MAJIS SPECTRAL MASKS

The large distance between Earth and Jupiter results in a signal round trip time of 1 hour 46 minutes, which requires careful preplanning of the observations and autonomous execution of operations by the JUICE spacecraft [60]. The data downlink is made through the non-steerable high-gain antenna of JUICE for a daily average data volume of $\sim$2.5 Gb [18, 78]. JUICE downlink activities include data retrieval from the instrument telemetry, auxiliary data from the Mission Operation Center (MOC), preliminary data processing and archiving, and quick look checks of the performed observations [60]. Current operations assume only one daily downlink session, considering data volume is shared between different science topics and not necessarily instruments [245]. Therefore, to reduce and optimize the downlink capabilities dedicated

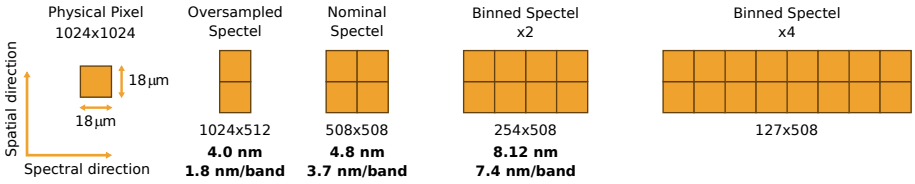

Figure 7.1: MAJIS binning techniques for the VIS-NIR channel from highest to lowest spectral resolution [135].

to MAJIS (∼220 Gb for the entire mission [245]), the definition of *spectral masks* was proposed by the MAJIS science team. The idea is to transmit only specific spectral ranges relevant to the scientific objectives of the mission, at the minimum spectral resolution required. A set of different spectral regions per acquisition type would represent a spectral mask. To avoid complex planning and ensure relative uniformity in MAJIS data, a very limited number of spectral masks (2-3) should be defined [245].

The Field of View (FoV) of each MAJIS channel, defined by the dimensions of the slit, illuminates only 800 consecutive centered rows of physical pixels, while the dispersion of wavelengths occurs over 1016 columns of physical pixels [77]. A nominal pixel for MAJIS is binned 2×2, to constitute one spectral element or *spectel*, which coincides with the width of the slit projected on the Focal Plane Array (FPA) [75]. The spatial resolution can be adapted by additional binning depending on the observational conditions [139]. Spectral regions of interest can be observed with *oversampled spectels*, which would be only binned in the spatial direction [135]. On the contrary, if the spectral region is not of interest, the spectral resolution can be decreased by binning the spectels or by selectively neglecting the information acquired by some of them. Figure 7.1 describes the binning possibilities available for MAJIS, with their corresponding spectral resolutions for the VIS-NIR channel [135].

Therefore, a given spectral region could be: transmitted with nominal spectral resolution, transmitted with high spectral resolution, transmitted with reduced spectral resolution, or not transmitted. Default spectral masks are proposed by the MAJIS team for both daytime and nighttime observations. The spectral mask proposed for daytime observations implies low spectral resolution for the VIS-NIR channel and not transmitted data at 1.65-1.75 μm and 2.27-2.34 μm [245], where the signal is expected to be too low to provide valuable scientific information. During nighttime observations, VIS-NIR data from MAJIS would

not be transmitted. As part of this work, the proposed spectral masks were preliminary assessed to confirm their impact on MAJIS's scientific observations.

7.2 OBSERVATION SCENARIO

The JUICE training plan includes seven opportunities identified during the cruise phase of the mission. These trainings were designed by the science team to exercise different aspects of the science operations through detailed scenarios. These scenarios are defined by challenging or representative parts of the planning segmentation for which in-depth analysis is needed to refine assumptions in collaboration with the instrument teams. Some of the objectives of these scenarios relate to a realistic estimation of the data volume generation for the flybys, and assessment of the planning process to generate relevant procedures and identify improvement opportunities [246].

The perijove 12 (PJ12) is the third detailed scenario exercise of the JUICE strategic science planning, after Callisto and Europa flybys scenarios. Among the different goals defined for the PJ12, it is necessary to prove the ability of the instrument teams to generate an observation schedule for the tour phase, and use the PJ12 analysis as a representative case of near-equatorial perijove pass ($\sim$10-15 Jupiter radii), for dayside and nightside geometry, with no flyby interruption. This enables MAJIS to test multiple observation types, and the possibility of working together with JANUS [246].

Several tools were developed by the Science Operations Center (SOC) to support JUICE planning activities. The Events and Segments Visualization and Coverage tool of JUICE [247] is used to analyze the distribution of events in a geometry of interest, including flybys, transits, and Earth, stellar and solar occultations. For assessing the MAJIS VIS-NIR capabilities in this work, this tool was used to identify JUICE perijoves and select the closest approach in which MAJIS could be able to perform nadir observations of the disk. These are the most common MAJIS observing types for Jupiter and are referred to as `MAJ_JUP_DISK_SCAN`. They require the use of the JUICE internal pointing mirror and were defined to perform observations of Jupiter clouds and spectroscopy of minor gasses, expecting to cover the entire equatorial region of Jupiter (-30° to +30°) during low inclination phases at both daytime and nighttime [248].

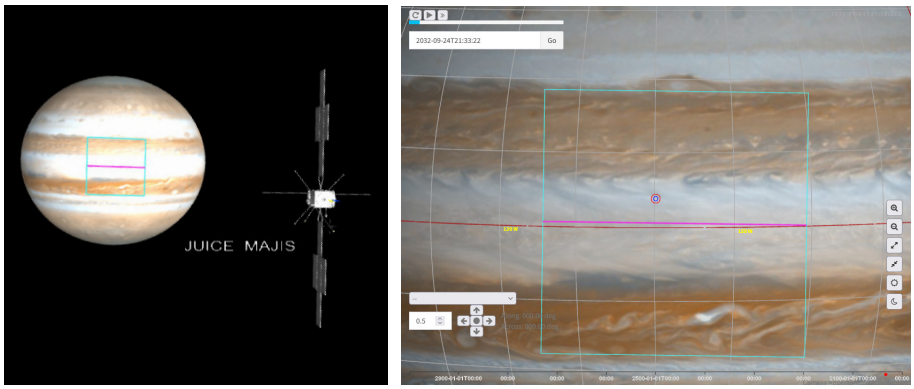

Figure 7.2: MAJIS observation geometry chosen for this work [2032-09-24T21h33m22s], as simulated by the JUICE Pointing Tool: (left) spacecraft view, (right) pointing view with longitude and latitude grid of the planet enabled. The cyan square represents MAJIS FoV, and the pink line corresponds to the VIS-NIR channel baseline.

The observation chosen for this work was extracted from the JUICE Consolidated Report on Mission Analysis (CReMA) version 5.1. It is part of the PJ12 observations and should take place on September 24th, 2032 at 21:33, when JUICE is at a distance from Jupiter of 762729.48 km with a phase angle of 16.35°. Figure 7.2 shows a simulated visualization of the Field of View (FoV) of MAJIS for the chosen observation. This was performed with the JUICE Pointing Tool[1] [249], which provides a 3D environment similar to Cosmographia [250], but with the advantage of being able to run with a web browser. The JUICE Pointing Tool supports the assisted creation of pointing requests for the JUICE planning activities [249].

7.3 FORWARD SIMULATION

The new version of ASIMUT-ALVL was used to perform forward simulations with the characteristics described in chapter 6. Jupiter's atmospheric temperature profile was taken from Moses et al. [4] and Seiff et al. [29] at pressure larger than 1 bar. The Volume Mixing Ratio (VMR) profile of every molecular species was taken from González et al. [196], extrapolated with the deep VMR values for each compound below 1 bar. CH_4 gas absorption was modeled through Look Up Tables

1 With the support from N. Ligier, researcher at the *Institut d'Astrophysique Spatiale* (IAS), for the configuration of the Planning Timeline Request (PTR) file

(LUTs) based on the model of Karkoschka et al. [198] for wavelengths smaller than 1.1 μm, and from Yurchenko et al. [199] data for longer wavelengths. NH_3 and H_2O gas absorption were modeled with data from Coles et al. [214], and Conway et al. [215], respectively, also as LUTs. Further details about each of the references are given in section 6.3.

Collision-Induced Absorption (CIA) cross-sections from H_2-H_2 and H_2-He were taken from Abel et al. [236] and Abel et al. [237], respectively. For wavelengths smaller than 1 μm, data for H_2-H_2 CIA was completed with cross-sections from Borysow [233], although it was demonstrated that CIA can be neglected at these wavelengths.

The aerosols model used for this work followed the *Crème Brulée* (CB) model proposed by Baines et al. [31], already validated in section 6.4. The wavelength-dependent scattering parameters of the different layers were determined from the Mie scattering code from Bohren & Huffman [172]. The computational formalism approaches the non-spherical particle case by smoothing the scattering phase function with the Henyey-Greenstein approximation, using 100 Legendre polynomials to expand it.

Three cases of spectral resolution were tested for this work: MAJIS oversampled spectel, MAJIS nominal spectel and MAJIS binned spectel x2. Figure 7.3 shows a comparison of the different spectra obtained for each case. According to the proposed spectral mask for daytime observations, the nominal resolution for this case would be the binned x2, except in the darker shadow areas which would correspond to no transmitted data. Note that the nominal spectrum is not so different from the oversampled spectrum. Indeed, most of the spectral features are noticeable under the nominal resolution since the relative mean difference between the oversampled and the nominal spectra is 1.6 %. However, the binned spectrum, which corresponds to the proposed resolution by the defined spectral masks, loses some spectral information, especially in the regions highlighted by Figure 7.3 (bottom). In this case, the relative mean difference between the nominal and the binned x2 spectrum is below 5 %. Therefore, the oversampling resolution would be recommended between 0.58 and 0.6 μm, for instance.

At this point, it is also possible to suggest the expansion of the neglected data above 2.09 μm and additionally neglect the spectral region between 1.35 and 1.40 μm. *I/F* values below 0.05 can also be discarded due to the low signal provided, except for the spectral region $\sim$2 μm where CIA due to H_2-H_2 is expected to be measured. Then,

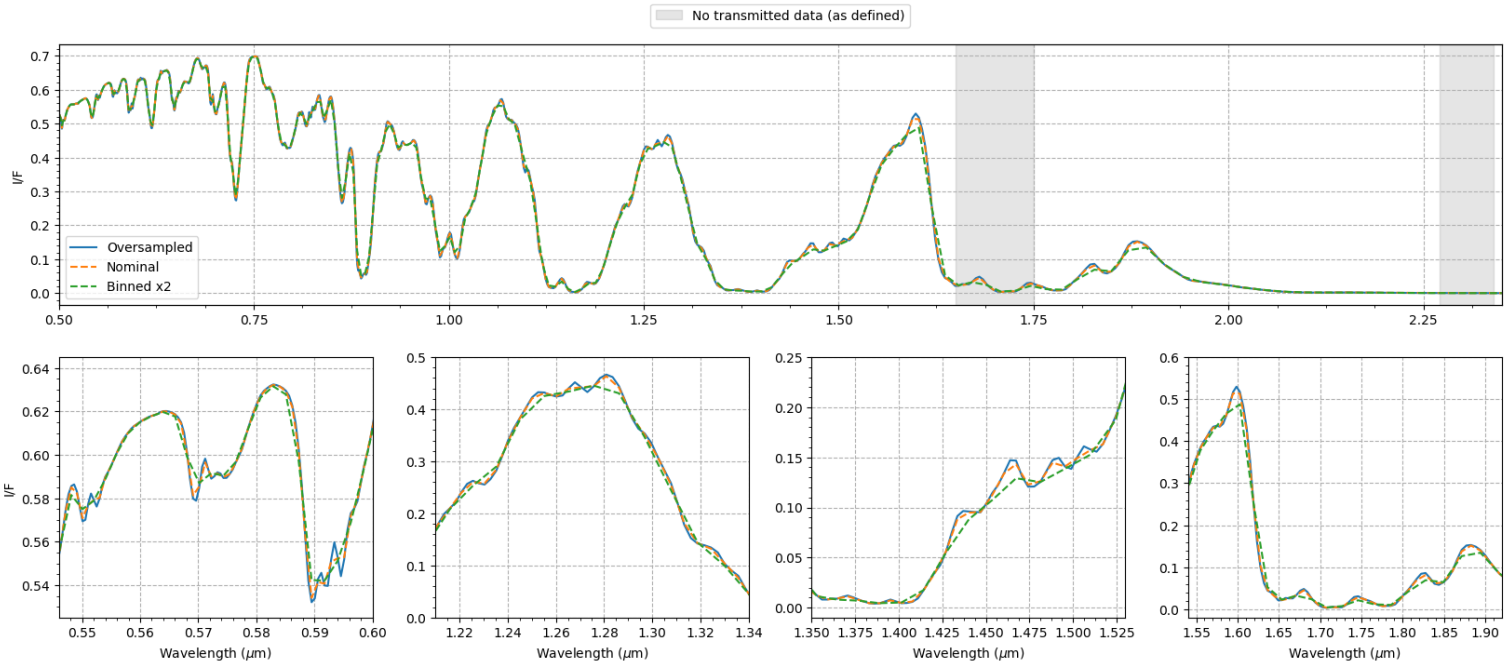

Figure 7.3: Forward simulation of Jupiter's atmosphere with different MAJIS spectral resolution modes. The top plot includes the complete VIS-NIR spectral range, while the bottom plots show some spectral regions that highlight the differences between the different spectral resolution modes. The dark shadow areas in the top plot correspond to regions discarded by the daytime spectral mask as originally defined to reduce more data volume. According to this spectral mask, the rest of the spectral range should be acquired in binned resolution x2.

an additional neglected spectral band can be at 1.13-1.18 μm, and the spectral band at 1.65-1.75 μm could be extended up to 1.78 μm. Note that these simulations (Figure 7.3) were not subjected to the noise extracted from the expected SNR. Moreover, stray light is expected to significantly affect data between 0.6 and 0.7 μm, which could also not be transmitted if necessary.

7.4 MAJIS RADIOMETRIC MODEL

Thanks to the radiometric calibration of the MAJIS instrument after the complete characterization of its detectors, it was possible for the *Institut d'Astrophysique Spatiale* (IAS) to develop the radiometric model of MAJIS and determine the expected signal level of a simulated radiance as a function of wavelength. Therefore, results from the forward model obtained from ASIMUT-ALVL can be used as inputs for the MAJIS radiometric model and simulate MAJIS observations based on its measured performances. The simulated signal depends on the optical efficiency of the telescope and the spectrometers, the transmission of the filters, and the quantum efficiency of the detectors [251]. This model is still under development but preliminary simulations, performed with version 1.3 of the tool, were performed for this analysis.

The MAJIS radiometric model, or MAJIS SNR simulator, is distributed to the MAJIS science team to support the science planning by providing the expected SNR of any observation considering de-spiking strategies that are compliant with the MAJIS software on board. It considers the geometry of observation, the temperature of the MAJIS Optical Head (OH) and Focal Plane Units (FPUs), and the read-out configuration for data processing from the detector (spatial windowing, spatial binning, frame binning, de-spiking, spectral oversampling or binning) [251]. The noise model under consideration estimates the standard deviation of the total noise of the instrument depending on the signal level measured, which contains the contribution of the measured shot noise and the Read-Out Noise (RON).

Figure 7.4 shows a comparison of the resultant SNR for the nominal and the binned resolution of the MAJIS VIS-NIR channel. It is worth mentioning that the simulator is still not able to consider the corresponding spectral calibration for other resolution modes than the nominal. Therefore, the SNR for binned resolution was multiplied by $\sqrt{2}$. As expected, binning the pixels increases the SNR but decreases

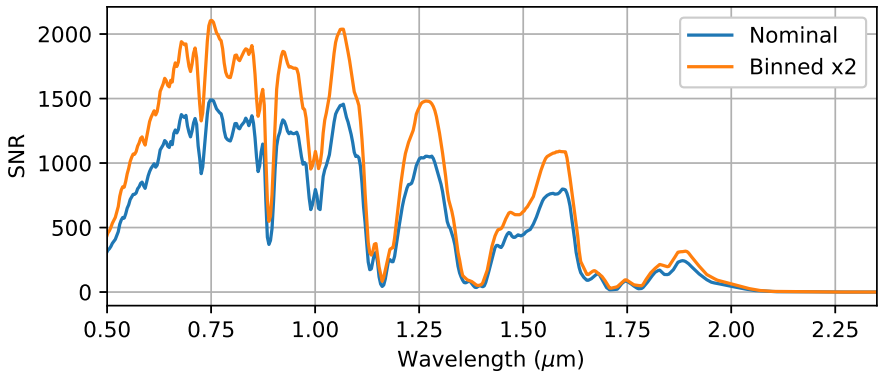

Figure 7.4: SNR of forward simulations of Jupiter's atmosphere with different MAJIS resolutions.

the spectral resolution achieved. A description of the input parameters used for the simulation can be found in Appendix C.

Figure 7.5 compares forward simulations considering the noise extracted from the ratio between the simulated radiance from the radiative transfer model of Jupiter's atmosphere and the SNR from the MAJIS radiometric model. The oversampled spectrum is kept as a reference and does not include noise levels. Due to the high levels of SNR, the noise level is almost not visible in the plot and looks pretty similar to Figure 7.3. Actually, the relative mean difference of the nominal I/F against their minimum and maximum expected values is below 0.2 % in both cases. Some spectral regions were selected to show better the noise level. For instance, there are some parts where the nominal and binned spectra include the expected signal for the oversampling resolution. In other cases, the spectrum is too softened with the binning mode, and some spectral information is lost. Special attention was given to those parts of the spectrum where the I/F is higher than 0.2, as is the case at wavelengths smaller than 0.75 μm. In any way, the high SNR levels achieved by MAJIS will reveal valuable information about the distribution and abundance of compounds in Jupiter's atmosphere, except probably at wavelengths where stray light is confirmed (<0.7 μm).

Taking as reference Figures 6.22 and 6.23, it is possible to identify which spectral signatures observed in the simulated spectra are more affected by the binned x2 resolution. For instance, signatures due to NH_3 absorption are missed at 0.59, 0.61, 0.83 and 1.51 μm, already in the

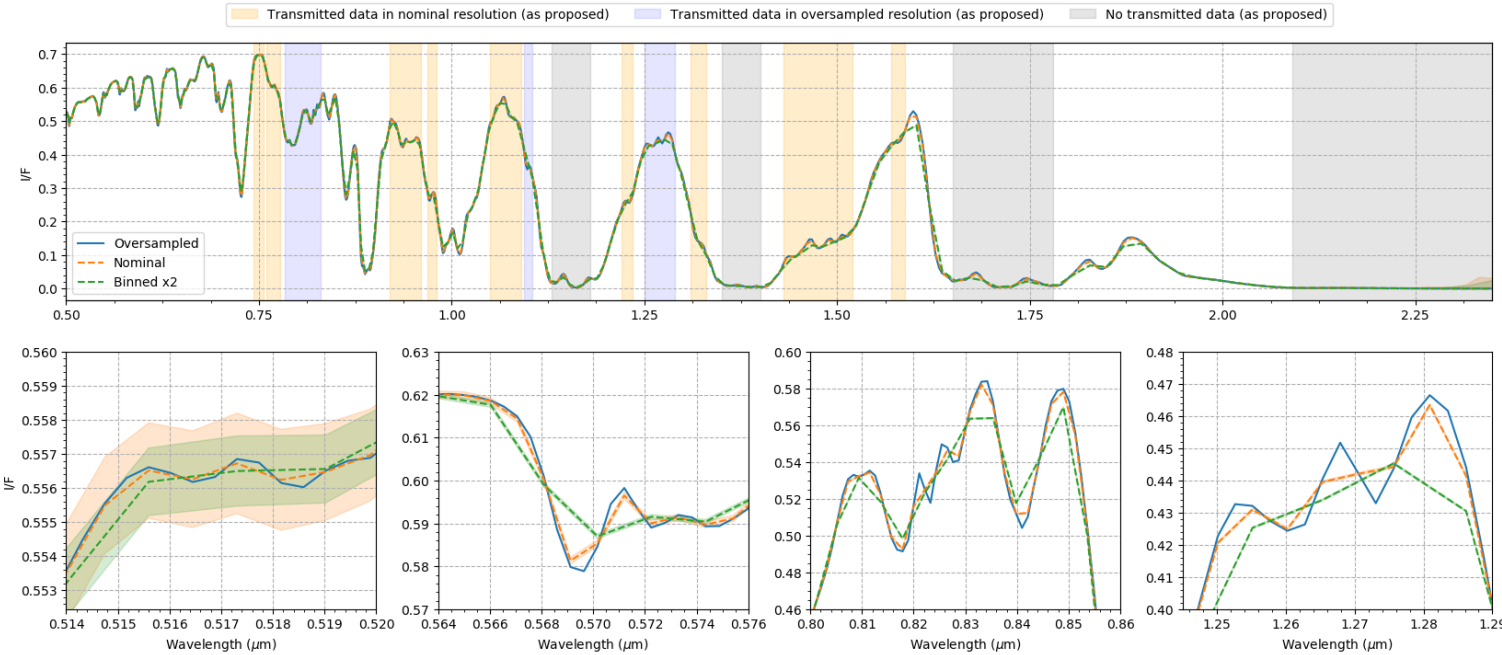

Figure 7.5: Forward simulation of Jupiter's atmosphere with different MAJIS spectral resolution modes including the expected noise level and the proposed spectral mask for daytime observations. The top plot includes the complete VIS-NIR spectral range, while the bottom plots show some spectral regions that highlight the differences between the different spectral resolution modes. The color shadow areas in the top plot correspond to the spectral regions that the new spectral mask proposes to observe at other than binned x2 resolution mode, while the grey areas correspond to proposed spectral regions that could be discarded to reduce data volume.

nominal spectrum. The binned x2 spectrum also misses signatures due to NH_3 absorption at 0.55, 0.63, 0.65, 0.94, and 1.27 μm; and due to CH_4 absorption at 0.89, 0.98, 1.00, 1.12, 1.33, 1.48 and 1.84 μm. The nominal spectrum misses additional spectral signatures at 0.59 and 0.79 μm due to CH_4 and NH_3. Similarly, the signature at 1.94 μm, which could be due to NH_3 or CIA, is also missed by the nominal spectrum. Therefore, the most affected spectral signature by the different spectral resolution modes is NH_3. In this sense, Figure 7.5 also proposes a new default spectral mask for daytime observations, in which some regions are proposed to be observed in oversampled resolution and others in nominal resolution. Appendix D details the wavelength values for the proposed spectral ranges and their main spectral signatures. Note that the impact of stray light has still to be estimated although it does not make part of this work.

The originally defined spectral mask for daytime default observations (Figure 7.3) transmits 91 % of the spectral data in binned x2 resolution and discards 9 % of the data. The spectral mask proposed in this work (Figure 7.5), discards 26.5 % of the data and transmits 54.0 % in binned x2 resolution, 14.3 % in nominal resolution, and 5.2 % in oversampled resolution. The next step consists of assessing the sensitivity of the MAJIS VIS-NIR channel to detect variations in the abundances of the simulated Jupiter's atmosphere, concerning NH_3, CH_4 and the Chromophore Haze (CH) layer of aerosols.

7.5 SENSITIVITY TO DIFFERENT ABUNDANCES

While it is common to use forward modeling to assess sensitivity, for this exercise, ASIMUT-ALVL was used to scale the molecular abundances of different species in Jupiter's atmosphere at the binned x2 spectral resolution of MAJIS. The results obtained for the different molecules are discussed in the following subsections.

7.5.1 *Variation in ammonia (NH_3)*

According to the work of Sromovsky et al. [46], a variation up to 74 % on NH_3 abundance between the South Tropical Zone (STrZ) and the South Equatorial Belt (SEB) of Jupiter is expected. At the STrZ, the NH_3 VMR could oscillate between -12 % and 14 % around its nominal value.

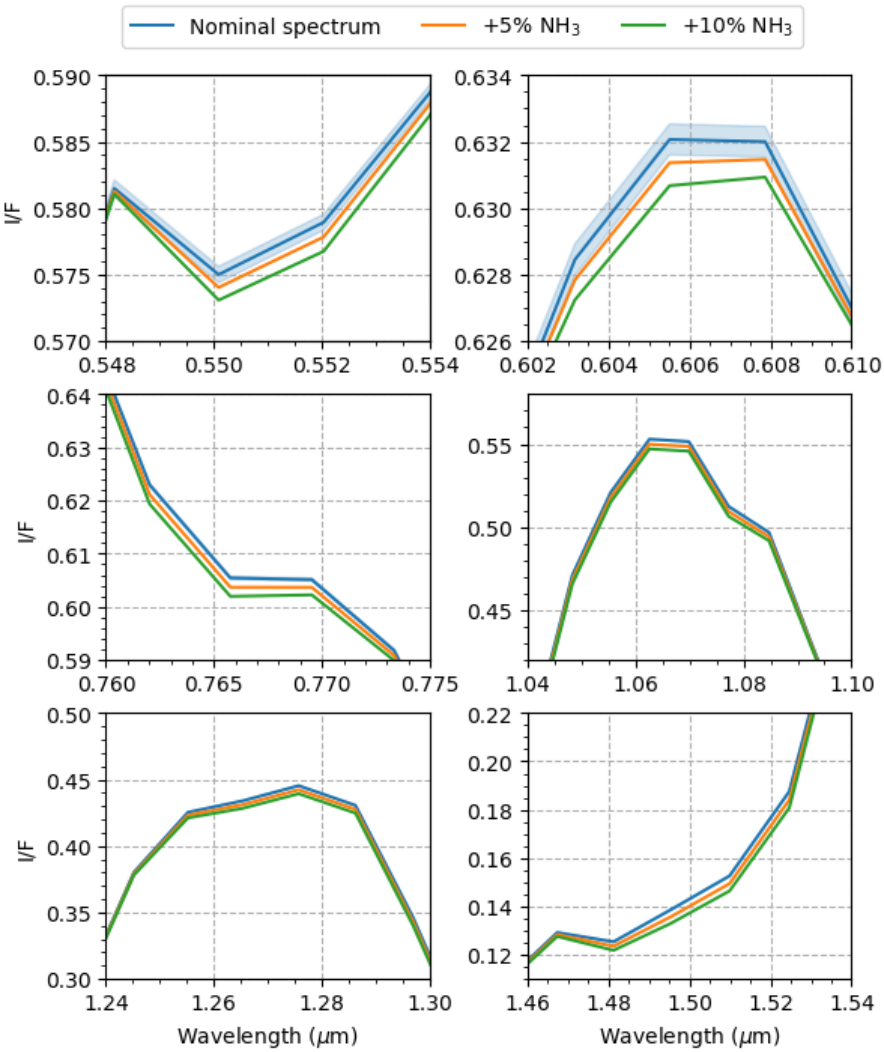

Figure 7.6: MAJIS sensitivity to NH_3 abundance variations of 5 % (orange) and 10 % (green) under the binned x2 spectral resolution mode in the VIS-NIR channel. The nominal abundance of NH_3 in the forward model (blue) includes the expected noise of the measurement. Note that at shorter wavelengths (top), the spectrum corresponding to the 5 % variation of NH_3 abundance is already in the detection limit of MAJIS. However, at the strongest spectral bands due to NH_3 absorption (middle and bottom), it will be possible to discriminate abundance variations up to 5 %.

Similarly, the nominal NH_3 VMR value is expected to vary between -10 % and 11 % at the SEB.

During this work, the abundance of NH_3 was incremented by 5 % and 10 % to assess the limit of variation that MAJIS will detect at the binned x2 spectral resolution, while the rest of the atmosphere was kept as defined in section 7.3. The absorption bands due to NH_3 become stronger than at nominal NH_3 abundance and are noticeable when compared against the simulated spectrum with the nominal Jupiter's atmosphere (Figure 7.6). A mean difference of -8.3$\times 10^{-11}$ in I/F is observed between the spectra obtained from the nominal atmosphere and the one with 10 % more NH_3. The mean difference in I/F corresponds to -4.2$\times 10^{-11}$ concerning the spectrum considering an atmosphere with 5 % more NH_3. Figure 7.6 shows some spectral regions where it is possible to observe that the limit of detection of MAJIS corresponds to the 5 % of the variation in NH_3, especially at its strongest absorption bands.

It is worth mentioning that this test was repeated considering the nominal resolution of MAJIS, and similar differences were observed. Therefore, in nominal or binned x2 spectral resolution, the obtained results suggest that MAJIS will be able to observe spatial variations of NH_3 at the limit of 5 %, which is smaller than the expected variation between different bands and zones ($\sim$12 %) [46].

7.5.2 *Variation in methane (CH_4)*

Since CH_4 constitutes the main molecular contribution in Jupiter's spectrum for VIS-NIR wavelengths, its abundance can be evaluated at several absorption bands in the spectrum and hence at different altitudes. CH_4 abundances are typically considered to vary up to 20 % in Jupiter's atmosphere, as was the case in the work of Sánchez-López et al. [61]. For this work, the abundance of CH_4 was incremented between 2.5 and 10 % to assess the limit of variation that MAJIS will be able to detect. As in the previous analysis, the rest of the atmosphere was kept as defined in section 7.3.

Figure 7.7 shows the resultant simulated spectrum of Jupiter's atmosphere with different abundances for CH_4. A mean difference of -2.8$\times 10^{-10}$ in I/F is observed between the spectra obtained from the nominal atmosphere and the one with 10 % more CH_4. The mean difference in I/F corresponds to -1.4$\times 10^{-10}$ concerning the spectrum considering an atmosphere with 5 % more CH_4. Finally, for an atmosphere with only 2.5 % more CH_4, the mean difference with respect to the nominal spectrum in I/F is -7.3$\times 10^{-11}$. This is the limit of

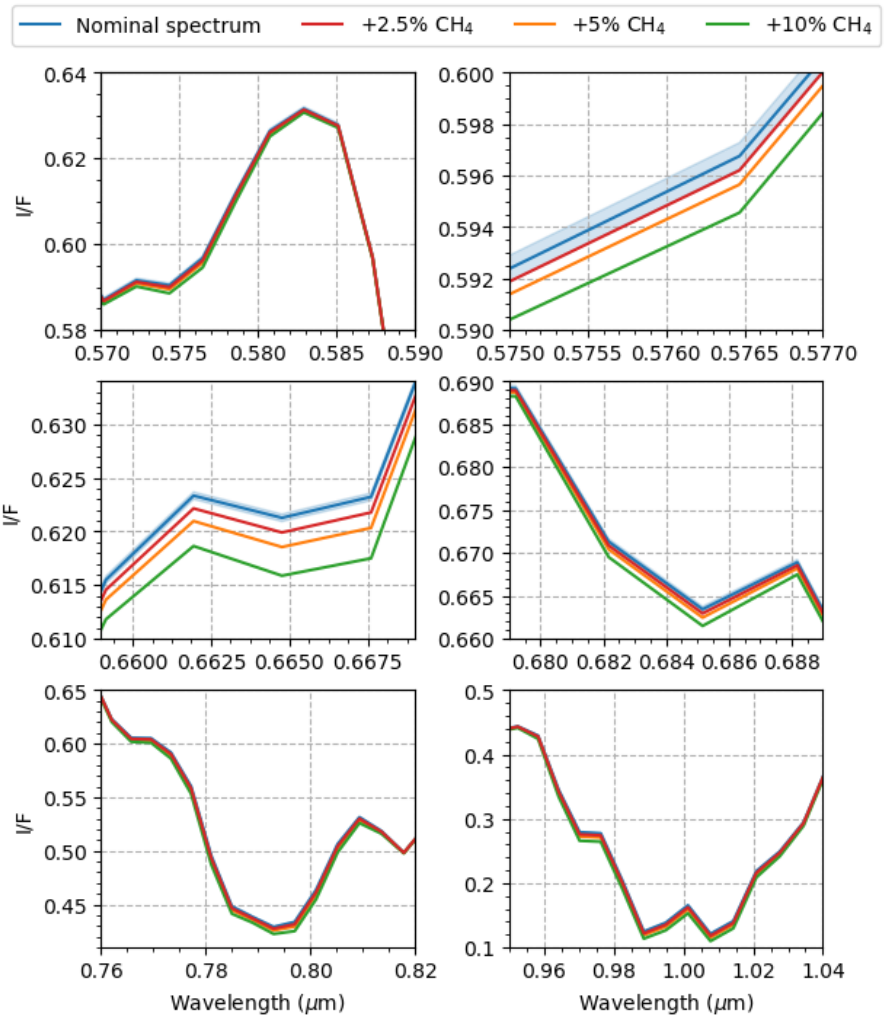

Figure 7.7: MAJIS sensitivity to CH_4 abundance variations of 2.5 % (red), 5 % (orange) and 10 % (green) under the binned x2 spectral resolution mode in the VIS-NIR channel. The nominal abundance of CH_4 in the forward model (blue) includes the expected noise of the measurement. Note that at shorter wavelengths (<0.6 μm), the spectrum corresponding to the 2.5 % variation of CH_4 abundance is already in the detection limit of MAJIS. However, at the strongest spectral bands due to CH_4 absorption, it will be possible to discriminate abundance variations up to 2.5 %.

detection of MAJIS for abundance variations in CH_4, either in MAJIS nominal or binned x2 spectral resolution. Therefore, realistic variations

of CH_4 abundance in Jupiter's atmosphere are expected to be detectable through the MAJIS VIS-NIR channel.

7.5.3 *Variation in the chromophore haze layer*

As discussed in section 6.3.3, the CB model of Baines et al. [31] is contributing to the shape of Jupiter's spectrum only at wavelengths smaller than 1 μm. Therefore, for this analysis, the VIS-NIR spectral range of MAJIS was analyzed between 0.5 and 1 μm. Following the variability reported by Baines et al. [31], the abundance of the chromophore haze is expected to vary between -13 % and +10 %. For this work, the chromophore abundance was incremented between 1 % and 10 % to assess the limit of variation that MAJIS can detect at the binned x2 spectral resolution. The rest of the atmosphere was kept as defined in section 7.3, with the nominal abundances for other aerosol layers.

Figure 7.8 shows the resultant simulated spectrum of Jupiter's atmosphere with different abundances for the chromophore haze. A mean difference of -7.8$\times10^{-10}$ in I/F is observed between the spectra obtained from the nominal atmosphere and the one with 10 % more chromophores. The mean difference in I/F corresponds to -3.9$\times10^{-10}$ concerning the spectrum considering an atmosphere with 5 % more chromophores. Finally, for an atmosphere with only 1 % more chromophores, the mean difference in I/F with respect to the nominal spectrum is -7.9$\times10^{-11}$. This is the limit of detection of MAJIS for abundance variations in the chromophore haze, either in MAJIS nominal or binned x2 spectral resolution. Note that, when compared against the nominal spectrum, the absorption due to higher chromophore abundance is mainly noticeable at wavelengths smaller than 0.7 μm, which is part of the wavelength range affected by stray light in the MAJIS instrument. In any way, MAJIS will be able to detect variations in the chromophore abundance up to 1 %, which is more than what is expected in reality for the chromophores to vary ($\sim$12 %).

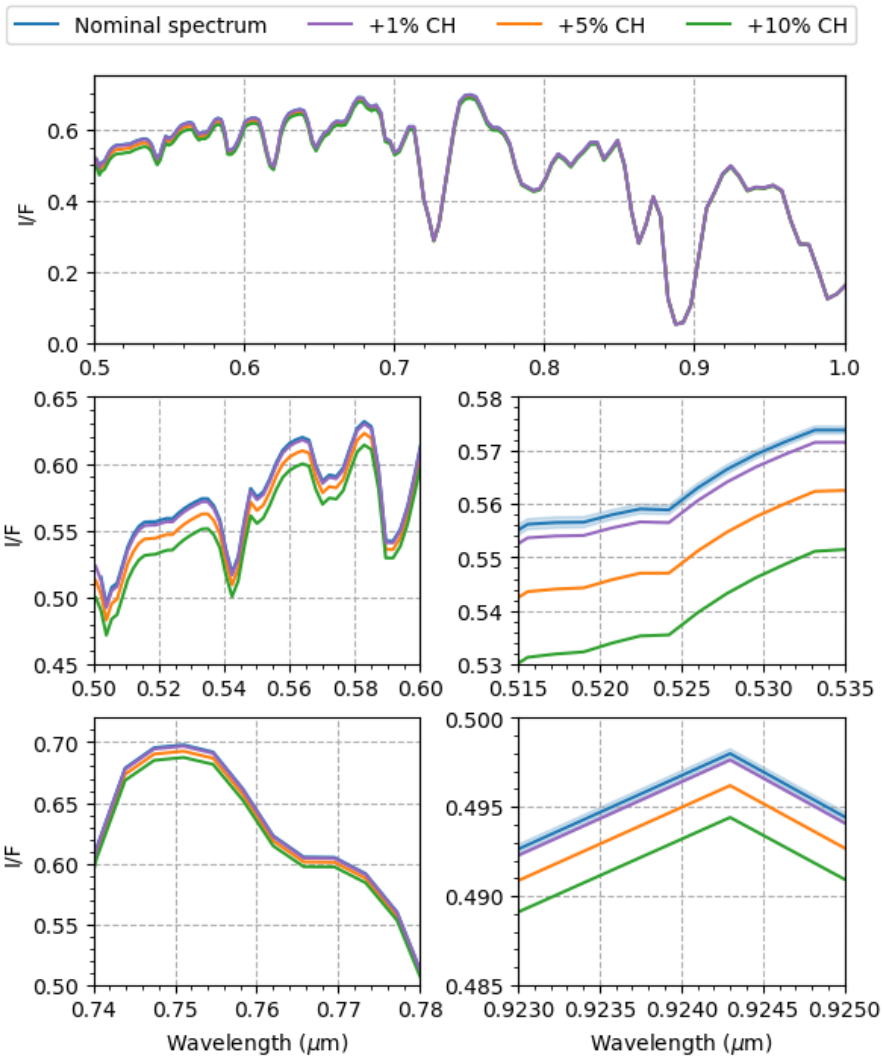

Figure 7.8: MAJIS sensitivity to Chromophore Haze (CH) abundance variations of 1 % (red), 5 % (orange) and 10 % (green) under the binned x2 spectral resolution mode in the VIS-NIR channel. The nominal abundance of CH in the forward model (blue) includes the expected noise of the measurement. Note that at wavelengths close to 1 μm, the spectrum corresponding to the 1 % variation of CH abundance is already in the detection limit of MAJIS. However, at the strongest spectral bands, it will be possible to discriminate abundance variations up to 1 %.

This work demonstrates that the VIS-NIR channel of MAJIS will be sensitive enough to detect the expected abundance variations of NH_3, CH_4, and the aerosols in the chromophore haze, which will contribute to the characterization of Jupiter's atmosphere. As mentioned in part I, constraining molecular abundances at different locations on the planet will reveal information about the dynamics and the mechanisms related to the global circulation of Jupiter compounds in the atmosphere. Moreover, characterizing the variability of aerosols in Jupiter's atmosphere also contributes to the study of the scattering properties of the particles. Finally, if the abundance of different compounds is further constrained, it will be possible to study the potential correlation between them and constrain their origin [62]. A similar analysis should be performed considering variations in the vertical distribution of these compounds in a future step.

7.6 COMPARISON AGAINST PREVIOUS INSTRUMENTS

In this section, different forward simulations were performed as if Jupiter's atmosphere were observed with instruments previous to MAJIS, including Juno/JIRAM [52], Cassini/VIMS [244], and Galileo/NIMS [48]. In this way, it is possible to visually compare the spectral resolution that each instrument would provide under the same geometry of observation (Figure 7.9). Spectral performances can be consulted in section 1.4.

In this analysis, the spectral coverage was limited to 0.5-2.35 μm, although this wavelength range was not covered by all of the instruments. For instance, MAJIS and VIMS are the only instruments that would provide information at wavelengths smaller than 0.7 μm. In this wavelength range, the spectral resolution of the MAJIS VIS-NIR channel is higher than that of the VIMS VIS channel, with a relative mean difference of 2.3 %. At this spectral region, it is possible to reveal several spectral signatures with MAJIS that would not be visible with VIMS. Between 0.7 and 1.0 μm, NIMS would also provide spectral information, although at lower resolution. The relative mean difference between NIMS and MAJIS at this spectral range corresponds to 13.9 %. NIMS notably missed absorption bands due to CH_4, as is the case close to 0.85 and 0.95 μm. MAJIS, VIMS and NIMS spectra look similar above 1 μm despite the different spectral resolution, although the relative mean difference between MAJIS and VIMS is now 3.2 %, and between MAJIS and NIMS 8.5 %. The spectral region between 1

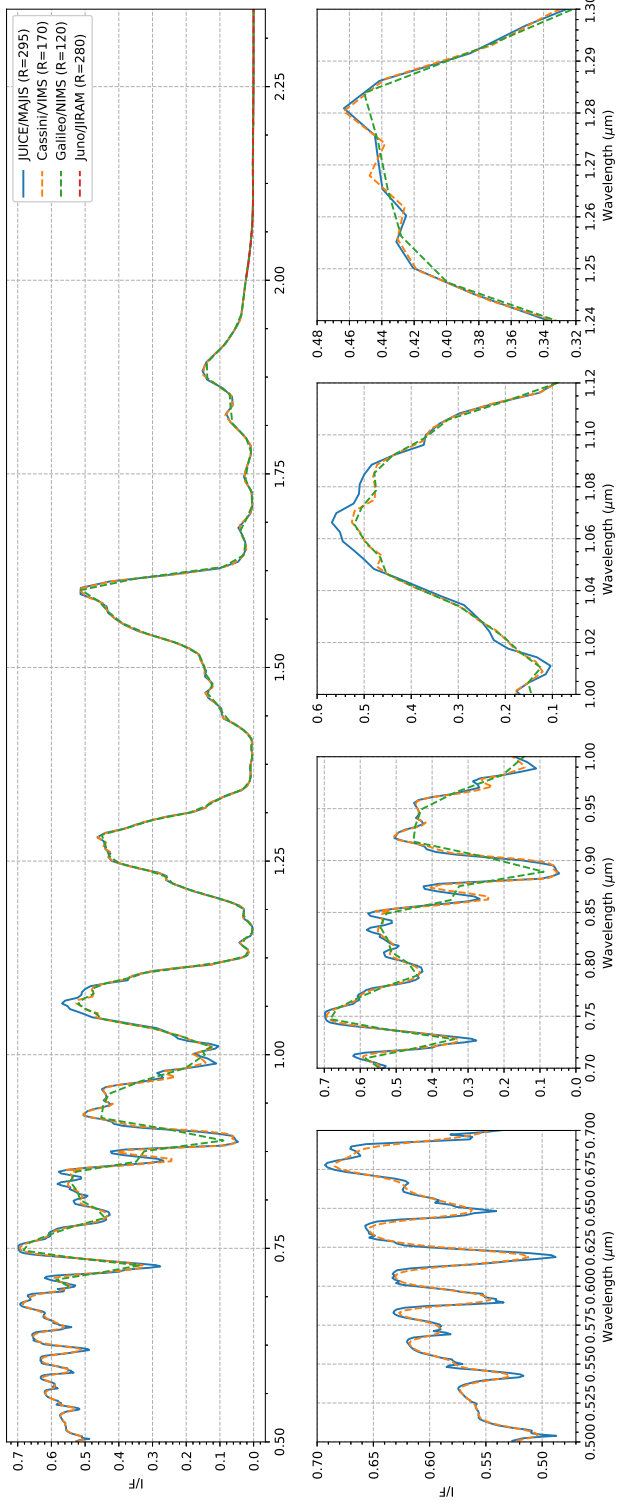

Figure 7.9: Forward simulations of Jupiter's atmosphere as observed with different instruments in their nominal spectral resolution. When the instrument is composed of different channels, the equivalent spectral power is given.

and 1.12 μm is mainly shaped by CH_4 absorption, while the spectral region between 1.24 and 1.30 μm is due to NH_3 absorption. JIRAM provides spectral information only above 2.0 μm, providing a relative mean difference against MAJIS of 12.6 %.

This work demonstrates the capabilities of MAJIS in terms of spectral resolution, which has improved against the capabilities of previous instruments dedicated to the study of Jupiter's atmosphere. In this way, MAJIS will be able to better differentiate between the spectral signatures of different molecules, in comparison with previous instruments. However, it is worth mentioning that the improved capabilities of MAJIS are not defined only by its resolving power but also by the broad spatial coverage due to the different orbit scenarios of the JUICE mission. In this way, it is complementary to the equatorial observations from Galileo and the polar orbits of Juno. Moreover, although MAJIS is more comparable to VIMS, its temporal coverage is larger since VIMS observed Jupiter only during Cassini's journey to Saturn, and did not approach Jupiter as much as JUICE will do.

8 SUMMARY AND CONCLUSIONS

This thesis work focused on the study of the VIS-NIR spectrum of Jupiter's atmosphere and supported technical and scientific activities of the MAJIS/JUICE team. The main purpose of this work included: the characterization of the VIS-NIR detectors of the MAJIS/JUICE instrument and the analysis of its performances for the scientific objectives of MAJIS. Therefore, two main products constitute the results of this work: one facility to characterize astronomical detectors from 0.4 to 2.65 μm, and a radiative transfer model with the current knowledge of Jupiter's atmospheric compounds to perform remote sensing simulations in the VIS-NIR range. In this chapter, a summary of the results and outcomes achieved during this work is presented.

8.1 THE VIS-NIR CHARACTERIZATION FACILITY

The analysis of the performances of the MAJIS instrument would not be possible without the characterization of its individual components and their interaction with radiation, especially at the pressure and temperature conditions to which they will be exposed during the mission. Among the different components of MAJIS, the Focal Plane Units (FPUs) are key in the definition of its final performances. After the careful definition from the MAJIS team of the properties that the detectors should provide, it was critical to confirm these were achieved after their manufacture. For this reason, an extensive characterization of its Quantum Efficiency (QE), Dark Current (DC), linearity, uniformity, Full-Well Capacity (FWC), and noise took place. This work supported the MAJIS team in the characterization of the VIS-NIR FPU and required the development of a characterization facility for this purpose.

As described in part II, the characterization facility was developed from the ground up as versatile as possible, not only to characterize the VIS-NIR detectors of MAJIS but to be used in further characterizations and extend its capabilities, especially for other wavelength ranges. In this way, the developed facility along this thesis work, offers the following capabilities to the scientific community:

- Certified ISO-5 area for the manipulation and characterization of detectors with monitored environmental conditions including temperature of 22±3 °C, relative humidity between 45 % and 65 %, pressure between 900 and 1080 mbar.
- Optical system to provide dark and uniform light conditions to the detector inside the cryostat, with up to 30 different levels of illumination with a stray light rejection of 10^{-8} and a tunable monochromatic beam. Absolute radiometry is also possible and the beam can be interrupted by an electronic shutter in 40 ms when needed.
- Closed cycle cryogenic system to thermalize detectors between 50 and 382 K with a precision of 7 mK and a maximum cooling rate of -0.9 K/min. The system offers up to 6 simultaneous temperature control loops. Detectors should not be larger than 138.5 mm × 106 mm × 111.5 mm.
- Optical and thermal ground support equipment to operate the facility remotely from another lab, except for the adjustment of the slit of the monochromator and the initialization of the cryogenic system.
- Robust security system to prevent vacuum loss, temperature outside allowed limits and overpressure. Monitoring in real-time is possible and status emails can be automatically sent if required. Unexpected events are communicated to the operators by SMS.

One of the main limitations of the facility in its current configuration is the integrating sphere at room temperature. To limit the thermal radiation from the viewport of the vacuum chamber in the field of view of the detector, cold Short-Wave Pass Filters (SWPFs) were implemented inside the vacuum chamber. Therefore, to extend the functionality of the facility to infrared wavelengths, it would be necessary to cool down other optical parts of the system, especially the integrating sphere. In this case, the use of vacuum-compatible photodiodes would be necessary as well. Moreover, by replacing the gratings of the monochromator, the facility could extend to ultraviolet (UV) wavelengths. In a later stage, a continuous level of illumination could be provided by replacing the Neutral Density (ND) filters with polarizers, but an additional system to avoid raising their temperature due to the power of the lamp should be considered.

During this work, the VIS-NIR characterization facility was developed and validated during 2018-2020 when the *Centre Nationale d'Études Spatiales* (CNES) approved its use for the characterization of the Flight Model (FM) of the MAJIS VIS-NIR detectors. I was mainly in charge of the cryogenic and security systems, including the preservation of the cleanliness level of the working environment and the training of the operators who participated in the installation of the FM FPU. Later in 2021, the facility was used to characterize the Spare Model (SM) of the FPU. Despite the stray light issues encountered in the first phases of the characterization facility, the MAJIS VIS-NIR detectors were successfully characterized and their measured performances allowed the development of the radiometric model of MAJIS [252], after the calibration of the instrument. The performances of the VIS-NIR detectors met the requirements defined by the science team although, at the instrument level, stray light affects the performances of the VIS-NIR channel between 0.6 and 0.7 μm.

After its use on the MAJIS project, the facility was used to support the thermal characterization of the GRAvimeter for Small Solar system bodies (GRASS) mission [134] in September 2023. An additional update to the facility is currently taking place to provide radiative cooling capabilities and perform thermal tests of the Comet Interceptor mission [83, 253]. Moreover, the heritage of the optical system of the facility was used for the characterization of the UV and visible (VIS) detectors of the Atmospheric Limb Tracker for Investigation of the Upcoming Stratosphere (ALTIUS) [254] mission, at room temperature. The test included QE, DC, linearity, and Photo-Response Non-Uniformity (PRNU) [83]. In this way, the facility constitutes a useful instrument that continued growing in versatility to support optical and thermal tests for new space missions with their particular requirements.

8.2 THE RADIATIVE TRANSFER MODEL OF JUPITER'S ATMOSPHERE

To generate spectra of Jupiter's atmosphere, as they will be observed by the VIS-NIR channel of MAJIS/JUICE, a radiative transfer model of Jupiter for wavelengths between 0.5 and 2.35 μm is required. During this work, the most updated knowledge of the different spectral contributions of Jupiter's atmosphere at the VIS-NIR spectral range was included in a radiative transfer model, which can be used by the scientific community as a fully validated tool in addition to KOPRA, NEMESIS and the Planetary Spectrum Generator (PSG). Moreover, it

provides BIRA-IASB with the opportunity to continue supporting the MAJIS science team in the assessment of observations and planning tasks, in preparation for the arrival of the JUICE mission in 2031.

The implementation and validation of the necessary functions and capabilities to constitute a complete VIS-NIR forward model of Jupiter's atmosphere, part of the existing radiative transfer tool ASIMUT-ALVL, took place between 2021-2023. During this time, the main contributions to the VIS-NIR spectrum of Jupiter were identified and studied from the approaches adopted by different authors. The model was validated against KOPRA and observational data from VIMS/Cassini. In the course of this work, I identified missing tools and developed them. Among them, it is possible to list the following ones:

- Reference Jupiter's atmospheric file based on the works of Moses et al. [4] and Seiff et al. [29] for the temperature profile, and González et al. [196] for the atmospheric composition.
- Look Up Tables (LUT) with the absorption cross-sections of CH_4, NH_3 and H_2O, the main molecules constituting Jupiter's atmosphere, after H_2 and He. Information for CH_4 is mainly taken from the band model of Karkoschka et al. [198], although cross-sections from ExoMol (Yurchenko et al. [199]) and generated from the HITRAN database [158] are also available. NH_3 and H_2O cross-sections come also from ExoMol, corresponding to the works of Coles et al. [214] and Polyansky et al. [217], respectively. For H_2O, the recommended dataset is generated from HITRAN [158] line lists, based on the recent work of Conway et al. [215]. All LUTs consider H_2 and He broadening parameters and cover the pressure and temperature conditions found in Jupiter's atmosphere.
- Python routine to obtain LUTs from correlated *k*-tables.
- Rayleigh scattering calculated from the refractive index of Jupiter's atmosphere, which is determined from the refractivities of H_2 (Peck & Huang [224]) and He (Mansfield & Peck [225]).
- Computation of the scattering parameters of aerosols possibly present in Jupiter's atmosphere based on Mie scattering theory and considering lognormal and gamma Particle Size Distributions (PSDs). The refractive indexes of different compounds were analyzed, including those constituting the aerosols *Crème Brulée* (CB)

model of Baines et al. [31] (<1 μm) and the aerosols proposed by López-Puertas et al. [26].

- Collision Induced Absorption (CIA) due to H_2-H_2 and H_2-He were implemented as simple cross-sections based on the works of Borysow [233] (<1 μm), Abel et al. [236] and Abel et al. [237].

Additionally during this work, the new version of ASIMUT-ALVL was already used to assess the definition of spectral masks, necessary to optimize the downlink capabilities of MAJIS. After the beginning of the science operations of the instrument, MAJIS will be able to map Jupiter's atmosphere at different latitudes and characterize the distribution of the atmospheric compounds on a local and global scale, including aerosols and their variability. Since the resulting levels of Signal-to-Noise Ratio (SNR) of MAJIS overpassed the requirements by one order of magnitude (from ∼100 to ∼1000), it will be possible to discriminate spectral signatures due to CH_4, NH_3 and H_2O absorption in the VIS-NIR range. Therefore, a new default spectral mask for daytime observations of Jupiter's atmosphere was proposed in this work. It combines the different spectral resolution modes offered by MAJIS and extends the amount of discarded spectral data to reduce data volume.

Moreover, the expected detection limits of the VIS-NIR channel of MAJIS were assessed at the binned x2 spectral resolution in this work. Therefore, during the closest approaches of the JUICE mission to Jupiter, MAJIS will be sensitive to abundance variations of up to 5 % for NH_3, 2.5 % for CH_4 and 1 % for the Chromophore Haze (CH) layer defined by the CB aerosols model of Baines et al. [31], between 0.5 and 2.35 μm. Thanks to these limits, realistic abundance variations of such compounds, which are expected to be between 10 and 20 %, will be available for MAJIS at their nominal and binned x2 spectral resolution. Naturally, other environments than the Great Red Spot (GRS) must be considered in the simulations, as their composition differs within the mentioned ranges. Therefore, similar analysis with Cassini/VIMS data can be performed in further stages to validate the forward model at other locations and assess the impact of H_2O.

The MAJIS VIS-NIR nominal spectral capabilities were also compared to previous instruments in this work, for the same geometry of observation, finding relative mean differences of 2.5 % with respect to Cassini/VIMS [244], 11 % with respect to Galileo/NIMS [48], and 13 % with respect to Juno/JIRAM [52].

Additional improvements can still be implemented in ASIMUT-ALVL. For instance, the proper computation of CIA considering cross-sections dependent on temperature and pressure, and the implementation of the new data from Vitali et al. [235], which was not available during the development of this work. The expansion of the CB model for near-infrared (NIR) wavelengths, especially for the study of chromophores in Jupiter's atmosphere. A starting point can be based on the work of Sromovsky et al. [46], who explored the possibility of using this model to reproduce the spectra of regions with fresh NH_3 clouds. This is necessary to support the MAJIS science team with the definition of browsing products, which so far were defined without a realistic MAJIS resolution and covering wavelengths only above 2 μm. Moreover, extending the radiative transfer model for the coverage of the wavelengths sensitive to the MAJIS IR channel is also of interest. The spectral information that can be extracted from both spectral channels is complementary and thus necessary to constrain atmospheric abundances and aerosols properties at the different locations of the planet. Covering IR wavelengths, with the radiative transfer model presented as one of the main products of this work, will require the addition of molecules such as phosphine (PH_3) and arsine (AsH_3), as well as an extended model of aerosols.

Thanks to this research work, it is possible to conclude that the improved spectral capabilities of the VIS-NIR channel of the MAJIS/JUICE instrument, in comparison to those of previous instruments, will be able to address the scientific objectives of the mission, even at the binned x2 spectral resolution, and especially concerning the characterization of Jupiter's atmospheric abundances and composition. Constraining the abundance of atmospheric compounds contributes to the study of the spatial distribution of molecules and aerosols, which allows the understanding of the dynamics and the mixing mechanisms in the atmosphere. The spectral resolution of MAJIS will allow the distinction of spectral features in Jupiter spectra that can be further analyzed to understand their origin.

This analysis would not have been possible without the realization of the main objectives of this work, which included the development of a facility to characterize the VIS-NIR detectors of MAJIS, and the development of a radiative transfer model of Jupiter's atmosphere validated for wavelengths between 0.5 and 2.35 μm. Both the charac-

terization facility and the radiative transfer model are available to the scientific community for their further use. As previously described, the characterization facility was already used for other space projects and continues growing in versatility mainly expanding spectral and temperature coverage. In parallel, ASIMUT-ALVL can now be used to continue supporting the MAJIS team in the definition of additional browsing products related to the VIS-NIR spectrum of Jupiter's atmosphere, and can additionally be expanded to IR wavelengths by including spectral data related to further molecules, aerosol models and CIA.

APPENDICES

A

PARTICLE SIZE DISTRIBUTIONS

Particle Size Distributions (PSDs) are probability density functions $f(r)$, typically normalized, that mathematically approximate the number density of particles $N(r)$ with an interval of radii r values [168, 174]:

$$PSD(r) = Nf(r) = \frac{dN(r)}{dr} \tag{A.1}$$

The total number density N is obtained after integrating for all sizes:

$$N = \int_0^\infty \frac{dN(r)}{dr}\, dr = \int_0^\infty PSD(r)\, dr \tag{A.2}$$

PSDs are characterized by the different *moments* of the function, defined as follows:

$$m_{(i)} = \int_0^\infty r^{(i)} PSD(r)\, dr \tag{A.3}$$

where i corresponds to the i-th moment of the PSD. Depending on the distribution used, the moments will be different, except for the o-th moment of the PSD, which always corresponds to N. Other parameters such as the *mean* or the expected value of the distribution r_m, and the *variance* or the expected deviation from the mean value s^2, can be defined from the moments of any function:

$$r_m = \langle r \rangle = \frac{\int_0^\infty rPSD(r)\, dr}{\int_0^\infty PSD(r)\, dr} = \frac{m_1}{m_0} \tag{A.4}$$

$$s^2 = \langle (r - r_m)^2 \rangle = \frac{m_2 - m_1^2}{m_0} \tag{A.5}$$

However, these parameters should be related to the scattering properties of particles, depending on the type of PSDs that describe them. Hansen & Travis [168] defined useful variables that are independent of the functional form of the PSD: r_{eff} and v_{eff}.

The *effective radius* r_{eff} of the distribution is defined from the ratio between the integrated volume of the particle V and the surface area of the spherical particle S_p, to be related to the extinction cross-section of the particle [174]:

$$r_{eff} = \frac{\langle 3V \rangle}{\langle S_p \rangle} = \frac{\langle r^3 \rangle}{\langle r^2 \rangle} = \frac{m_3}{m_2} \tag{A.6}$$

while v_{eff} corresponds to the *effective variance* of the distribution and is unitless:

$$v_{eff} = \frac{\langle \pi r^2 (r - r_{eff})^2 \rangle}{\langle N \pi r^2 r_{eff}^2 \rangle} = \frac{m_2 m_4}{m_3^2} - 1 \tag{A.7}$$

Lognormal and gamma distributions are often used to describe aerosols PSDs, as was the case in this work. Since analytical relations can be derived between r_{eff} and r_m, and between v_{eff} and s, for different PSDs, their corresponding functions and relations will be described in the next sections.

Additionally in this work, numerical integrations over the PSDs were performed to provide the scattering parameters of the different aerosols. Therefore, the PSDs were limited by defining a minimum and maximum radius (respectively r_{min} and r_{max}), in terms of the standard deviation s of the distribution. For this work, we consider $4s$ (99.994 %) of the particle radii in the PSD.

By considering the *Cumulative Distribution Function* (CDF) of any distribution, it is possible to provide the probability for a variable to take a value less than or equal to a certain value, in this case r_{min} or r_{max}:

$$CDF(r_{min}) = \int_{-\infty}^{r_{min}} f(r)\, dr \tag{A.8}$$

$$CDF(r_{max}) = \int_{-\infty}^{r_{max}} f(r)\, dr \tag{A.9}$$

In this way, r_{min} corresponds to a certain probability q value of the CDF, and r_{max} to $1 - q$. The resultant interval of $1 - 2q$ between r_{min} and r_{max} corresponds to the part of the CDF relevant for the PSD:

$$CDF(r_{max}) - CDF(r_{min}) = 1 - 2q \tag{A.10}$$

A.1 LOGNORMAL DISTRIBUTION

The log-normal distribution is a right-skewed continuous probability density function constructed from a normal distribution in a logarithmic scale:

$$PSD(r) = \frac{N}{rs\sqrt{2\pi}} e^{-\frac{1}{2}\left[\frac{\ln(r/r_m)}{s}\right]^2} \tag{A.11}$$

$$r_{eff} = r_m e^{\frac{5}{2}s^2} \tag{A.12}$$

$$v_{eff} = e^{s^2} - 1 \tag{A.13}$$

The CDF of a normal distribution is given by:

$$CDF(r) = \frac{1}{2}\left[1 + \Phi\left(\frac{r - r_m}{s\sqrt{2}}\right)\right] \tag{A.14}$$

where Φ refers to the *error function*, which directly describes the probability that a random variable r falls in a determined range of the distribution ($[r_{min}, r_{max}]$):

$$r_{min} = r_m - n_s s \tag{A.15}$$

$$q = CDF(r_{min}) = \frac{1}{2}\left[1 - \Phi\left(\frac{-n_s}{\sqrt{2}}\right)\right] \tag{A.16}$$

The CDF of the lognormal distribution is defined as:

$$CDF(r) = \frac{1}{2}\left[1 + \Phi\left(\frac{\ln(r/r_m)}{s\sqrt{2}}\right)\right] \tag{A.17}$$

where r_{min} and r_{max} are derived after constructing expressions equivalent to equation A.15 in a logarithmic scale:

$$r_{min} = r_m e^{-n_s s} = r_m e^{s\sqrt{2}\Phi^{-1}(2q-1)} \tag{A.18}$$

$$r_{max} = r_m e^{n_s s} = r_m e^{s\sqrt{2}\Phi^{-1}(1-2q)} \tag{A.19}$$

A.2 GAMMA DISTRIBUTION

The gamma distribution used in this work is actually the generalized gamma distribution introduced in 1963 to represent PSDs for Earth's atmosphere [168]:

$$PSD(r) = \frac{N(ab)^{(2b-1)/b}}{\Gamma\left[(1-2b)/b\right]} r^{(1-3b)/b} e^{-r/ab} \tag{A.20}$$

where Γ corresponds to the *ordinary gamma function*[1] evaluated in the given variables, a corresponds to r_{eff} and b to v_{eff}.

$$r_m = r_{eff}(1 - 2v_{eff}) \tag{A.21}$$

$$s^2 = r_{eff}^2 v_{eff}(1 - 2v_{eff}) \tag{A.22}$$

The CDF of the gamma distribution is defined in terms of the *incomplete gamma function*[2], as it is not defined up to infinity:

$$CDF(r) = \gamma(\alpha, r\beta) \tag{A.23}$$

$$r_{min} = \frac{1}{\beta}\gamma^{-1}(\alpha, q) \tag{A.24}$$

$$r_{max} = \frac{1}{\beta}\gamma^{-1}(\alpha, 1 - q) \tag{A.25}$$

where α corresponds to the *shape* parameter of the gamma distribution, and β to the *rate* of the distribution, defined as follows:

$$\alpha = \frac{1 - 2b}{b} \tag{A.26}$$

$$\beta = \frac{1}{ab} \tag{A.27}$$

1 $\Gamma(z) = \int_0^\infty t^{z-1}e^{-t}\,dt$, where z is a complex number with positive real part
2 $\gamma(z, x) = \int_0^x t^{z-1}e^{-t}\,dt$, where $0 < x < \infty$

B

INPUT FILE FOR ASIMUT-ALVL

ASIMUT (Atmospheric Spectra Inversion Modular Utility Tool) is a radiative transfer program for planetary atmospheres, developed by the Royal Belgian Institute for Space Aeronomy (BIRA-IASB) [152], and extensively used to characterize the atmospheres of Earth [179], Mars [180] and Venus [181]. During this work, ASIMUT-ALVL was updated to include the possibility of modeling Jupiter's atmosphere as well. An example of a typical input file for a nadir simulation, such as those used to assess the MAJIS VIS-NIR capabilities in chapter 7, is given hereafter. Details of each definition can be found in [151].

```
[Set]
zType                       = File
zScale                      = CremeBrulee_zScale.dat
nbSpectra                   = 1

[Planet]
Planet                      = jupiter
RefractiveIndex             = jupiter

[SP1]
FenList                     = [1,2]
DataType                    = radiance
Geometry                    = nadir
source                      = planet
HObs                        = 708779.5815
IncludeSolarSource          = yes
Sun_sza                     = 36.24
Refraction                  = no
NeglectThermalSource        = yes
NeglectThermalReflection    = yes
resolution                  = 38
step                        = 16
ils                         = gaussian
```

```
[SP1_FEN1]
pass                    = 1
wavemin                 = 9091
wavemax                 = 20000
snr                     = 100
molecules               = CH4_Karkoschka2010, NH3_TauREx,
                          H2O_HITRAN
FitMolecules            = [0 0 0]
AprioriMolecules        = [model model model]
rayleigh                = yes
Ts                      = 0
Albedo                  = 0
RTstreams               = 24
CrossSections           = H2H2b, H2HeA
aerosols                = StratosphericHaze, ChromophoreHaze,
                          TroposphericCloud
filelidortflags         = Lidort_LogicFlags_f90.inp
filelidortlog           = lidortlog.txt

[SP1_FEN2]
pass                    = 1
wavemin                 = 4255
wavemax                 = 9091
snr                     = 100
molecules               = CH4_TauREx, NH3_TauREx, H2O_HITRAN
FitMolecules            = [0 0 0]
AprioriMolecules        = [model model model]
rayleigh                = yes
Ts                      = 0
Albedo                  = 0
RTstreams               = 24
CrossSections           = H2H2a, H2HeA
aerosols                = StratosphericHaze, ChromophoreHaze,
                          TroposphericCloud
filelidortflags         = Lidort_LogicFlags_f90.inp
filelidortlog           = lidortlog.txt

[Solar]
FileSolar               = Solar_irradiance_ACESOLSPEC_2015.dat
```

```
[AtmosphericModels]
model                   = 0
atmFile                 = Galileo+LopezPuertas/LopezPuertas+
                          Seiff1998a+H2H2+H2He_res.dat
atmFileType             = col
zptType                 = std
density                 = nowater

[Continua]
Rayleigh                = jupiter

[Molecules]
fileHitran              = HITRAN2016.par

[CH4_Karkoschka2010LP]
DBname                  = CH4
isotope                 = 999
model                   = 0
type                    = lut
File                    = LUT-CH4_Karkoschka2010-IR_MeanVMR_
                          Galileo+LopezPuertas.h5
FBord                   = 50
fact                    = 1

[CH4_TauRExLP]
DBname                  = CH4
isotope                 = 999
model                   = 0
type                    = lut
File                    = LUT_CH4_TauREx_2024.h5
FBord                   = 50
fact                    = 1

[NH3_TauRExLP]
DBname                  = NH3
isotope                 = 999
model                   = 0
type                    = lut
File                    = LUT_NH3_TauREx.h5
FBord                   = 50
```

```
fact                    = 1

[H2O_HITRANLP]
DBname                  = H2O
isotope                 = 999
model                   = 0
type                    = lut
File                    = Jupiter_LUT_H2O_full_T20_dT5_dnu1.
                          0_SminNone_dp20_compress.h5
FBord                   = 50
fact                    = 1

[H2H2aXS]
ATMname                 = H2
File                    = CIA/HITRAN/H2-H2_Main/H2-H2_2011_2
                          00K_cm2.dat
type                    = ascii
model                   = 0
function                = Nearest
Temperature             = [200]

[H2H2bXS]
ATMname                 = H2
File                    = CIA/Borysow/H2-H2_CIA_LT-Borysow_1
                          50K_cm2.dat
type                    = ascii
model                   = 0
function                = Nearest
Temperature             = [150]

[H2HeAXS]
ATMname                 = H2
File                    = CIA/HITRAN/H2-He_Main/H2-He_2011_2
                          00K_cm2.dat
type                    = ascii
model                   = 0
function                = Nearest
Temperature             = [200]

[H2HeBXS]
```

```
ATMname          = H2
File             = CIA/LopezPuertas/H2He/H2-He_CIA_LopezPuert
                   as_160K_cm2.dat
type             = ascii
model            = 0
function         = Nearest
Temperature      = [160]

[StratosphericHazeAER]
type             = LidortG
scattering       = 1
NbLegendreCoef   = 100
NaerType         = File
Naer             = Chromophores/Number_Densities/Baines2019_t
                   0.074_P40mbar_r0.25um_1.4+i0_Fit.dat
gFileName        = Chromophores/1.4+i0_gamma_reff0.25um+veff0
                   .1/RI_Carlson2016_i0_extBaines_gamma_reff0
                   .25um_LidortG_veff0.1.dat

[ChromophoreHazeAER]
type             = LidortG
scattering       = 1
NbLegendreCoef   = 100
NaerType         = File
Naer             = Chromophores/Number_Densities/Baines2019_t
                   0.194_P212mbar_r0.141um_Carlson2016_Fit.dat
gFileName        = Chromophores/Carlson2016_gamma_reff0.141um
                   +veff0.1/RI_Carlson2016_extBaines_log+_gam
                   ma_reff0.141um_LidortG_veff0.1.dat

[TroposphericCloudAER]
type             = LidortG
scattering       = 1
NbLegendreCoef   = 100
NaerType         = File
Naer             = Chromophores/Number_Densities/Baines2019_t
                   28.5_P3940mbar_r1.08um_1.4+i0_Fit.dat
gFileName        = Chromophores/1.4+i0_gamma_reff1.08um+veff0
                   .1/RI_Carlson2016_i0_extBaines_gamma_reff1
                   .08um_LidortG_veff0.1.dat
```

C

INPUT PARAMETERS FOR MAJIS SNR SIMULATOR

The MAJIS SNR simulator is a tool developed by the *Institut d'Astrophysique Spatiale (IAS)* and distributed to the MAJIS science team to support the science planning during the mission, by providing the de-spiking strategy compliant with the MAJIS onboard software and the expected Signal-to-Noise Ratio (SNR) of any observation [252]. Specifically, the tool is able to simulate observations of different targets, including satellite surfaces, Jupiter's atmosphere, exospheres, and Jupiter's rings. Moreover, various conditions of radiance, dwell time, number of spatial pixels along the field of view (referred to as PPE), phase angles, instrument temperatures, and impact rate because of the jovian radiation environment, can be considered, based on actual performances of the instrument. With the MAJIS SNR simulator, it is possible to optimize instrument parameters such as de-spiking strategies, spectral editing, spatial sampling, frame binning, integration time, among other parameters [252].

For this work, the executable application was used in *Manual Observation* mode, in which the user can define a radiance file and modify each of the required inputs step by step. The radiance file was generated with the updated version of ASIMUT-ALVL for a defined MAJIS observation geometry (section 7.2). The radiance must be given in $W/m^2/sr/\mu m$, and the wavelength in nanometers.

Hereafter, there is the definition of the input parameters defined for the simulations performed during this work. The geometrical parameters do not need to be specified, as they should be already considered in the radiance file. The wavelengths observed are considered values to propose de-spiking strategies, the wavelength of the simulation is given by the wavelength range defined by the radiance file.

```
Target:                          Jupiter
VIS-NIR impact rate:             0.015 (default value)
IR impact rate:                  0.0235 (default value)

[Environmental parameters]
OH temperature (K):              126
```

```
FPA VI temperature (K):          126
FPA IR temperature (K):          88

[Instrumental parameters]
PPE:                             400 (default value)
CU-TREP (ms):                    2100 (recommended value)
Spatial binning:                 1

[Geometrical parameters]
Phase angle:                     0
Incidence angle:                 0
Emergence angle:                 0

[Wavelengths observed]
VIS-NIR wavelengths (nm):        1000-1900
IR wavelengths (nm):             2200-2320

[Radiance files]
1. 241023-MAJIS_NL_Ray+B2019C+3mol+2CIAcm2_NS.txt
2. 241023-MAJIS_NL_Ray+B2019C+3mol+2CIAcm2_BS.txt

[Chosen de-spiking strategies (VIS-NIR channel)]
1. SNR (1.0um):                  795
   SNR (1.9um):                  209
   Resid. Spik. (%):             0.08
   FWC (%):                      54
2. SNR (1.0um):                  771
   SNR (1.9um):                  205
   Resid. Spik. (%):             0.08
   FWC (%):                      54
```

D

PROPOSED SPECTRAL MASK

Wavelength range (μm)	Resolution mode	Main contribution
0.500 - 0.743	Binned x2	CH_4, continuum
0.743 - 0.756	Nominal	CH_4
0.756 - 0.760	Binned x2	CH_4, NH_3
0.760 - 0.777	Nominal	CH_4, NH_3, H_2O
0.777 - 0.784	Binned x2	CH_4, NH_3, H_2O
0.784 - 0.830	Oversampled	H_2O
0.830 - 0.920	Binned x2	CH_4
0.920 - 0.960	Nominal	NH_3
0.960 - 0.968	Binned x2	NH_3
0.968 - 0.980	Nominal	NH_3, CH_4
0.980 - 1.050	Binned x2	CH_4
1.050 - 1.090	Nominal	NH_3
1.090 - 1.094	Binned x2	CH_4
1.094 - 1.104	Oversampled	NH_3
1.104 - 1.130	Binned x2	CH_4
1.130 - 1.180	Not transmitted	-
1.180 - 1.220	Binned x2	CH_4
1.220 - 1.235	Nominal	CH_4, NH_3
1.235 - 1.250	Binned x2	CH_4, NH_3
1.250 - 1.290	Oversampled	NH_3
1.290 - 1.310	Binned x2	CH_4
1.310 - 1.330	Nominal	CH_4
1.330 - 1.350	Binned x2	CH_4
1.350 - 1.400	Not transmitted	-
1.400 - 1.430	Binned x2	CH_4
1.430 - 1.520	Nominal	CH_4, NH_3

1.520 - 1.570	Binned x2	CH_4, NH_3
1.570 - 1.588	Nominal	NH_3
1.588 - 1.650	Binned x2	CH_4
1.650 - 1.780	Not transmitted	-
1.780 - 2.090	Binned x2	CIA
2.090 - 2.350	Not transmitted	-

E

LIST OF PUBLICATIONS

All the publications authored during this PhD thesis are listed below, including a summary of the main specific contributions performed (see italics). Moreover, several internal documents were written in the frame of the MAJIS VIS-NIR detectors characterization, including procedures, technical notes, reports and design diagrams. These documents were distributed among the *Institut d'Astrophysique Spatiale (IAS)* and the European Space Agency (ESA) and are kept as a reference for the activities performed.

E.1 PEER-REVIEWED PUBLICATIONS

- **M. E. Cisneros González**, J. Erwin, D. Grassi, F. Poulet, S. Robert. Assessment of MAJIS/JUICE VIS-NIR channel for future observations. (In preparation): *M. E. Cisneros González developed the VIS-NIR forward model of Jupiter's atmosphere, and implemented the aerosols model of Sromovsky et al. [46] in ASIMUT-ALVL.*

- Y. Langevin, F. Poulet, G. Piccioni, G. Filacchione, C. Dumesnil, A. Barbis, J. Carter, P. Haffoud, L. Tomassi, M. Vincendon, ..., **M. Cisneros**, +10 contributors. Calibration of MAJIS (Moons And Jupiter Imaging Spectrometer): IV. Radiometric calibration. *Review of Scientific Instruments*, 95:111301, November 2024. [doi: 10.1063/5.0202702]: *M. Cisneros performed the preliminary analysis of the thermal behavior of the MAJIS VIS-NIR FPU, and participated in the characterization of the MAJIS VIS-NIR detectors, together with the development and validation of the VIS-NIR characterization facility.*

- F. Poulet, G. Piccioni, Y. Langevin, C. Dumesnil, L. Tommasi, V. Carlier, G. Filacchione, M. Amoroso, A. Arondel, E. D'Aversa, ..., **M. Cisneros González**, +77 contributors. Moons and Jupiter Imaging Spectrometer (MAJIS) on Jupiter Icy Moons Explorer (JUICE). *Space Science Reviews*, 220:27, March 2024. [doi: 10.1007/s11214-024-01057-2]: *M. Cisneros González participated in the characterization of the MAJIS VIS-NIR detectors, including the development and validation of the characterization facility.*

- **M. E. Cisneros-González**, D. Bolsée, N. Pereira, L. Van Laeken, L. Jacobs, A. C. Vandaele, C. Lauzin, S. Robert. Facility for the radiometric characterization of space-based visible-near infrared detectors. *Journal of Astronomical Telescopes and Instruments (JATIS)*, 9:03, August 2023. [doi: 10.1117/1.jatis.9.3.036001]: *M. E. Cisneros-González designed, developed and validated the cryogenic system, the security system and the working environment of the VIS-NIR characterization facility, and participated in the preliminary design of its optical system.*

E.2 CONFERENCE PROCEEDINGS PUBLICATIONS

- **M. E. Cisneros-González**, M. Lopez-Puertas, J. Erwin, A. C. Vandaele, C. Lauzin, F. Poulet, S. Robert. Validation of ASIMUT-ALVL against observational data of Jupiter's Atmosphere. *European Planetary Science Congress (EPSC)*, 16:145, September 2022. [doi: 10.5194/epsc2022-145]: *M. E. Cisneros-González developed the VIS-NIR radiative transfer model of Jupiter's atmosphere, and performed the withdrawal of the Great Red Spot (GRS) spectrum.*

- N. Pereira, **M. E. Cisneros-Gonzalez**, D. Bolsée, L. Van Laeken, A. C. Vandaele, S. Guissot, Y. Langevin, P. Haffoud, F. Poulet. MAJIS VIS-NIR channel: Performances of the Spare Model focal plane unit. *SPIE Astronomical Telescopes+ Instrumentation*, 12180, August 2022. [doi: 10.1117/12.2642675]: *M. E. Cisneros-Gonzalez performed the analysis of the thermal behavior of the VIS-NIR SM FPU and participated in its characterization.*

- P. Haffoud, A. Arondel, D. Bolsée, V. Carlier, J. Carter, **M. E. Cisneros-González**, ... +18 contributors and the MAJIS Team. MAJIS VIS-NIR channel: Performances of the focal plane unit – Flight Model. *SPIE Astronomical Telescopes+ Instrumentation*, 12180, August 2022. [doi: 10.1117/12.2628884]: *M. E. Cisneros-González performed the analysis of the thermal behavior of the VIS-NIR FM FPU and participated in its characterization.*

- **M. E. Cisneros-González**, S. Robert, J. Erwin, A. C. Vandaele, C. Lauzin, F. Poulet, G. Piccioni. Simulating Spectra of Jupiter's Atmosphere based on MAJIS VIS-NIR characteristics. *European Planetary Science Congress (EPSC)*, 15:764, September 2021. [doi: 10.5194/epsc2021-764]: *M. E. Cisneros-González developed the VIS-*

NIR radiative transfer model of Jupiter's atmosphere and simulated Jupiter's VIS-NIR spectrum based on the expected performances of the MAJIS VIS-NIR channel.

- **M. E. Cisneros-González**, D. Bolsée, N. Pereira, L. Van Laeken, C. Depiesse, L. Jacobs, ..., +13 contributors. MAJIS/JUICE VIS-NIR FM and SM detectors Characterization. *SPIE Astronomical Telescopes+ Instrumentation*, 114431L, December 2020. [doi: 10.1117/12.2562063]: *M. E. Cisneros-González participated in the characterization of the MAJIS VIS-NIR FM detector, the development and validation of the characterization facility, and performed the preliminary analysis of the thermal behavior of the MASIS VIS-NIR FPU.*

- D. Bolsée, L. Van Laeken, **M. E. Cisneros-González**, N. Pereira, C. Depiesse, L. Jacobs, S. Robert, ..., +11 contributors. Characterization facility for the MAJIS/JUICE VIS-NIR FM and SM detectors. *SPIE Astronomical Telescopes+ Instrumentation*, 11443, December 2020. [doi: 10.1117/12.2576319]: *M. E. Cisneros-González designed, developed and validated the cryogenic system, the security system and the working environment of the VIS-NIR characterization facility, and participated in the preliminary design of its optical system.*

- **M. E. Cisneros-González**, D. Bolsée, L. Van Laeken, N. Pereira, P. Gerard, S. Robert, A. C. Vandaele, ..., +8 contributors. The Thermal-Vacuum and security system of the characterization facility for MAJIS/JUICE VIS-NIR FM and SM detectors. *SPIE Astronomical Telescopes+ Instrumentation*, 114437G, December 2020. [doi: 10.1117/12.2576308]: *M. E. Cisneros-González designed, developed and validated the cryogenic system and the security system of the VIS-NIR characterization facility.*

LIST OF ACRONYMS

3GM	Geodesy and Geophysics of Jupiter and the Galilean Moons
ASIMUT	Atmospheric Spectra Inversion Modular Utility Tool
AU	Astronomical Units
ALTIUS	Atmospheric Limb Tracker for Investigation of the Upcoming Stratosphere
ARS	Advanced Research Systems
B.RCLab	Belgian Radiometric Characterization Laboratory
BIRAIASB	Royal Belgian Institute for Space Aeronomy
B.USOC	Belgian User Support and Operations Center
BW	BandWidth
CB	*Crème Brulée*
CCD	Charge-Coupled Device
CDF	Cumulative Distribution Function
CDMS	Cologne Database for Molecular Spectroscopy
CH	Chromophore Haze
CIRS	Composite Infrared Spectrometer
CMOS	Complementary Metal-Oxide Semiconductor
CNES	*Centre Nationale d'Études Spatiales*
CSL	*Centre Spatial de Liège*
CTE	Charge Transfer Efficiency
CTE	Coefficient of Thermal Expansion
CVCM	Collected Volatile Condensable Materials
DAQ	Data AcQuisition
DC	Dark Current
DCL	Detectors Characterization Laboratory
DSNU	Dark Signal Non-Uniformity
DU	Digital Units
ECCM	Equilibrium Cloud Condensation Model
EM	Engineering Model
EMVA	European Machine Vision Association
ESA	European Space Agency
ESCC	European Space Components Coordination
EUV	Extreme Ultraviolet
ExoMol	High-temperature molecular line lists for modelling exoplanet atmospheres
EZ	Equatorial Zone
FM	Flight Model
FM	Folding Mirror number
FoV	Field of View
FPA	Focal Plane Array

FPU	Focal Plane Unit
FWC	Full-Well Capacity
GALA	Ganymede Laser Altimeter
GCO	Ganymede Circular Orbit
GEISA	*Gestion et Etude des Informations Spectroscopiques Atmosphériques*
GRASS	GRAvimeter for Small Solar system bodies
GRS	Great Red Spot
GSE	Ground Support Equipment
HAPI	HITRAN Application Programming Interface
HAWAII	HgCdTe Astronomical Wide Area Infrared Imager
HEnd	End altitude of light path
HITEMP	HIgh-TEMPerature molecular spectroscopic database
HITRAN	HIgh-resolution TRANsmission molecular absorption database
HST	Hubble Space Telescope
HWHM	Half-Width at Half-Maximum
IAA	*Instituto de Astrofísica de Andalucía*
IAPS	*Istituto di Astrofisica e Planetologia Spaziali*
IAS	*Institut d'Astrophysique Spatiale*
IAU	*International Astronomical Union*
ICU	Internal Calibration Unit
IDTL	Independent Detector Testing Laboratory
ILS	Instrumental Line Shape
IR	Infrared wavelengths
IS	Integrating Sphere
ISO	Infrared Space Observatory
ISO	International Organization for Standarization
ISS	Imaging Science Subsystem
IT	Integration Time
J-MAG	JUICE Magnetometer
JANUS	*Jovis, Amorum ac Natorum Undique Scrutator*
JATIS	Journal of Astronomical Telescopes, Instruments and Systems
JIRAM	Jovian Infrared Auroral Mapper
JUICE	Jupiter ICy moons Explorer
JWST	James Webb Space Telescope
KOPRA	Karlsruhe Optimized and Precise Radiative transfer Algorithm
L-class	Large class
LBL	Line-By-Line
LED	Ligth-Emitting Diode
LEGA	Lunar-Earth Gravity Assist
LIDORT	Linearized Discrete Ordinate Radiative Transfer
LN2	Liquid Nitrogen
LUT	Look Up Table
LVF	Linear Variable Filter
LSST	Large Synoptic Survey Telescope
LTE	Local Thermodynamic Equilibrium

MAJIS	Moons And Jupiter Imaging Spectrograph
MLI	Multi-Layer Insulation
MOC	Mission Operation Center
MOC	Molecular Organic Contamination
MOSFET	Metal-Oxide-Semiconductor Field-Effect Transistor
MPI	Max Planck Institute
MTF	Modulation-Transfer Function
MWR	Microwave Radiometer
N/A	Not Applicable
NASA	National Aeronautics and Space Administration
ND	Neutral Density
NEMESIS	Non-linear Optimal Estimator for MultivariatE Spectral analySIS
NI	National Instruments
NIMS	Near-Infrared Mapper Spectrometer
NIR	Near-Infrared wavelengths
NIRSpec	Near-Infrared Spectrograph
NEB	North Equatorial Belt
NPR	North Polar Region
NNTeB	North North Temperate Belt
NNTeZ	North North Temperate Zone
NTeB	North Temperate Belt
NTeZ	North Temperate Zone
NTrB	North Tropical Belt
NTrZ	North Tropical Zone
OFHC	Oxygen Free High-Conductivity Copper
OH	Optical Head
PA/QA	Product and Quality Assurance
PEI	PolyEtherimIde
PEP	Particle Environmental Package
PFO	Particle Fall-Out
PIC	Proportional-Integrative-Derivative
PJ	PeriJove
ppm	Parts Per Million
PPR	Photopolarimeter-Radiometer
PRIDE	Planetary Radio Interferometry and Doppler Experiment
PRNU	Photo-Response Non-Uniformity
PSD	Particle Size Distribution
PSG	Planetary Spectrum Generator
PT	Platinum resistance thermometer
PTB	*Physikalisch-Technische Bundesanstalt*
PTFE	PolyEetraFluoroEthylene
PTR	Planning Timeline Request
QE	Quantum Efficiency
QTH	Quartz-Tungsten-Halogen
RIME	Radar for Icy Moons Exploration

ROB	Royal Observatory of Belgium
RON	Read-Out Noise
RPWI	Radio and Plasma Wave Investigation
RS	Rayleigh Scattering
RTD	Resistance Temperature Detector
SAM	SIDECAR Acquisition Module
SEBn	South Equatorial Belt at north
SEBs	South Equatorial Belt at south
SH	Stratospheric Haze
SIDECAR	System Image, Digitizing, Enhancing, Controlling, And Retrieving
SM	Spare Model
SMS	Short Message Service
SNR	Signal-to-Noise Ratio
SOC	Science Operations Center
SPR	South Polar Region
SSA	Single Scattering Albedo
SSI	Solid-State Imager
SSTeB	South South Temperate Belt
SSTeZ	South South Temperate Zone
STeB	South Temperate Belt
STeZ	South Temperate Zone
STM	Structural Model
STrZ	South Tropical Zone
SWI	Submillimeter Wave Instrument
SWPF	Short Wave Pass Filter
TauREx	*Tau* Retrieval for EXoplanets
TC	Tropospheric Cloud
TGSE	Thermal Ground Support Equipment
TMA	Three Mirrors Anastigmatic
TML	Total Mass Lost
ULB	Ultra-Low Background
UPS	Uninterruptible Power Supply
UTC	Coordinated Universal Time
UV	Ultraviolet wavelengths
UVIS	Ultraviolet Imaging Spectrograph
UVS	Ultraviolet Spectrometer/Spectrograph
VIMS	Visual and Infrared Mapping Spectrometer
VIRTIS	Visible and Infrared Thermal Imaging Spectrometer
VIS	Visible wavelengths
VLT	Very Large Telescope
VMR	Volume Mixing Ratio
WFC3	Wide Field Camera 3
WP	Working Plane

LIST OF SYMBOLS

B_λ	Blackbody radiation
$E_p x$	Photon energy
F_k	King correction factor
F_R	Light signal from the detector after registers reset
F_{CDS}	Light signal from the detector after CDS technique
F_{IT}	Light signal from the detector at certain IT
F_{WP}	Light signal from the detector after data correction
G	Electronic conversion gain
H	Homogeneity propagation function
I_λ	Intensity of radiation
J_λ	Source function
L	Radiance
N	Column number density
P	Pressure
P_0	Standard pressure
P_λ	Scattering phase function
P_{IS}	Spectral power at the integrating sphere
P_{WP}	Spectral power at a certain point in the facility working plane
Q_a	Absorption efficiency
Q_e	Extinction efficiency
Q_s	Scattering efficiency
R	Spectral resolving power
R_0	Transfer function between different optical powers
S	Line intensity
S_p	Surface area of a spherical particle
S_{IS}	Photodiode net signal at the output of the integrating sphere
S_{WP}	Photodiode net signal at the facility working plane
T	Temperature
T_0	Standard temperature
T_λ	Transmittance
V	Volume
XS	Geometric cross-section
α	Shape of the gamma distribution
α_D	HWHM for Doppler line profile
α_L	HWHM for Lorentz line profile
β	Rate of the gamma distribution
β_a	Absorption coefficient
β_e	Extinction coefficient
β_s	Scattering coefficient
Γ	Ordinary gamma function
γ	Incomplete gamma function
λ	Wavelength
ν	Molecular transition
Ω	Solid angle of incident radiation

Ω'	Solid angle of scattered radiation
Φ	Error function
ρ_n	Depolarization ratio
σ	Cross-section
σ_a	Absorption cross-section
$\sigma_a^{(2)}$	Absorption cross-section by two molecules
σ_e	Extinction cross-section
σ_s	Scattering cross-section
σ_{eff}	Effective variance
τ	Optical depth
$\tilde{\nu}$	Wavenumber
$\tilde{k}$	Cross-section of a volume containing n_0 molecules
a	Equivalent to r_{eff}
b	Equivalent to v_{eff}
c	Volume mixing ratio
f	Probability density function
g	Asymmetry parameter
k	k-absorption coefficient
k_λ	Imaginary part of the refractive index
m	Moment of the probability density function
m_λ	Complex refractive index
n	Partial number density
n_0	Loschmidth's number
n_s	Times the geometric standard deviation should be considered
n_λ	Real part of the refractive index
p	Partial pressure
q	Probability value
r	Radius
r_m	Mean radius
r_{eff}	Effective radius
s	Geometric standard deviation
v_{eff}	Effective variance
x	Size parameter
x, y	Spatial dimensions
x_0	Median average signal value of the reference pixels in one row
y_0	Median average signal value of the reference pixels in one column
z	Altitude
z	Thickness of the layer

BIBLIOGRAPHY

[1] F. Bagenal, T. E. Dowling, W. B. McKinnon, et al., editors. *Jupiter: the planet, satellites and magnetosphere*. Cambridge University Press, 2006. [ISBN: 978-0-521-03545-3].

[2] P. Irwin. *Giant planets of our solar system: atmospheres, composition, and structure*. Springer-Praxis books in Astronomy and Planetary Sciences. 2nd edition, 2009. [ISBN:978-3-540-85157-8].

[3] NASA. Jupiter Fact Sheet, January 2021. https://nssdc.gsfc.nasa.gov/planetary/factsheet/jupiterfact.html.

[4] J. I. Moses, T. Fouchet, B. Bézard, et al. Photochemistry and diffusion in Jupiter's stratosphere: Constraints from ISO observations and comparisons with other giant planets. *Journal of Geophysical Research: Planets*, 110, August 2005. [doi: 10.1029/2005JE002411].

[5] NASA. Earth Fact Sheet, January 2024. https://nssdc.gsfc.nasa.gov/planetary/factsheet/earthfact.html.

[6] S. M. Wahl, W. B. Hubbard, B. Militzer, et al. Comparing Jupiter interior structure models to *Juno* gravity measurements and the role of a dilute core. *Geophysical Research Letters*, 44(10):4649–4659, May 2017. [doi: 10.1002/2017GL073160].

[7] D. R. Buccino, R. Helled, M. Parisi, et al. Updated Equipotential Shapes of Jupiter and Saturn Using Juno and Cassini Grand Finale Gravity Science Measurements. *Journal of Geophysical Research: Planets*, 125(8), August 2020. [doi: 10.1029/2019JE006354].

[8] G. F. Lindal, G. E. Wood, G. S. Levy, et al. The atmosphere of Jupiter: An analysis of the Voyager radio occultation measurements. *Journal of Geophysical Research: Space Physics*, 86(A10):8721–8727, September 1981. [doi: 10.1029/JA086iA10p08721].

[9] A. Sanchez-Lavega. *An Introduction to Planetary Atmospheres*. CRC Press, Florida, USA, 2011. [ISBN: 978-1-4200-6735-4].

[10] P. K. Seidelmann and N. Divine. Evaluation of Jupiter longitudes in System III (1965). *Geophysical Research Letters*, 4(2):65–68, February 1977. [doi: 10.1029/GL004i002p00065].

[11] M. Saillenfest, G. Lari, and A. Courtot. The future large obliquity of Jupiter. *Astronomy & Astrophysics*, 640:A11, August 2020. [doi: 10.1051/0004-6361/202038432].

[12] G. W. Petty. *A first course in atmospheric radiation*. Sundog Publishing LLC, 2006. [ISBN: 978-0-9729033-1-8].

[13] D. M. Stam, J. W. Hovenier, and L. Waters. Using polarimetry to detect and characterize Jupiter-like extrasolar planets. *Astronomy & Astrophysics*, 428(2):663–672, December 2004. [doi: 10.1051/0004-6361:20041578].

[14] H. D. Goodfellow and E. F. Curd. Industrial ventilation design guidebook: Physical fundamentals. pages 39–109. Academic Press, 2nd edition, 2020. [ISBN: 978-0-12-816780-9].

[15] NASA Science. Jupiter, 2024. https://science.nasa.gov/jupiter/.

[16] C. Barbieri, J. H. Rahe, T. V. Johnson, and A. M. Sohus, editors. *The Three Galileos: The Man, the Spacecraft, the Telescope*. Springer Netherlands, Dordrecht, 1998. [ISBN: 978-90-481-4955-1 978-94-015-8790-7].

[17] NASA Hubble Site. Jupiter, 2024. https://hubblesite.org/contents/media/images/2024/.

[18] L. N. Fletcher, T. Cavalié, D. Grassi, et al. Jupiter Science Enabled by ESA's Jupiter Icy Moons Explorer. *Space Science Reviews*, 219(7):53, October 2023. [doi: 10.1007/s11214-023-00996-6].

[19] D. Grassi, A. Mura, G. Sindoni, et al. On the clouds and ammonia in Jupiter's upper troposphere from Juno JIRAM reflectivity observations. *Monthly Notices of the Royal Astronomical Society*, 503(4):4892–4907, April 2021. [doi: 10.1093/mnras/stab740].

[20] G. Sindoni, D. Grassi, A. Adriani, et al. Characterization of the white ovals on Jupiter's southern hemisphere using the first data by the Juno/JIRAM instrument. *Geophysical Research Letters*, 44(10):4660–4668, May 2017. [doi: 10.1002/2017GL072940].

[21] N. Gavriel and Y. Kaspi. The number and location of Jupiter's circumpolar cyclones explained by vorticity dynamics. *Nature Geoscience*, 14(8):559–563, August 2021. [doi: 10.1038/s41561-021-00781-6].

[22] Encyclopedia Britannica Inc. Jupiter: The atmosphere, 2011. https://www.britannica.com/place/Jupiter-planet/.

[23] V. Hue, F. Hersant, T. Cavalié, et al. Photochemistry, mixing and transport in Jupiter's stratosphere constrained by Cassini. *Icarus*, 307:106–123, June 2018. [doi: 10.1016/j.icarus.2018.02.018].

[24] J. N. Yates, L. C. Ray, N. Achilleos, et al. Magnetosphere-Ionosphere-Thermosphere Coupling at Jupiter Using a Three-Dimensional Atmospheric General Circulation Model. *Journal of Geophysical Research: Space Physics*, 125(1), January 2020. [doi: 10.1029/2019JA026792].

[25] J. Coakley and Y. Ping. *Atmospheric Radiation. A primer with illustrative solutions*. Atmospheric Physics and Remote Sensing. Wiley, Germany, 2014. [ISBN: 978-3-527-68144-0].

[26] M. López-Puertas, P. Montañés-Rodríguez, E. Pallé, et al. Aerosols and Water Ice in Jupiter's Stratosphere from UV-NIR Ground-based Observations. *The Astronomical Journal*, 156(4):169, October 2018. [doi: 10.3847/1538-3881/aadcef].

[27] R. A. West, D. F. Strobel, and M. G. Tomasko. Clouds, aerosols, and photochemistry in the Jovian atmosphere. *Icarus*, 65(2-3):161–217, February 1986. [doi: 10.1016/0019-1035(86)90135-1].

[28] N. J. Chanover, D. M. Kuehn, and R. F. Beebe. Vertical Structure of Jupiter's Atmosphere at the Galileo Probe Entry Latitude. *Icarus*, 128(2):294–305, August 1997. [doi: 10.1006/icar.1997.5737].

[29] A. Seiff, D. B. Kirk, T. Knight, et al. Thermal structure of Jupiter's atmosphere near the edge of a 5-m hot spot in the north equatorial belt. *Journal of Geophysical Research: Planets*, 103(E10):22857–22889, September 1998. [doi: 10.1029/98JE01766].

[30] E. K. Dahl, N. J. Chanover, G. S. Orton, et al. Vertical Structure and Color of Jovian Latitudinal Cloud Bands during the Juno Era. *The Planetary Science Journal*, 2(1):16, February 2021. [doi: 10.3847/PSJ/abd400].

[31] K. H. Baines, L. A. Sromovsky, R. W. Carlson, et al. The visual spectrum of Jupiter's Great Red Spot accurately modeled with aerosols produced by photolyzed ammonia reacting with acetylene. *Icarus*, 330:217–229, September 2019. [doi: 10.1016/j.icarus.2019.04.008].

[32] R. W. Carlson, K. H. Baines, M. S. Anderson, et al. Chromophores from photolyzed ammonia reacting with acetylene: Application to Jupiter's Great Red Spot. *Icarus*, 274:106–115, August 2016. [doi: 10.1016/j.icarus.2016.03.008].

[33] L. A. Sromovsky, K. H. Baines, P. M. Fry, and R. W. Carlson. A possibly universal red chromophore for modeling color variations on Jupiter. *Icarus*, 291:232–244, July 2017. [doi: 10.1016/j.icarus.2016.12.014].

[34] A. S. Braude, P. Irwin, G. S. Orton, and L. N. Fletcher. Colour and tropospheric cloud structure of Jupiter from MUSE/VLT: Retrieving a universal chromophore. *Icarus*, 338:113589, March 2020. [doi: 10.1016/j.icarus.2019.113589].

[35] M. H. Wong, G. L. Bjoraker, C. Goullaud, et al. Deep Clouds on Jupiter. *Remote Sensing*, 15(3):702, January 2023. [doi: 10.3390/rs15030702].

[36] P. M. Fry and L. A. Sromovsky. Investigating temporal changes in Jupiter's aerosol structure with rotationally-averaged 2015–2020 HST WFC3 images. *Icarus*, 389:115224, January 2023. [doi: 10.1016/ j.icarus.2022.115224].

[37] M. J. Loeffler, R. L. Hudson, N. J. Chanover, and A. A. Simon. The spectrum of Jupiter's Great Red Spot: The case for ammonium hydrosulfide (NH4SH). *Icarus*, 271:265–268, June 2016. [doi: 10.1016/j.icarus.2016.02.010].

[38] X. Zhang, R. A. West, D. Banfield, and Y. L. Yung. Stratospheric aerosols on Jupiter from Cassini observations. *Icarus*, 226(1):159–171, September 2013. [doi: 10.1016/j.icarus.2013.05.020].

[39] R. W. Carlson and D. L. Judge. Pioneer 10 ultraviolet photometer observations at Jupiter encounter. *Journal of Geophysical Research*, 79(25):3623–3633, September 1974. [doi: 10.1029/JA079i025p03623].

[40] S. F. Pellicori, E. E. Russell, and L. A. Watts. Pioneer Imaging Photopolarimeter Optical System. *Applied Optics*, 12(6):1246, June 1973. [doi: 10.1364/AO.12.001246].

[41] S. C. Chase, R. D. Ruiz, G. Münch, et al. Pioneer 10 Infrared Radiometer Experiment: Preliminary Results. *Science, New Series*, 183(4122):315–317, 1974. [doi: 10.1126/science.183.4122.315].

[42] Jet Propulsion Laboratory (JPL), NASA. Voyager instruments, 2024. https://voyager.jpl.nasa.gov/mission/spacecraft/instruments/.

[43] K. P. Wenzel, R. G. Marsden, D. E. Page, and E. Smith. The Ulysses mission. *Astronomy and Astrophysics Supplement Series*, 92:207, January 1992. [Bibliographic code: 1992AAS...92..207W].

[44] S. J. Bolton, C. J. Hansen, D. L. Matson, et al. Cassini/Huygens flyby of the Jovian system. *Journal of Geophysical Research: Space Physics*, 109(A9), September 2004. [doi: 10.1029/2004JA010742].

[45] S. Hamilton and H. Hart. Operational Pre-Planning for Intensive Science Periods: The New Horizons Jupiter Flyby. In *AIAA SPACE 2008 Conference & Exposition*, San Diego, California, September 2008. American Institute of Aeronautics and Astronautics. [doi: 10.2514/6.2008-7653].

[46] L. A. Sromovsky and P. M. Fry. Composition and structure of fresh ammonia clouds on Jupiter based on quantitative analysis of Galileo/NIMS and New Horizons/LEISA spectra. *Icarus*, 307:347–370, June 2018. [doi: 10.1016/j.icarus.2017.10.037].

[47] M. Belton, K. P. Klaasen, M. C. Clary, et al. The Galileo Solid-State Imaging experiment. *Space Science Reviews*, 60(1):413–455, May 1992. [doi: 10.1007/BF00216864].

[48] R. W. Carlson, P. R. Weissman, W. D. Smythe, et al. Near-Infrared Mapping Spectrometer experiment on Galileo. In *The Galileo mission*, pages 457–502. Springer, 1992. [ISBN: 978-94-010-5108-8].

[49] C. W. Hord, W. E. McClintock, A. Stewart, et al. Galileo Ultraviolet Spectrometer experiment. In *The Galileo mission*, pages 503–350. Springer, 1992. [ISBN: 978-94-010-5108-8].

[50] E. E. Russell, F. G. Brown, R. A. Chandos, et al. Galileo Photopolarimeter/Radiometer experiment. *Space Science Reviews*, 60(1):531–563, May 1992. [doi: 10.1007/BF00216867].

[51] S. J. Bolton, J. Lunine, D. Stevenson, et al. The Juno Mission. *Space Science Reviews*, 213(1-4):5–37, November 2017. [doi: 10.1007/s11214-017-0429-6].

[52] A. Adriani, A. Coradini, G. Filacchione, et al. JIRAM, the Image Spectrometer in the Near Infrared on Board the Juno Mission to Jupiter. *Astrobiology*, 8(3):613–622, June 2008. [doi: 10.1089/ast.2007.0167].

[53] The Ultraviolet Spectrograph on NASA's Juno Mission. *Space Science Reviews*, 213(1-4):447–473, November 2017. [doi: 10.1007/s11214-014-0040-z].

[54] M. A. Janssen, J. E. Oswald, S. T. Brown, et al. MWR: Microwave Radiometer for the Juno Mission to Jupiter. *Space Science Reviews*, 213(1-4):139–185, November 2017. [doi: 10.1007/s11214-017-0349-5].

[55] L. D. Jaffe and L. M. Herrell. Cassini/Huygens Science Instruments, Spacecraft, and Mission. *Journal of Spacecraft and Rockets*, 34(4):509–521, July 1997. [doi: 10.2514/2.3241].

[56] P. Rodríguez-Ovalle, S. Guerlet, T. Fouchet, et al. Stratospheric aerosols and C_6H_6 in Jupiter's south polar region from JWST/MIRI observations. *Astronomy & Astrophysics*, 691:A51, November 2024. [doi: 10.1051/0004-6361/202451453].

[57] H. Melin, J. O'Donoghue, L. Moore, et al. Ionospheric irregularities at Jupiter observed by JWST. *Nature Astronomy*, 8(8):1000–1007, June 2024. [doi: 10.1038/s41550-024-02305-9].

[58] R. Hueso, A. Sánchez-Lavega, T. Fouchet, et al. An intense narrow equatorial jet in Jupiter's lower stratosphere observed by JWST. *Nature Astronomy*, 7(12):1454–1462, October 2023. [doi: 10.1038/s41550-023-02099-2].

[59] J. Norwood, J. Moses, L. N. Fletcher, et al. Giant Planet Observations with the James Webb Space Telescope. *Astronomical Society of the Pacific*, 128(959), January 2016. [doi: 10.1088/1538-3873/128/959/018005].

[60] JUICE Science Study Team. JUICE Definition Study Report. Red Book, European Space Agency, September 2014. [Bibliographic code: ESA/SRE 2014/1].

[61] A. Sánchez-López, M. López-Puertas, M. García-Comas, et al. The CH4 abundance in Jupiter's upper atmosphere. *Astronomy & Astrophysics*, 662:A91, June 2022. [doi: 10.1051/0004-6361/202141933].

[62] F. Poulet, G. Piccioni, Y. Langevin, et al. Moons and Jupiter Imaging Spectrometer (MAJIS) on Jupiter Icy Moons Explorer (JUICE). *Space Science Reviews*, 220:27, March 2024. [doi: 10.1007/s11214-024-01057-2].

[63] U. A. Dyudina, A. P. Ingersoll, and G. E. Danielson. Interpretation of NIMS and SSI Images on the Jovian Cloud Structure. *Icarus*, 150(2):219–233, April 2001. [doi: 10.1006/icar.2000.6582].

[64] R. G. Prinn and J. S. Lewis. Phosphine on Jupiter and Implications for the Great Red Spot. *Science*, 190(4211):274–276, October 1975. [doi: 10.1126/science.190.4211.274].

[65] O. Grasset, M. K. Dougherty, A. Coustenis, et al. JUpiter ICy moons Explorer (JUICE): An ESA mission to orbit Ganymede and to characterise the Jupiter system. *Planetary and Space Science*, 78:1–21, April 2013. [doi: 10.1016/j.pss.2012.12.002].

[66] J. H. Roberts, W. B. McKinnon, C. M. Elder, et al. Exploring the Interior of Europa with the Europa Clipper. *Space Science Reviews*, 219(6):46, September 2023. [doi: 10.1007/s11214-023-00990-y].

[67] L. Prockter, E. Bunce, M. Choukroun, and JUICE-Clipper Steering Committee. Exploring the Jupiter System through unique joint JUICE and Europa Clipper observations. pages EGU24–6262. Copernicus Meetings, March 2024. [doi: 10.5194/egusphere-egu24-6262].

[68] IAS. Institut d'Astrophysique Spatiale. https://www.ias.universite-paris-saclay.fr/fr/content/juicemajis.

[69] IAPS. Istituto di Astrofisica e Planetologia Spaziali. https://www.iaps.inaf.it/en/progetti-di-ricerca/majis.

[70] Leonardo Company. Leonardo Company. Aerospace, Defense and Security. https://www.leonardo.com/en/.

[71] A. Coradini, F. Capaccioni, P. Drossart, et al. VIRTIS: An Imaging Spectrometer for the Rosetta Mission. *Space Science Reviews*, 128(1-4):529–559, February 2007. [doi: 10.1007/s11214-006-9127-5].

[72] P. Drossart, G. Piccioni, A. Coradini, et al. VIRTIS imaging spectrometer for the ESA/Venus Express mission. In *Infrared Spaceborne Remote Sensing XII*, volume 5543, pages 175–185. SPIE, 2004. [doi: 10.1117/12.557427].

[73] I. Guerri, A. Fabbri, L. Tommasi, et al. The optical design of the MAJIS instrument on board of the JUICE mission. In *Optical Design and Engineering VII*, page 49, Frankfurt, Germany, June 2018. SPIE. [doi: 10.1117/12.2312013].

[74] G. Piccioni, A. Bini, G. Bugetti, et al. Scientific goals and technical challenges of the MAJIS imaging spectrometer for the JUICE mission. In *2019 IEEE 5th International Workshop on Metrology for AeroSpace (MetroAeroSpace)*, pages 318–323, Torino, Italy, June 2019. IEEE. [doi: 10.1109/MetroAeroSpace.2019.8869566].

[75] Y. Langevin, F. Poulet, G. Piccioni, et al. Calibration of MAJIS (Moons And Jupiter Imaging Spectrometer): IV. Radiometric calibration. *Review of Scientific Instruments*. Accepted.

[76] Specim. Smile and keystone, February 2021. https://www.specim.com/smile-and-keystone/.

[77] G. Filacchione, P. Haffoud, F. Poulet, et al. Calibration of MAJIS (Moons And Jupiter Imaging Spectrometer). II. Spatial calibration. *Review of Scientific Instruments*, 95(4):041301, April 2024. [doi: 10.1063/5.0203872].

[78] Y. Langevin, G. Piccioni, G. Filacchione, et al. MAJIS, the VIS-IR imaging spectrometer of JUICE. In *International Workshop on Instrumentation for Planetary Missions*, Berlin, Germany, 2018. Universität Berlin. [Bibliographic code: 2018ipm..confE...1L].

[79] L. Tommasi, G. Bugetti, A. Fabbri, et al. The Advanced Optical and Thermomechanical Design of the JUICE/MAJIS Spectrometer. In *2018 5th IEEE International Workshop on Metrology for AeroSpace*

(MetroAeroSpace), pages 247–251, Rome, June 2018. IEEE. [doi: 10.1109/MetroAeroSpace.2018.8453533].

[80] P. Haffoud, A. Arondel, D. Bolsée, et al. MAJIS VIS-NIR channel: performances of the focal plane unit - flight model. In *Space Telescopes and Instrumentation 2022: Optical, Infrared, and Millimeter Wave*, page 165, Montréal, Canada, August 2022. SPIE. [doi: 10.1117/12.2628884].

[81] Y. Langevin, G. Piccioni, P. Eng, et al. The MAJIS VIS-NIR Imaging Spectrometer for the JUICE mission. In *45th Lunar and Planetary Science Conference*, page 2493, 2014. [Bibliographic code: 2014LPI....45.2493L].

[82] M. E. Cisneros-González, D. Bolsée, N. Pereira, et al. Facility for the radiometric characterization of space-based visible-near infrared detectors. *Journal of Astronomical Telescopes, Instruments, and Systems*, 9(03), August 2023. [doi: 10.1117/1.JATIS.9.3.036001].

[83] BIRA-IASB. Belgian Radiometric Characterization Laboratory (B.RCLab). https://brclab.aeronomie.be/.

[84] BIRA-IASB. Royal Belgian Institute for Space Aeronomy. https://www.aeronomie.be/index.php/en.

[85] J. D. Vincent, S. Hodges, J. Vampola, et al. *Fundamentals of Infrared and Visible Detector Operation and Testing*. John Wiley & Sons, 2 edition, 2015. [ISBN: 978-1-119-01187-3].

[86] S. B. Howell. *Handbook of CCD astronomy*. Number 5 in Cambridge observing handbooks for research astronomers. Cambridge University Press, Cambridge, 2 edition, 2006. [ISBN: 978-0-521-61762-8].

[87] R. A. Jansen. *Astronomy with Charged Coupled Devices*. Instrumentation and Data Reduction Course. ASU, 2006. [Bibliographic code: AST 598].

[88] Officina Turini. Basic CCD. https://www.officinaturini.com/ccd.html.

[89] Teledyne Technologies. Hybrid binning, 2024. https://www.teledynevisionsolutions.com/learn/learning-center/choosing-a-vision-solution/hybrid-binning/.

[90] R. Blank, S. Anglin, J. W. Beletic, et al. The HxRG Family of High Performance Image Sensors for Astronomy. volume 437 of *ASP Conference*, page 383. Astronomical Society of the Pacific, April 2011. [Bibliographic code: 2011ASPC..437..383B].

[91] A. Daniels. *Field guide to infrared systems, detectors, and FPAs*. Number FG40 in SPIE field guide. SPIE Press, Washington, USA, 3 edition, 2018. [ISBN: 978-1-5106-1864-0].

[92] P. Capper and J. Garland, editors. *Mercury-Cadmium-Telluride: growth, properties, and applications*. Materials for electronic and optoelectronic applications. Wiley, New Jersey, USA, 2011. [ISBN: 978-0-470-69706-1].

[93] P. Norton. HgCdTe infrared detectors. *Opto-Electronincs Review*, 10(3):159–174, 2002. https://optor.wat.edu.pl/.

[94] J. R. Janesick. *Photon transfer: DN [lambda]*, volume PM170. SPIE, 2007. [ISBN: 978-0-8194-6722-5].

[95] C. A. Shapiro, R. M. Smith, E. M. Huff, et al. Precision Projector Laboratory: detector characterization with an astronomical emulation testbed. *Journal of Astronomical Telescopes, Instruments, and Systems*, 5(4):041503, 2019. [doi: 10.1117/1.JATIS.5.4.041503].

[96] A. BenMoussa, S. Gissot, U. Schühle, et al. On-orbit degradation of solar instruments. *Solar Physics*, 288(1):389–434, 2013. [doi: 10.1007/s11207-013-0290-z].

[97] J. R. Janesick, editor. *Scientific Charge-Coupled Devices*. SPIE Press, 2001. [ISBN: 0-8194-3698-4].

[98] B. Serra, A. Secroun, J. C. Clémens, et al. Characterization of Euclid-like H2RG IR detectors for the NISP instrument. In *UV/Optical/IR Space Telescopes and Instruments: Innovative Technologies and Concepts VII*, volume 9602 of *Proc. SPIE*, pages 167–180, September 2015. [doi: 10.1117/12.2188439].

[99] T. S. Lomheim, L. W. Schumann, and S. E. Kohn. Experimental characterization, evaluation, and diagnosis of advanced hybrid infrared focal plane array electro-optical performance. In *Infrared Detectors and Focal Plane Arrays V*, volume 3379 of *Proc. SPIE*, pages 520–554, July 1998. [doi: 10.1117/12.317621].

[100] U. Jain. Characterization of CMOS image sensor. Master's thesis, Delft University of Technology, Delft, Netherlands, 2016. [Repository].

[101] G. Orias. Accurate, high-throughput, low-cost testing of infrared focal plane arrays for defense-related systems. In *Smart Focal Plane Arrays and Focal Plane Array Testing*, volume 2474 of *Proc. SPIE*, pages 265–273, May 1995. [doi: 10.1117/12.210561].

[102] P. Verhoeve, T. Prod'homme, T. Oosterbroek, et al. CCD characterization for astronomy space missions at ESA. In *High Energy, Optical, and Infrared Detectors for Astronomy VI*, volume 9154 of *Proc. SPIE*, pages 359–371, July 2014. [doi: 10.1117/12.2058110].

[103] European Space Agency (ESA). Optics and Opto-Electronics Laboratory, 2022. https://technology.esa.int/lab/optics-and-opto-electronics-laboratory.

[104] Goddard Space Flight Center. Detector Characterization Laboratory, 2010. https://detectors.gsfc.nasa.gov/DCL/.

[105] P. Verhoeve, N. Boudin, U. Telljohann, et al. ESA's CCD test bench for the Euclid visible channel. In *High Energy, Optical, and Infrared Detectors for Astronomy V*, volume 8453 of *Proc. SPIE*, pages 617–628, September 2012. [doi: 10.1117/12.926016].

[106] A. Secroun, B. Serra, J. C. Clémens, et al. Characterization of H2RG IR detectors for the Euclid NISP instrument. In *High Energy, Optical, and Infrared Detectors for Astronomy VII*, volume 9915 of *Proc. SPIE*, pages 649–657, July 2016. [doi: 10.1117/12.2232070].

[107] B. J. Rauscher, O. Fox, P. Ferruit, et al. Detectors for the JWST NIR Spectrograph. I. Readout Mode, Noise Model, and Calibration Considerations. *Publications of the Astronomical Society of the Pacific*, 119(857):768–786, July 2007. [doi: 10.1086/520887].

[108] D. F. Figer, B. J. Rauscher, M. W. Regan, et al. Independent testing of JWST detector prototypes. In *Focal Plane Arrays for Space Telescopes*, volume 5167 of *Proc. SPIE*, pages 270–301, January 2004. [doi: 10.1117/12.505787].

[109] D. Hall, D. Atkinson, R. Blank, et al. Performance of the first science grade λc=2.5μm HAWAII 4RG-15 array in the laboratory

and at the telescope. In *High Energy, Optical, and Infrared Detectors for Astronomy VII*, volume 9915 of *Proc. SPIE*, pages 317–326, August 2016. [doi: 10.1117/12.2234369].

[110] I. V. Kotov, J. Haupt, P. O'Connor, et al. Characterization and acceptance testing of fully depleted thick CCDs for the large synoptic survey telescope. In *High Energy, Optical, and Infrared Detectors for Astronomy VII*, page 99150V, Edinburgh, UK, August 2016. SPIE. [doi: 10.1117/12.2231925].

[111] P. E. Crouzet, L. Duvet, F. De Wit, et al. Quantum efficiency test set up performances for NIR detector characterization at ESTEC. In *High Energy, Optical, and Infrared Detectors for Astronomy VI*, volume 9154 of *Proc. SPIE*, pages 476–488, July 2014. [doi: 10.1117/12.2054925].

[112] W. J. Koshak, M. F. Stewart, H. J. Christian, et al. Laboratory calibration of the optical transient detector and the lightning imaging sensor. *Journal of Atmospheric and Oceanic Technology*, 17(7):905–915, 2000. [doi: 10.1175/1520-0426].

[113] A. Christov, S. Karpov, M. Prouza, and A. Bajat. Test stand for characterization of optical sensors for astronomy. *Journal of Astronomical Telescopes, Instruments, and Systems*, 5(4):041504–041504, 2019. [doi: 10.1117/1.JATIS.5.4.041504].

[114] D. P. Weatherill, K. Arndt, R. Plackett, and I. Shipsey. An electro-optical test system for optimising operating conditions of CCD sensors for LSST. *Journal of Instrumentation*, 12(12):C12019, 2017. [doi: 10.1088/1748-0221/12/12/C12019].

[115] T. Biesiadzinski, W. Lorenzon, R. Newman, et al. Measurement of Reciprocity Failure in Near-Infrared Detectors. *Publications of the Astronomical Society of the Pacific*, 123(900):179, 2011. [doi: 10.1086/658282].

[116] R. Coles, J. Chiang, D. Cinabro, et al. An automated system to measure the quantum efficiency of CCDs for astronomy. *Journal of Instrumentation*, 12(04), 2017. [doi: 10.1088/1748-0221/12/04/C04014].

[117] D. F. Figer, B. J. Rauscher, M. W. Regan, et al. Independent detector testing laboratory and the NGST detector characterization

project. In *IR Space Telescopes and Instruments*, volume 4850 of *Proc. SPIE*, pages 981–1000, March 2003. [doi: 10.1117/12.461889].

[118] N. Bezawada, D. Atkinson, N. Shorrocks, et al. Characterisation activities of new NIR to VLWIR detectors from Selex ES Ltd at the UK ATC. In *High Energy, Optical, and Infrared Detectors for Astronomy VI*, volume 9154 of *Proc. SPIE*, pages 201–211, Jul. 2014. [doi:10.1117/12.2056631].

[119] R. Cosentino, M. Hernandez, H. Ventura, et al. Laboratory test of the VIS detector system of SOXS for the ESO-NTT Telescope. In *Ground-based and Airborne Instrumentation for Astronomy IX*, volume 12184 of *Proc. SPIE*, pages 1759–1767, August 2022. [doi: 10.1117/12.2628246].

[120] R. J. Hill, E. Malumuth, R. Foltz, et al. Reciprocity failure in 1.7 μm cut-off HgCdTe detectors. In *High Energy, Optical, and Infrared Detectors for Astronomy IV*, volume 7742 of *Proc. SPIE*, pages 608–614, September 2010. [doi: 10.1117/12.857218].

[121] P. E. Crouzet, J. ter Haar, F. de Wit, et al. Test set up description and performances for HAWAII-2RG detector characterization at ESTEC. In *High Energy, Optical, and Infrared Detectors for Astronomy V*, volume 8453 of *Proc. SPIE*, pages 680–687, September 2012. [doi: 10.1117/12.924972].

[122] D. Hall, G. Luppino, K. W. Hodapp, et al. A 4K x 4K HgCdTe astronomical camera enabled by the JWST NIR detector development program. *Optical and Infrared Detectors for Astronomy*, 5499:1–14, 2004. [doi: 10.1117/12.554733].

[123] N. Pereira, M. E. Cisneros-González, D. Bolsée, et al. MAJIS VIS-NIR channel: performances of the spare model focal plane unit. In *Space Telescopes and Instrumentation: Optical, Infrared, and Millimeter Waves*, Proc. SPIE, pages 1269–1282, August 2022. [doi: 10.1117/12.2642675].

[124] European Space Components Coordinator (ESCC). *Electro-Optical Test Methods for Charged Coupled Devices*. European Space Agency (ESA), January 2014. [ESCC Basic Specification No. 25000].

[125] European Machine Vision Association (EMVA). *Standard for Characterisation of Image Sensors and Cameras. Release 3.1*. European Space Agency (ESA), 2016. [EMVA Standard 1288].

[126] D. Bolsée, L. Van Laeken, M. E. Cisneros-González, et al. Characterization facility for the MAJIS/JUICE VIS-NIR FM and SM detectors. In *Space Telescopes and Instrumentation: Optical, Infrared, and Millimeter Waves*, volume 11443 of *Proc. SPIE*, pages 1214–1233, December 2020. [doi: 10.1117/12.2576319].

[127] PAR Group Ltd. *SSUSTAPEI*, 2020. [Technical datasheet].

[128] M. E. Cisneros-González, D. Bolsée, L. Van Laeken, et al. Thermal-vacuum and security system of the characterization facility for the MAJIS/JUICE VIS-NIR FM and SM detectors. In *Space Telescopes and Instrumentation 2020: Optical, Infrared, and Millimeter Wave*, volume 114437G of *Proc. SPIE*, pages 1–12, Dec. 2020. [doi: 10.1117/12.2576308].

[129] L. Van Laeken. Development of experimental benches for radiometric characterization: Application to space instrument MAJIS VIS-NIR on JUICE. Master's thesis, Université de Liège, Liège, Belgium, 2019. [doi: 2268.2/8417].

[130] M. E. Cisneros-González, D. Bolsée, N. Pereira, et al. MAJIS/JUICE VIS-NIR FM and SM detectors characterization. In *Space Telescopes and Instrumentation: Optical, Infrared, and Millimeter Waves*, volume 11443 of *Proc. SPIE*, pages 271–285, December 2020. [doi: 10.1117/12.2562063].

[131] S. Seshadri, D. M. Cole, B. R. Hancock, and R. M. Smith. Mapping electrical crosstalk in pixelated sensor arrays. In *High Energy, Optical, and Infrared Detectors for Astronomy III*, volume 7021 of *Proc. SPIE*, pages 54–64, 2008. [doi: 10.1117/12.790150].

[132] Bentham Instruments Limited. DTMc300 Double-monochromator with triple grating turret, 2023. https://www.bentham.co.uk/products/components/dtmc300-double-monochromator-39/.

[133] P. Guiot, M. Vincendon, J. Carter, et al. Characterization of transient signal induced in IR detector array by Jupiter high-energy electrons and implications for JUICE/MAJIS operability. *Planetary and Space Science*, 181:104782, 2020. [doi: 10.1016/j.pss.2019.104782].

[134] M. Noeker, E. Van Ransbeeck, B. Ritter, and Ö. Karatekin. The grass gravimeter rotation mechanism for esa hera mission onboard juventas deep space cubesat. In *Proceedings of the 46th*

Aerospace Mechanisms Symposium, Virtual, pages 159–172, 2022. [Bilbiographic code: SCART-2023-0076].

[135] P. Haffoud, F. Poulet, M. Vincendon, et al. Calibration of MAJIS (Moons and Jupiter Imaging Spectrometer). III. Spectral calibration. *Review of Scientific Instruments*, 95(3), March 2024. [doi: 10.1063/5.0188944].

[136] MAJIS FPU VISNIR Requirement Specifications (1.1). Technical Report [JUI-IAS-MAJ-RS-021-1.1], IAS, September 2018.

[137] Teledyne technologies, 2024. https://www.teledyne.com/en-us.

[138] Y. Langevin, V. Carlier, C. Hannou, et al. H1RG readout procedures for MAJIS, the VIS/NIR imaging spectrometer of JUICE: impacts on the performances. In *Space Telescopes and Instrumentation 2022: Optical, Infrared, and Millimeter Wave*, volume 12180, pages 1167–1177. SPIE, August 2022. [doi: 10.1117/12.2629310].

[139] F. Poulet, G. Piccioni, Y. Langevin, et al. The Visible and Infrared Imaging Spectrometer MAJIS on ESA JUICE Mission. In *54th Lunar and Planetary Science Conference, Texas, USA*, 2023. [LPI Contrib. No. 2806].

[140] L. Van Laeken, M. Cisneros, and D. Bolsée. Facility validation with MAJIS VIS-NIR STM. Technical Report [IASB-MAJ-VR-002-1.6], BIRA-IASB, Brussels, Belgium, April 2020.

[141] D. Bolsée, M. Cisneros, L. Van Laeken, et al. Facility validation with MAJIS VIS-NIR EM. Technical Report [IASB-MAJ-VR-004-0.8], BIRA-IASB, Brussels, Belgium, September 2020.

[142] D. Bolsée, L. Van Laeken, M. Cisneros, et al. MAJIS VIS-NIR FM Characterization Campaign. Technical Report [IASB-MAJ-VR-010-2.2], BIRA-IASB, Brussels, Belgium, October 2020.

[143] Lambda-X. Masters in innovation, 2024. https://lambda-x.com/.

[144] D. Bolsée, L. Van Laeken, M. Cisneros, et al. MAJIS VIS-NIR SM Characterization Campaign. Technical Report [IASB-MAJ-VR-014-1.4], BIRA-IASB, Brussels, Belgium, October 2020.

[145] K. N. Liou. *An introduction to atmospheric radiation*. Number 84 in International Geophysics Series. Academic Press, 2 edition, 2002. [ISBN: 978-0-12-451451-5].

[146] P. Irwin, N. A. Teanby, R. De Kok, et al. The NEMESIS planetary atmosphere radiative transfer and retrieval tool. *Journal of Quantitative Spectroscopy and Radiative Transfer*, 109(6):1136–1150, April 2008. [doi: 10.1016/j.jqsrt.2007.11.006].

[147] G. A. Shaw and H. K. Burke. Spectral Imaging for Remote Sensing. *Lincoln Laboratory Journal*, 14(1):1–26, May 2003. [Bilbiographic code: paper/Shaw2003].

[148] G. B. Rybicki and A. P. Lightman. *Radiative processes in astrophysics*. Physics textbook. Wiley, May 2004. [ISBN: 978-0-471-82759-7].

[149] Wikipedia. Inverse-square law, May 2024. https://en.wikipedia.org/wiki/nverse-square_law.

[150] G. Villanueva. *Fundamentals of the Planetary Spectrum Generator (PSG)*. NASA, USA, 2022. [ISBN: 978-0-578-36143-7].

[151] ASIMUT-ALVL LIDORT User Manual and Science Description. Manual Version 1.2, Release 11.0.

[152] A. C. Vandaele, M. Kruglanski, and M. De Mazière. Modeling and retrieval of atmospheric spectra using ASIMUT. volume SP-628, Frascati, Italy, July 2006. [Bibliographic code: 2-s2.0-33749160613].

[153] P. R. Bunker and P. Jensen. *Fundamentals of molecular symmetry*. Number 1 in Series in chemical physics. Institute of Physics Publishing, USA, 2005. [ISBN: 978-0-7503-0941-7].

[154] M López-Puertas and F W Taylor. *Non-LTE Radiative Transfer in the Atmosphere*, volume 3 of *Series on Atmospheric, Oceanic and Planetary Physics*. World Scientific, December 2001. [ISBN: 978-981-02-4566-5 978-981-281-149-3].

[155] X. Huang and Y. L. Yung. A Common Misunderstanding about the Voigt Line Profile. *Journal of the Atmospheric Sciences*, 61(13):1630–1632, July 2004. [doi: 10.1175/1520-0469].

[156] K. L. Chubb, M. Rocchetto, S. N. Yurchenko, et al. The ExoMolOP database: Cross sections and k -tables for molecules of interest in high-temperature exoplanet atmospheres. *Astronomy & Astrophysics*, 646:A21, February 2021. [doi: 10.1051/0004-6361/202038350].

[157] R. M. Goody and Y. L. Yung. *Atmospheric radiation: theoretical basis*. Oxford University Press, 2 edition, 1989. [ISBN: 978-0-19-505134-6].

[158] I. E. Gordon, L. S. Rothman, R. J. Hargreaves, et al. The HITRAN 2020 molecular spectroscopic database. *Journal of Quantitative Spectroscopy and Radiative Transfer*, 277:107949, January 2022. [doi: 10.1016/j.jqsrt.2021.107949].

[159] J. Tennyson, S. N. Yurchenko, A. F. Al-Refaie, et al. The ExoMol database: Molecular line lists for exoplanet and other hot atmospheres. *Journal of Molecular Spectroscopy*, 327:73–94, September 2016. [doi: 10.1016/j.jms.2016.05.002].

[160] H. Keller-Rudek, G. K. Moortgat, R. Sander, and R. Sörensen. The MPI-Mainz UV/VIS Spectral Atlas of Gaseous Molecules of Atmospheric Interest. *Earth System Science Data*, 5:365–373, December 2013. [doi: 10.5194/essd-5-365-2013].

[161] L. S. Rothman, I. E. Gordon, R. J. Barber, et al. HITEMP, the high-temperature molecular spectroscopic database. *Journal of Quantitative Spectroscopy and Radiative Transfer*, 111(15):2139–2150, October 2010. [doi: 10.1016/j.jqsrt.2010.05.001].

[162] T. Delahaye, R. Armante, N. A. Scott, et al. The 2020 edition of the GEISA spectroscopic database. *Journal of Molecular Spectroscopy*, 380:111510, July 2021. [doi: 10.1016/j.jms.2021.111510].

[163] C. P. Endres, S. Schlemmer, P. Schilke, et al. The Cologne Database for Molecular Spectroscopy, CDMS, in the Virtual Atomic and Molecular Data Centre, VAMDC. *Journal of Molecular Spectroscopy*, 327:95–104, September 2016. [doi: 10.1016/j.jms.2016.03.005].

[164] M. Rey, A. V. Nikitin, Y. L. Babikov, and V. G. Tyuterev. TheoReTS – An information system for theoretical spectra based on variational predictions from molecular potential energy and dipole moment surfaces. *Journal of Molecular Spectroscopy*, 327:138–158, September 2016. [doi: 10.1016/j.jms.2016.04.006].

[165] M. Rey, A. V. Nikitin, B. Bézard, et al. New accurate theoretical line lists of 12CH4 and 13CH4 in the 0–13400 cm 1 range: Application to the modeling of methane absorption in Titan's atmosphere. *Icarus*, 303:114–130, March 2018. [doi: 10.1016/j.icarus.2017.12.045].

[166] M. Rey, A. V. Nikitin, and V. G. Tyuterev. Theoretical hot CH_4 lists up to T=2000K for astrophysical applications. *The Astrophysical Journal*, 789(1):2, June 2014. [doi: 10.1088/0004-637X/789/1/2].

[167] P. Irwin, L. Sromovsky, E. Strong, et al. Improved near-infrared methane band models and k-distribution parameters from 2000 to 9500 cm1 and implications for interpretation of outer planet spectra. *Icarus*, 181(1):309–319, March 2006. [doi: 10.1016/j.icarus.2005.11.003].

[168] J. E. Hansen and L. D. Travis. Light scattering in planetary atmospheres. *Space Science Reviews*, 16(4):527–610, October 1974. [doi: 10.1007/BF00168069].

[169] C. Tomasi, V. Vitale, B. Petkov, et al. Improved algorithm for calculations of Rayleigh-scattering optical depth in standard atmospheres. *Applied Optics*, 44(16):3320, June 2005. [doi: 10.1364/AO.44.003320].

[170] M. Sneep and W. Ubachs. Direct measurement of the Rayleigh scattering cross section in various gases. *Journal of Quantitative Spectroscopy and Radiative Transfer*, 92(3):293–310, May 2005. [doi: 10.1016/j.jqsrt.2004.07.025].

[171] H. C. Van de Hulst. *Light scattering by small particles*. Dover classics of science and mathematics. Dover Publications, New York, USA, 1981. [ISBN: 978-0-486-64228-4].

[172] C. F. Bohren and D. R. Huffman. *Absorption and scattering of light by small particles*. Wiley, New York, USA, 1983. [ISBN: 978-0-471-05772-7].

[173] M. Wendisch and P. Yang. *Theory of atmospheric radiative transfer: a comprehensive introduction*. Wiley, 2012. [ISBN: 978-3-527-40836-8].

[174] P. Vanhellemont. *Remote sounding of the atmosphere by the Occultation Radiometer: an original retrieval method and study of the relaxation of Mount Pinatubo stratospheric aerosols*. PhD thesis, Royal Belgian Institute for Space Aeronomy, June 2001. [Bibliographic code: 7327].

[175] A. Krayem, F. Bernardin, and A. Münch. Identification of fog Particle Size Distribution by a radiative transfer equation inver-

sion. *Journal of Quantitative Spectroscopy and Radiative Transfer*, 317:108923, April 2024. [doi: 10.1016/j.jqsrt.2024.108923].

[176] J. M. Hartmann, C. Boulet, and D. Robert. *Collisional Effects on Molecular Spectra. Laboratory Experiments and Models. Consequences for Applications*. Elsevier, 2 edition, 2021. [ISBN: 978-0-12-822364-2].

[177] T. Karman, I. E. Gordon, A. Van Der Avoird, et al. Update of the HITRAN collision-induced absorption section. *Icarus*, 328:160–175, August 2019. [doi: 10.1016/j.icarus.2019.02.034].

[178] A. Borysow. Fortran program and data for modeling CIA opacities of various molecular complexes for application to planetary and stellar atmospheres, January 2002. https://www.astro.ku.dk/ aborysow/programs/.

[179] M. Zhou, Z. Deng, C. Robert, et al. The First Global Map of Atmospheric Ammonia (NH3) as Observed by the HIRAS/FY-3D Satellite. *Advances in Atmospheric Sciences*, 41:379–390, January 2024. [doi: 10.1007/s00376-023-3059-9].

[180] S. Aoki, K. Shiobara, N. Yoshida, et al. Depletion of 13C in CO in the Atmosphere of Mars Suggested by ExoMars-TGO/NOMAD Observations. *The Planetary Science Journal*, 4(5):97, May 2023. [doi: 10.3847/PSJ/acd32f].

[181] C. F. Wilson, E. Marcq, C. Gillmann, et al. Possible Effects of Volcanic Eruptions on the Modern Atmosphere of Venus. *Space Science Reviews*, 220(3):31, April 2024. [doi: 10.1007/s11214-024-01054-5].

[182] C. D. Rodgers. *Inverse methods for atmospheric sounding: theory and practice*. Number 2 in Series on atmospheric, oceanic and planetary physics. World Scientific, Singapore, 2000. [ISBN: 978-981-02-2740-1].

[183] G. P. Stiller, T. Von Clarmann, B. Funke, et al. Sensitivity of trace gas abundances retrievals from infrared limb emission spectra to simplifying approximations in radiative transfer modelling. *Journal of Quantitative Spectroscopy and Radiative Transfer*, 72(3):249–280, February 2002. [doi: 10.1016/S0022-4073(01)00123-6].

[184] C. Castagnoli, M. Lpez-Puertas, B. M. Dinelli, et al. Modelling of the CH4 limb radiance measured by Juno/JIRAM at Jupiter's mid-and equatorial latitudes. In *AGU Fall Meeting Abstracts*, volume 2023, pages P23C–307, December 2023. [Bibliographic code: 2023AGUFM.P23C.307C].

[185] L. N. Fletcher. NEMESIS for Newbies, June 2018. [Manuals].

[186] P. Irwin, S. B. Calcutt, and F. W. Taylor. Radiative transfer models for Galileo NIMS studies of the atmosphere of Jupiter. *Advances in Space Research*, 19(8):1149–1158, January 1997. [doi: 10.1016/S0273-1177(97)00266-4].

[187] S. N. Yurchenko, D. S. Amundsen, J. Tennyson, and I. P. Waldmann. A hybrid line list for CH_4 and hot methane continuum. *Astronomy & Astrophysics*, 605:A95, September 2017. [doi: 10.1051/0004-6361/201731026].

[188] J. Leconte. Spectral binning of precomputed correlated- k coefficients. *Astronomy & Astrophysics*, 645:A20, January 2021. [doi: 10.1051/0004-6361/202039040].

[189] S. Pérez-Hoyos, A. Sánchez-Lavega, J. F. Sanz-Requena, et al. Color and aerosol changes in Jupiter after a North Temperate Belt disturbance. *Icarus*, 352:114031, December 2020. [doi: 10.1016/j.icarus.2020.114031].

[190] R. S. Giles, L. N. Fletcher, and P. Irwin. Cloud structure and composition of Jupiter's troposphere from 5-um Cassini VIMS spectroscopy. *Icarus*, 257:457–470, September 2015. [doi: 10.1016/j.icarus.2015.05.030].

[191] L.A. Sromovsky and P.M. Fry. Jupiter's Cloud Structure as Constrained by Galileo Probe and HST Observations. *Icarus*, 157(2):373–400, June 2002. [doi: 10.1006/icar.2002.6844].

[192] P. Irwin, N. Bowles, A. S. Braude, et al. Analysis of gaseous ammonia (NH3) absorption in the visible spectrum of Jupiter - Update. *Icarus*, 321:572–582, March 2019. [doi: 10.1016/j.icarus.2018.12.008].

[193] M. Coutelier, D. Cordier, B. Seignovert, et al. Distribution and intensity of water ice signature in South Xanadu

and Tui Regio. *Icarus*, 364:114464, August 2021. [doi: 10.1016/j.icarus.2021.114464].

[194] G. Thuillier, M. Hersé, D. Labs, et al. The Solar Spectral Irradiance from 200 to 2400 nm as measured by the SOLSPEC spectrometer from the ATLAS and EURECA missions. *Solar Physics*, 214:1–22, May 2003. [doi: 10.1023/A:1024048429145].

[195] E. Lellouch, B. Bézard, T. Fouchet, et al. The deuterium abundance in Jupiter and Saturn from ISO-SWS observations. *Astronomy & Astrophysics*, 370(2):610–622, May 2001. [doi: 10.1051/0004-6361:20010259].

[196] A. Gonzalez, P. Hartogh, and M. Lara. Photochemistry in the Jovian atmosphere: preparation for water observations with Herschel. In *Advances in Geosciences: Planetary Science (PS)*, volume 25, pages 209–218. World Scientific, July 2011. [doi: 10.1142/9789814355377$_0$016.

[197] H. B. Niemann, S. K. Atreya, G. R. Carignan, et al. The composition of the Jovian atmosphere as determined by the Galileo probe mass spectrometer. *Journal of Geophysical Research: Planets*, 103(E10):22831–22845, September 1998. [doi: 10.1029/98JE01050].

[198] E. Karkoschka and M. G. Tomasko. Methane absorption coefficients for the jovian planets from laboratory, Huygens, and HST data. *Icarus*, 205(2):674–694, February 2010. [doi: 10.1016/j.icarus.2009.07.044].

[199] S. N. Yurchenko, A. Owens, K. Kefala, and J. Tennyson. ExoMol line lists – LVII. High accuracy ro-vibrational line list for methane (CH_4). *Monthly Notices of the Royal Astronomical Society*, 528(2):3719–3729, January 2024. [doi: 10.1093/mnras/stae148].

[200] I. E. Gordon, L. S. Rothman, C. Hill, et al. The HITRAN2016 molecular spectroscopic database. *Journal of Quantitative Spectroscopy and Radiative Transfer*, 203:3–69, December 2017. [doi: 10.1016/j.jqsrt.2017.06.038].

[201] R. J. Hargreaves, I. E. Gordon, M. Rey, et al. An Accurate, Extensive, and Practical Line List of Methane for the HITEMP Database. *The Astrophysical Journal Supplement Series*, 247(2):55, April 2020. [doi: 10.3847/1538-4365/ab7a1a].

[202] A. Anguiano-Arteaga, S. Pérez-Hoyos, A. Sánchez-Lavega, et al. Vertical Distribution of Aerosols and Hazes Over Jupiter's Great Red Spot and Its Surroundings in 2016 From HST/WFC3 Imaging. *Journal of Geophysical Research: Planets*, 126(11), November 2021. [doi: 10.1029/2021JE006996].

[203] P. Irwin. Gas Data. https://users.ox.ac.uk/ atmp0035/gas.html.

[204] B. A. Antipov and V. A. Sapozhnikova. Definitions and dimensions for gas absorption coefficients. *Soviet Physics Journal*, 17(3):398–400, March 1974. [doi: 10.1007/BF00893962].

[205] J. Erwin. pytran, July 2022. https://github.com/jterwin/pytran.

[206] ExoMol. The MM dataset for 12C1H4. https://www.exomol.com/data/molecules/CH4/12C-1H4/MM/.

[207] P. A. Coles, R. I. Ovsyannikov, O. L. Polyansky, et al. Improved potential energy surface and spectral assignments for ammonia in the near-infrared region. *Journal of Quantitative Spectroscopy and Radiative Transfer*, 219:199–212, November 2018. [doi: 10.1016/j.jqsrt.2018.07.022].

[208] N. Bowles, S. Calcutt, P. Irwin, and J. Temple. Band parameters for self-broadened ammonia gas in the range 0.74 to 5.24 m to support measurements of the atmosphere of the planet Jupiter. *Icarus*, 196(2):612–624, August 2008. [doi: 10.1016/j.icarus.2007.12.029].

[209] D. Grassi, A. Adriani, A. Mura, et al. Preliminary results on the composition of Jupiter's troposphere in hot spot regions from the JIRAM/Juno instrument. *Geophysical Research Letters*, 44(10):4615–4624, May 2017. [doi: 10.1002/2017GL072841].

[210] S. Guerlet, A. Spiga, H. Delattre, and T. Fouchet. Radiative-equilibrium model of Jupiter's atmosphere and application to estimating stratospheric circulations. *Icarus*, 351:113935, November 2020. [doi: 10.1016/j.icarus.2020.113935].

[211] P. Irwin, N. Bowles, A. Braude, et al. Analysis of gaseous ammonia (NH3) absorption in the visible spectrum of Jupiter. *Icarus*, 302:426–436, March 2018. [doi: 10.1016/j.icarus.2017.11.031].

[212] L. P. Giver, H. M. Jacob, and W. B. Robert. A laboratory atlas of the 51 NH3 absorption band at 6475 Å with applications to Jupiter

and Saturn. *Icarus*, 25(1):34–48, May 1975. [doi: 10.1016/0019-1035(75)90187-6].

[213] B. L. Lutz and T. Owen. The visible bands of ammonia - Band strengths, curves of growth, and the spatial distribution of ammonia on Jupiter. *The Astrophysical Journal*, 235:285, January 1980. [doi: 10.1086/157632].

[214] P. A. Coles, S. N. Yurchenko, and J. Tennyson. ExoMol molecular line lists – XXXV. A rotation-vibration line list for hot ammonia. *Monthly Notices of the Royal Astronomical Society*, 490(4):4638–4647, December 2019. [doi: 10.1093/mnras/stz2778].

[215] E. K. Conway, I. E. Gordon, A. A. Kyuberis, et al. Calculated line lists for H216O and H218O with extensive comparisons to theoretical and experimental sources including the HITRAN2016 database. *Journal of Quantitative Spectroscopy and Radiative Transfer*, 241:106711, January 2020. [doi: 10.1016/j.jqsrt.2019.106711].

[216] ExoMol. The POKAZATEL dataset for 1H216O. https://www.exomol.com/data/molecules/H2O/1H2-16O/POKAZATEL/.

[217] O. L. Polyansky, A. A. Kyuberis, N. F. Zobov, et al. ExoMol molecular line lists XXX: a complete high-accuracy line list for water. *Monthly Notices of the Royal Astronomical Society*, 480(2):2597–2608, October 2018. doi: 10.1093/mnras/sty1877].

[218] L. A. Sromovsky and P. M. Fry. The source of widespread 3-m absorption in Jupiter's clouds: Constraints from 2000 Cassini VIMS observations. *Icarus*, 210(1):230–257, November 2010. [doi: 10.1016/j.icarus.2010.06.039].

[219] P. Montañés-Rodríguez, B. González-Merino, E. Pallé, et al. Jupiter as an exoplanet: UV to NIR transmission spectrum reveals hazes, a Na layer, and possibly stratospheric H2O ice clouds. *The Astrophysical Journal*, 801(1):L8, February 2015. [doi: 10.1088/2041-8205/801/1/L8].

[220] A. L. Ford and J. C. Browne. Rayleigh and Raman cross sections for the hydrogen molecule. *Atomic Data and Nuclear Data Tables*, 5(3):305–313, 1973. [doi: 10.1016/S0092-640X(73)80011-7].

[221] A. Dalgarno and D. A. Williams. Rayleigh Scattering by Molecular Hydrogen. *The Astrophysical Journal*, 136:690, September 1962. [doi: 10.1086/147428].

[222] Y. M. Chan and A. Dalgarno. The refractive index of helium. *Proceedings of the Physical Society*, 85(2):227–230, February 1965. [doi: 10.1088/0370-1328/85/2/304].

[223] R. L. Kurucz. Atlas: a Computer Program for Calculating Model Stellar Atmospheres. *SAO Special Report*, 309, February 1970. [Bibliographic code: 1970SAOSR.309.....K].

[224] E. R. Peck and S. Huang. Refractivity and dispersion of hydrogen in the visible and near infrared. *Journal of the Optical Society of America*, 67(11):1550, November 1977. [doi: 10.1364/JOSA.67.001550].

[225] C. R. Mansfield and E. R. Peck. Dispersion of Helium. *Journal of the Optical Society of America*, 59(2):199, February 1969. [doi: 10.1364/JOSA.59.000199].

[226] S. Parthasarathy. Light Scattering in Gases. *Indian Journal of Physics*, 25:21–24, August 1951.

[227] G. Villanueva. Planetary Spectrum Generator (PSG). https://psg.gsfc.nasa.gov/.

[228] R. Mastrapa, M. Bernstein, S. Sandford, et al. Optical constants of amorphous and crystalline H2O-ice in the near infrared from 1.1 to 2.6 m. *Icarus*, 197(1):307–320, September 2008. [doi: 10.1016/j.icarus.2008.04.008].

[229] S. G. Warren and R. E. Brandt. Optical constants of ice from the ultraviolet to the microwave: A revised compilation. *Journal of Geophysical Research: Atmospheres*, 113(D14):2007JD009744, July 2008. [doi: 10.1029/2007JD009744].

[230] J. V. Martonchik, G. S. Orton, and J. F. Appleby. Optical properties of NH_3 ice from the far infrared to the near ultraviolet. *Applied Optics*, 23(4):541, February 1984. [doi: 10.1364/AO.23.000541].

[231] B. N. Khare, C. Sagan, W. R. Thompson, et al. Solid hydrocarbon aerosols produced in simulated Uranian and Neptunian stratospheres. *Journal of Geophysical Research:*

Space Physics, 92(A13):15067–15082, December 1987. [doi: 10.1029/JA092iA13p15067].

[232] F. Vitali. Experimental results on the H2-H2 and H2-He collisional-induced absorption coefficients at typical Jupiter's upper tropospheric conditions, February 2024. During MAJIS Science Team WG4 virtual meeting.

[233] A. Borysow. Collision-induced absorption coefficients of H_2 pairs at temperatures from 60 K to 1000 K. *Astronomy & Astrophysics*, 390(2):779–782, August 2002. [doi: 10.1051/0004-6361:20020555].

[234] L. Kedziora-Chudczer and J. Bailey. Modelling the near-infrared spectra of Jupiter using line-by-line methods: Modelling the spectra of Jupiter. *Monthly Notices of the Royal Astronomical Society*, 414(2):1483–1492, June 2011. [doi: 10.1111/j.1365-2966.2011.18488.x].

[235] F. Vitali, S. Stefani, G. Piccioni, et al. Experimental results on the H2-H2 and H2 -He collisional-induced absorption coefficients at typical Jupiter's upper tropospheric conditions. volume 12107, Vienna, Austria, March 2024. EGU. [doi: 10.5194/egusphere-egu24-12107].

[236] M. Abel, L. Frommhold, X. Li, and K. Hunt. Collision-Induced Absorption by H2 Pairs: From Hundreds to Thousands of Kelvin. *The Journal of Physical Chemistry A*, 115(25):6805–6812, June 2011. [doi: 10.1021/jp109441f].

[237] M. Abel, L. Frommhold, X. Li, and K. Hunt. Infrared absorption by collisional H2–He complexes at temperatures up to 9000 K and frequencies from 0 to 20 000 cm1. *The Journal of Chemical Physics*, 136(4):044319, January 2012. doi: [10.1063/1.3676405].

[238] M. A. López-Valverde, M. López-Puertas, B. Funke, et al. Modeling the atmospheric limb emission of CO2 at 4.3 m in the terrestrial planets. *Planetary and Space Science*, 59(10):988–998, August 2011. [doi: 10.1016/j.pss.2010.02.001].

[239] M. García-Comas, M. López-Puertas, B. Funke, et al. Analysis of Titan CH4 3.3m upper atmospheric emission as measured by Cassini/VIMS. *Icarus*, 214(2):571–583, August 2011. [doi: 10.1016/j.icarus.2011.03.020].

[240] A. Stolzenbach, M. Valverde, A. Brines, et al. Martian Atmospheric Aerosols Composition and Distribution Retrievals During the First Martian Year of NOMAD/TGO Solar Occultation Measurements: 1. Methodology and Application to the MY 34 Global Dust Storm. *Journal of Geophysical Research*, 128(11), November 2023. [doi: 10.1029/2022JE007276].

[241] F. Schreier, M. Milz, S. A. Buehler, and T. Von Clarmann. Intercomparison of three microwave/infrared high resolution line-by-line radiative transfer codes. *Journal of Quantitative Spectroscopy and Radiative Transfer*, 211:64–77, May 2018. [doi: 10.1016/j.jqsrt.2018.02.032].

[242] T. von Clarmann, A. Dudhia, D. P. Edwards, et al. Intercomparison of radiative transfer codes under non-local thermodynamic equilibrium conditions. *Journal of Geophysical Research: Atmospheres*, 107(D22):ACH 12–1–ACH 12–11, 2002. [doi: 10.1029/2001JD001551].

[243] L. S. Rothman, I. E. Gordon, Y. Babikov, et al. The HITRAN 2012 molecular spectroscopic database. *Journal of Quantitative Spectroscopy and Radiative Transfer*, 130:4–50, November 2013. [doi: 10.1016/j.jqsrt.2013.07.002].

[244] R. H. Brown, K. H. Baines, G. Bellucci, et al. The Cassini Visual and Infrared Mapping Spectrometer (VIMS) Investigation. *Space Science Reviews*, 115:111–168, November 2004. [doi: 10.1007/s11214-004-1453-x].

[245] D. Grassi. Definition of spectral masks for Jupiter science, October 2023. During MAJIS Science Team WG4 virtual meeting.

[246] European Space Agency (ESA). JUICE PJ12 Detailed Scenario Documentation, 2023. https://juicesoc.esac.esa.int/detailed_scenario/.

[247] European Space Agency (ESA). Events and Segments Visualisation and Coverage tool. https://juicesoc.esac.esa.int/event_tool/.

[248] European Space Agency (ESA). JSOC Uplink Core System. https://juicesoc.esac.esa.int/readonly_admin/.

[249] European Space Agency (ESA). JUICE Pointing Tool, 2017. https://juicept.esac.esa.int/starter/welcome.

[250] NASA. SPICE-enhanced Cosmographia Mission Visualization Tool, April 2024. https://naif.jpl.nasa.gov/naif/cosmographia.html.

[251] P. Haffoud, Y. Langevin, F. Poulet, et al. Radiometric Simulator of MAJIS Onboard the JUICE Mission: A Case Study of Jupiter Hotspot. In *54th Lunar and Planetary Science Conference, Texas, USA*, page 1430, 2023. [LPI Contrib. No. 2806].

[252] F. Mourlin. The MAJIS radiometric simulator tool. User Manual [JUI-IAS-MAJ-TN-102], IAS, Orsay, France, October 2024.

[253] G. H. Jones, C. Snodgrass, C. Tubiana, et al. The Comet Interceptor Mission. *Space Science Reviews*, 220(1):9, January 2024. [doi:10.1007/s11214-023-01035-0].

[254] D. Fussen, N. Baker, J. Debosscher, et al. The ALTIUS atmospheric limb sounder. *Journal of Quantitative Spectroscopy and Radiative Transfer*, 238:106542, November 2019. [doi:10.1016/j.jqsrt.2019.06.021].